LARGER AREA SINGLE CRYSTAL DIAMOND SUBSTRATE FORMATION WITH A MOSAIC TILING PROCESS

By

Ramón D. Díaz

A DISSERTATION

Submitted to
Michigan State University
in partial fulfillment of the requirements
for the degree of

Electrical Engineering - Doctor of Philosophy

2021

ABSTRACT

LARGER AREA SINGLE CRYSTAL DIAMOND SUBSTRATE FORMATION WITH A MOSAIC TILING PROCESS

By

Ramón D. Díaz

Diamond is a material known for its extraordinary optical, mechanical, thermal, and electrical properties. The ultra-low carrier density in intrinsic diamond makes it an extreme insulator, but it can be doped to achieve relatively high electrical conductivity. A wide band gap, high carrier saturation velocity, high dielectric strength, as well as the highest thermal conductivity of all materials, translate to figures of merit several orders of magnitude greater than silicon, making diamond stand out as the ultimate material for a new generation of electronic devices. The technology developed so far has not been able to take full advantage of this extreme potential because unlike Silicon, a straightforward method for producing large wafers of high-quality single crystal diamond has not yet been perfected.

This investigation explores the production of large area diamond substrates based on Microwave Plasma-Assisted Chemical Vapor Deposition to grow a continuous layer of single crystal diamond across an array of individual diamond plates in a process known as the mosaic technique. The project addressed a set of challenges related to this mosaic tiling technique, including developing high precision lattice orientation measurements; establishing the process of modifying individual orientations by laser cutting and polishing adjustments; developing a new tile assembly structure and fabrication process; and establishing the growth conditions necessary for uniform single layer diamond homoepitaxy as an extension on previous work optimizing crystal quality and area enlargement by enhanced lateral growth.

Several analysis techniques were developed as part of the investigation, such as Regional

Etch Pit Density Analysis and two independent relative misorientation measurements based on X-Ray Topography and X-Ray Rocking Curve scans. Definitions for characterizing the observations have been settled, coining new terms and concepts such as three types of relative misorientation: Tilt, Torsion and Twist, and new metrics such as Aggregate Mosaicity and a formal definition of what constitutes a Mosaic Boundary. The necessary conditions to evaluate when mosaic boundaries are indistinguishable from single crystal regions have been determined. New software was developed in MATLAB to analyze these new types of measurement metrics and measurement methods.

Thick samples were grown and produced with a total grown diamond thickness up to 4mm. The grown diamond of the mosaic plate was characterized at different thicknesses and how the mosaic boundary spread and position behaved and could be controlled throughout the process was studied. A clear set of substrate preparation and growth parameters were identified and listed as necessary conditions for successful mosaic growth serving as a roadmap leading to large area single crystal diamond substrates.

A process for the plate lift-off of diamond substrates via an ion implantation process followed by diamond growth and then electrochemical separation was investigated. Deposition parameters were refined to overcome known difficulties related to shallow implantations from low energy ion implantation of commercial providers. This lift-off process is a necessary final step in large area diamond plate fabrication, as the procedure is the only known reasonable way to produce large area plates with minimal material loss. Successful plate lift-off from low energy implantations performed by easily accessible commercial providers was demonstrated and this process will facilitate diamond plate production at industrial scales.

Progress established throughout this study resulted in plates composed of 4 tiles grown up to 10mm x 10mm using this mosaic tiling technique.

To my wife, Sandra, whose love and encouragement has made this possible.

ACKNOWLEDGMENTS

This project advanced with no significant setbacks and with constant incremental progress from start to finish. It would be unwise to take sole credit for this uncommon feat in experimental research, as there is a long list of contributors who have been essential throughout the process. Michigan State University has provided ideal conditions on many levels. All technical and human resources available on campus have been extraordinary.

I had the privilege of working with Dr. Grotjohn who has served as an excellent advisor. Technical advice was plentiful, but the best type of advice was always helping me identify what were the critical elements in the wide set of challenges presented throughout the investigation. The project itself was only possible by applying great work established by Dr. Asmussen and his students. This includes several whom I have only met through the product of their research, such as Jing Lu, Shreya Nad, and Yajun Gu. Amazing and unique results are much easier to obtain when working with amazing and unique systems that they all helped develop. The two most recent students, Amanda Charris and Matthias Muehle were proven to be extremely valuable throughout this investigation. Matthias was always readily available with hands-on experience, and Amanda has always been one quick call away with valuable feedback regarding the deposition system or her essential experimental results.

Aaron Hardy has been brilliant in handling everything related to diamond polishing, including all the necessary calculations for offcut adjustments, as well as all the laser-cutting operations. In other words, every practical application of the concepts covered in Chapter 6 has been a product of Aaron's skill in handling diamond samples with impressive precision.

All the X-Ray analysis developed throughout this investigation was made possible with constant support and feedback from Dr. Garratt and his students at the Measurement and

Analysis Group, including Shengyuan Bai and Erik Vyhmeister-Cancel. We have discussed concepts, techniques, and approaches for hours and hours on end. Always informative, and always productive. I hope we find a way to continue working together in the future. Paul Quayle has also been a valuable resource when discussing XRD measurements, as well as many other key concepts in this and other diamond growth projects.

At our research facilities, Fraunhofer USA in general has been outstanding at handling issues that inevitably arise from time to time. Jan Kamman and other members of the Systems Group were always extremely efficient in resolving technical issues with the equipment. I don't even remember having a full day off from a disabled system waiting for repairs. Same with the IT group led by Robert Rechenberg, who by the way, also frequently provided key advice with reactor operations.

Robert Bennett at the Physics Machine Shop always produced high quality sample holders. Working with Molybdenum is not easy, but you would never suspect it just by looking at the finished products. From the College of Engineering, Karl Dersch and Brian Wright were always amazingly effective in pulling the right tool from the right box within minutes whenever there was a technical issue.

It's not much of a surprise how such a friction-less and abundantly resourceful environment would inevitably lead to great work and great results.

TABLE OF CONTENTS

LIST OF TABLES

LIST OF FIGURES

Chapter 1

Introduction

1.1 Motivation

The semiconductor industry would be undeniably disrupted if some of the extraordinary electrical properties of grown Single Crystal Diamonds (SCD) such as high electric mobility, wide band gap, high saturation velocity and high breakdown voltage are raised close to their theoretical limits. Diamond electronic devices developed so far have not been able to take full advantage of their extreme potential because, unlike Silicon, a straightforward method for producing high volumes of ultra-pure diamond has not been perfected yet. Research efforts on techniques related to diamond doping [1] and device fabrication [2–4] have been progressing steadily, but the two fundamental factors limiting device development from reaching industrial scales are crystal quality and substrate size. Both limitations are bound by their own set of challenges [5], and so far, when efforts are directed towards achieving higher sample quality, the resulting size of the produced substrates are very limited, and if efforts are directed towards increasing the substrate size, there is an inevitable reduction in sample quality. The best example of this trade-off is heteroepitaxial growth, one prominent case has been reported by Schrek et. al. [6], where the group produced an SCD wafer with a diameter of 92 mm, but the dislocation density for this substrate is estimated up to $4 \times 10^7\,\mathrm{cm}^{-2}$. The project

outlined in this dissertation also prioritizes area expansion at the expense of sample quality by applying the mosaic technique, defined as tiling together separate substrates to generate a crystallographically aligned seed. Efforts have been directed at reducing defects generated at the interface from the inevitable lattice mismatch by improving the seed alignment process, and incorporating a series of additional parameters and growth strategies previously developed by our group which favors lateral growth and promotes the overall quality of the grown surface [7].

Mosaic large substrates are expected to have defective boundary regions between tiles, but this effect does not necessarily invalidate the approach. Many single crystal applications would greatly benefit from the increased area. Medium capacity device fabrication assembly lines, for example, are structured to work with a minimum of 4-inch diameter substrates. Most of the area on a mosaic large single crystal diamond wafers would still be composed of high quality material. The exact position of any defective regions would be known such that the patterning process can effectively distribute devices accordingly. Polycrystalline diamond plates are already being used in high energy particle detectors and is currently considered the best material for the application by all metrics [8, 9]. If the volume on these detectors were to be upgraded to single crystal, particle detector capabilities would certainly improve even further. Given how the potential for large area substrates can not be overstated on these and many other applications, this work is focused on maximum area gains by solving the challenges related to mosaic growth for diamond substrate production.

1.2 Research Objectives

This project is based on two fundamental concepts/conjectures: (1) tile alignment is critical, and (2) an improvement in lattice boundary quality is expected as samples grow thicker. This approach implies working on a series of challenges, which will be addressed and expanded throughout the rest of this document. A condensed summary of each challenge is outlined in the following list.

- Establishing measurement techniques to measure precise initial sample orientations.
- Developing procedures for adjusting and fine-tuning these orientations based on polishing and laser-cutting adjustments.
- Conserving alignments as mosaic seed assemblies are loaded onto the deposition system.
- Optimizing deposition parameters for direct lateral growth in order to conserve initial surface area as samples are grown thick over a series of deposition runs.
- Developing techniques to analyze boundary quality over grown layers.
- Determining how the known deposition parameters must be modified to maintain high quality growth over significantly larger areas.
- Exploring how this process can be reliably reproduced at high volumes for large area SCD plate production.

1.3 Dissertation Outline

This dissertation is divided in nine chapters. Chapter 2 covers all the significant information related to single crystal diamonds, including a list of many of its physical properties and how they compare with other materials and semiconductors, followed by some of the applications that have been produced and are expected from diamond based devices. This chapter

also outlines essential principles on diamond growth covering two relevant techniques, High Pressure High Temperature (HPHT) synthesis, and Chemical Vapor Deposition (CVD) with some quality/surface characteristics from each.

Chapter 3 summarizes all the literature review related to sample growth known to produce large area substrates and how they compare with each other.

Chapter 4 covers the experimental setup, including specific details on the Microwave Plasma Assisted CVD diamond reactors used in the study, and some of the processes used in sample preparation.

Chapter 5 includes all the analysis techniques that were applied and in some cases developed in the project to measure and analyze samples, and all the metrics related to boundary quality at mosaic interfaces.

Chapter 6 outlines the techniques that were developed to measure lattice orientations on each tile, and the process that was developed to align the mosaic seed.

Chapter 7 details the analysis tools that were developed to characterize mosaic boundaries based on x-ray rocking curve data.

Chapter 8 interprets the data obtained from the developed tools described in Chapter 7 and correlates the information with the other analysis techniques listed in Chapter 5.

Chapter 9 covers the developments and accomplishments obtained from exploring the low energy ion implantation and lift-off technique used to produce SCD plates.

Chapter 10 summarizes the accomplishments, comparing the obtained results with reported data from other groups. This section lists all the publications and patents originated from this study and evaluates the current status and pending work related to the mosaic technique.

Chapter 2

Background: Single Crystal Diamond

2.1 Diamond Properties

Diamond is universally listed as the highest valued precious gemstone. What is not well known is that in addition to its high subjective value, diamond is also ranked highest in a few other categories. For example, a thermal conductivity of $2200\,\mathrm{W\,m^{-1}\,K^{-1}}$ makes diamond the best heat conductor of all known materials. This value is four times higher than the second rated material, silver, and five times higher than copper [10]. Diamond is also the hardest of all materials, and in terms of optical properties, diamond is not only translucent in the visible range, it also holds the widest transmission window among all known materials, ranging from mid infra-red ($50\,\mu\mathrm{m}$) up to extreme ultra-violet ($220\,\mathrm{nm}$). Table 2.1 shows a detailed list of diamond properties as they compare with some of the most commonly known semiconductors.

All these extraordinary values emerge from its atomic structure, defined as a face centered cubic lattice with carbon atoms in two basis points: $\vec{\mathbf{b}}_1 = 0$ and $\vec{\mathbf{b}}_2 = \frac{a_0}{4}(\hat{\mathbf{x}} + \hat{\mathbf{y}} + \hat{\mathbf{z}})$, where a_0 is the conventional unit lattice constant, measuring approximately $0.357\,\mathrm{nm}$ at room temperature. The lattice is easier to visualize as the resulting pattern when every carbon atoms is arranged in a tetrahedral structure, forming sp^3 bonds, with each adjacent neighbor

	Diamond	Si	SiC	AlN	GaN	GaAs	Unit	References
Atomic Number	6	14	-	-	-	-	-	[11]
Atomic Density *	**1.77×10^{23}**	4.50×10^{22}	-	-	-	-	cm^{-3}	[11]
Displacement Energy †	42	20	25	19	32	9	eV/atom	[8, 12–15]
Debye Temperature *	**2230**	540	1200	1150	600	360	K	[11, 16]
Knopp Hardness *	**9000**	1150	2970	1230	1700	765	kg/mm^2	[17–20]
Young's Modulus *	**1100**	127	466	210	210	85	GPa	[21–25]
Fracture Toughness †	10.3	1.3	5.5	5.9	0.8	0.44	$MPa\,m^{1/2}$	[26–31]
Speed of Sound *	**18.4**	8.2	13.1	5.8	8.0	5.2	km/s	[32–35]
Thermal Conductivity (RT) *	**22.0**	1.5	4.9	2.8	2.1	0.55	W/(cm K)	[36–39]
Bandgap	5.48	1.12	3.27	6.09	3.4	1.4	eV	[36, 37, 40, 41]
Resistivity †	1×10^{16}	2×10^5	1×10^6	6.9×10^3	3×10^7	1×10^9	Ω cm	[37, 42–44]
Intrinsic Carrier Density *	**1×10^{-27}**	1.1×10^{10}	5×10^{-9}	9.4×10^{-34}	1.9×10^{-10}	1×10^6	cm^{-3}	[25, 45–48]
Electron Mobility	4500	1400	900	4500	2000	8500	$cm^2/(V\,s)$	[36, 38]
Hole Mobility †	3800	450	120	14	50	400	$cm^2/(V\,s)$	[36, 49, 50]
Electron Saturation Velocity †	2.7	1.0	2.0	1.4	2.5	2.0	$\times 10^7$ cm/s	[37, 38]
Breakdown Field	10.0	0.3	3.0	15.0	2.5	0.4	MV/cm	[36, 38]
Dielectric Constant	5.7	11.9	9.7	8.5	8.9	12.9	-	[36–38]
Optical Transparency (min) *	**225**	1,200	450	300	350	900	nm	[23, 39, 51, 52]
Optical Transparency (max) *	**100,000**	15,000	7,500	6,500	7,500	20,000	nm	

Table 2.1 Physical properties of diamond compared to silicon and some of the most widely applied materials in the semiconductor industry. The table is divided in four parts; atomic, mechanical, electronic, and optical properties. Highlighted values show some of the cases where diamond is ranked highest among all known materials (∗), or highest among some of the most commonly used semiconductors (†).

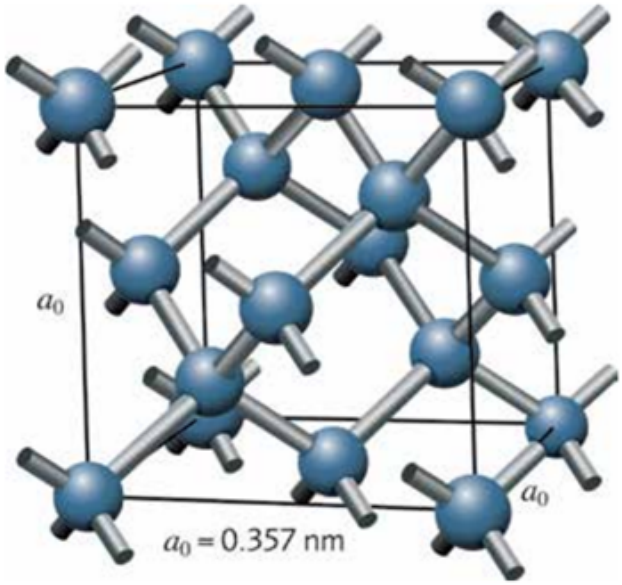

Figure 2.1: Face Centered Cubic Diamond lattice. Blue spheres represent carbon atoms, and gray connectors represent sp^3 bonds between them [53]. For interpretation of the references to color in this and all other figures, the reader is referred to the electronic version of this thesis.

as illustrated in Figure 2.1. The diamond structure has a atomic packing factor of 34%, which is low relative to closed packed structures such as the single basis FCC with a factor of 74%, but carbon is a small and lightweight atom, which results in diamond having the highest atomic density of all materials and a relatively high overall density of $3.515\,\mathrm{g/cm^3}$. Strong covalent bonds on such a dense structure leads to all its outstanding thermal and mechanical properties.

2.2 Diamond Applications

Intrinsic diamond is an extreme insulator, but when doped, it has high carrier mobilities which lead to applications that require high electrical currents [36]. A high band gap and high mobility leads to high power diodes. If you include the high saturation velocity it should lead to high frequency transistors. These combinations of properties, defined as Figures of Merit (FOM), are listed in Table 2.2 and are considered measures to evaluate the utility of general materials for specific applications. In most cases, diamond stands out as the ultimate material for device fabrication.

Figure of Merit	Definition	Si	SiC	GaN	Diamond	Application	Ref.
Baliga [54]	$BFOM = \varepsilon\mu E_g^3$	1	440	2,950	473,078	High Voltage Unipolar Devices	[3]
Baliga HF [54]	$BHFOM = \mu E_B^2\sqrt{\frac{V_G}{4V_B^3}}$	1	58	237	12,510	High Freq. Unipolar Switches	[3]
Johnson [55]	$JFOM = E_B^2 v_s^2/4\pi^2$	1	410	280	8200	High Freq. Power Transistors	[56]
Keyes [57]	$KFOM = \kappa\sqrt{cv_s/4\pi\varepsilon}$	1	5.1	0.8	32	High Speed Switches	[56]

Table 2.2 Figures of Merit, normalized with respect to silicon, where ε is the dielectric constant, μ is the carrier mobility, E_g is the bandgap, E_B is the critical breakdown field, V_G is the gate drive voltage, V_B is the breakdown voltage, v_s is the saturation velocity, κ is the thermal conductivity, and c represents the speed of light.

Any application relying on a high Baliga FOM, especially those cases where high temperatures, or heat dissipation is critical, could potentially benefit from diamond-based power devices. Improvements on bipolar junction transistors [58], Schottky diodes [59], Field Effect Transistors [60], MOSFETs [61], UV LEDs [62], and even tunable LEDs [63] are improving every year. Taking the high carrier mobility and high carrier velocity of diamond into account means that high power could also be handled at high frequencies, as evaluated by the Johnson FOM, with applications such as broadcasting stations, radar systems, and many other Radio Frequency technologies. Diamond could be the first solid state device built to handle cases like communication satellites, where vacuum tubes are still used due to lack of materials capable of operating at ranges as high as 120 W at 10 GHz [64].

There is a wide array of applications besides electronic device fabrication which make use of many of the extraordinary properties of diamond, such as the wide transparency range for optical components including high power lasers [65] and Raman lasers [66, 67] as the Raman figure of merit is also greatly enhanced with respect to competing technologies [68, 69].

When we consider the extended transparent electromagnetic window, which ranges below 0.4 nm with very low absorption, this makes diamond useful for X-Ray optical components [70–73], and detectors [74]. Superior thermal conductivity leads to almost two orders of magnitude greater heat dissipation rate relative to other optical materials. Additional benefits, such as high fracture toughness and large Young's modulus, lead to mechanically stable thinner designs. Considering diamond's hardness, this leads to an added benefit of ultimate scratch resistance.

Extremely low charge carrier density combined with high radiation hardness and high thermal conductivity makes diamond the perfect material for designing high energy particle detectors [8, 40, 75, 76]. Silicon sensors on the other hand need to be replaced frequently

from radiation damage. When compared with other materials such as germanium and gallium nitride, diamond is also shown to have better signal to noise ratio, less multiple scattering, faster timing, less disturbance in charge center of gravity and much better particle identification capabilities, the only drawback listed with diamond is their available size [9].

In terms of mechanical properties, apart from hard coatings [77], single crystal diamonds are useful in other fields. For example, nanomechanical resonators operating in the GHz range have been produced due to the rigidity from its Young's modulus [78], and SCD based resonators have been able to reach quality factors (Q-factor) exceeding 1 million [79].

In terms of detectors, diamond can also be used in dosimetry applications for quantifying the effect of heavy charged ions, which is a significant component of galactic cosmic rays. As diamond is composed of carbon atoms, diamond based sensors hold tissue equivalence, avoiding the need for atomic number correction factors. Diamond based technology may even lead to radioprotection applications in space environments [80].

When considering thermal and chemical stability, as boron doped diamond holds the widest solvent window of all electrode materials in aqueous solutions, it is perfect for harsh environments. Some of these properties are ideal for electrochemical sensing [81], and advanced oxidation processes [82]. An additional benefit of diamond is how it is composed of carbon atoms, making it extremely bio-compatible with applications in medical fields [83, 84].

A new field currently being explored is based on applying the quantum mechanical behavior of NV^- centers, a specific kind of point defect in the diamond lattice, to design ultra-precise magnetic sensors with sub-pico-Tesla level resolution [85], or using each defect as a single qubit for quantum computing [86–88].

The list of current and potential applications is virtually endless and is expected to expand rapidly as larger diamond substrates become readily available.

2.3 Single Crystal Diamond Growth

2.3.1 Carbon Phase Diagram

Graphite is the most stable carbon allotrope under atmospheric conditions up to a wide range of pressures and temperatures, as can be seen in its phase diagram illustrated in Figure 2.2.

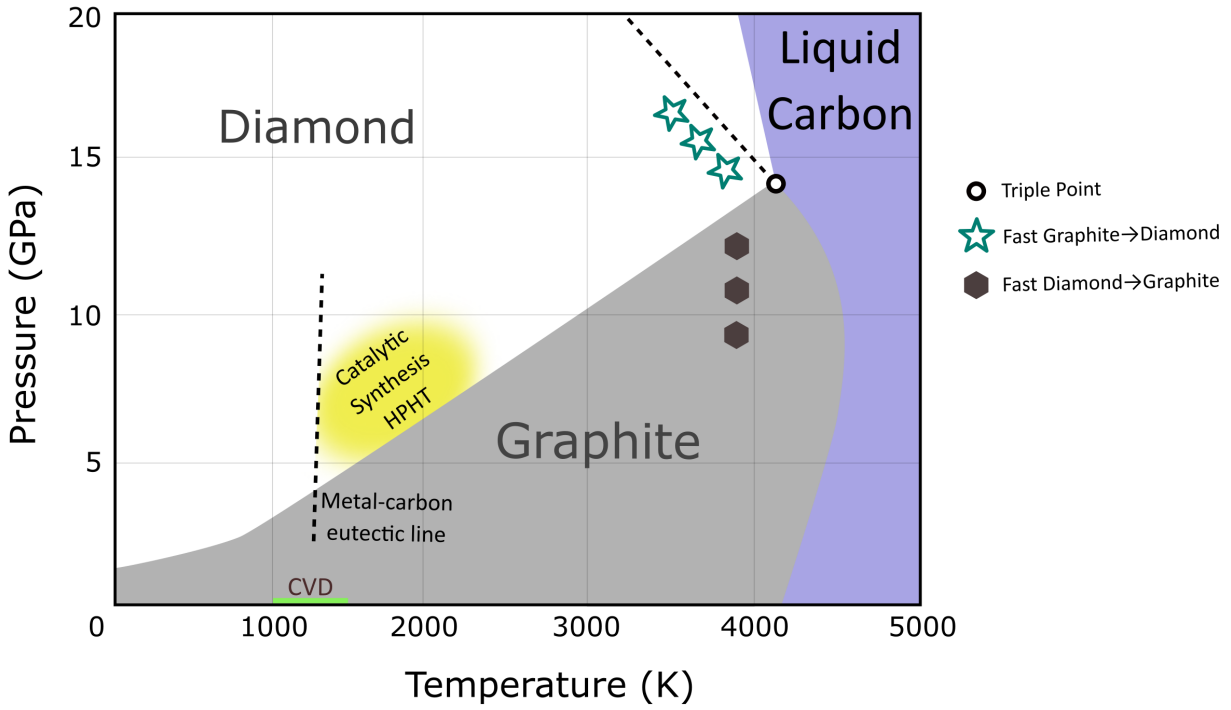

Figure 2.2: Carbon phase diagram, adapted from [89], [90], [36], and [32].

The relatively high melting point at 4000 K over this illustrated range is direct evidence of the strong sp^2 and sp^3 covalent bonds between carbon atoms. Phase transitions from graphite to diamond have been widely studied [91–94] and there is no clear consensus for exact transition mechanisms, but the ultimate energy differences are known. Diamond is 0.02 eV/atom less stable than graphite at 0 K [95], but the tetrahedral configuration of diamond has a very high cohesive energy of 717 kJ/mol [96], translating to a high activation barrier over this phase transition, which makes for an extremely slow, virtually undetectable

conversion rate. Faster transitions in both directions are observed only as conditions approach the diamond/graphite/liquid triple point [90, 97]. The two main synthesis techniques where carbon conserves its diamond meta-stable structure under atmospheric conditions are the High Pressure High Temperature (HPHT) technique, and Chemical Vapor Deposition (CVD). Operational ranges for both techniques are overlaid in the figure and will be covered in the following sections.

2.3.2 HPHT Diamond Synthesis

HPHT Diamond synthesis, first reported in 1955 [98], is achieved by using a large multi-anvil press. An example of this approach is the split sphere design [99], illustrated in Figure 2.3.

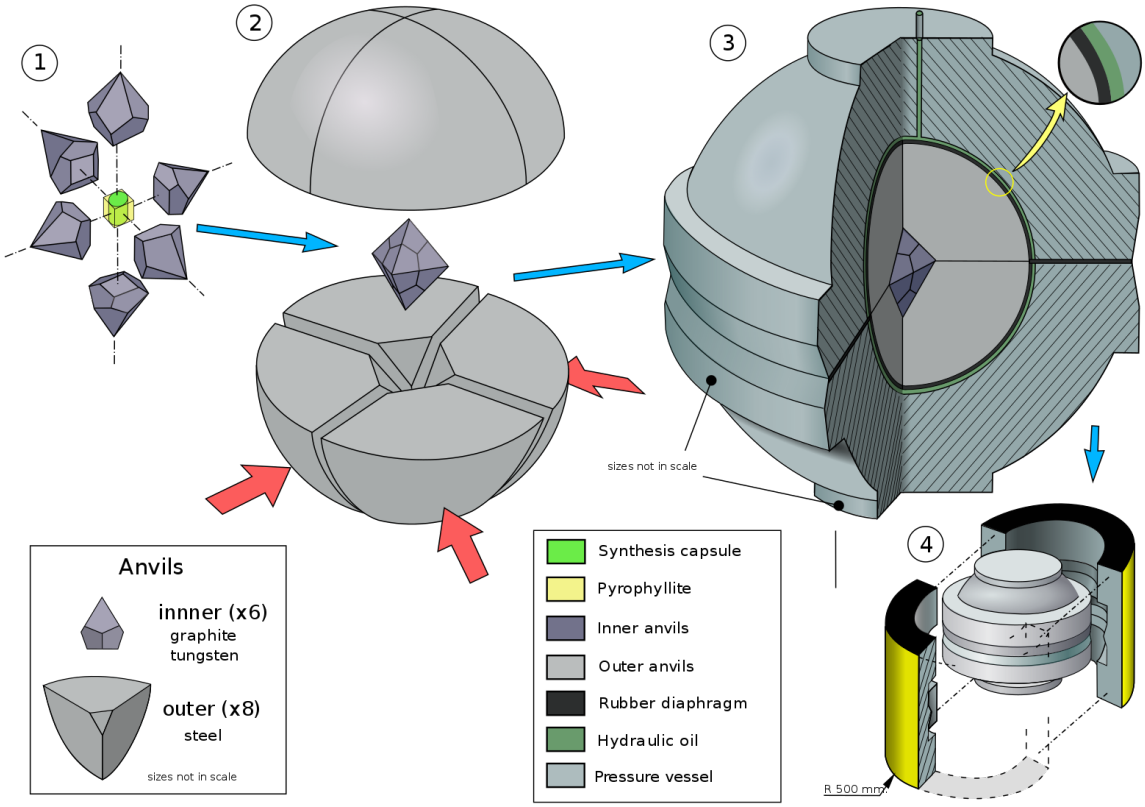

Figure 2.3: Schematic of a BARS type HPHT synthesis system. The BARS acronym derives from the Russian translation of a "press-free high-pressure split-sphere setup" [100].

Spontaneous graphitization is not easily avoided, especially when the synthesis conditions should be as close as possible to the triple point, which implies temperatures and pressures as high as 3200 K and 15 GPa, as estimated in Figure 2.2. One way to avoid these extreme values is by using a different strategy based on creating an eutectic mixture of carbon from a high purity graphite source, and liquefied metal, typically Fe, Co or Ni [101]. The approach in essence is to control the conditions, which for these mixtures can be as low as 1300°C and 5.5 GPa [36], such that carbon supersaturates the solution. As the solution is cooled through a temperature gradient, carbon atoms will then proceed with secondary nucleation over the structure of a strategically placed diamond seed in the capsule increasing its volume at a rate as high as 20 mg/h [99].

Given how controlling the amount of impurities in the precursor down to electronic grade levels is next to impossible with this method, most of the samples grown using this technique have a high impurity content. These synthesized diamonds are, for example, typically yellow in color as they contain 10-100ppm N_2 from the atmosphere [36]. As crystal planes tend to grow at different rates, any sample large enough will eventually exhibit growth sectors as illustrated in Figure 2.4.

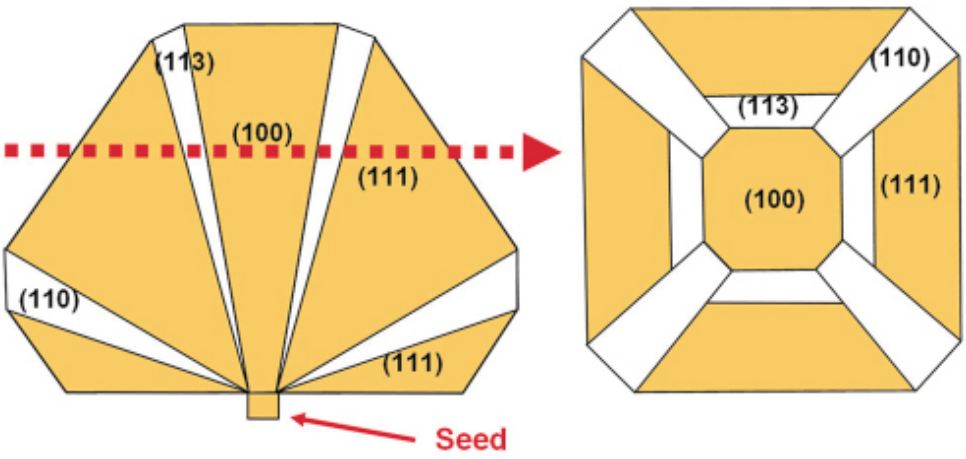

Figure 2.4: Growth sectors emerging from an HPHT synthesis. [102]

As impurities tend to be incorporated at different rates depending on the orientation of the crystal facet [103–105], these will not necessarily be uniformly distributed over the grown sample, as seen by the different cross-sections in Figure 2.5. These characteristic shapes over produced wafers are in many cases visible with the naked eye, and will be present in some of the larger seeds used in this study.

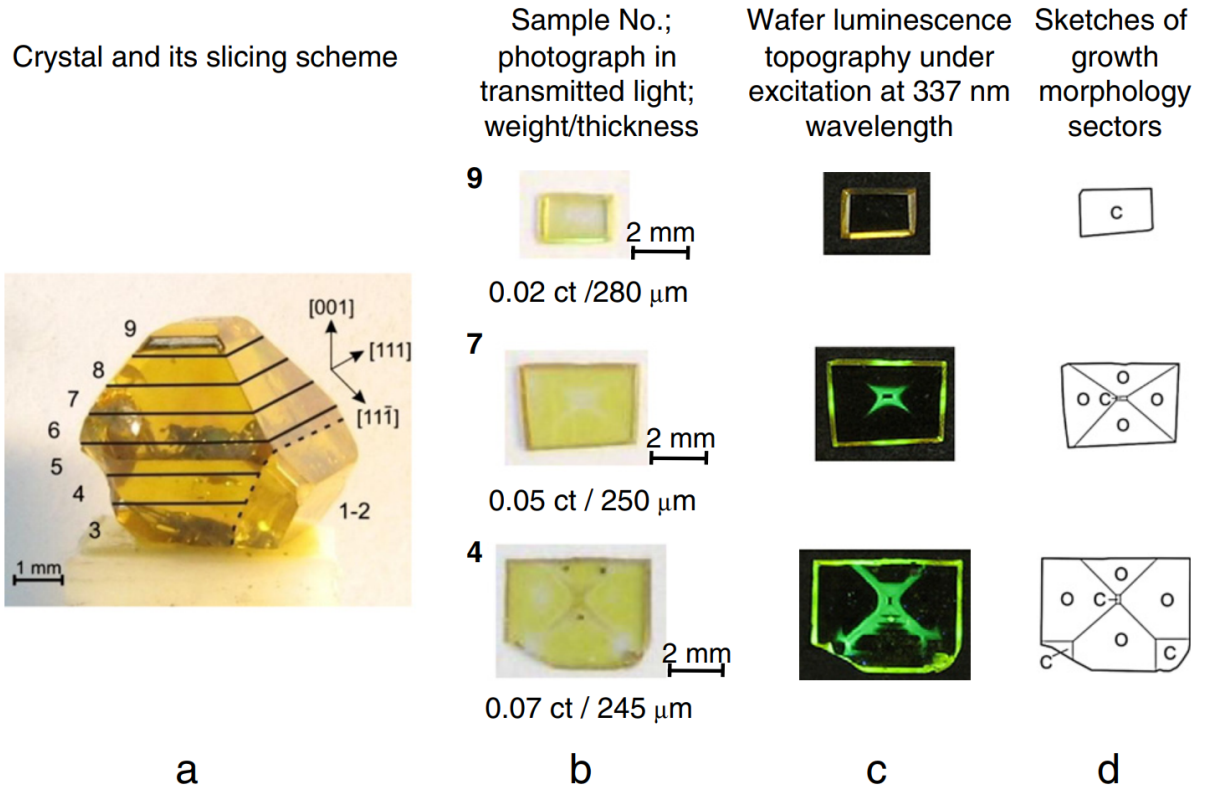

Figure 2.5: (a) As-grown crystal and corresponding scheme of wafers sliced from the sample; (b) Weight, dimensions and pictures of the as-polished diamond wafers taken in transmitted light (c) Fluorescence topographs under excitation by ultraviolet light (d) Idealized sketches of growth-morphology sectors. "C" denotes cube sectors, "O" indicates octahedral sectors. [106]

Even though the impurity content and their distribution density over HPHT diamonds are not ideal, the crystallinity obtained from this technique is extraordinarily high [107], making these samples particularly useful as crystallographic seeds for other growth methods that require an initial crystal structure as part of the process.

Throughout this document, HPHT seeds illustrated in a diagram or schematic will be colored with uniform yellow hues to identify their shape and placement.

2.3.3 CVD Diamond Growth

Chemical Vapor Deposition is defined as the process of chemically reacting a volatile compound of a material to be deposited, with other gases, to produce a non-volatile solid that deposits atomistically on a suitably placed substrate [108]. There are many variants on this approach, but every CVD process will follow a series of sequential steps, as outlined by Ohring [108]:

1. Transport of reactants from gas inlets to the reaction zone.
2. Activating chemical reactions in the gas phase producing new reactive species.
3. Transport of reactants and new products to the substrate surface.
4. Adsorption of reactive species on the substrate surface.
5. Surface reactions leading to film formation.
6. Desorption of volatile by-products from surface reactions.
7. Transport of by-products away from the reaction zone.

Diamond growth using chemical vapor deposition narrowly pre-dates HPHT synthesis [32,109], but was publicly reported years later with a patent in 1962 by William G. Eversole [110]. The reactant gas used in the process was carbon monoxide (CO) making gas-solid contact with diamond powder at pressures of 20-2500atm with temperatures of 900-1100°C. Eventually, more effective reactant combinations and ways to generate activation energies were developed such as using a 6 kW Xenon tube [111], or focusing high intensity infrared lamps [112]. One process developed in the early 1980's and still widely used to this day is based on flowing an electrical current through a tungsten filament to generate thermal energy for activation.

This process, relevant for the literature review discussed in the next chapter, is known as Hot Filament Chemical Vapor Deposition (HFCVD) [113]. The early years of diamond growth by CVD has been described by J.C. Angus [114], a key figure in the early development of the deposition techniques. The historical review paper covers a conceptual overview of explored chemical precursors and activation techniques leading up to the latest and most common approach today: microwave plasma activation, first developed by Kamo et. al. [115]. This microwave plasma based approach has dominated for decades the vast majority of leading edge research on diamond growth, and over the years has expanded into a very wide array of applications and commercial implementations all over the world [116–125]. The latest iteration along the branch of systems developed at Michigan State University [126–128] has been the Type C reactor used for this investigation. The reactor has been described previously in full detail [129], but an overview of the system and mode of operation is outlined in Chapter 4 where the applied experimental setup for this project has been summarized.

2.3.3.1 Surface Chemistry

A wide set of chemical compounds and potential gas mixtures based on carbon have been explored [130], but present day CVD reactors including Microwave Plasma and Hot Filament systems have settled on using hydrogen (H_2) and methane (CH_4) as the main gas reactants at an approximate ratio of 20:1. Even though the gas activation technique and species transport mechanisms might be significantly different depending on system configurations, the chemical reactions leading to species adsorption and desorption are considered similar for CVD diamond growth when based on this mixture. The vapor-solid surface reactions assume activation of the input reactants generating multiple ionized species, the most critical of which is a necessarily large concentration of hydrogen radicals (H^*). It was known early

on [131–136] that the reactant combination must rely heavily on hydrogen as these radicals serve several key roles in the reaction mechanisms:

1. Carbon containing radical activation - Atomic hydrogen initiates exothermic processes in the discharge region that lead to production of carbon containing free radicals such as methyl (CH_3^*) [114], the basic building block in diamond epitaxy.
2. Maximizing Carbon solubility - With hydrogen, carbon reaches a maximum "solubility" as defined by Anthony [134] at $1000^\circ C$, leading to the largest possible number of carbon containing free radicals near this temperature.
3. Preventing Polymer Build-up - Hydrogen radicals react readily with long-chain hydrocarbons preventing polymers in the gas phase and polymer build-up in the surface of the sample. [137]
4. Graphite Etching - H radicals can react with any carbon dimer, but they will preferentially etch sp^2 sites much faster than sp^3 sites [138], therefore, when exposed long enough to ionized hydrogen, only diamond surfaces remain available for chemical interaction.
5. Surface Stabilization - Dangling bonds on diamond surfaces are inherently unstable, but if the sites are terminated with single hydrogen radicals, the sp^3 coordination of carbon atoms can be maintained, stabilizing the exposed surface [134, 139].
6. Vacant surface site production - The hydrogen-carbon bond is stronger than the carbon-carbon bond, which suppresses growth on a hydrogen terminated surface, but plenty of hydrogen radicals can still react with hydrogen terminations, temporarily activating the bond site for hydrocarbon chemisorption [131].
7. Abstraction of hydrogen from hydrocarbons at the surface - Hydrocarbons attached to

a diamond activated site are not structurally stable, for example CH_3^* has a trihydride structure, which is readily etched by hydrogen radicals [140]. As hydrogen atoms are removed from the hydrocarbons at surface sites, the remaining carbon atoms systematically build upon the pre-existing diamond structure.

In terms of chemical reactions, the full set of possible hydrocarbon radicals that can be generated in the activated gas phase ranges from carbon monoxide to poly-cyclic aromatic carbons and can reach a total as high as 28 chemical species, with a combined 131 elementary reactions between them [141]. The most widely accepted theoretical mechanism leading to diamond epitaxy under these conditions is a simplified vapor-surface interaction described by the Harris-Goodwin model [142–144], where the only significant hydrocarbon species produced from methane CH_4 are methyl radicals CH_3^*. We can begin the model with a diamond seed that has been exposed to a hydrogen plasma discharge, resulting in a full hydrogen terminated surface where each site is represented by the notation: $C_d - H$. The set of five reactions begin with a steady state dynamic equilibrium of hydrogen abstraction (2.1), where an activated site is created at the diamond surface C_d^*, followed by hydrogen adsorption (2.2) where the site returns to a state of hydrogen termination. For all reactions, k_n are defined as the resulting reaction rates, with n corresponding to each direction.

$$C_d - H + H^* \xrightarrow{k_1} C_d^* + H_2 \tag{2.1}$$

$$C_d^* + H^* \xrightarrow{k_2} C_d - H \tag{2.2}$$

The rate at which open sites are activated are given by the ratio $\frac{k_1}{k_1+k_2}$, which should be set as high as possible to promote diamond growth [145]. According to Silva et. al., this value

depends only on surface temperature [146]. Diamond growth begins when CH_3^* radicals are adsorbed on an open site, which can also be desorbed as a reversible reaction (2.3).

$$C_d^* + CH_3^* \underset{k_4}{\overset{k_3}{\rightleftharpoons}} C_d - CH_3 \tag{2.3}$$

When two separate hydrogen radicals react with the exposed hydrogen bonds from the adsorbed methyl radical (2.4) and (2.5), the carbon atom is effectively bonded and hydrogen terminated at the diamond site.

$$C_d - CH_3 + H^* \xrightarrow{k_5} C_d - CH_2^* + H_2 \tag{2.4}$$

$$C_d - CH_2^* + H^* \xrightarrow{k_6} C_d - C_d - H + H_2 \tag{2.5}$$

Figure 2.6 shows a simplified schematic illustrating the Harris-Goodwin diamond growth model. If we combine the reaction rates, surface density n_s, and molar density n_d with the hydrogen and methyl concentrations at the surface $[H]_s$ and $[CH_3^*]_s$, we can calculate [143] the resulting growth rate (2.6).

$$G = k_3 \frac{n_s}{n_d} \left(\frac{k_1}{k_1 + k_2} \right) \frac{[\mathrm{CH_3^*]_s[H]_s}}{\frac{k_4}{k_5} + [\mathrm{H}]_\mathrm{s}} \tag{2.6}$$

With $n_s \approx 2.61 \times 10^{-9}\,\mathrm{mol\,cm^{-1}}$ for $\{001\}$ surfaces, molar density of $n_d \approx 0.2939\,\mathrm{mol\,cm^{-3}}$, and reaction rates given by Goodwin [143], under an approximate surface concentration of $[H]_s \approx 10^{-8}\,\mathrm{mol\,cm^{-3}}$ with 5% methane, the resulting growth rate is $G_{\{001\}} = 50\,\mu\mathrm{m\,h^{-1}}$, close to the $30\,\mu\mathrm{m\,h^{-1}}$ reported for Reactor Type C [7].

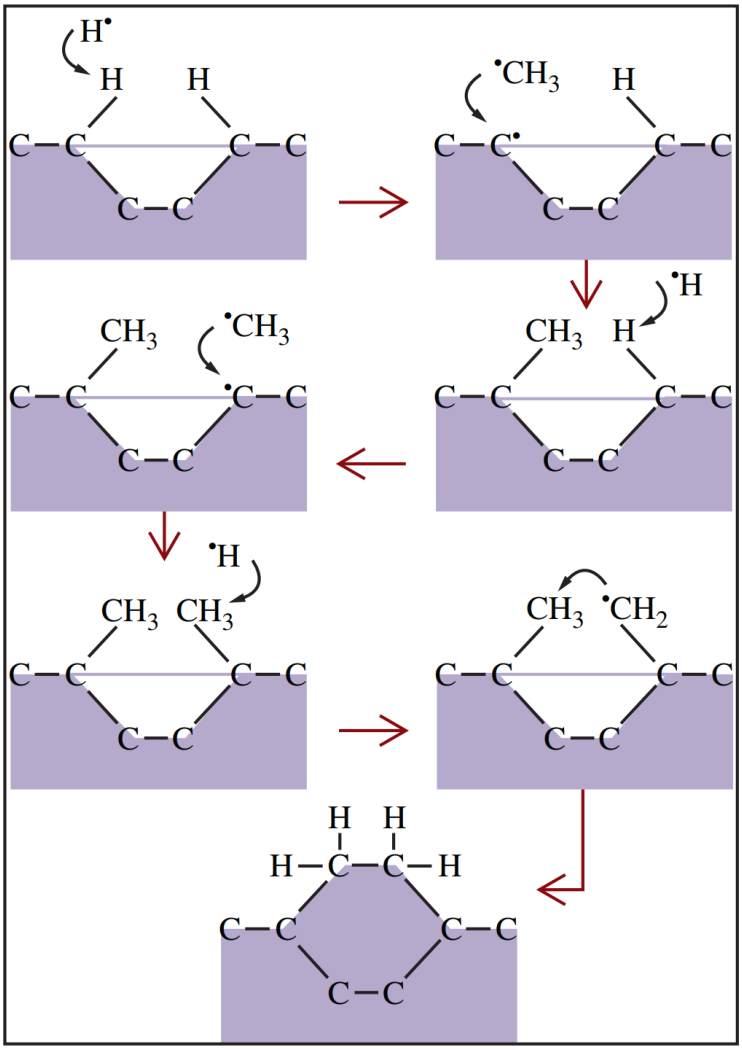

Figure 2.6: Schematic illustrating site activation, methyl adsorption and dehydrogenation leading to diamond growth [137].

2.3.3.2 Step Flow Growth

When we expand our focus from growth at individual sites up to growth over atomic surfaces, one possibility is for hydrogen atoms, methyl, and other carbon containing bridging groups to migrate in two dimensions. Hydrogen and surface radical migrations between sites are computed to be fast, and nearly isotropic in both directions along dimer chains and rows [147]. If we consider that these vicinal crystal planes do not necessarily coincide with the top facet of the substrate, adsorbed species are then forced to interact with a surface which now has

monoatomic discontinuities, illustrated in Figure 2.7, and defined as Terraces, Steps, and Kinks [148, 149]. Migration over steps and terraces are both listed as examples of diffusion in Figure 2.8, but given how the potential energy of an atom's position on a crystal is determined by the number of bonds shared with neighboring atoms, the energy barriers required to overcome the thermodynamic stability associated with each site are not necessarily equal.

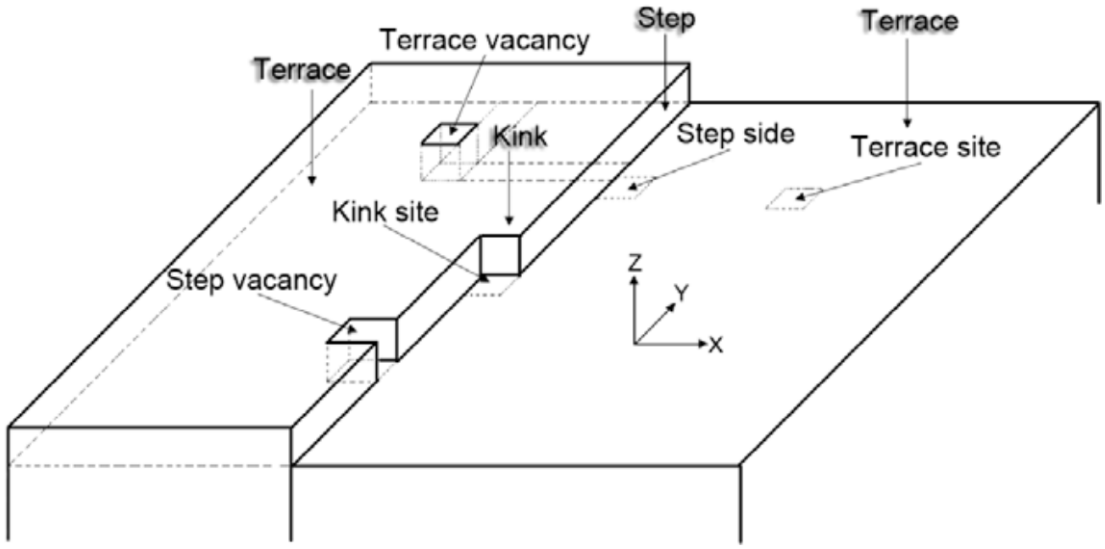

Figure 2.7: Schematic diagram of a substrate surface as described by the Terrace-Step-Kink model. The illsutrated terraces correspond to vincinal planes within the crystal [150].

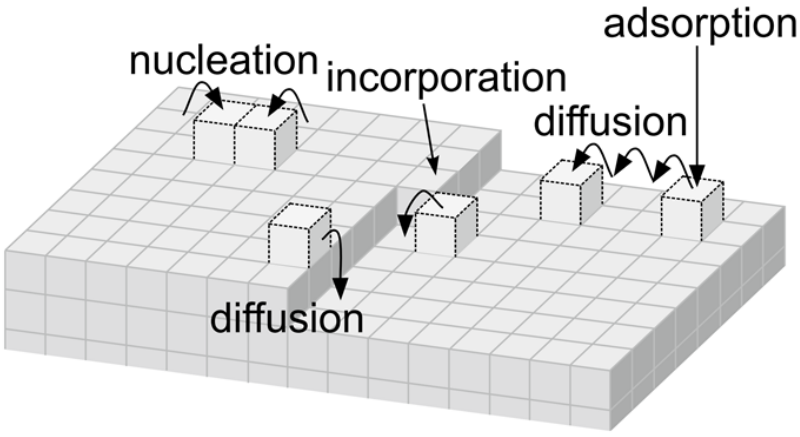

Figure 2.8: Schematic of atomistic rate processes in epitaxial growth. Diffusion can proceed laterally across a terrace, or over a step, but energy barriers are not equal for both cases. [151].

We can lay out an intuitive picture of the energy barriers associated with diffusion across terrace steps if we consider the net difference in number of nearest neighbors between adsorption sites. Movement across a relatively wide terrace requires a minimal amount of energy with no net change in nearest neighbors. Movement from upper to lower terraces require overcoming an additional energy barrier as the adsorbed species detaches from second nearest neighbors at the upper terrace during the transition. In the opposite direction, movement from lower to upper terraces require the largest amount of activation energy as atoms from the lower terrace share at least two direct neighbors. The resulting configuration is known as the Ehrlich-Schwoebel barrier [152,153], illustrated in Figure 2.9a. The associated energy profile leads to at least two main effects, the first being a net asymmetry in the probability of adspecies being captured across terraces, and a net shifting position of these edges as steps advance laterally through incorporation of species diffusing onto step sides as this results in the most stable configuration. Both effects are illustrated in Figure 2.9b.

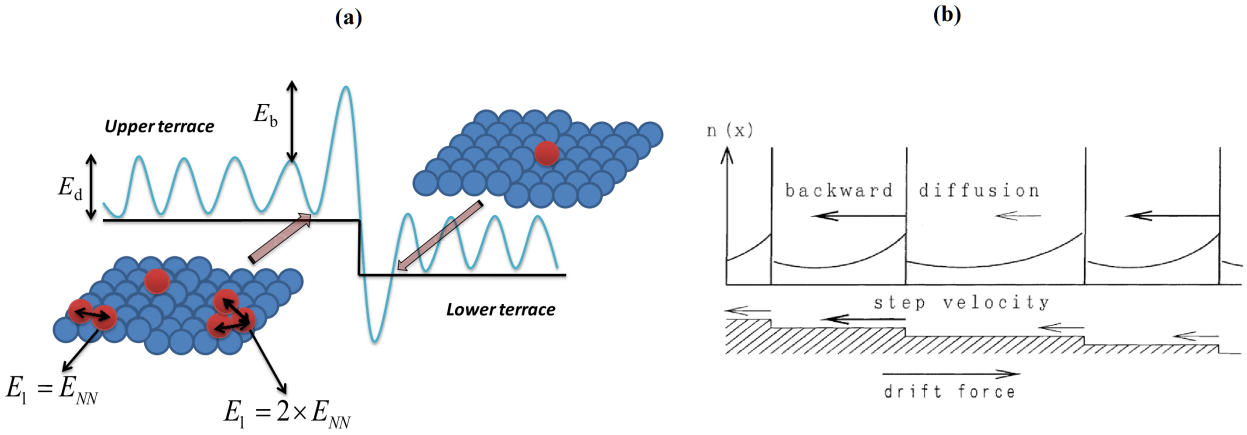

Figure 2.9: a) Energetic barrier of single or bonded adspecies (red spheres) near vincinal planes (blue spheres). E_d corresponds to potential energy fluctuations in free adspecies over terrace planes, E_{NN} represents single nearest neighbor bonding energy and E_l the net lateral bonding energy. E_b is the energy required to overcome migration from upper to lower terraces [154]. b) Density profile $n(x)$ of adspecies over a terraced surface under steady-state conditions and a net lateral movement represented as a dirft force resulting from energy differences across terrace steps [155].

A final effect from these conditions is how terraces with larger areas will adsorb more species, making individual step velocities proportional to their corresponding terrace widths. Slight variations in size from random initial conditions will then reinforce step velocities in a positive feedback loop leading to step bunching as some of the smaller terraces will tend to disappear as illustrated in Figure 2.10.

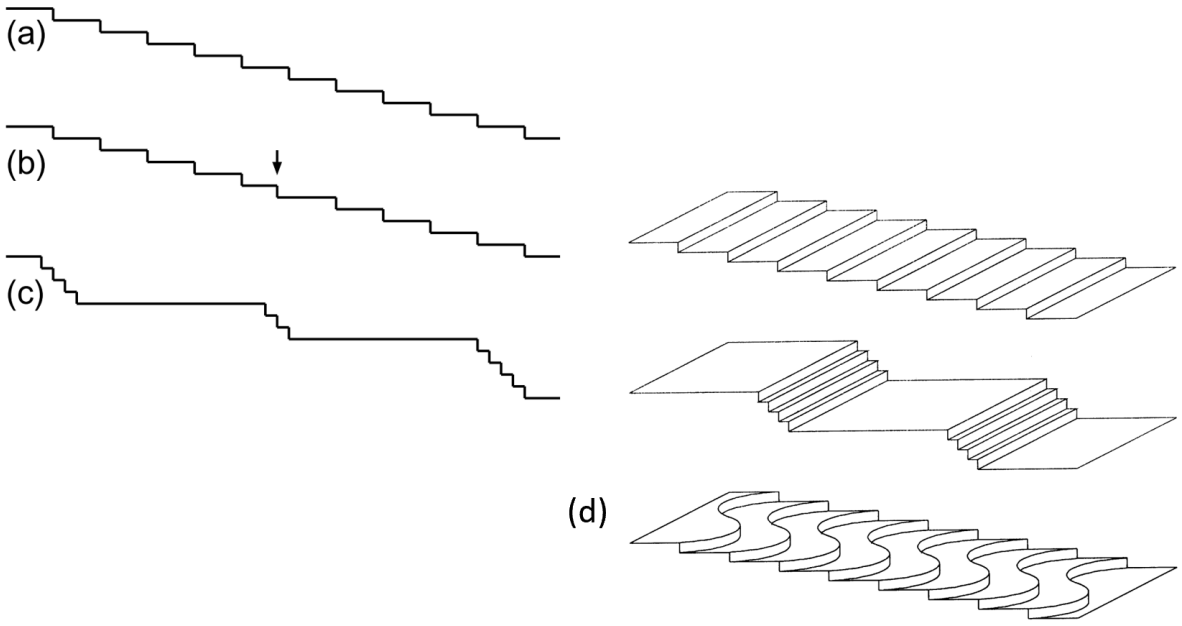

Figure 2.10: a) Equidistant surface steps. b) Any terrace affected by size variations from random initial conditions, c) leading to step bunching [151]. d) 3D render of the step bunching process leading up to microscopic variations and step warping at larger scales [155].

Step bunching is reinforced by other factors, such as temperature, initial height variations, surface diffusivity, or supersaturation conditions [151]. Doping with nitrogen [156] or any other impurities such as phosphorus [157] will also affect step-terrace ratios. The cumulative effects of step bunching extends well up to macro scales, and can be appreciated even under relatively low magnification levels as illustrated in Figure 2.11, where the step flow direction can serve as a qualitative indicator of underlying crystal orientations.

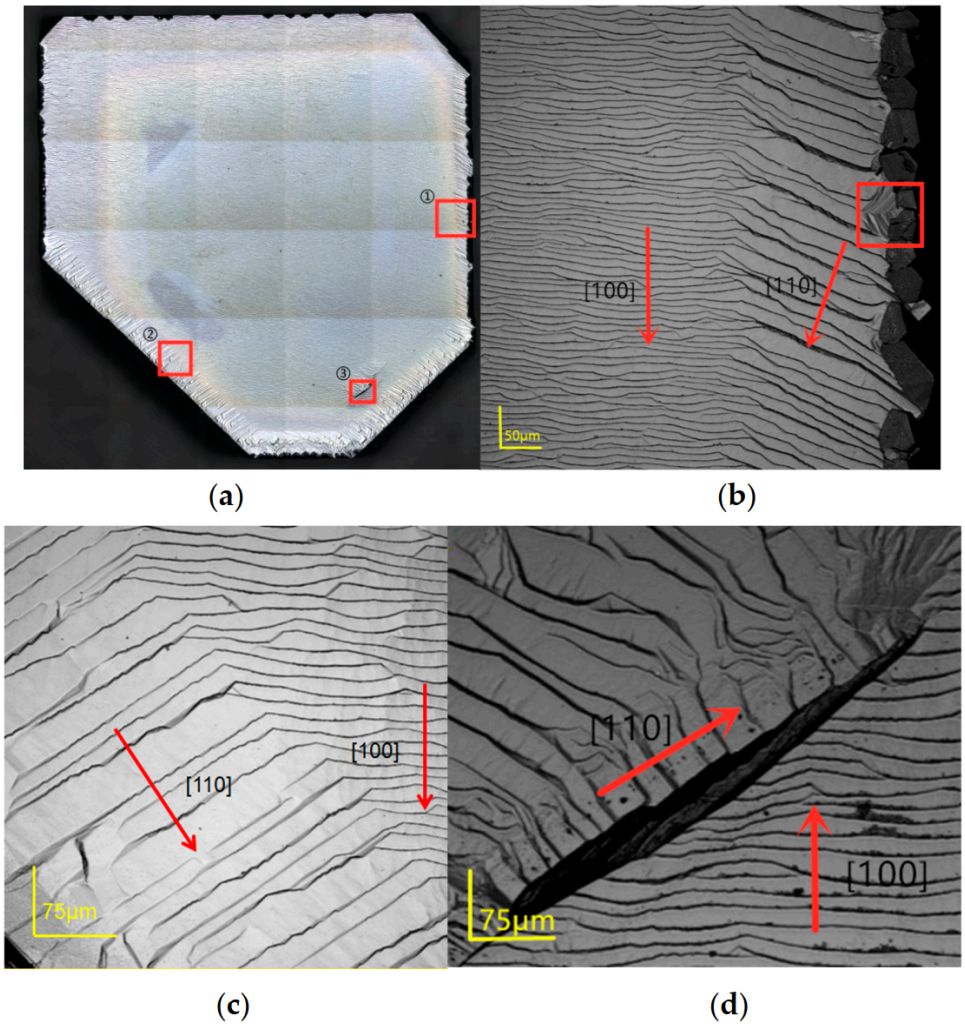

Figure 2.11: Step bunching forming macro steps separated by as much as 26 µm. Their propagation directions can be interpreted as indicators of underlying crystal orientation growth fronts [158].

2.3.4 Growth Defects

When deposited diamond layers are not perfectly arranged given applied process conditions, the sample ends up with grown defects. These can be broadly described under three categories. The first type are fundamental defects caused by imperfect or incomplete chemical reactions during epitaxy, where adsorbed radicals might interact with each other and not complete the reaction sequence described in section 2.3.3.1, resulting in graphitic sp^2 bonding instead

of extending the underlying diamond lattice. This type of defect was considered in the Harris-Goodwin model and will be briefly described. The second type are point defects, which for the most part only affect single sites in the 3D lattice, such as substitutional impurities, vacancies or interstitials. These types of defects will always be present to a certain degree depending on how well the CVD atmosphere is kept under control. These point defects are definitely critical for many applications such as quantum or electronic device fabrication, but their effects are beyond the scope of this project and will not be discussed in great detail. The third type of defect, much more likely to occur on samples produced under this investigation, are caused when the lattice structure itself is imperfect. These are called lattice dislocations, and are not necessarily limited to a single point or region as subsequent growth might continue to build upon any local imperfections causing defect propagation as diamond layers are added. These types of defects will be described and categorized in this section.

2.3.4.1 sp^2 Defects

Only diamond (100% sp^3 bonds) and graphite (100% sp^2 bonds) have been discussed as possibilities so far, but as carbon and hydrogen atoms are stacked over a substrate, their structure can be arranged at any $sp^3 : sp^2 : H$ ratios as illustrated in Figure 2.12. These intermediate amorphous mixtures are called Diamond-Like-Carbon (DLC), and are known to have intermediate properties ranging between diamond and graphite, which leads to a wide set of applications [160]. The relevance of DLC for this project is that this type of sp^2 defects are easily formed if process parameters are not kept under control and as close to diamond growth conditions as possible. The growth model developed by Goodwin took this possibility into account and included an extension analyzing graphitic reaction rates and how these relate to diamond growth rates. The basic assumption in this defect formation model

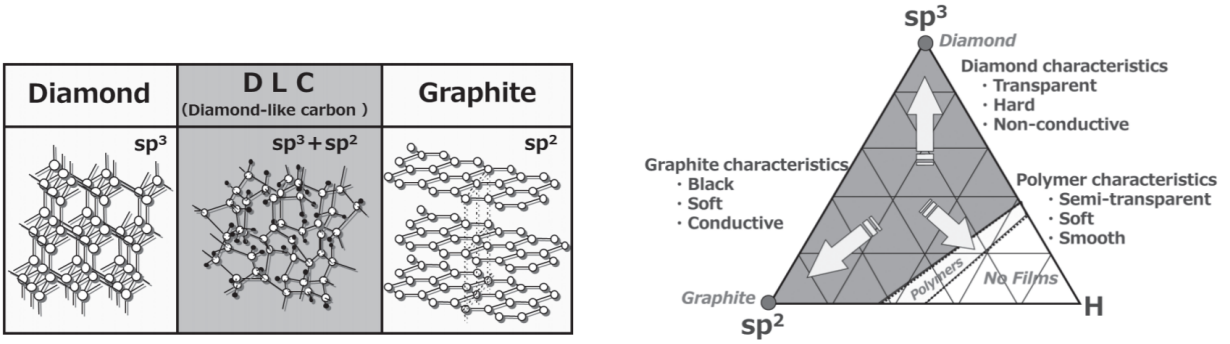

Figure 2.12: Diamond-like carbon defined as a mixture between diamond, graphite and hydrogen as an amorphous solid structure [159].

is that defects are generated when nearby adsorbates react before they are fully incorporated into the lattice and are then overgrown locking in an sp^2 defect [143]. The model concludes that under steady-state conditions, the defect fraction X_{def}, defined as a ratio of the defect formation rate over the carbon incorporation rate, will effectively be

$$X_{def} \propto \frac{G}{[H]_S^n} \tag{2.7}$$

where n must be determined experimentally. This relatively simple expression shows how higher growth rates will be accompanied by higher defect concentrations. When considering the growth rate derived in Eq. 2.6, and how the methyl concentration is proportional to the methane/hydrogen concentration in the gas reactants, this implies

$$X_{def} \propto \frac{[CH_4]}{[H_2][H]_S^{n-2}} \tag{2.8}$$

reinforcing the list outlined in section 2.3.3.1 on why the hydrogen content must be relatively high to produce high quality growth.

2.3.4.2 Dimensional Lattice Defects

Point defects (0-Dimensions) in a diamond lattice, namely vacancies, interstitials or substitutions, will affect the electronic behavior of a substrate as well as growth rates and step flow growth mechanisms [156], but the structure of the lattice will remain mostly unchanged.

Line defects (1-Dimension) on the other hand, will effectively result in lattice dislocations. There are two main types of single crystal linear lattice dislocations: Edge dislocations and Screw dislocations, illustrated in Figures 2.13 and 2.14, respectively.

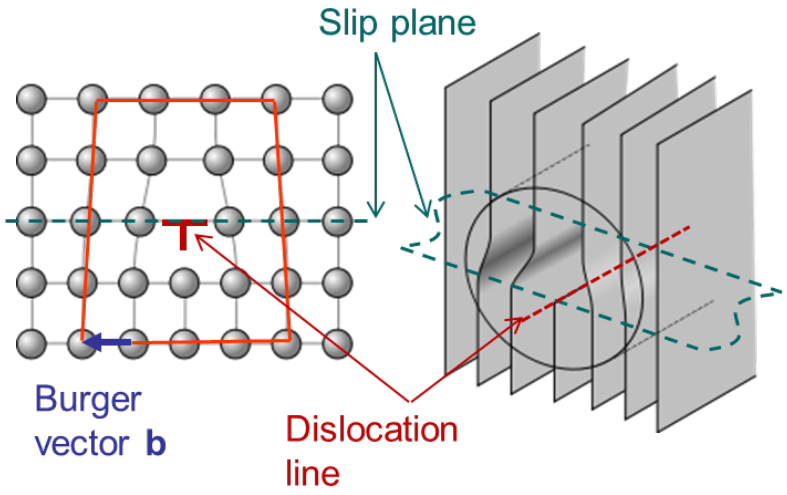

Figure 2.13: Illustrated edge dislocation [161]

Edge dislocations are considered a source of stress on the lattice at its point of origin. If no additional defects are present far enough from the stress point, the lattice eventually relaxes into a perfectly ordered structure.

Screw dislocations on the other hand continue to propagate as the defect has a permanent step at the top surface which attracts adsorbates. Step flow growth proceeds with the known mechanism, but the effective direction of the lateral growth is constantly rotating and expanding radially from the screw dislocation line.

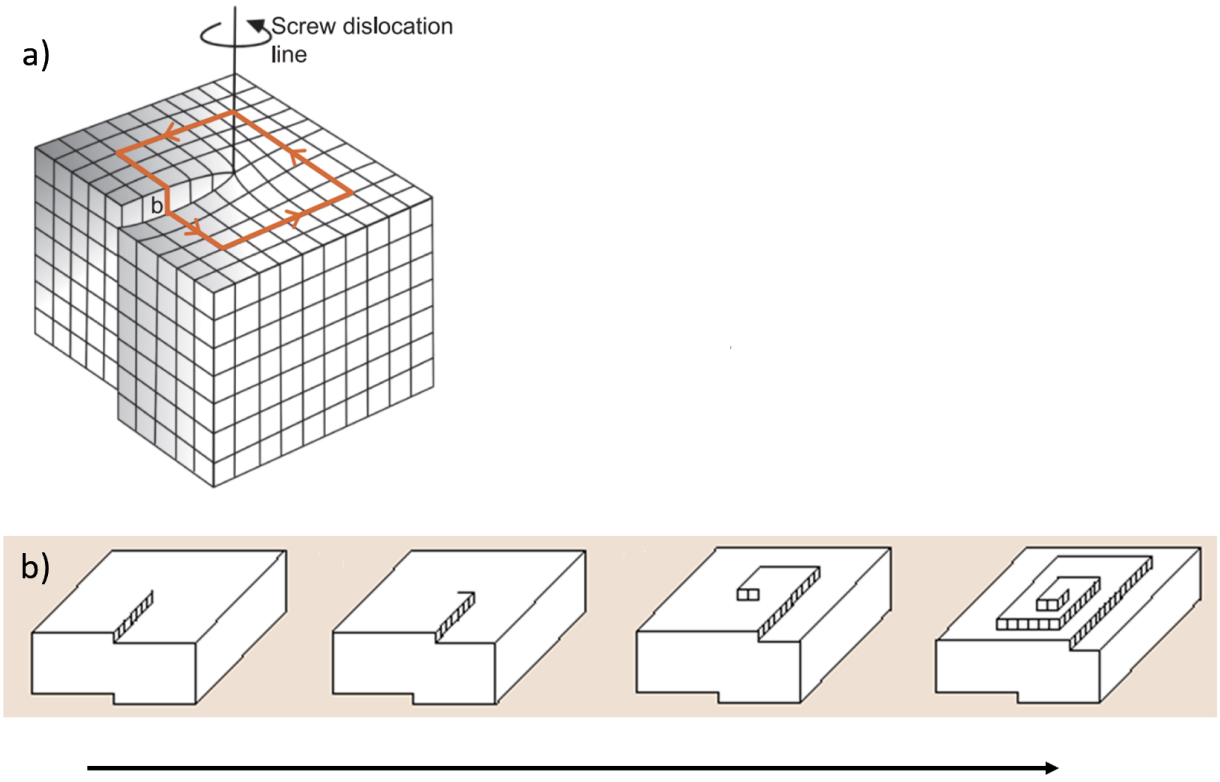

Figure 2.14: a) Illustrated screw dislocation [162]. b) Time series outlining how screw dislocations propagate cyclically and expand around the initial screw dislocation line [163].

Planar Defects (2-Dimensions) cover a wider range of conditions, including stacking faults, grain boundaries, and twinning defects. These types of boundaries can be present in polycrystalline samples, and expected to be found at the interface region of mosaic samples. It is known that the majority of diamond crystals have a very high density of {111} twins and {111} stacking faults [164]. Plane defects of this type are commonly found even on the most highly crystalline HPHT samples [101, 165]. These {111} planes are separated by relatively large distances within the diamond lattice, which makes them have the weakest local structural bonds. It is also not surprising that diamond tends to preferentially crack and cleave at these planes.

Bulk Defects (3-Dimensions) can be described as macroscopic defects. These include large

voids, or large groups of any other type of defects. It is safe to say that samples exhibiting these characteristics have deviated significantly from well controlled growth procedures. Cracks are also considered a bulk defect, and their presence reveal internal levels of stress that exceed maximum mechanical thresholds within the sample.

2.3.4.3 Misfit and Threading Dislocations

There are two additional types of dislocations that emerge when we consider epitaxial growth over substrates with different lattice constants. Misfit Dislocations can be defined as a type of linear defect initiated at the dangling bonds located at the interface between mismatched lattices [166]. The stress associated with this mismatch generates a series of regularly spaced dislocations where their separation will be randomly distributed, but their density determined by geometric considerations, as illustrated with an example in Figure 2.15.

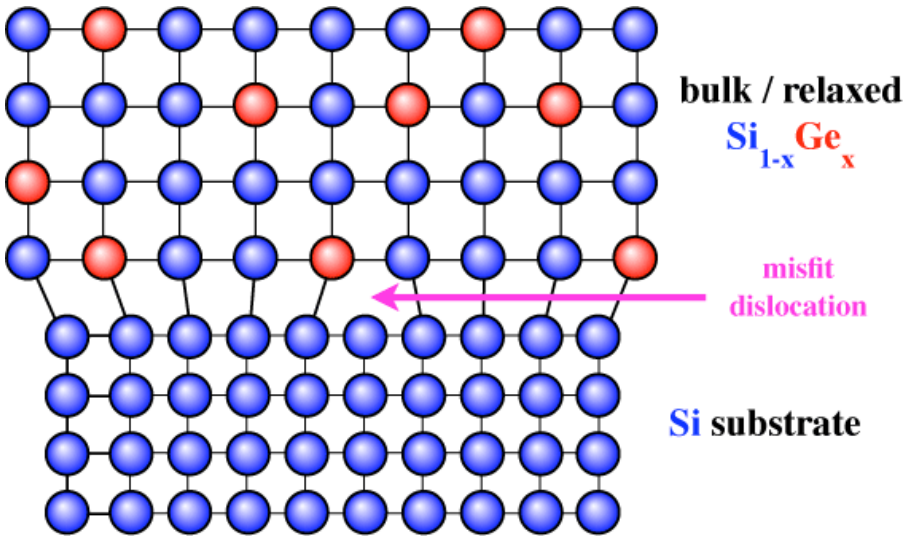

Figure 2.15: Misfit Dislocation concept applied to a silicon layer doped with germanium grown over a silicon substrate [166].

Threading dislocations are closely related phenomenon which can be defined as a dislocation that extends from the surface of a strained layer system which bends at the interface

from a misfit dislocation [167]. In essence, a 3D geometric effect resulting from mismatched lattices settling into the lowest energy configuration. This condition always ends up forming a pair of line dislocations generated at the substrate which extend in the growth direction at angles also determined by particular geometric considerations, as illustrated with a silicon germanium example in Figure 2.16.

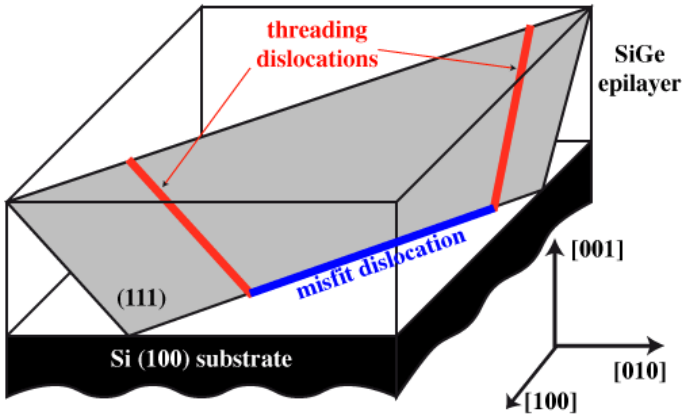

Figure 2.16: Threading dislocations applied to a germanium doped silicon layer grown over a silicon substrate [166].

Mismatch and threading dislocations are factors to consider in diamond as different doping levels are known to affect their lattice constants [168, 169]. A study by Tsuboshi et. al. reported a 0.7% lattice mismatch from a difference of only one order of magnitude in nitrogen concentration between substrate and grown layer [170]. This difference is too large to be attributed exclusively to direct lattice mismatch, but they surmise a difference of thermal expansion coefficients, also an effect of different impurity levels, might have led to thermal strain which resulted in lattice distortion at the interface. Due to these and other factors, such as polishing damage serving as primary nucleation sites, every time a new layer is grown over a substrate, new dislocations are always expected to be generated from new grown layers, including growth resumptions [171–173]. Figure 2.17 shows a pair of threading dislocations propagating from the surface of a diamond substrate.

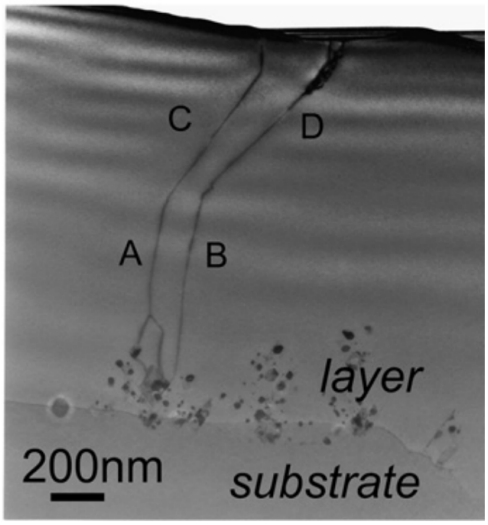

Figure 2.17: TEM cross-sectional image exhibiting two threading dislocations (vertical segments A and B, inclined segments C and D) originating from dark inclusions at the top surface of the substrate [174].

2.3.4.4 Hillocks

A common type of defect in CVD grown diamond are known as Hillocks [174]. These can be subdivided as Pyramidal Hillocks(PC), Flat Hillocks(FH), and Unepitaxial Crystals(UC). Their behaviors are closely related. The concept is illustrated in Figure 2.18 and it can be described as a spiral growth propagating as a triangular screw dislocation when observed from {111} oriented surfaces [140]. The source of these defects might be caused by a non-epitaxial crystallite, close grouping of penetration twins, a graphitized bundle, or even a surface contaminant. Either way, the initial step is generated by contact nucleation, and subsequent steps continuously replicate at a higher rate than its surroundings as a growth spiral [176]. When observed from {100} oriented surfaces, pyramidal hillock defects appear as quadrangular pyramids with sides facing along {110} directions as captured in Figure 2.19. In this case, macrosteps are also observed to rotate away from its center in a spiral pattern. Unepitaxial crystallites have a similar structure, except with a small crystallite with

random orientation is usually found at the center of the hillock, either burried or at its apex. Hillocks are a notoriously undesirable effect, especially for device fabrication applications, as the defect tends to increase current leakage in the region, and weaken dielectric breakdown ranges [140].

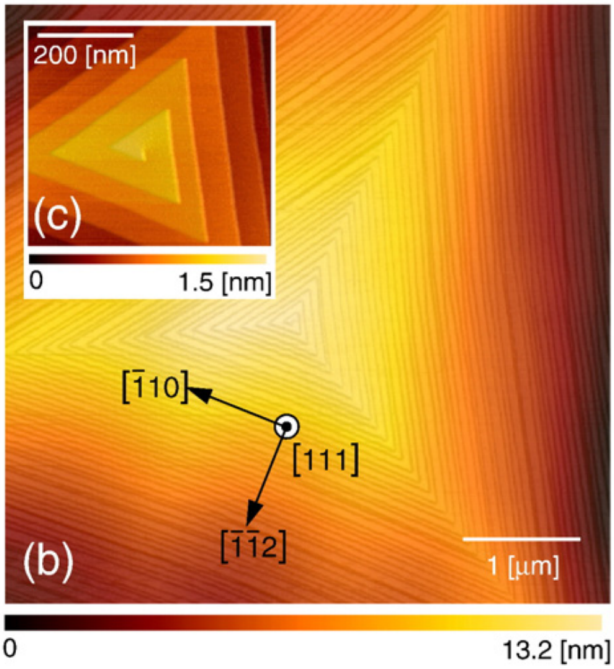

Figure 2.18: AFM image of a typical screw dislocation over a {111} oriented surface forming a pyramidal hillock defect [175].

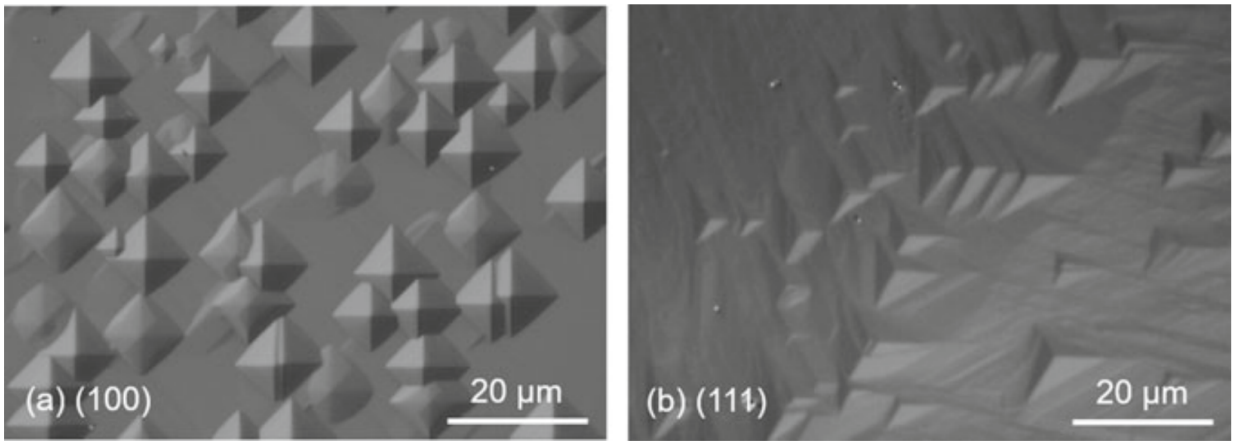

Figure 2.19: SEM pictures comparing pyramidal hillocks when observed from {100} and {111} oriented facets [140].

2.3.4.5 Suppression of Propagating Defects

One way to suppress hillocks from propagating is by reducing the methane concentration. If the adsorbate concentration is too high, adsorbed radicals might cluster together causing 2D nucleation leading to saturation conditions, making them less likely to migrate towards a step. A cluster of unincorporated carbon containing adsorbates might end up creating the seed condition for hillock formation. When methane concentrations are even higher, adsorbates will incorporate into the surface with almost no migration at all, developing into a random growth morphology. These outcomes are illustrated in Figure 2.20 and show again why the hydrogen concentration must remain relatively high as discussed in section 2.3.3.1. One way to suppress hillock formation or threading dislocations from propagating over grown layers is

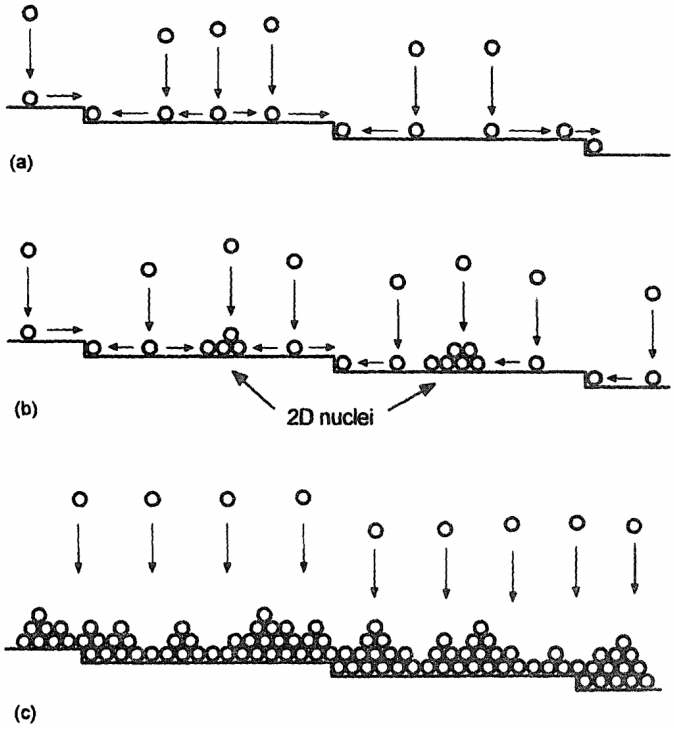

Figure 2.20: Growth mechanisms for different CH_4 concentrations. a) Low methane concentration leading to smooth step flow growth b) Hillock growth starting to form around 2D nuclei with a medium CH_4 concentration, and c) Random growth with a high CH_4 concentration [177].

by promoting step flow growth conditions. If the step velocity is high enough, the resulting lateral growth conditions will suppress defect propagation before they get a chance to expand, as illustrated in Figure 2.21. Step flow growth can be promoted by inducing a misorientation angle in the sample such that vincinal planes are tilted relative to the top facet. Deposition temperatures must also fall within a certain range. Surface morphology maps, as illustrated in Figure 2.22 can be produced to identify the regimes at which the misorientation angle and methane concentration will lead to unepitaxial crystallites, pyramidal hillocks, step flow growth and step bunching effects, or atomically flat surfaces. Atomically flat surfaces are ideal, but such low methane concentrations imply prohibitively low growth rates, therefore, the best way to avoid propagating defects, such as hillocks and threading dislocations is by inducing a misorientation angle on diamond seed substrates.

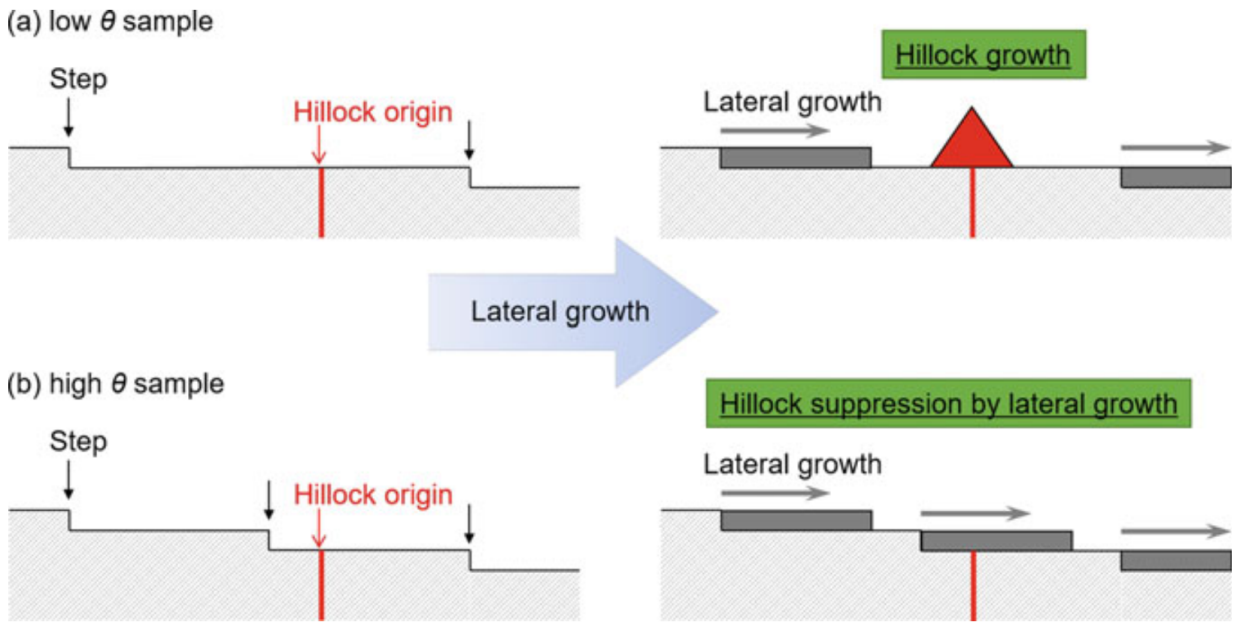

Figure 2.21: Hillock suppression by lateral growth on samples having a) low, and b) high misorientation angles θ [140]. The concept also applies for threading dislocations.

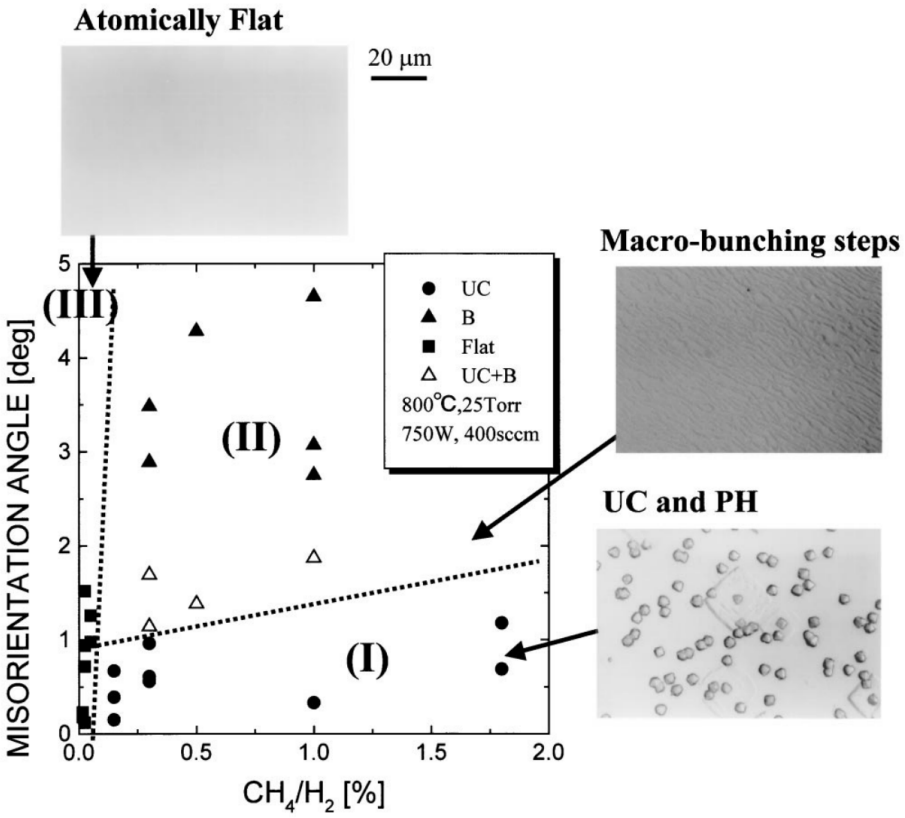

Figure 2.22: Map of surface morphologies as a function of both the misorientation angles of diamond substrates and CH_4/H_2 ratios. Filled circles represent unepitaxial crystallites (UC), filled triangles represent macro-bunching steps, and filled squares represent atomically flat surfaces. Films with macro-bunching steps, unepitaxial crystallites, and pyramidal hillocks (PH) are represented by white triangles. The dotted lines only serve as a general guide dividing this parameter space into three regions: I–III [178].

2.4 Diamond Classifications

Diamonds are classified based on their impurity composition. The most common type, corresponding to more than 98% of natural diamonds [179], are labeled Type I and are defined by a high nitrogen content. These diamonds usually have a pale to sharp yellow up to light brown color depending on the amount of nitrogen content within the lattice, ranging from 1 part per million (ppm) up to thousands of ppm. These Type I diamonds can be subdivided depending on how the impurities are aggregated and combined with hydrogen or vacancies, as they produce different effects and have a wide range of potential

applications [180]. Type II diamonds are defined as having N_2 impurity levels below 1-2 ppm. These are subdivided as Type IIa, where no impurities are detectable, and Type IIb, where the lattice contains a measurable level of boron. These have a light to sharp blue tint and are extremely rare in nature, but their production is straightforward by incorporating boron containing precursors during the CVD process. Figure 2.23 shows a diagram summarizing the main types of diamond classifications.

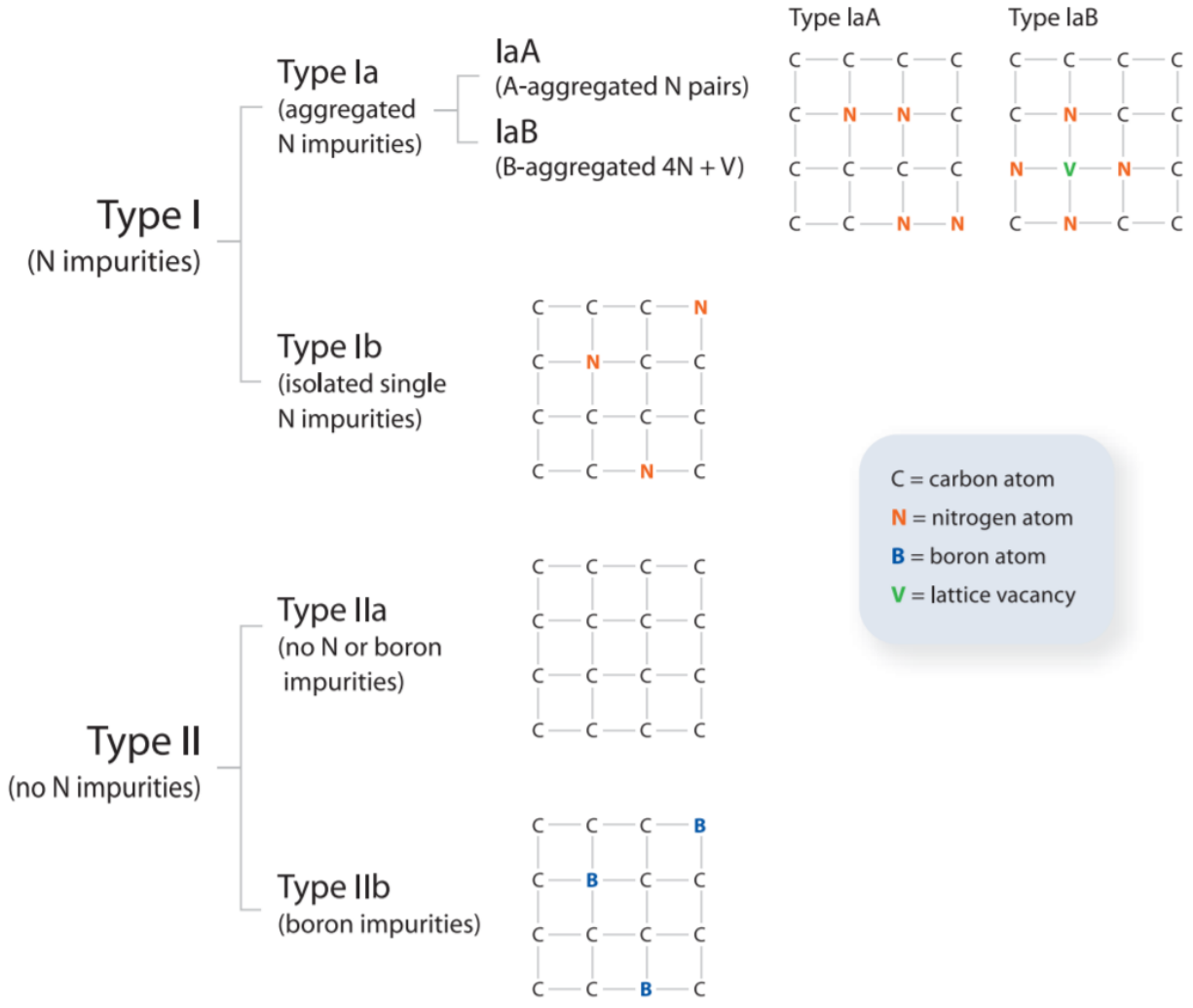

Figure 2.23: Main diamond classifications. [181].

Chapter 3

Literature Review: Diamond Substrate Production

3.1 Substrate Production Challenges

Most diamond applications, especially all technology based on electronic device fabrication, are in fundamental need of quality diamond substrates. These substrates must have the lowest possible defect densities, starting with point defects in terms of desirable impurity levels in order to engineer device components with precision. Line defects in terms of dislocation densities must be reduced as low as possible to make sure devices perform at their highest capability. Plane and bulk defects are just unacceptable as they would render any substrate unreliable. On top of these ideally low defect concentrations, substrate areas must be as large as possible for industry leaders to even consider diamond as a base material.

This literature review chapter is structured in a way that explores the prevalent techniques and approaches that have been developed over the years to produce diamond substrates and the particular challenges they encountered. Every approach, and every technique will be highlighted by a summary of one or two particular research groups that have reported the best results. For the mosaic approach, all relevant publications will be covered in more

detail, as all have contributed with practical and theoretical concepts applied throughout this investigation. The last section will outline the current set of commercially available substrates showcasing the current state of the art in diamond substrate production.

In general, the challenge of lowering initial dislocation densities tends to be addressed by using HPHT substrates. Substrates with defect densities as low as $10^3\,\mathrm{cm}^{-2}$ are readily available. This value is at least an order of magnitude lower than any other type of single crystal diamond growth reported so far, and several orders of magnitude lower than any natural diamond [171]. The challenge of lowering impurity homogeneity and concentration is usually addressed by applying CVD growth. The wide set of process parameters from this approach can be easily extended by techniques based on this method. Work developed by each group will be prefaced by a short overview of the CVD system used, followed by the strategies applied to address specific substrate production challenges.

3.2 Direct Lateral Growth

The first approach is area expansion by direct lateral growth. In this case, conditions are controlled such that the overall area of the top grown surface is larger than the seed substrate. Conditions for this type of growth have been developed in both open and enclosed type sample holder configurations, where diamond seeds are either grown over a flat surface directly exposed to the plasma, or enclosed on the sides within a sample holder.

3.2.1 Open Holder Design

The research group based at the Laboratorie des Sciences des Procédés et des Matériaux, France with their 2.45 GHz Microwave Plasma Assisted CVD (MPACVD) based LIMHP

reactor [118], has been by far the most productive at increasing sample areas based on the use of an open holder configuration. Their research is based on the observation that rectangular seeds directly exposed to a plasma discharge region under slightly different steady state conditions resulted in different geometric shapes, as shown in Figure 3.1. The direct conclusion from these results is that different crystal planes grow at different rates. The group developed a crystal growth model based on purely geometric considerations where the premise is that growth conditions, namely pressure, temperature, and CH_4 concentration will cause the {100}, {111}, {110}, and {113} planes to grow at different rates. The model defines geometric parameters α, β and γ by normalizing each growth rate relative to {100} planes, and adjusting them by their interplanar distances [183]. The parameters are listed in Figure 3.2 as well as the color code used to represent crystal plane facets throughout their publications. The shape that grown samples tend to take, including corners and edges, are then predictable as a function of time, illustrated by an example in Figure 3.3.

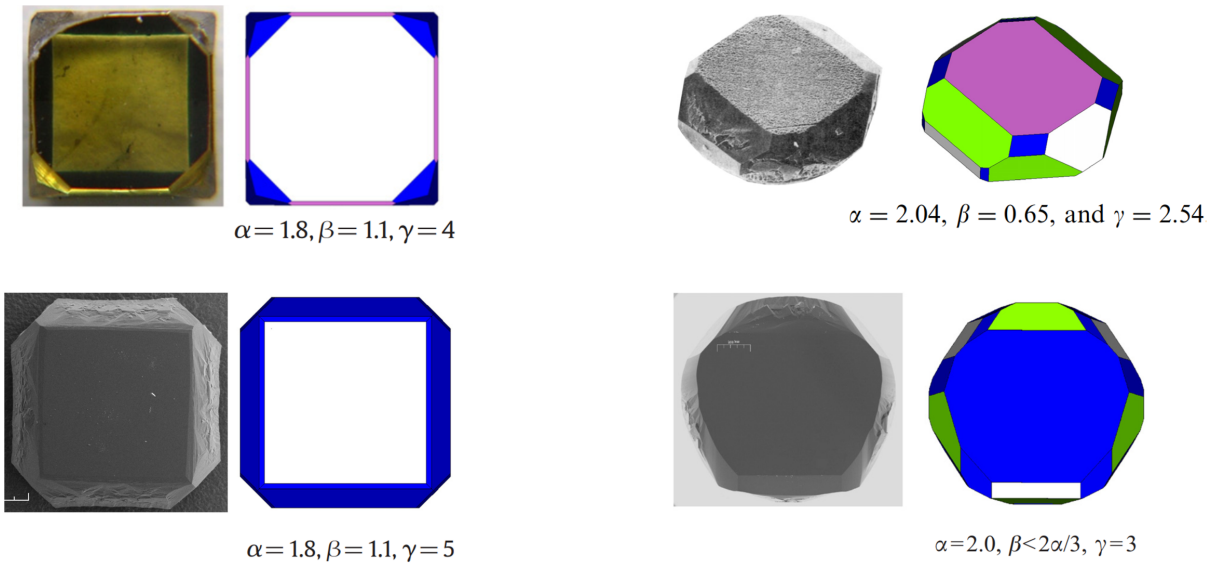

Figure 3.1: As-grown samples from rectangular substrates grown under different steaty state conditions, resulting in different grown shapes [146, 182, 183].

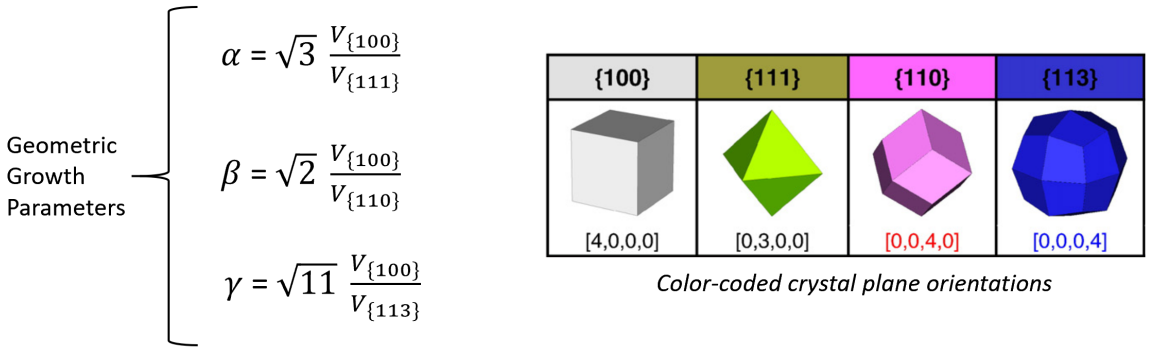

Figure 3.2: Growth parameter definitions and color codes used throughout their publications to represent different crystal plane facets. [146, 183]

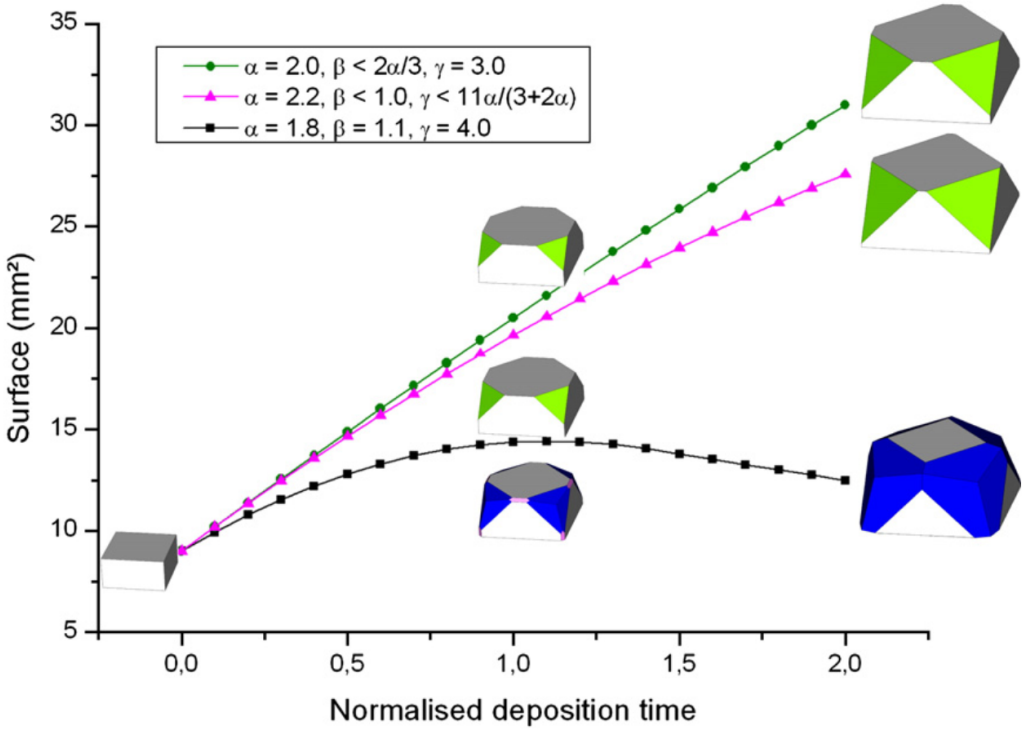

Figure 3.3: Modeling of the top surface area evolution measured in normalized deposition time. In this case, the initial seed starts from a half cube {100} plane top and side facets measuring 3mm on each edge, plotted under three different geometric growth parameter combinations [182].

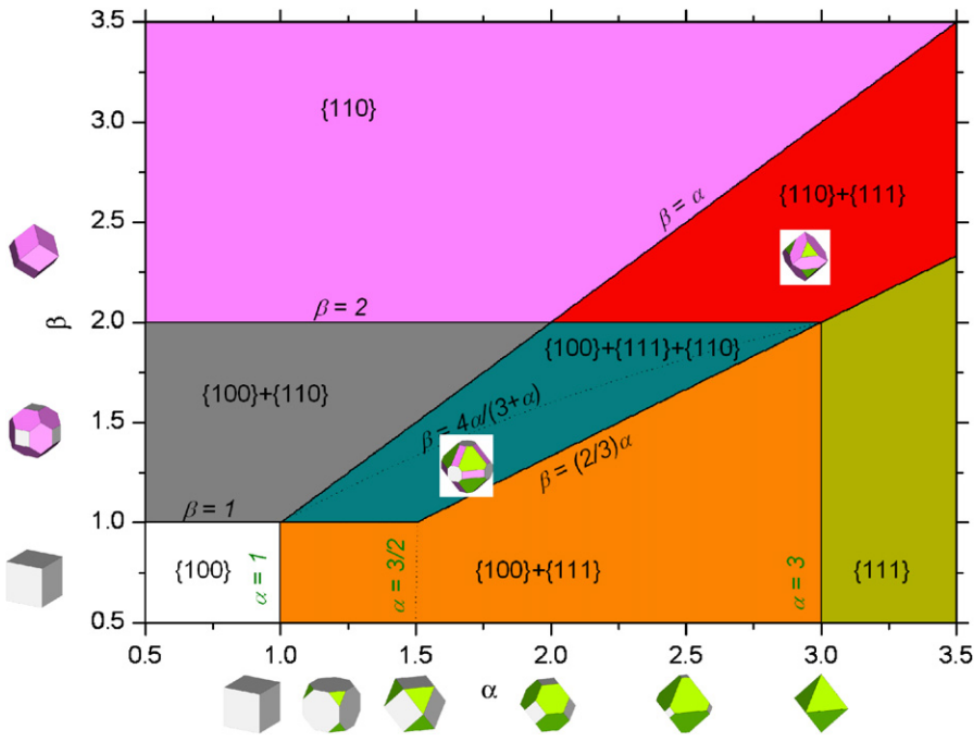

Figure 3.4: Example morphology diagram including crystals showing how the α and β parameter ratios result in steady state equilibrium {100},{111}, and {110} facet combinations [183].

As time extends indefinitely, samples will eventually reach their final steady state, illustrated in diagram form in Figure 3.4. The strategy is then to perform direct experiments to measure the growth rates of the crystal facets, then use the observed trends as they correlate with growth parameters in order to maximize top surface areas. Their feedback loop has been effective, as they have been consistently increasing sample areas on their grown samples. At the beginning, the corners showed pronounced {111} and {113} plane formations, as illustrated in Figure 3.5b. Further development a few years later led to better suppresion of undesired planes at the corners, increasing sample sizes up to 5.3 mm, as seen in Figure 3.5d.

Work by the team where they use and apply this strategy is under ongoing development. The group reported sizes up to 8 mm in diameter at the 2019 Fall MRS conference, corresponding to a 4x increase in area. These latest results are yet unpublished, but progress in

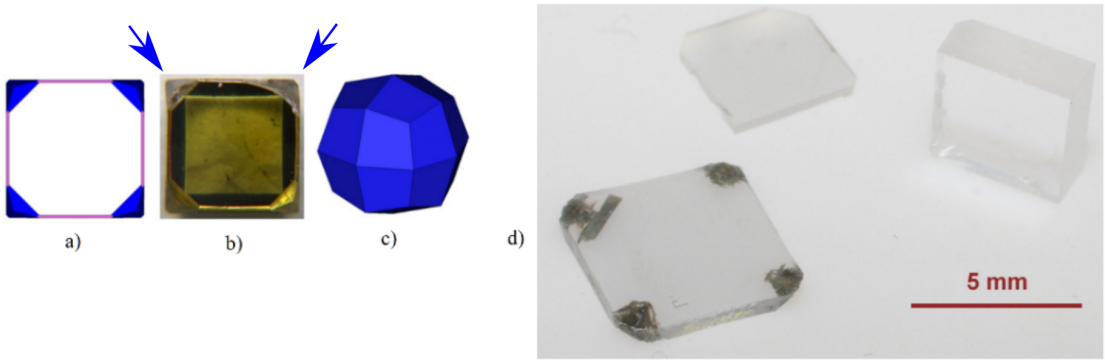

Figure 3.5: a) Top view crystal shape based on the growth model. b) Top surface of the grown sample showing the occurrence of {113} faces on all four corners of the crystal. c) Expected steady state shape showing how the total area would be eventually reduced if the growth time were extended indefinitely [146]. d) High purity CVD sample showing improvement over growth at the corners of the sample. [171]

substrate enlargement based on this direct approach has been clearly demonstrated. The problem with the approach is how the laterally grown region around the corners tend to have higher stress and defect concentrations.

This group has also explored several strategies geared towards defect reduction in general, such as pyramidal shaped substrates to bend dislocations towards the edges [184, 185], or exploring lateral growth over a deliberate macroscopic hole in the substrate as a way to reduce dislocation densities in the overgrown area [186]. The best solution so far to address this issue is to begin with higher quality substrates. The group has reported dislocation densities as low as $10^3\,\mathrm{cm}^{-2}$ based on using top crystalline quality HPHT Type IIa substrates provided by New Diamond Technologies (NDT) [187].

3.2.2 Enclosed Holder

The parameters for a geometric growth progression are expected to hold if conditions are unchanged vs. growth time. This will always remain true, but not realistic for an indefinite period. As the sample grows thicker, the non-linear distribution of the nearby plasma

discharge distribution will come into effect and the steady state shape is never expected to reach completion. This makes the original assumption of constant conditions based on constant parameters inaccurate relatively quickly.

One way to force more stable conditions for the seed and nearby region is to build a sample holder that restricts the distribution of the discharge region. This was first attempted by the group at the Diamond Research Center of the National Institute of Advanced Industrial Science and Technology (AIST) from Osaka University in Japan. They first reported results on the concept of an "enclosed type" molybdenum holder in 2005 [188]. The design was straightforward. It was based on placing the substrate inside a hole drilled into a molybdenum rod, as illustrated in Figure 3.6.

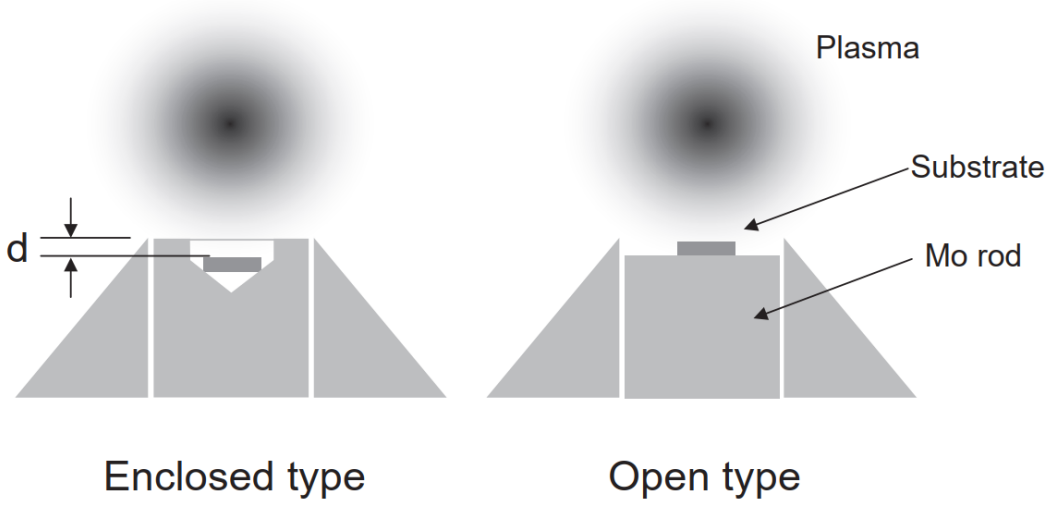

Figure 3.6: Schematic illustration of the open and enclosed type sample holders [188].

The modified growth conditions obtained from this configuration resulted in a marked improvement on overall sample quality when the depth of the diamond relative to the top surface of the holder is kept within a reasonable window, as can be seen on Figure 3.7. This result also confirms the poor grown quality at the corners of square substrates directly exposed to the plasma.

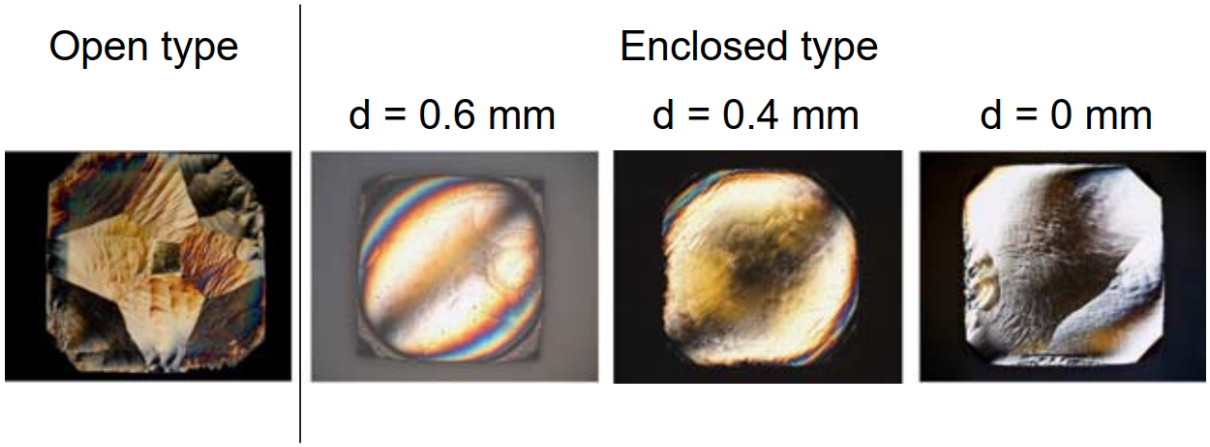

Figure 3.7: DICM pictures of samples grown at different depths [188].

The marked difference in sample quality and shape shows how the geometric growth parameters discussed in the previous section without a doubt no longer apply directly when considering samples enclosed in a holder. The group started analyzing the growth dynamics by simulating the new conditions, and concluded that some experimental results could indeed be numerically predicted, such as the relationship between growth rate and power density over the top surface. They also found other factors that were possibly affected by the new configuration, such as temperature, or gas flow, illustrated in Figure 3.8.

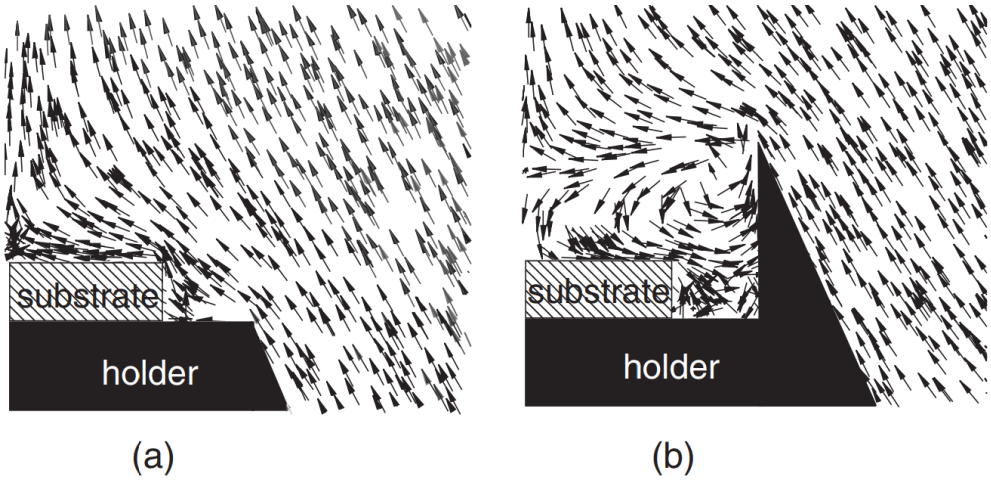

Figure 3.8: Simulated gas flow patterns near substrate for open and enclosed type sample holders. [189].

A fully coupled simulation was not achieved given how other factors might need to be considered for full quantitative comparison with experimental data, such as inhomogeneous gas temperatures, ion dynamics, gas composition, radiation, and chemical reactions [189]. Further experiments consisting of separating the top layer of the Mo rod with a plate, while keeping all other parameters constant, led the researchers to conclude that at least for samples with area less than $1\,\mathrm{cm}^2$, the most critical factor influencing the macroscopic surface shape is temperature distribution. When samples are larger, the power density distribution over the top surface becomes more significant. Figure 3.9 shows the experimental setup and resulting schematic of grown sample profiles demonstrating how temperature uniformity is a critical factor at these ranges.

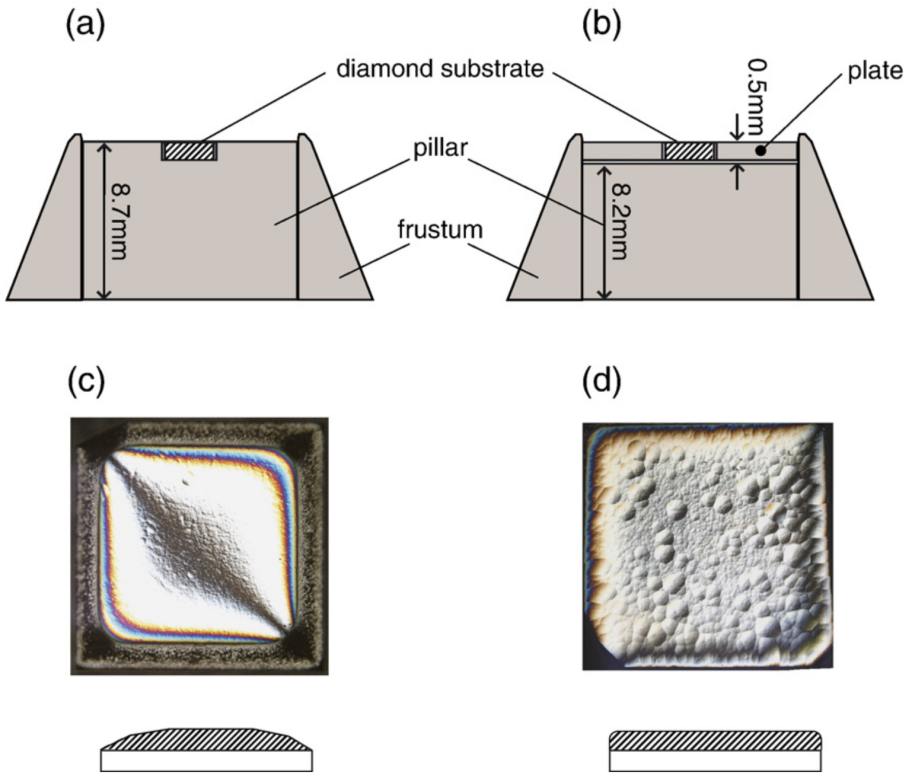

Figure 3.9: Cross-sectional views of open and enclosed sample holder configurations and schematic of grown sample profiles. DICM top view pictures of both samples are shown for each case. [190].

An additional benefit of using a rod is that when a sample grows too large, the rod can be lowered, and the sample re-grown under similar conditions. This strategy was carried out by growing samples upwards of 30+ times. Single crystal diamonds as large as 4.4 carat were obtained, resulting in diamonds with lengths up to 10 mm, as shown in Figure 3.10.

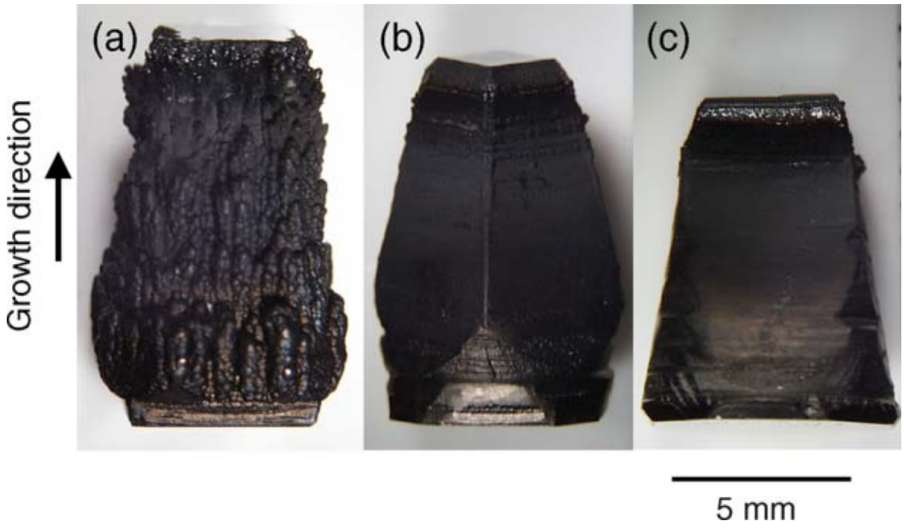

Figure 3.10: Single Crystal Diamonds produced by multiple regrowths on enclosed type holders. a) 10mm, 4.7ct. b) 9.6mm, 3.5ct c) 8.7mm, 4.4ct. [191].

Given how the thermal environment is strongly affected by enclosed sample holders, the research group at Michigan State University (MSU) started exploring optimal conditions for different holder configurations [192, 193]. The circular aspect of the Mo rods was maintained, but the depth of the cylinder was reduced to a minimum, making sure the cooling mechanism had a more significant impact on the setup. By then, the cooling component of the deposition system had been identified and controlled as an effective parameter in obtaining grown polycrystalline diamond (PCD) film uniformity on substrates as large as 100 mm [194]. The end product is labeled as a Pocket Holder design, illustrated in Figure 3.11 next to some grown examples. Growth conditions are kept as stable as possible by making power adjustments throughout the run to maintain a constant temperature.

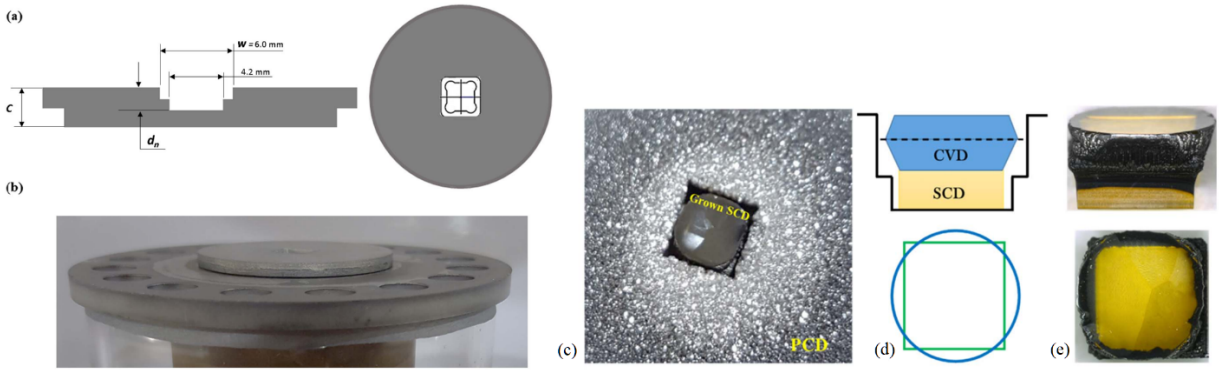

Figure 3.11: a) Pocket holder geometry for SCD growth. b) Pocket Holder placed over the cooling stage. c) SCD grown sample surrounded by PCD growth over the Mo sample holder. d) Cross sectional schematic of the sample as grown inside the holder and diagram of the resulting shape of the top surface. e) Grown sample. [193].

This is the process used throughout this present investigation. A description of the deposition system, growth parameters and overall experimental process will be discussed with more detail in Chapter 4. Samples grown with this setup do not necessarily show the same geometric trends as samples grown over open holders. These new growth conditions then add new parameters to consider, such as pocket depth, width, thickness, and relative position and size of the sample within the pocket, but making these adjustments is straightforward, and leads to a quantifiably simple approach to parameter optimization. Further exploration of pocket holder dimensions, resulted in samples that not only show no sign of polycrystalline formation at the edges, but also showed signs of direct lateral expansion. This research has led to area gains of 2+ times the initial HPHT area on a single run [195]. Figure 3.12 shows a few pictures of samples grown using this process. Multiple growths are possible with deeper holders, but decreasing areas, as shown in Figure 3.13, are an unavoidable limit due to PCD formation encroaching in from the inner rims of the pocket. The approach then becomes an optimization problem within an entirely different parameter space. This research is currently ongoing with plenty of potential for improvement.

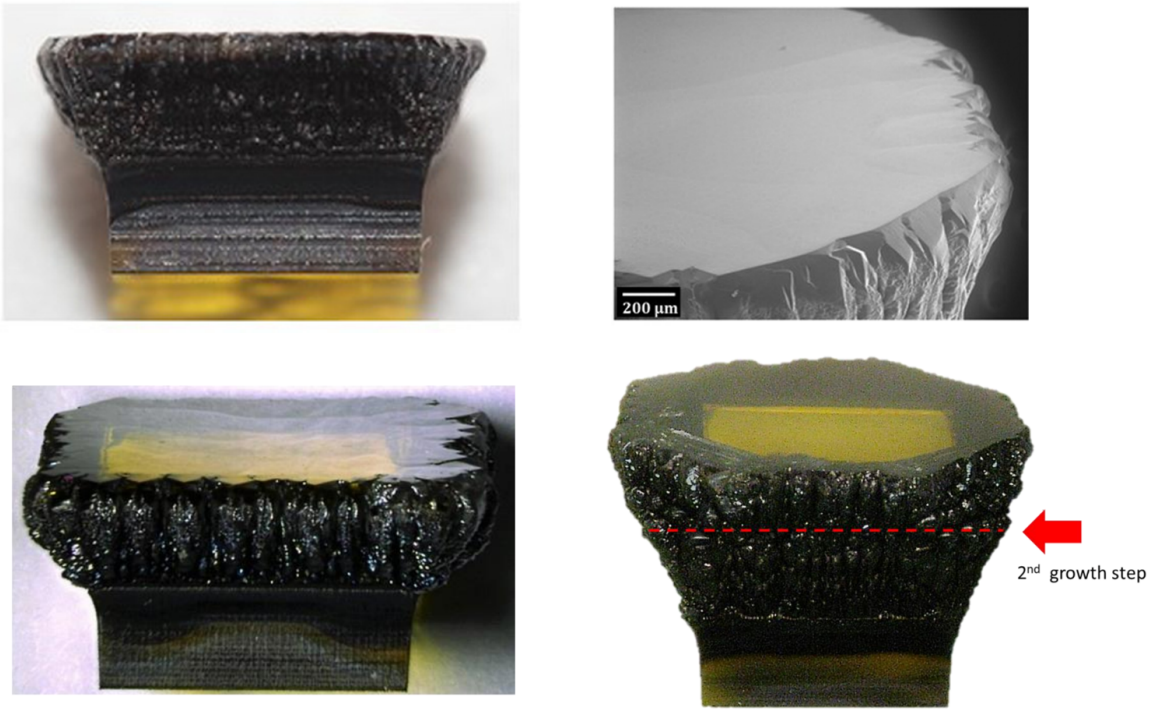

Figure 3.12: a) Grown samples showing area enlargement with no PCD formation at the edges using the process refined by Charris et. al. at MSU [7].

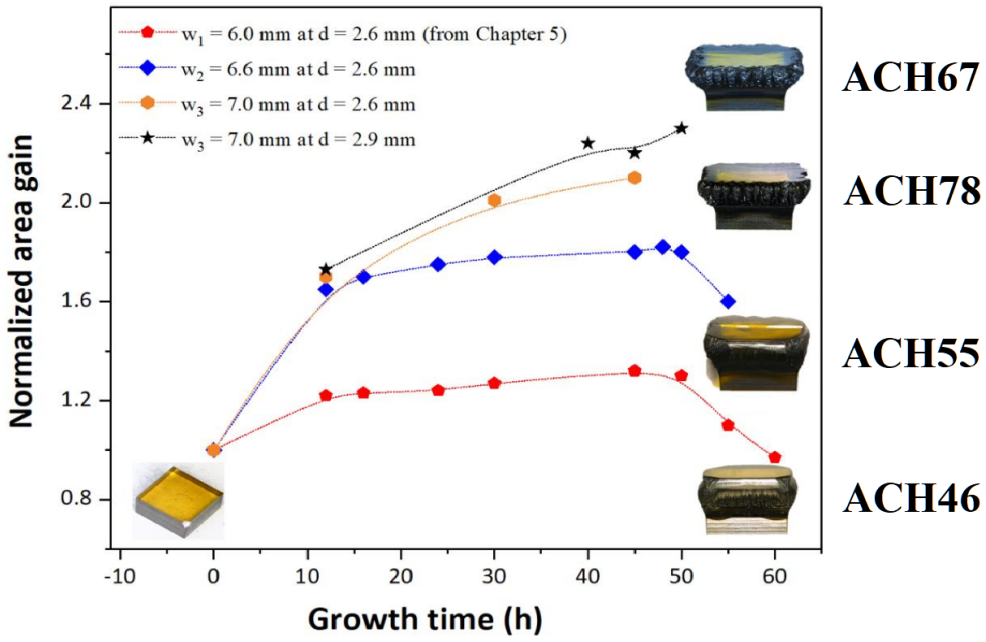

Figure 3.13: Normalized area gains as a function of time for different pocket configurations [7].

In recent years, China has established several research groups working on developing diamond growth. One of the groups at the School of Power and Mechanical Engineering from Wuhan University designed and built their 2.45 GHz MPACVD reactor [125], where based on simulations and experimental results they have confirmed that an enclosed holder configuration yields improved results, especially when aiming for a reduction of PCD formation and overall quality at the edges. Their reports show an electron density gradient in the axial direction is the main cause for PCD formation at the edges [196], not the power density as surmised by the Japanese group, or the temperature distribution which was claimed to be uniform across the sample. Their results also confirm that optimal cavity depths can be found under given conditions, as shown in Figure 3.14. The temperature in this study was kept constant by adjusting the incident power at 3000 - 3500 W, and the pressure at 180 - 210 mbar for each growth.

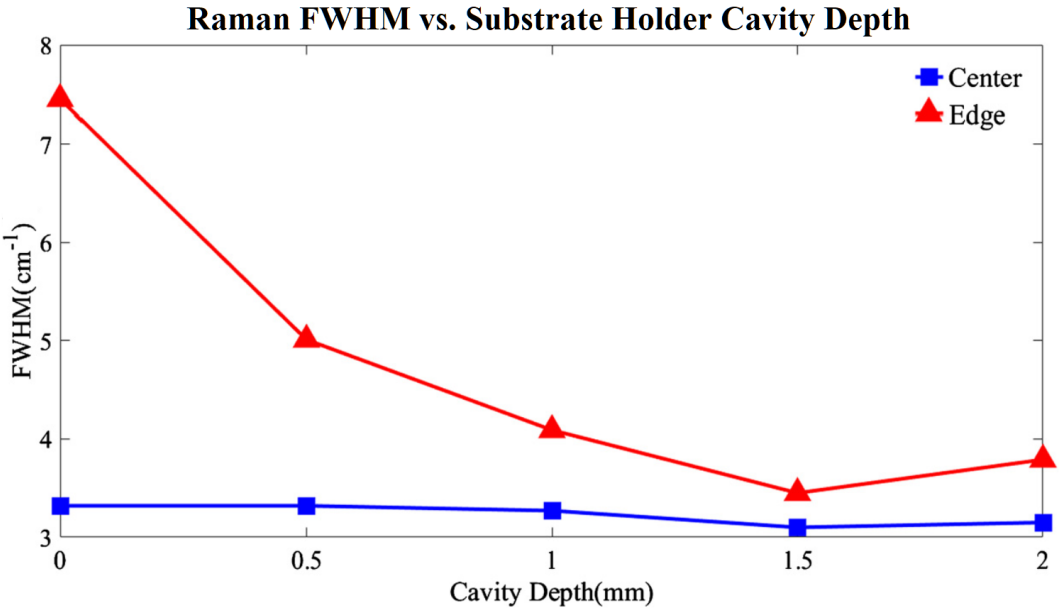

Figure 3.14: Raman spectroscopy showing sample quality can be optimized based on the depth of the substrate holder [196].

The School of Microelectronics at Xidian University in Xi'an China recently published an MPACVD system with the added functionality of a moving cooling stage. Under this setup, all parameters can be kept constant as the samples grow thicker just by adjusting the height of the sample holder. Working at low pressure, the plasma could be expanded, and multiple samples were grown simultaneously at a reported 3x increase in area relative to their initial seeds. Resulting samples are shown as-grown in Figure 3.15. The high quality of the resulting samples was demonstrated by Rocking Curve FWHM measurements ranging between $40 - 50''$ [197, 198]. For these reports, the groups have not disclosed substrate production capability yet, but the preliminary area enlargement has been clearly demonstrated based on the enclosed holder approach.

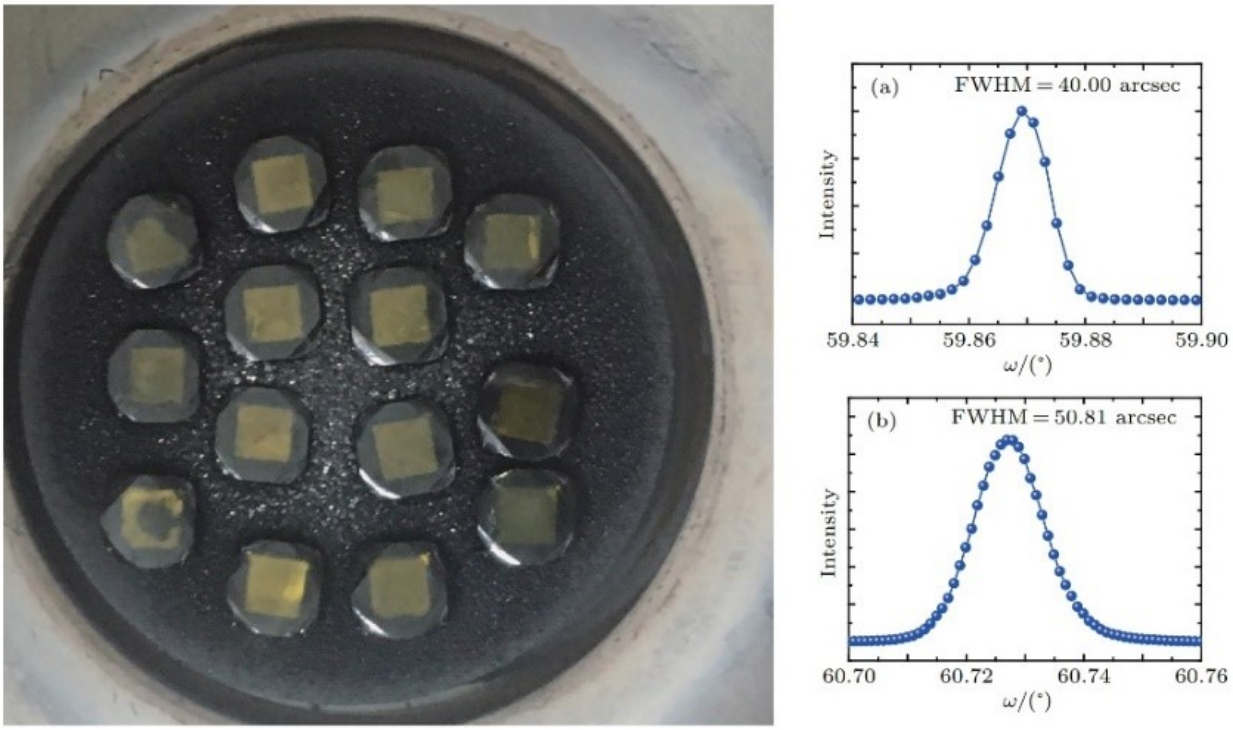

Figure 3.15: a) Enlarged growth of 14 SCD samples. b) FWHM measurements of samples grown at 3% and 5% CH_4 [198].

3.3 Plate Slicing Techniques

Every substrate production process must include a reliable method to slice thin plates out of a bulk grown source. The challenge with diamond is that any attempt to use traditional slicing will always fail because there are no materials harder than diamond. Jewel makers have historically relied on cleaving large crystals, but producing plates this way would be extremely unreliable and is discarded an option. Alternative plate slicing techniques must be developed.

3.3.1 Laser Ablation

The process currently used by jewelers and substrate producers in general is laser ablation. Cutting standard size 3.5 mm x 3.5 mm x 1.4 mm HPHT samples is straightforward, and only takes about five minutes with a commonly used 18 W Nd:YAG laser operating at 1064 nm with a spot size focused to a range of approximately 20 µm in diameter [199]. The problem with this process is that current laser technologies at this power level are not perfectly collimated. The most relevant drawback for using this tool in substrate production is that cutting through samples deeper than the approximate spot size will then require triangular cutting profiles to maintain a focused cutting point, resulting in ever increasing kerf losses, as illustrated in Figure 3.16. With all this additional material removal, a 7 mm x 7 mm substrate takes about 20 min and ends up easily removing a day's worth of diamond growth [199]. Larger areas will quickly result in prohibitive kerf losses. An additional secondary effect from laser ablation in substrate production is how the diverged component of the beam will cause sub-surface damage below the cut planes. The process itself also generates intense focused heating. All this additional strain tends to crack highly stressed samples. Laser ablation has

been demonstrated to work and serves an effective tool for substrate recovery [199], which can be re-used in subsequent growths as an industrial process, but this is only valid for substrate sizes several milimeters wide. Larger areas will eventually require further development in laser collimation, or exploring new types of substrate slicing technologies.

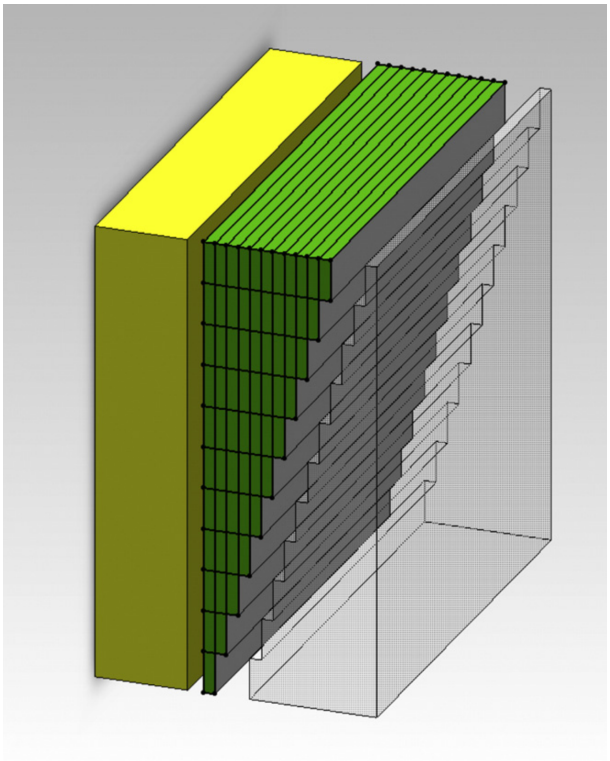

Figure 3.16: Yellow represents the original seed substrate, and grey the CVD-grown material. The green sections correspond to the ablated diamond material, outlining the effective cutting profile for seed substrate separation. Each segment in this example corresponds to a grown section 25 µm wide and 90 µm deep. [199]

3.3.2 Ion Implantation and Lift-off

The ion implantation approach is based on a common technique used in device fabrication, where dopants are directly penetrated into a substrate by ion bombardment. Dopant depth and distributions within substrates are controlled by adjusting the flux and kinetic energy of incoming ions. If the subsurface damage is not too significant, subsequent annealing will

diffuse the implanted dopants throughout the lattice [200]. A variation of this technique was first applied on diamond in the 90's [201, 202] where instead of dopants, additional carbon atoms are bombarded into a diamond substrate. The goal is generating sub-surface damage to induce graphitization while keeping the initial intrinsic concentration on the substrate. This damaged region is then much more vulnerable to chemical attack, opening up the possibility of detaching sections of the substrate with additional processing. For this approach to work, the kinetic energy of the bombarded carbon ions must be high enough such that when they start penetrating the surface of the substrate, they share no significant interaction time with fixed carbon atoms within the lattice. The amount of energy for this condition to apply is usually relatively high and depends on both the mass of the bombarded ions, and the displacement energy of atoms within the lattice. In case of carbon ions implanted on diamond, the lowest energy reported of 180 keV can be supplied by a medium range ion implanter, illustrated in Figure 3.17.

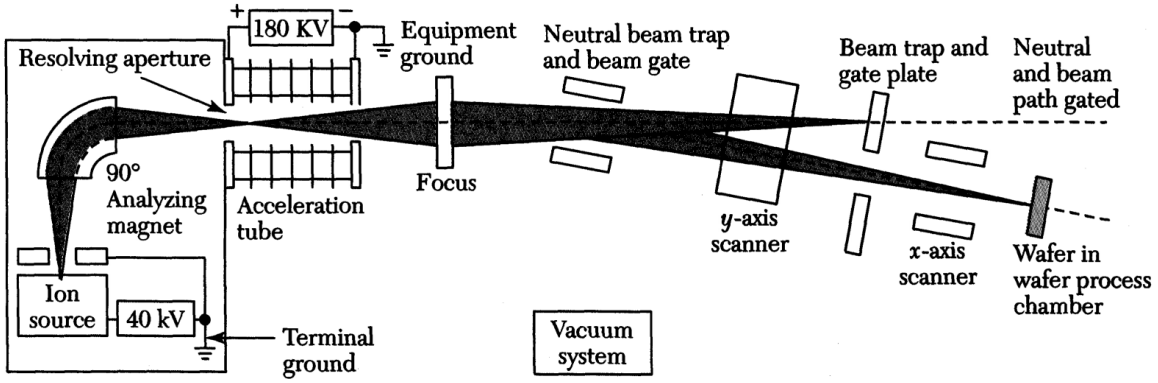

Figure 3.17: Schematic for a medium range 180 keV ion implanter [25].

During early interactions, most of this high kinetic energy will be lost via electronic collisions in terms of electron-hole generation pairs or electronic excitations to higher energy levels. These initial energy transfers will therefore not produce any significant lattice

displacements at the surface. Eventually, as ion energy is reduced, nuclear stopping power becomes dominant, and as expected from a head-on collision of two hard spheres with equal mass, large part of the remaining energy will then be transferred to lattice atoms at the end of the ion range, causing potential cascades of secondary displacements in random directions. Figure 3.18 shows an example of linear energy loss per unit ion track lengths for electronic and nuclear interactions of oxygen ions on a diamond lattice.

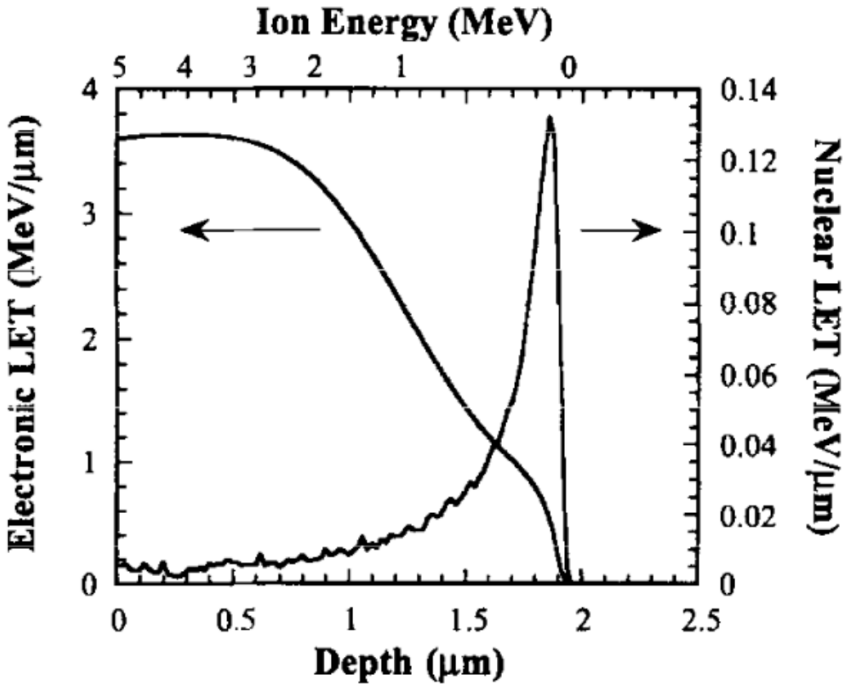

Figure 3.18: Linear energy transfer (LET) defined as the energy loss per unit ion track length, due to electronic and nuclear scattering at different depths. Data profiled from simulating 5 MeV oxygen ions incident on diamond [203].

These nuclear collisions concentrated at the end of the ion range have the net effect of confining most of the lattice disorder within a relatively narrow region at a certain depth buried below the surface. Figure 3.19 illustrates the expected range and damage from a single light weight ion, like boron (B), compared to the immediate damage caused by a heavier ion such as arsenic (As) on a silicon substrate.

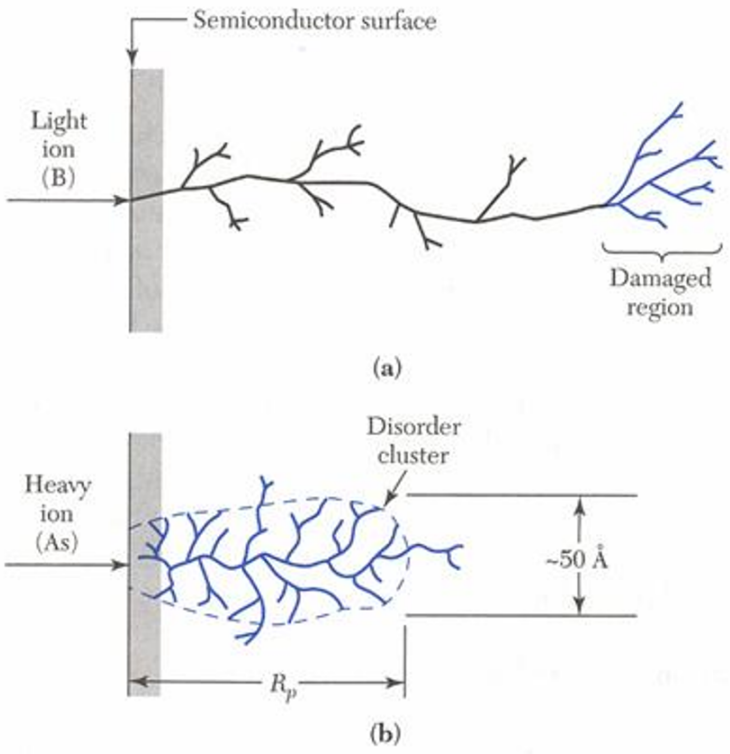

Figure 3.19: Example shematic of different penetration depths and range of damaged region within the lattice caused by: a) light (boron) and b) heavy (arsenic) ions implanted on a substrate [25].

The width of this damaged region ends up being independent of the initial kinetic energy, but the depth at which these nuclear collisions occur is controllable, and can be calculated by Monte Carlo SRIM (Stopping Range of Ions in Matter) simulation software [204] for different types of ions and lattice compositions. Figure 3.20 illustrates the penetration ranges of hydrogen, carbon and oxygen as a function of incident energy on a diamond lattice.

The other critical factor when analyzing implantation effects is ion dosage. At low doses ($<1.5 \times 10^{15}\,\mathrm{cm}^{-2}$ at 100 keV), the damage is almost completely recoverable by thermal annealing, and at high doses ($>10^{16}\,\mathrm{cm}^{-2}$ at 100 keV) the diamond spontaneously graphitizes [201, 205]. The range between these values graphitizes the damaged region at 600 - 950°C in vacuum.

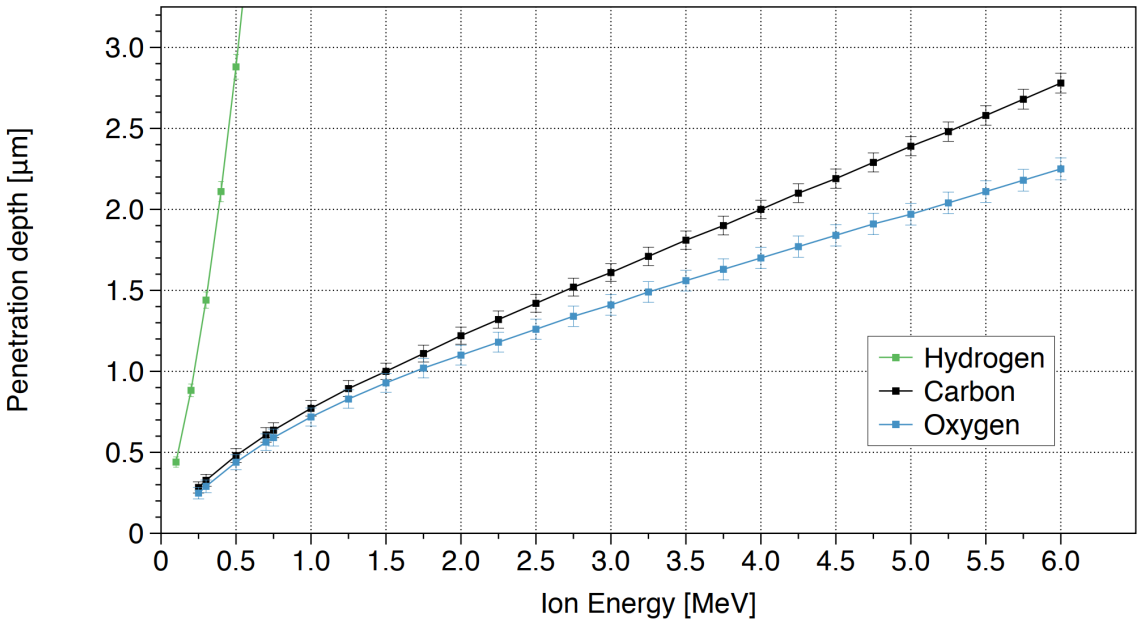

Figure 3.20: SRIM simulations for different ion types and energies on a diamond lattice. The error bars represent the standard deviation ("straggle") of the simulated ion penetration depth distributions. [199]

The top surface of the sample retains its crystallinity and can still be used as a seed for diamond deposition. The damaged region can be graphitized by annealing [201], destroying the sp^3 bonds at this depth. This graphitized region can then be removed by different means, for example, either exposing it to oxygen [201], immersing the sample in hot chromic acid [203], H_2 cleaving [206], thermal oxidation [145], or electrochemical etching [207]. Once the chemical process is complete, the grown substrate layers are effectively separated from the initial seed with minimal kerf losses. Figure 3.21 shows a diagram of the wafer production steps in lift-off with ion implantation.

The first application of this approach for diamond plate separation with grown layers thicker than 200 µm were achieved with carbon implantation at energies of 3 MeV and 180 keV [209]. The lower 180 keV case was reported to have many hillocks on the grown

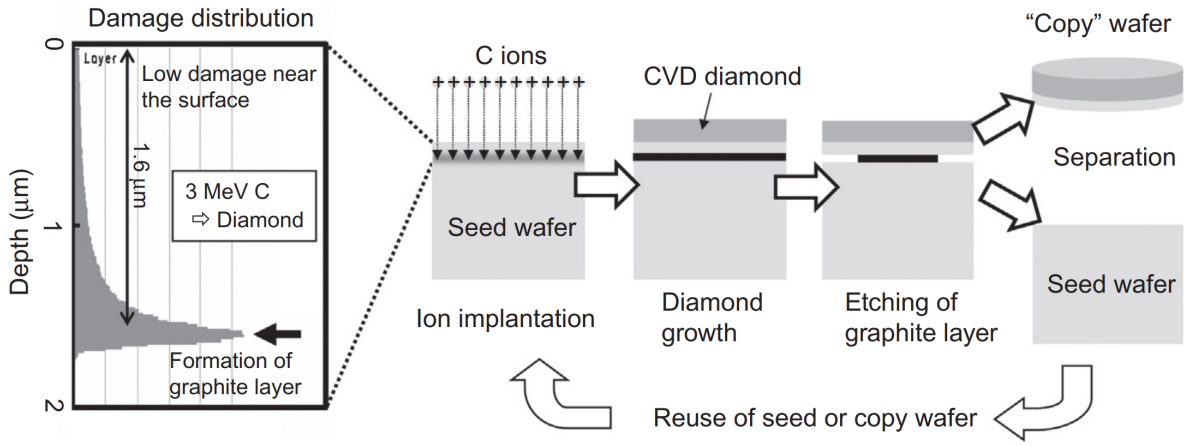

Figure 3.21: Sub-surface damage distribution within a carbon-implanted seed, and schematic illustrating the wafer replication process by re-using the seed wafer [208].

surface, as illustrated in Figure 3.22, suggesting that the damaged region for low energy implantations begin at a range too close to the surface, then the initial stages of the deposition process, i.e. hydrogen ramp-up step to reach the operational pressure, produced anisotropic etching, generating too many dislocation defects at the nucleation layer just before the deposition step.

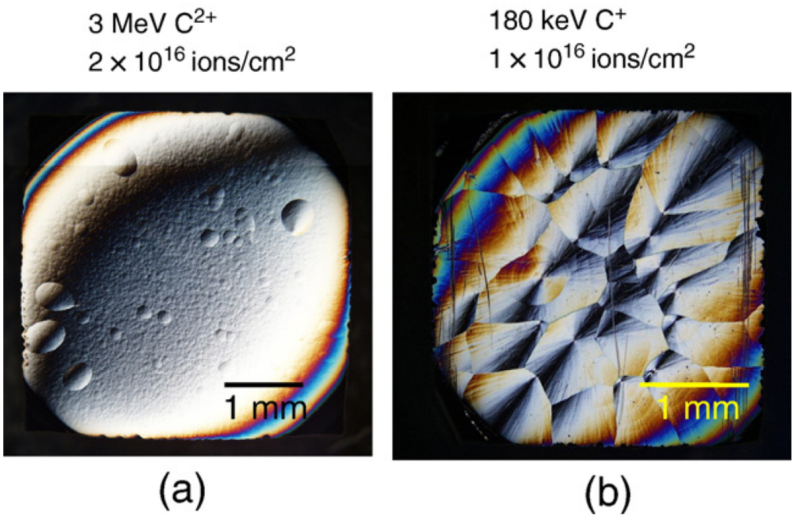

Figure 3.22: DICM images of CVD diamond films grown on carbon ion implanted substrates at (a) 3 MeV and (b) 180 keV [209].

Samples implanted at 3 MeV have been confirmed to have remarkable crystallinity. The optical transparency of these samples in the wavelength range of 220-2500 nm have been measured to be comparable to that of high quality HPHT type-IIa diamond for plates as large as 9 mm x 9 mm x 470 µm [210]. The reported sample did show the presence of internal strain and some threading dislocations, but the results are comparable to direct growth in terms of dislocation densities, therefore confirming ion implantation as an effective technique for large plate production with no inherent size limitations.

3.4 Flip Seed Technique

One feature of the direct lateral growth approach is how the linear growth rate tends to be faster than the lateral growth rate. Based on this premise, and the cubic crystal symmetry of the {001} planes, one approach towards area enlargement is to maximize area gain rates by flipping the sample on its side and continuing growth. The concept of this approach is called the Flip Seed method, and is illustrated in Figure 3.23. For this technique to work, substrates must be grown linearly until the total gain is thicker than the overall width of the sample. Two grown examples are illustrated in Figures 3.24 and 3.25.

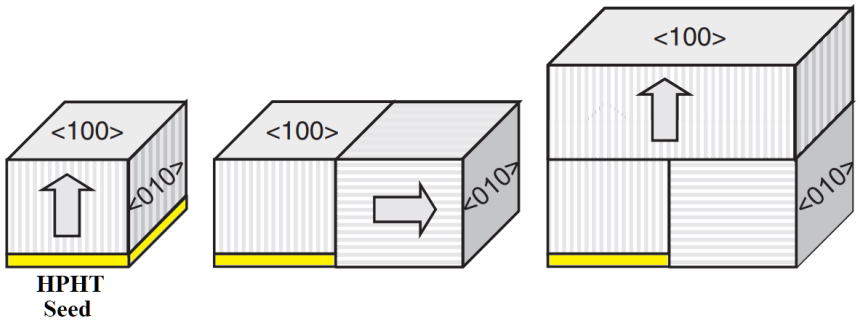

Figure 3.23: Flip Seed Method. Arrows illustrate the growth direction for each step. Each side facing equivalent {100} planes. Image adapted from [211].

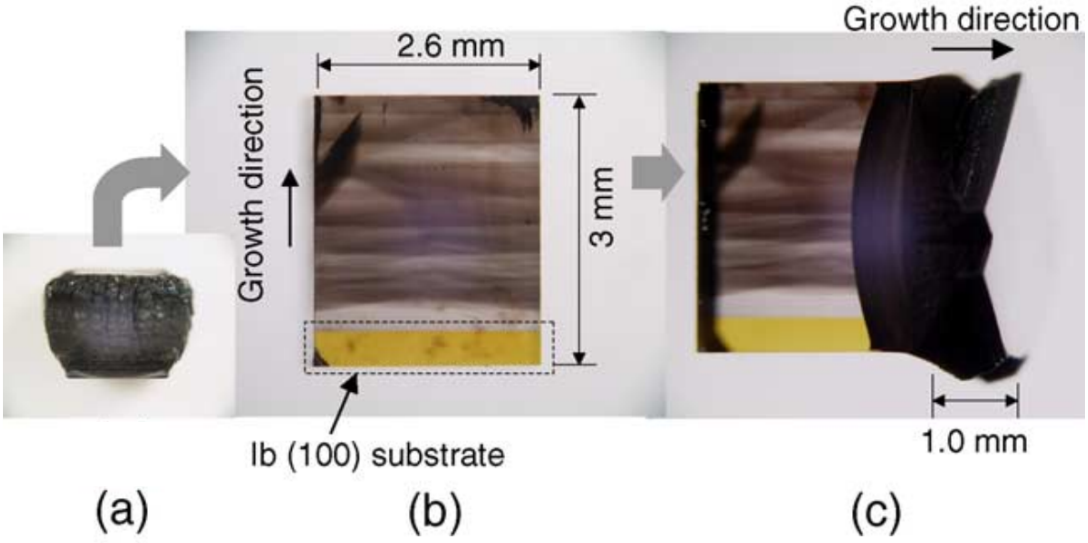

Figure 3.24: (a) As-grown diamond over 3 mm x 3 mm x 0.5 mm seed. This sample was re-grown 9 times and shows how the linear growth rate is much faster than the lateral growth rate. (b) Cut and polished sides. (c) Sample re-grown three more times on its side [188].

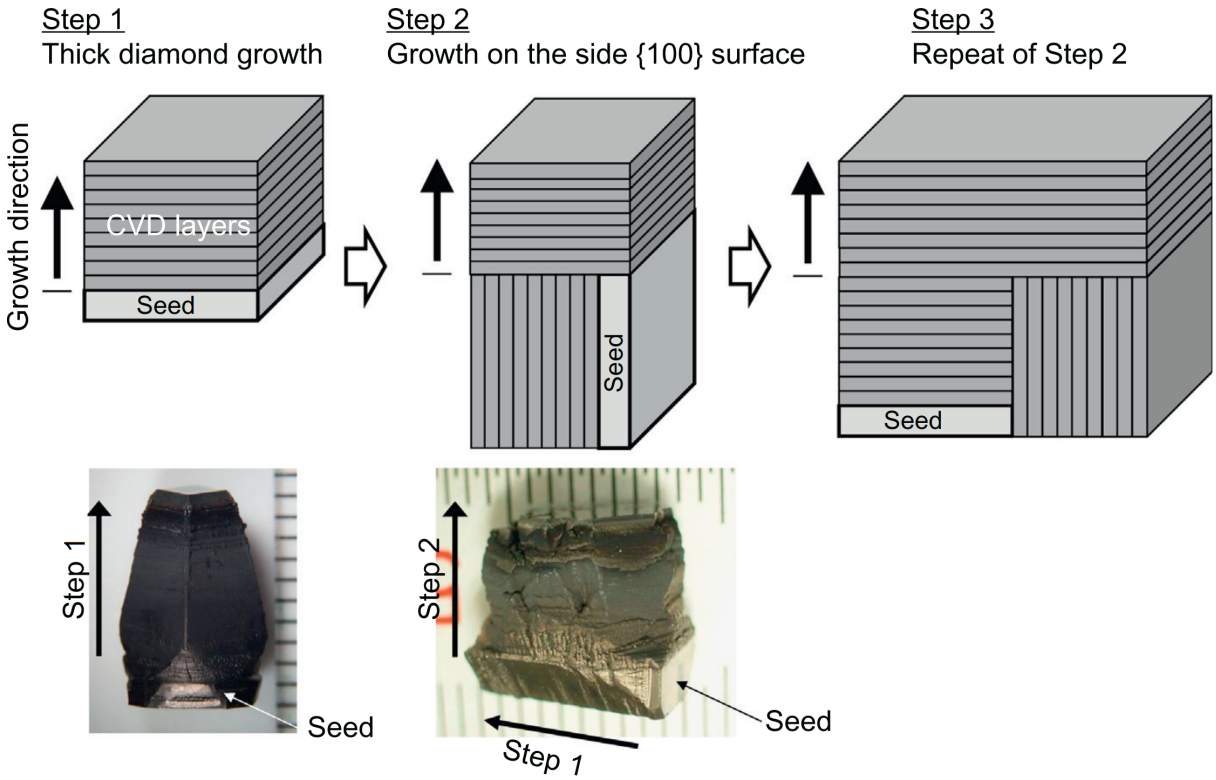

Figure 3.25: Two step flip seed growth [4, 208].

This technique has an added benefit in terms of reducing dislocation densities. Figure 3.26 shows how threading dislocations tend to propagate along the growth direction, but when the substrate is flipped, the surface dislocations are effectively limited as growth proceeds over side facets with reduced defect densities.

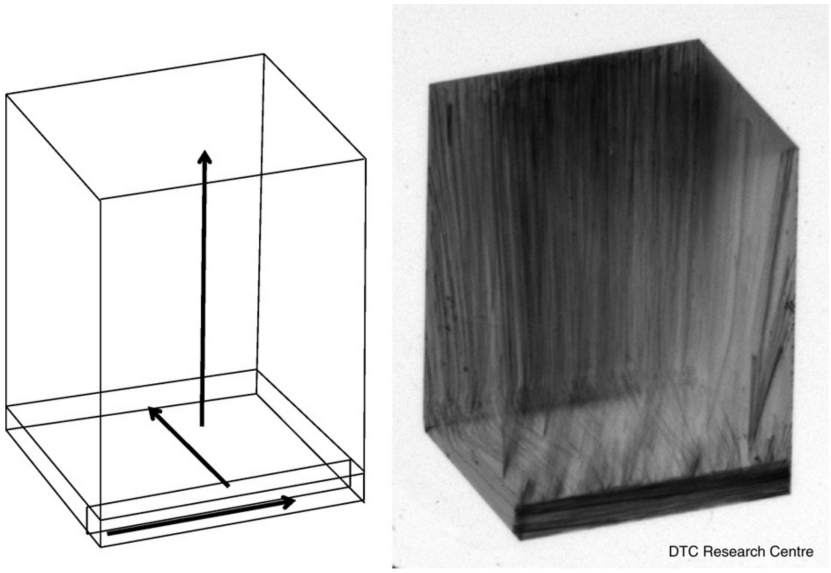

Figure 3.26: X-ray topography measurement of a block of single crystal CVD diamond produced in three sequential growth stages for which the {001} growth directions were orthogonal to each other, as illustrated in the accompanying diagram. Dislocation densities are significantly reduced for each growth step [212].

This method still eventually requires extremely long growth times for large areas, but the process is definitely proven to work at scales up to 10 mm [191]. With research groups developing moving stages into their systems [198, 213, 214], this technique is definitely considered a feasible option for plate production.

One way to improve this technique is by applying an ion implantation and lift off procedure to produce final plates and minimize kerf losses in the last growth step. Figure 3.27 shows a diagram of the process with a highlighted as-grown sample, and Figure 3.28b shows the final half-inch plate produced by Mokuno et. al.

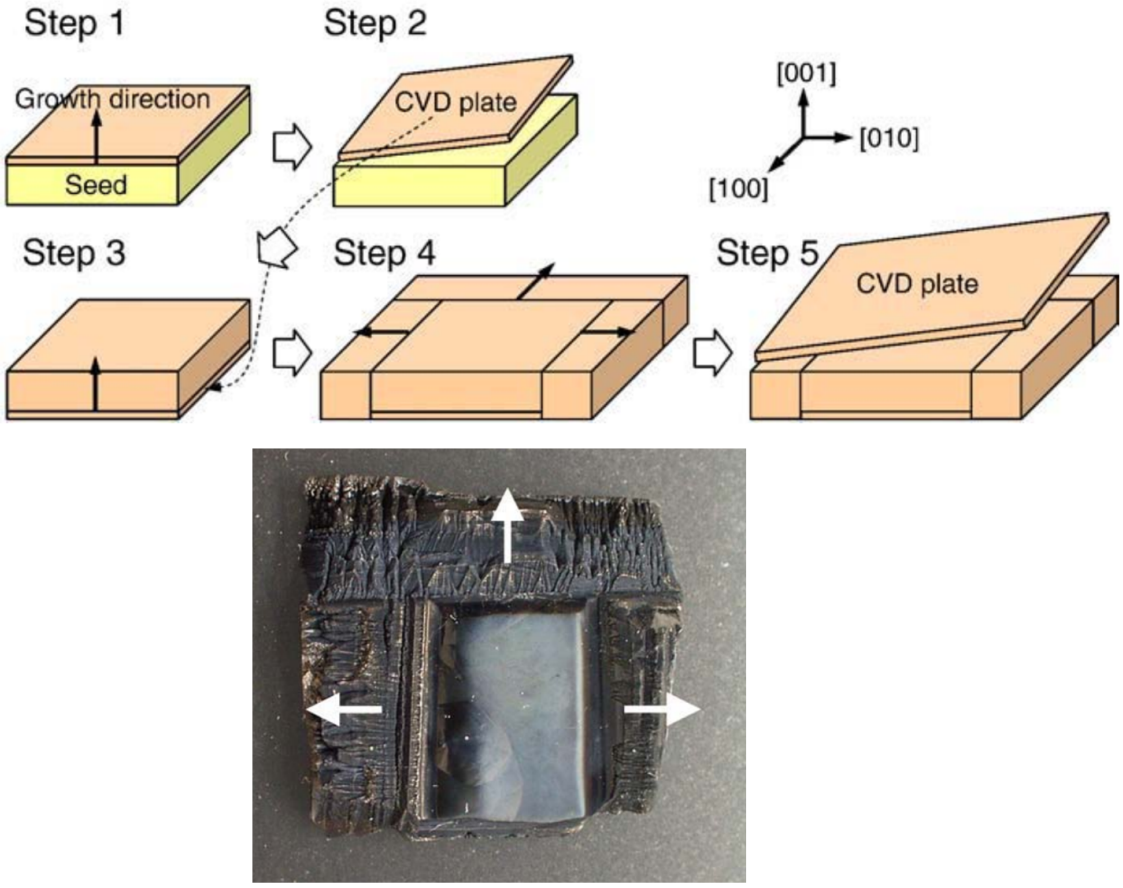

Figure 3.27: Schematic illustration of multiple side-surface growths by flip seed technique, and lift-off process. The picture below shows the as-grown 12.6 mm x 13.3 mm x 3.7 mm sample corresponding to step 4 in the diagram [215].

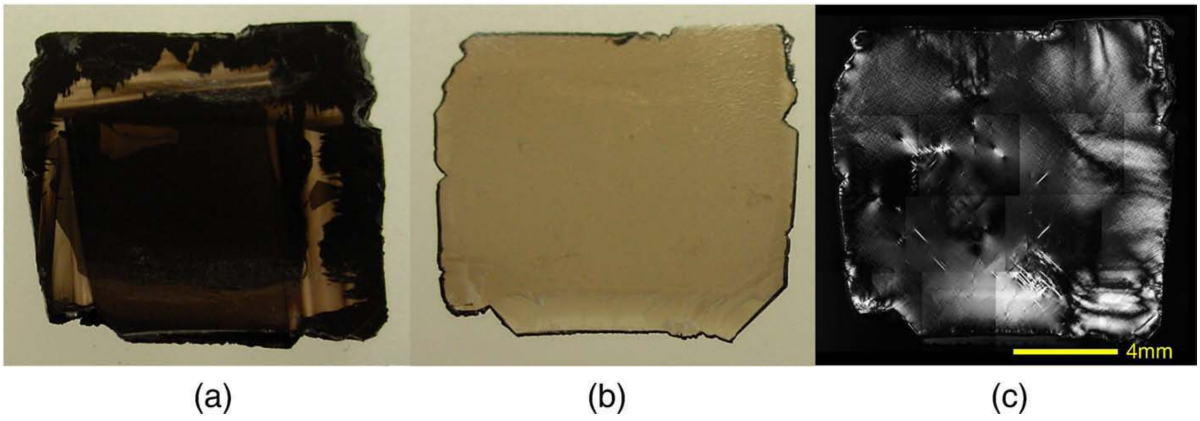

Figure 3.28: (a)Transmission picture of the as-grown sample corresponding to step 4 in Figure 3.27. (b) Polished plate produced by lift-off process using ion implantation, corresponding to step 5 in Figure 3.27. (c) Birefringence image. [215].

3.5 Heteroepitaxial Growth

One way to obtain large areas is by avoiding the need to use a diamond seed substrate in the first place. Heteroepitaxy is a very common technique used in material science, given how size restrictions are only limited by substrate dimensions, and quality is limited in part by the lattice mismatch between the grown and substrate materials [216]. Researchers at the Universität Augsburg, Institut für Physik, in Augsburg, Germany have been developing this diamond synthesis approach since the late 90's [217], settling early on for a substrate combination of Ir and $SrTiO_3$ on silicon [218]. The most recent combination replaces the first interlayer with ZrO_2, known as yttria-stabilized zirconia (YSZ) [6], first reported by Gsell et. al. [219]. The final structure is outlined in Figure 3.29.

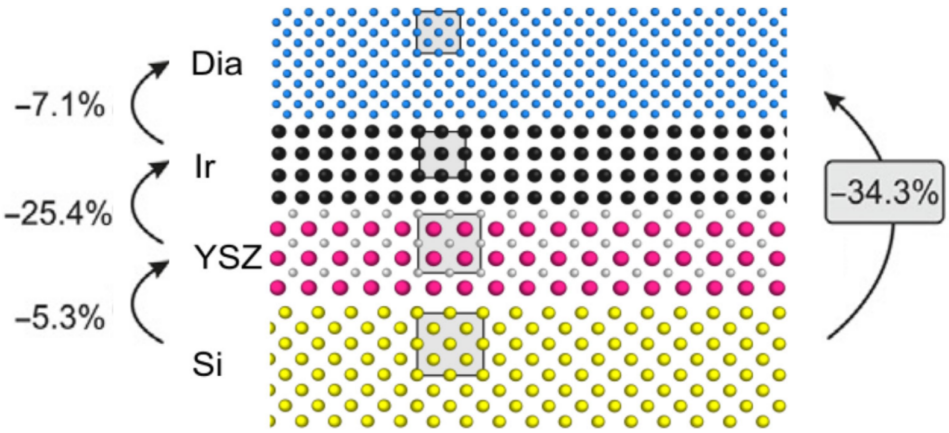

Figure 3.29: Schematic outlining the material deposition sequence of YSZ and Iridium ending with single crystal diamond based on a silicon substrate. Emphasis on the lattice mismatch is illustrated by highlighting a pair of conventional unit cell cross-sections for each layer. Image adapted from [208] and [4].

The process begins with either a thin layer of YSZ to keep the Ir film from reacting with the Si substrate. The Ir film is then bombarded with carbon atoms via Bias Enhanced Nucleation (BEN), this process generates a thin 1.2 nm hydrogenated carbon layer which does not grow thicker with time since it appears to reach a balance with the H_2 etch rate. During this

process of apparent equilibrium, diamond nucleation regions begin to generate spontaneously, forming diamond crystallites at primary nucleation sites. These crystallites are suspected to be connected to each other and eventually covered by a highly defective crystalline matrix which also limits the crystallite height. Below this defective matrix, crystallites grow laterally at a rate of approximately 6 µm/h. The process is suspected to be similar to CVD growth but limited to pure solid state reactions since the atoms are not in direct contact with the gas phase. This unique mechanism has been defined as IBI-BLG (Ion Bombardment Induced - Buried Lateral Growth) [6]. The team was able to produce a 90 mm diameter single crystal substrate with a thickness of 1.6 mm, illustrated in Figure 3.30, weighing in at 155 carat.

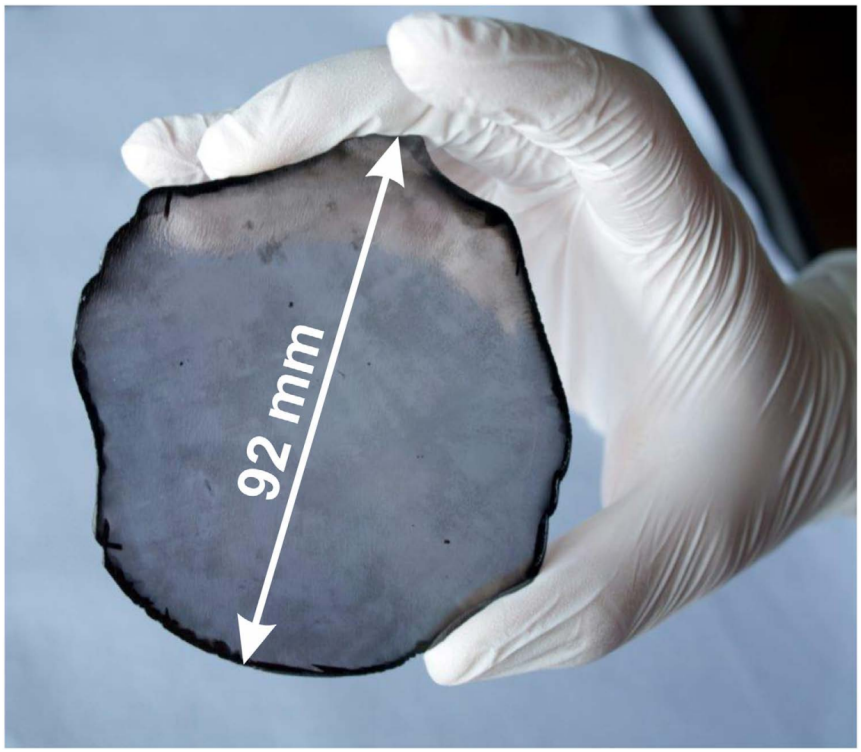

Figure 3.30: Freestanding, unpolished SCD synthesized by heteroepitaxy on Ir/YSZ/Si [6].

The dislocation density for these substrates improves significantly when the layers are grown thicker, as measured by Raman peak widths in Figure 3.31a, or measured by etch pit densities as illustrated in Figure 3.31b. The etch pit density of the final wafer was measured in

the range of 4×10^7 cm^{-2} [6], smaller than natural Type IIa diamonds at $10^8 - 10^9$ cm^{-2} [56]. Rocking curve measurements over the (004) plane also improved as the layers were grown thicker, as illustrated in Figure 3.31c. The final top surface averaged $0.064 \pm 0.011°$. This amount is close to five times wider than high quality CVD grown material, but it also lies in the low range of natural Type IIa diamonds [220], as illustrated in Figure 3.31d.

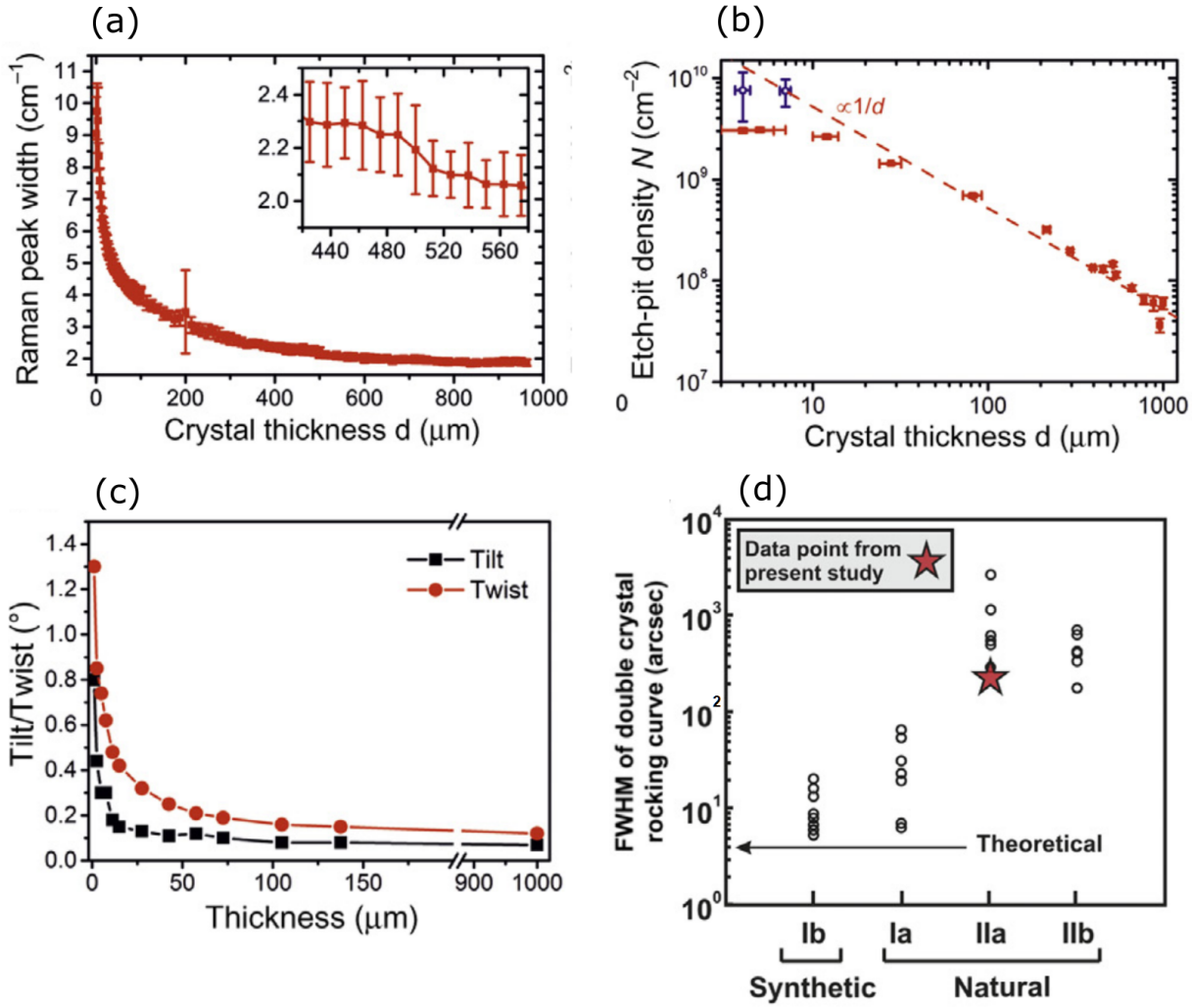

Figure 3.31: Dislocation densities as measured by: a) Raman peak widths, b) Etch pit densities and c) Tilt and Twist mosaicity measurements as a function of sample thickness. d) Figure comparing final mosaicity measurements relative to synthetic and natural diamonds [208].

A recently published report on diamond heteroepitaxy comes from the department of Electrical and Electronic Engineering at Saga University in Japan. Their approach begins with a $(11\bar{2}0)$ (a-plane), sapphire substrate with an Ir buffer layer and continues with Bias Enhanced Nucleation to nucleate the diamond layer. An additional step used for wafer separation is the application of the microneedle technique, which are formed by selectively etching the initial diamond layers using a Ni mask to form vertically aligned pillars called microneedles. These microneedles tend to relax residual strain caused by a mismatched coefficient of thermal expansion between substrate layers and the grown diamond. When the final deposition cools down, the top diamond layer naturally delaminates from the substrate without any cracking [221]. The process is illustrated in Figure 3.32.

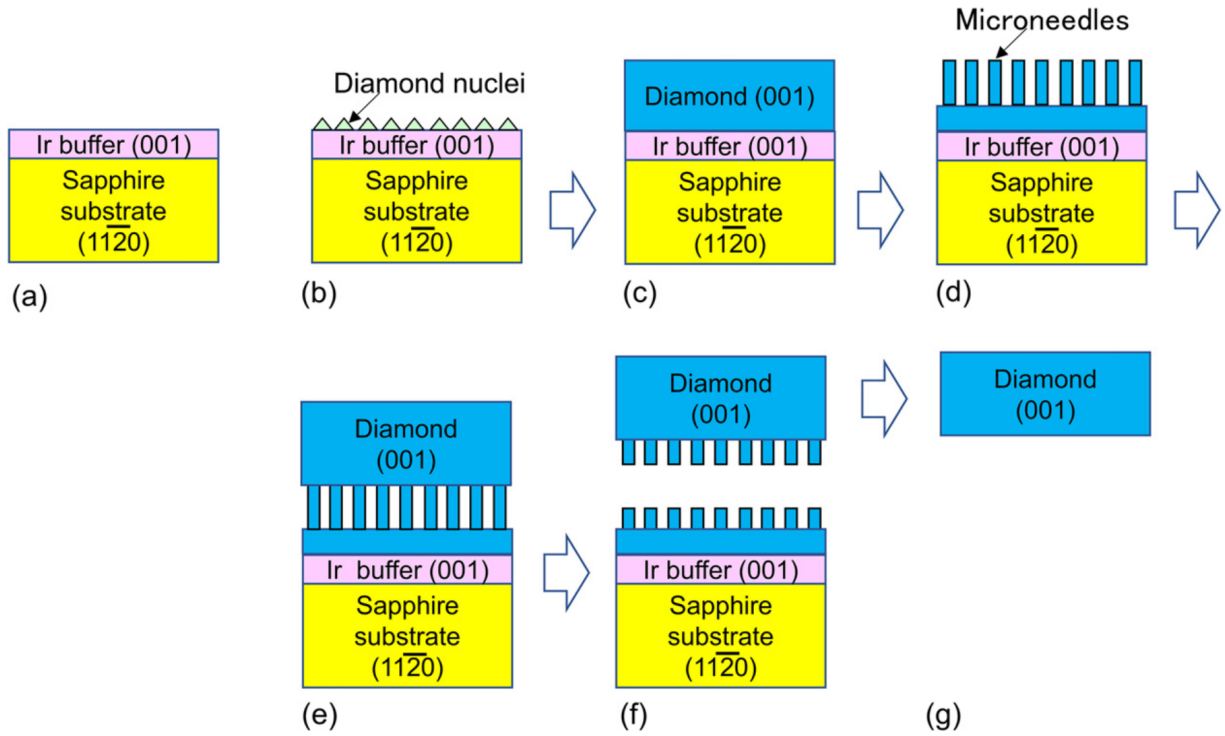

Figure 3.32: Heteroepitaxial diamond procedure over a Ir buffer and sapphire substrate. (a) Ir buffer layer on the sapphire $(11\bar{2}0)$ substrate, (b) diamond bias-enhanced nucleation (BEN), (c) diamond-layer growth on the Ir/sapphire substrate, (d) microneedle formation, (e) diamond layer overgrowth, (f) delamination, (g) polishing, and planarization to produce a free-standing single crystal diamond plate [221].

The final one-inch diameter wafer was planarized through chemical polishing has a thickness of 500-600 µm, is being called the "Kenzan Diamond ®", illustrated in Figure 3.33. The wafer did not break during growth or polishing, but unfortunately, the wafer cracked during a photomask patterning process as electronic devices were being fabricated on the substrate.

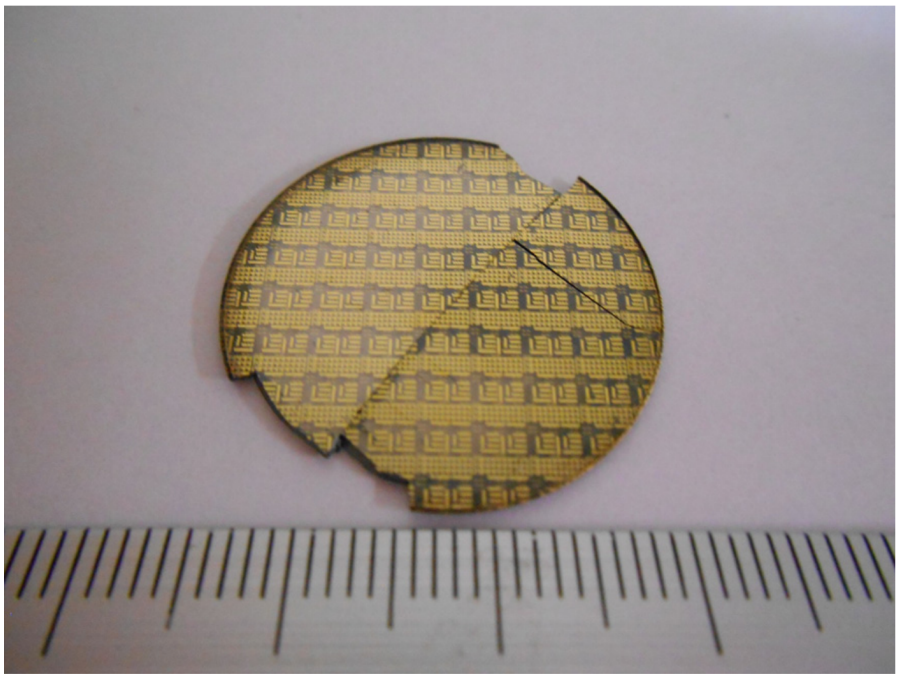

Figure 3.33: One-inch free standing single crystal diamond wafer after photolitography [221].

The diamond layer was characterized as a single crystal with no twinning as measured by x-ray pole measurements, and having x-ray rocking curve widths of 113.4 arcsec for the (004) plane. The total dislocation density was estimated at $1.4 \times 10^7\,\mathrm{cm}^{-2}$ as measured by plain view transmission electron microscopy, less than but within the same order of magnitude as the wafer produced by Schreck et. al. [6]. The radius of curvature for this wafer was measured at 90.6 cm. One improvement reported by this investigation is how the quality was high enough to fabricate lateral structure MOSFETs with a Baliga FOM of $145\,\mathrm{MW\,cm}^{-2}$, the highest ever reported for diamond.

Another approach improving on heteroepitaxy could be argued to be an extension on work by the 2017 report from Tallaire et. al. where they reduced the number of dislocations by lateral growth over a macroscopic hole [186]. As this concept was shown to work when there is no underlying diamond, then some of the highly defective diamond layers from heteroepitaxy could be masked away with a grid, then higher quality diamond would overgrow over each individual area. The approach, illustrated in Figure 3.34, resulted in a dislocation density of $9 \times 10^6\,\mathrm{cm}^{-2}$ the lowest ever reported for diamond heteroepitaxy by 2019.

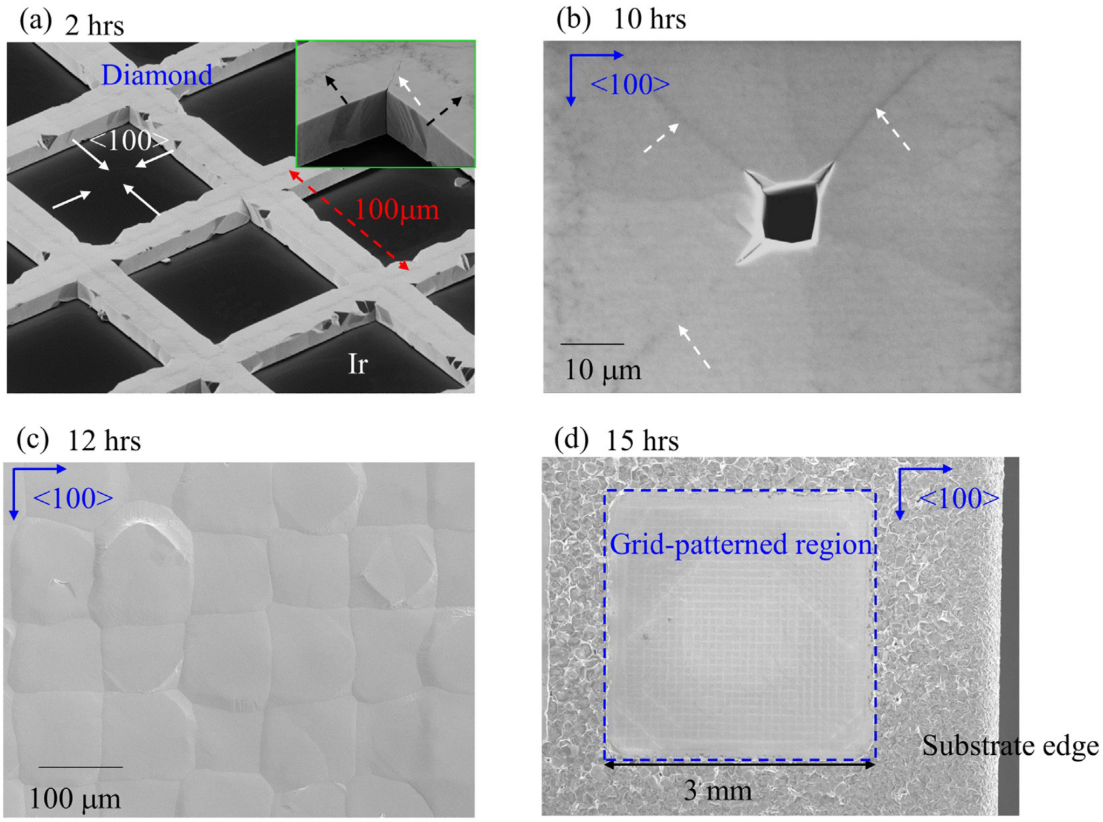

Figure 3.34: Heteroepitaxial diamond growth from grid-patterned nucleation region with grid spacing intervals of 100 µm. (a) SEM image of epitaxial diamond grown for 2 h. Inset is magnified image in corner. Plain-view SEM image of diamond surface grown for (b) 10h focused at the center of the grid, and (c) 12 h. (d) Surface morphology after 15 h growth. [222]

The same french group that published the macroscopic hole study [186] went ahead and replicated this approach but this time with laser piercing direct micrometric hole arrays instead

of using a mask. Combined with years of refinements on process parameter optimizations, in 2021 they reported even further improvements in average dislocation density measurements at $4.6 \times 10^6\,\mathrm{cm}^{-2}$, and dropping as low as $6 \times 10^5\,\mathrm{cm}^{-2}$ within the overgrown regions. This value now includes samples grown by heteroepitaxy within the range typically measured for commercial type Ib single crystal diamond [223]. These latest results, as they compare with previous studies in HPHT and CVD Homoepitaxy, are illustrated in Figure 3.35.

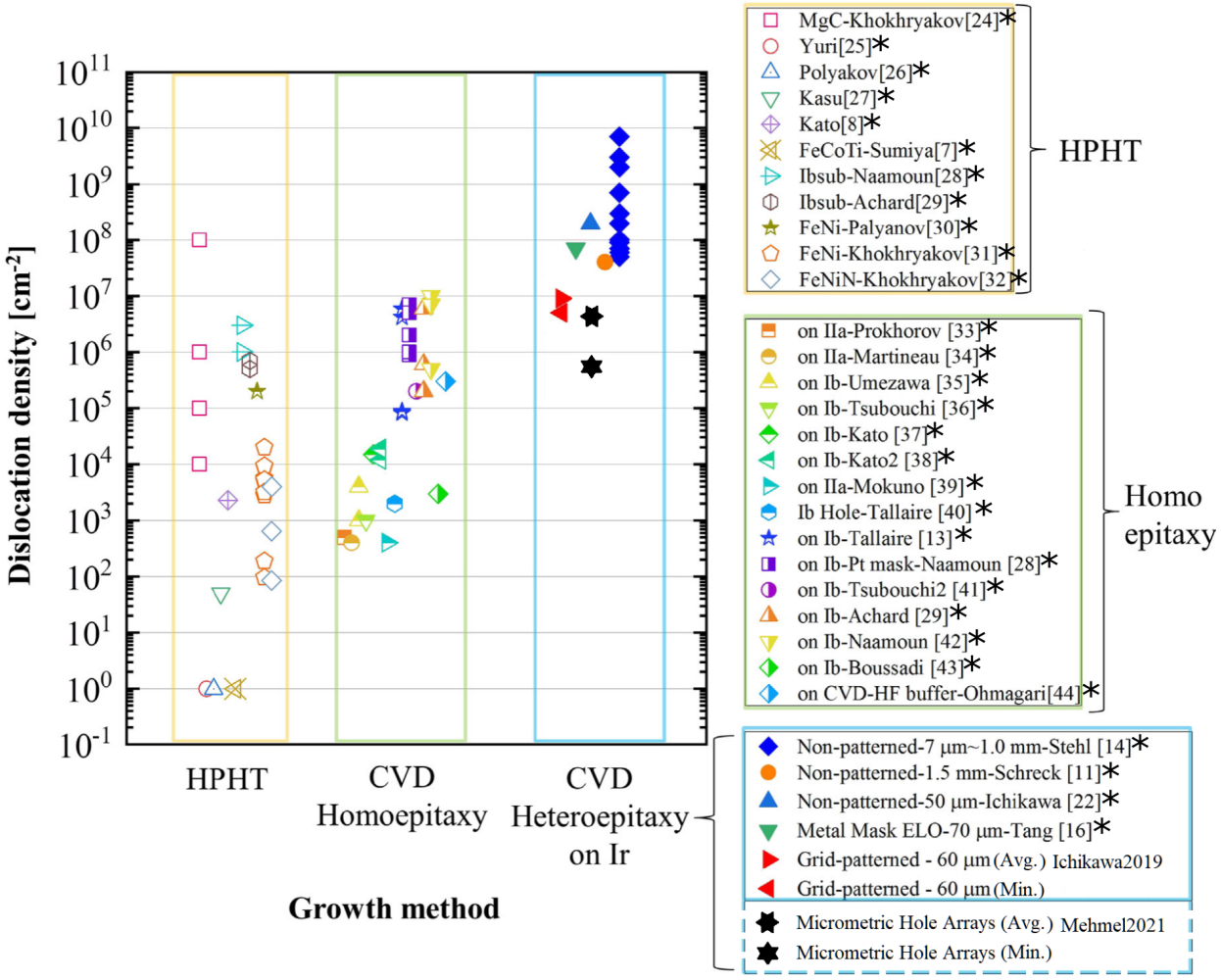

Figure 3.35: Dislocation density in single crystal diamond grown by HPHT and CVD. Each dislocation density was measured by Etch pit method, TEM or X-ray topography. Defect-free diamond is plotted as $1\,\mathrm{cm}^{-2}$ for this semi-logarithmic plot. Image adapted from [222]. Please refer to [222] for all reference numbers labeled with an asterisk. "Ichikawa2019" corresponds to ref. [222], and "Mehmel2021" corresponds to ref. [223].

3.6 Mosaic Technique

One way to achieve instant area gains is by tiling together separate substrates to generate a crystallographically aligned seed. Figure 3.36 shows the general idea, where a large plate can be grown and separated from the mosaic substrate as long as the lattice mismatch between the tiles is reduced to a minimum. If the difference in orientation is indistinguishable between regions grown from separate tiles, the produced plates are then, by definition, single crystal substrates.

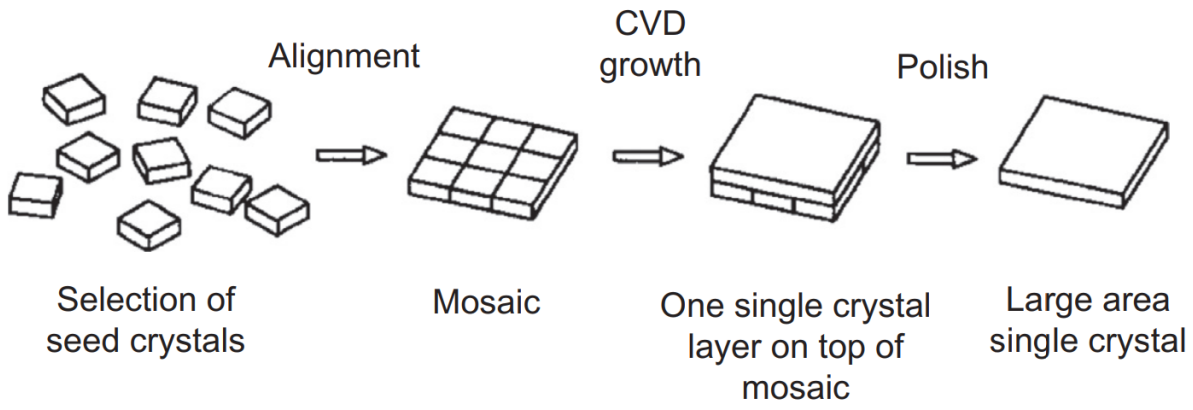

Figure 3.36: Large area substrate produced by mosaic growth [208, 224].

The approach has gained attention since the early days of single crystal diamond growth and several attempts to produce mosaic substrates have been made throughout the years. The technique has been revisited and effectively enhanced as new technologies in diamond deposition have been developed. This section will review every publication on the technique, as relevant details from each report are highlighted. Several aspects need to be taken into consideration, tile alignment parameters, growth conditions, and post-deposition analysis of the grown boundary regions, to name a few. Plenty of details and takeaways will be summarized by the end of this section, where even the arguably conflicting conclusions lead to enriched understanding of the challenges and ongoing improvements on the mosaic technique.

The mosaic reports have been categorized in four sub-sections, divided by how the tiles are sourced, as it makes a significant difference if the tiles originate from the same crystal, or if they were selected separately and assembled together. The reports are then subdivided by research groups. This makes the final sequence roughly chronological, as new developments have led to larger areas based on refined techniques.

3.6.1 Cubic Micro-Tiles

The first demonstration that the mosaic tiling technique was experimentally viable was reported early by Geis et. al. in 1994 at MIT Lincoln Laboratory [225]. The mosaic approach kicked off with the extreme case of using several hundred cubic micro-tiles, defined here as diamond cubes with sides no larger than 300 µm. Their cubed shape, shown in Figure 3.37, arises from naturally occurring {100} crystal facets forming as they grew in size during HPHT synthesis.

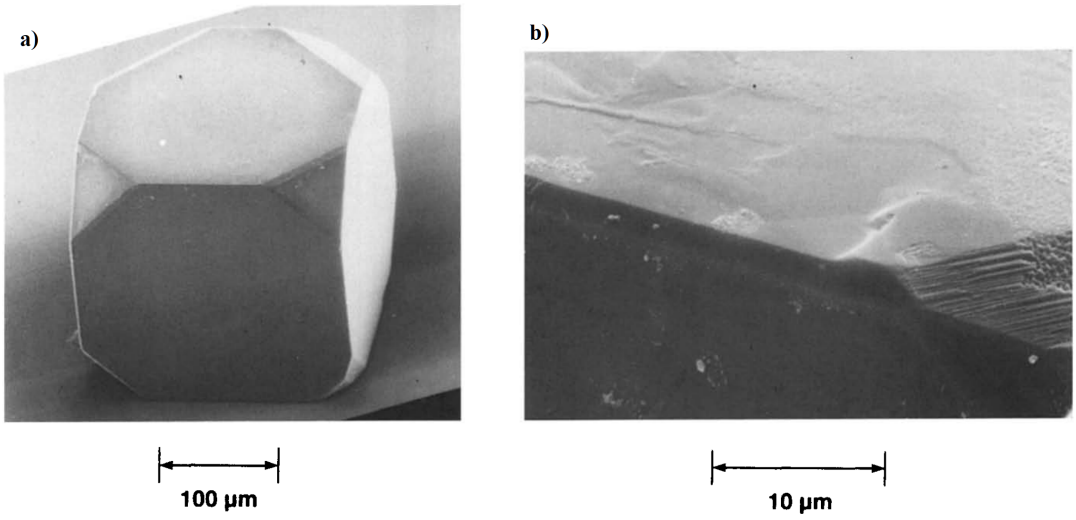

Figure 3.37: (a) Scanning Electron Microsope picture of a single cubic HPHT crystal. The square faces of the cube are {100} planes and the corners are faced with {111} planes. (b) Higher magnification of the top corner of the crystal demonstrates relatively smooth surfaces [225]

Crystal tile sizes and shapes were sorted by means of meshes and a tilted vibrating table [226]. The selected cubes were coalesced together using a viscous mixture of glycerin and isopropyl to help keep the micro-tiles together. The team reported a few ways of achieving this, the most effective was by pressing the tiles together into a square frame over a polished silicon wafer as illustrated in Figure 3.38. Their final positions were then fixed with a novolac-based polymer to help load the mosaic substrate onto the diamond reactor. This polymer was easily removed by exposure to an oxygen plasma prior to deposition.

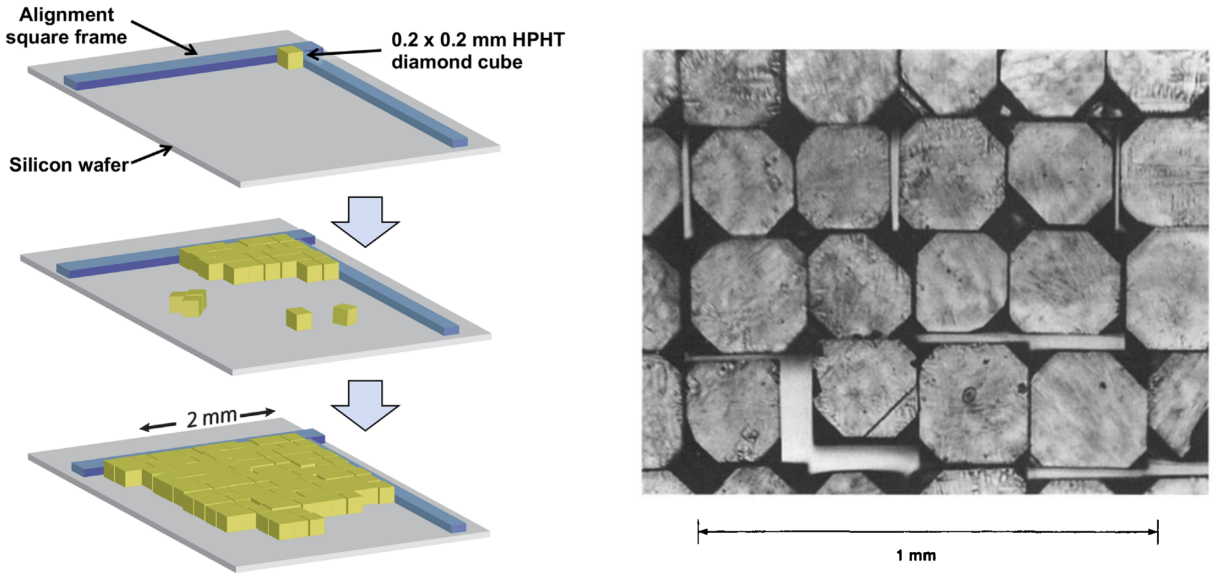

Figure 3.38: a) Aligning HPHT cubic micro-tiles [4]. b) Optical micrograph of coalesced cubic subcrystal mosaic assembly [225].

Approximately 20 µm of homoepitaxial diamond was grown over this substrate using Hot Filament Deposition, forming a continuous layer over the mosaic substrate as illustrated in Figure 3.39. The resulting layer was highly defective, with many hillocks on the top surface and multiple twinned regions which are described as difficult to overcome with additional defect-free homoepitaxial diamond layers. In terms of orientation, the greatest misalignment source was attributed to cube size distributions, estimated at 250 µm with a

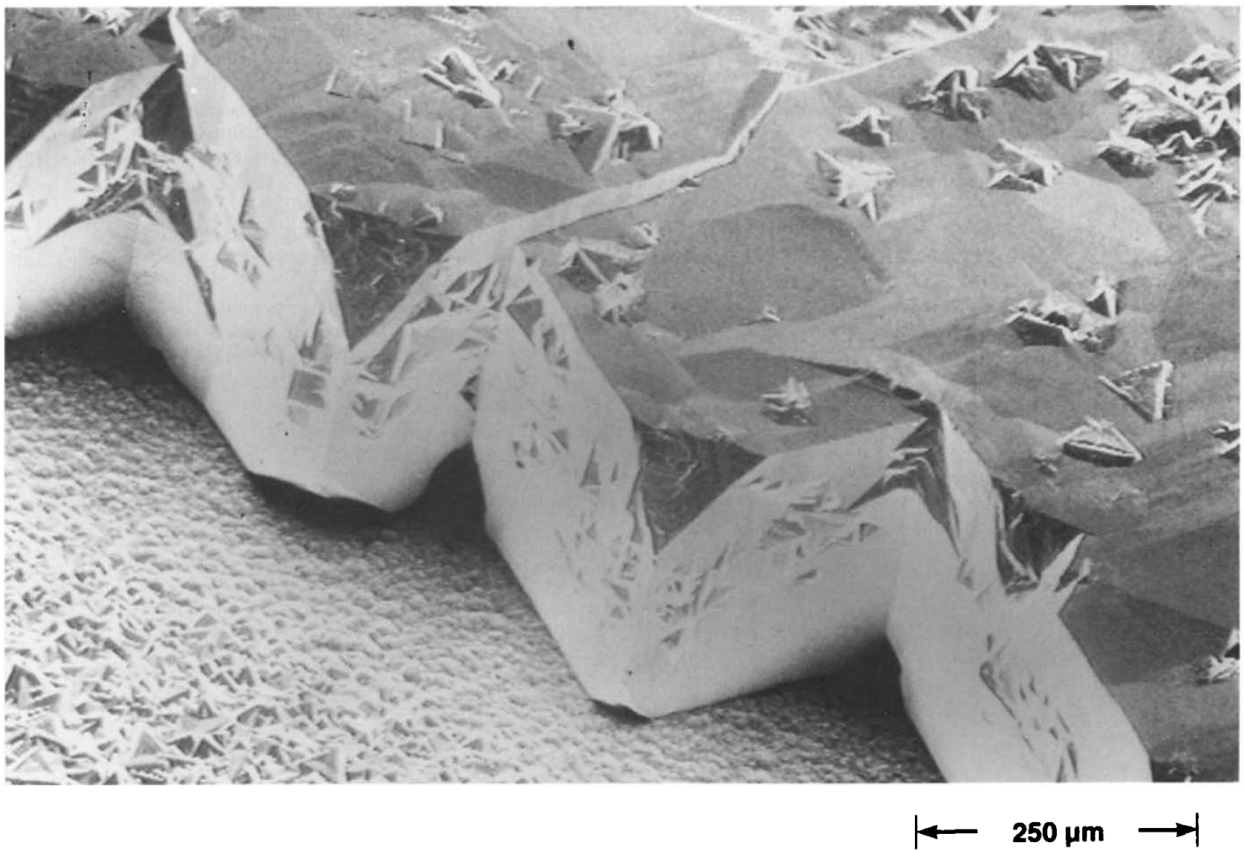

Figure 3.39: Scanning electron micrograph of the edge of a diamond substrate consisting of oriented cubic micro-tiles overgrown with approximately 20 µm of homoepitaxy [225].

standard deviation of 20 µm, resulting in smaller cubes having more liberty to rotate relative to their neighbors. Figure 3.40 shows how this effect was measured with randomly distributed in-plane angular rotations with a standard deviation of 1.7°. The variation in orientation of the (100) planes, as shown in Figure 3.41, is much smaller, with a standard deviation down to a few tenths of a degree. The limiting factor in this case is the roughness of the facets, which is not greater than a few microns, as appreciated in Figure 3.37. The main takeaway from this micro-tile approach is validating the concept of mosaic growth, and demonstrating that a continuous homoepitaxial layer can be achieved even with multiple interfaces and imperfect alignment between tiles. The study also shows how quantitative evaluation of relative misalignments is straightforward, regardless of the number of tiles.

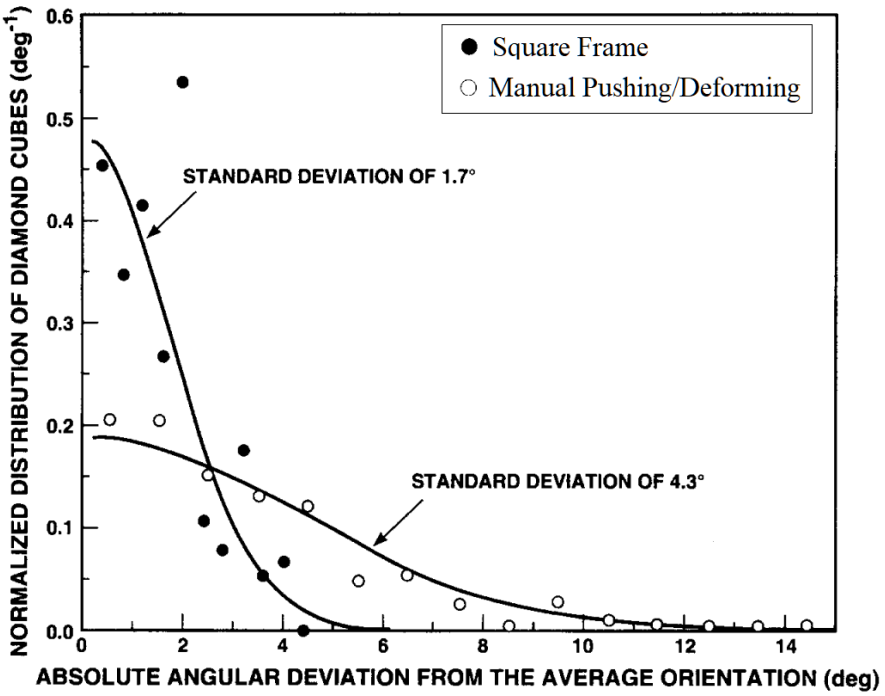

Figure 3.40: Comparing how the in-plane orientation of the diamond cubes were distributed from two different alignment methods. The square frame resulted in better alignment than a manual process of pushing and deforming the coalesced domains [225].

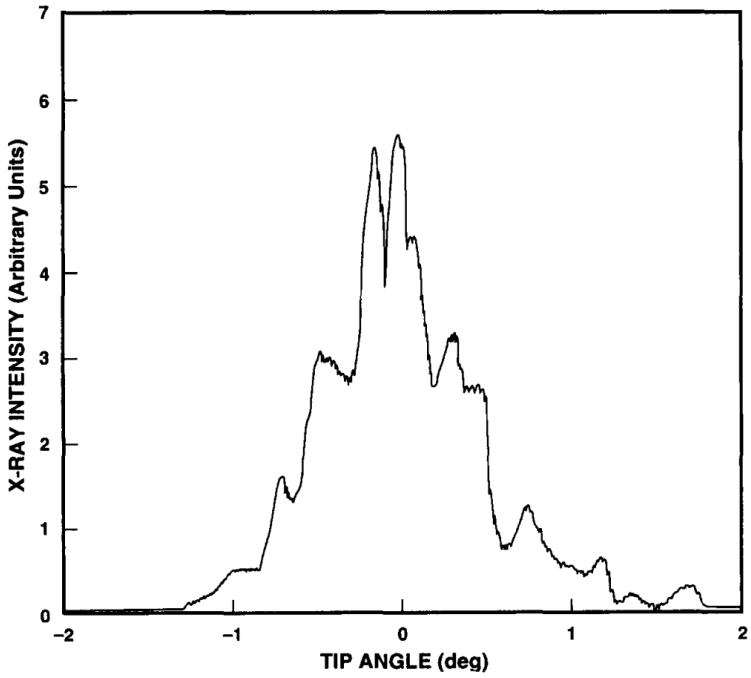

Figure 3.41: Relative distribution of the (100) planes of the coalesced cubes [225].

The micro-tile approach was not limited to this study. There were few, slightly earlier reports by the same group of researchers [226–228] now expanded to Wayne State University in Michigan [229]. The strategy to improve alignment was based on using the underlying silicon substrate not just as a flat surface, but as an actual crystallographic reference. The process, illustrated in Figure 3.42, involves etching tetrahedral pits on a (100)-oriented silicon wafer then seeding these shallow gratings with similarly sized diamonds, this time selected to be 75-100 µm wide and faceted by (111) planes [227]. Since silicon and diamond have the same atomic structure, the lattices on these micro-tiles would be theoretically aligned.

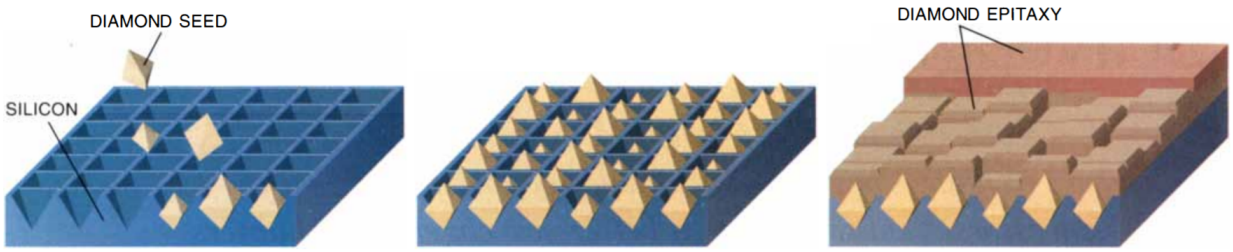

Figure 3.42: Silicon substrate with an array of pyramidal pits seeded with (111) faceted micro-tiles [226].

Plasma assisted [229], and torch diamond growth techniques were used to obtain diamond films, but the best results were obtained with hot filament deposition [227]. A film as thick as 250 µm was deposited on the array over a span of 80 hours, and while the original seeds were completely buried, some holes were still present from unseeded pits, as illustrated in Figure 3.43.

Despite the holes, the overgrown surface was relatively uniform resulting in a smooth specimen with local surface roughness of a few microns [229]. These films were characterized by x-ray topography, x-ray diffraction, microfocus Raman, and by fabricating preliminary electronic devices over their surface. Figures 3.44 and 3.45 show the angular distribution of the seeds relative to the crystallographic substrate normal and in-plane rotations.

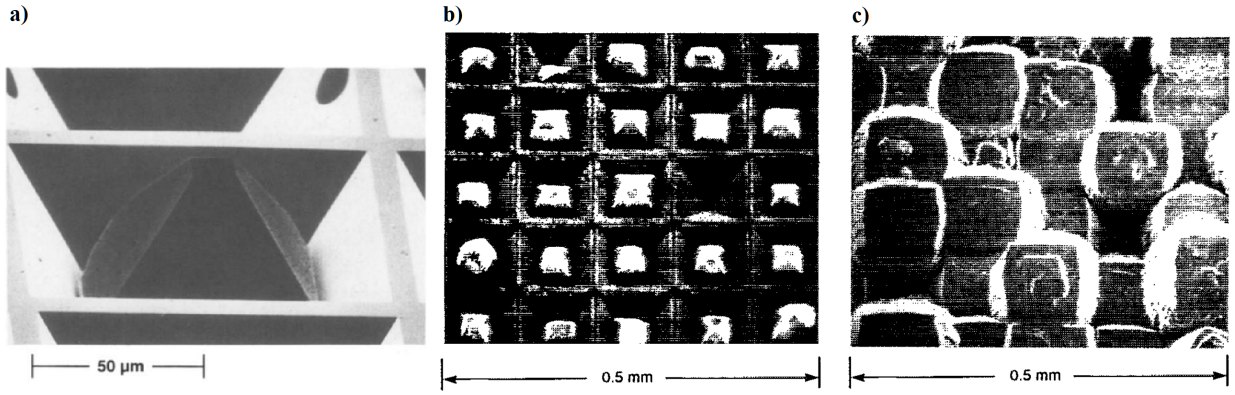

Figure 3.43: a) Scanning electron microscope of a diamond settled in an etched Si structure [228]. b) Array of pyramidal pits with one unseeded pit in the second column from the right. [227] c) Sample after epitaxia1 diamond overgrowth, pictured at the same scale [227].

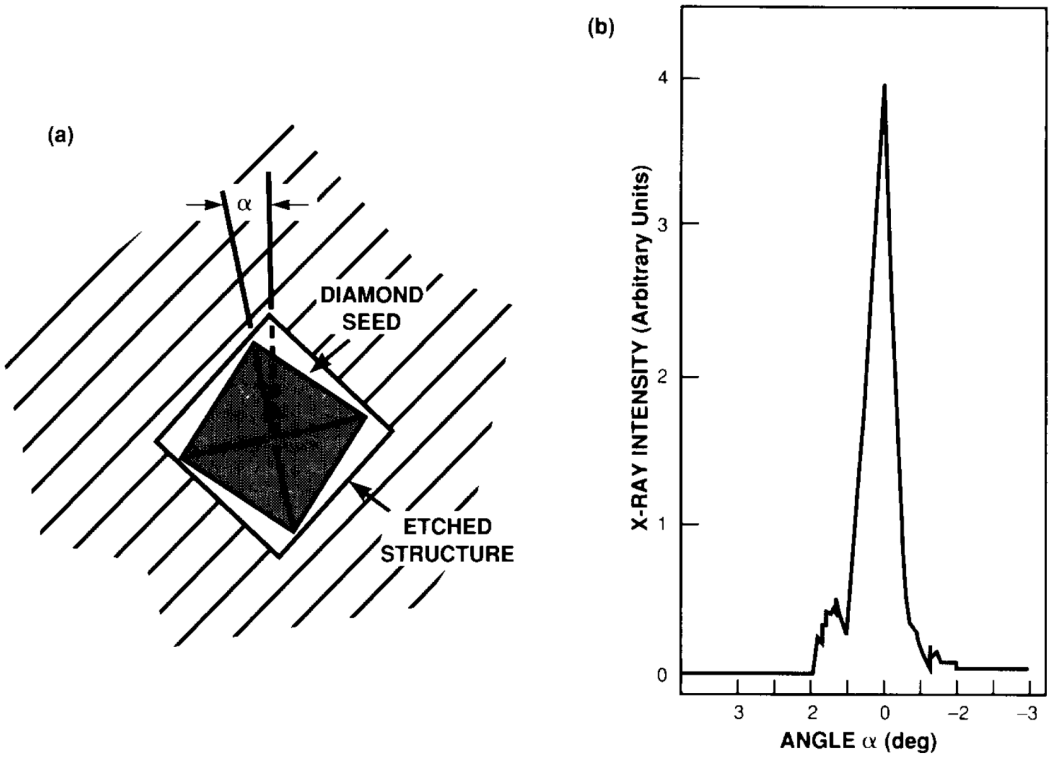

Figure 3.44: a) Schematic top view of an etched structure containing a diamond seed whose crystallographic axis is rotated by an angle α from the (100) in-plane axis on the Si substrate. (b) Typical distribution of diamond seed orientations as a function of α [228].

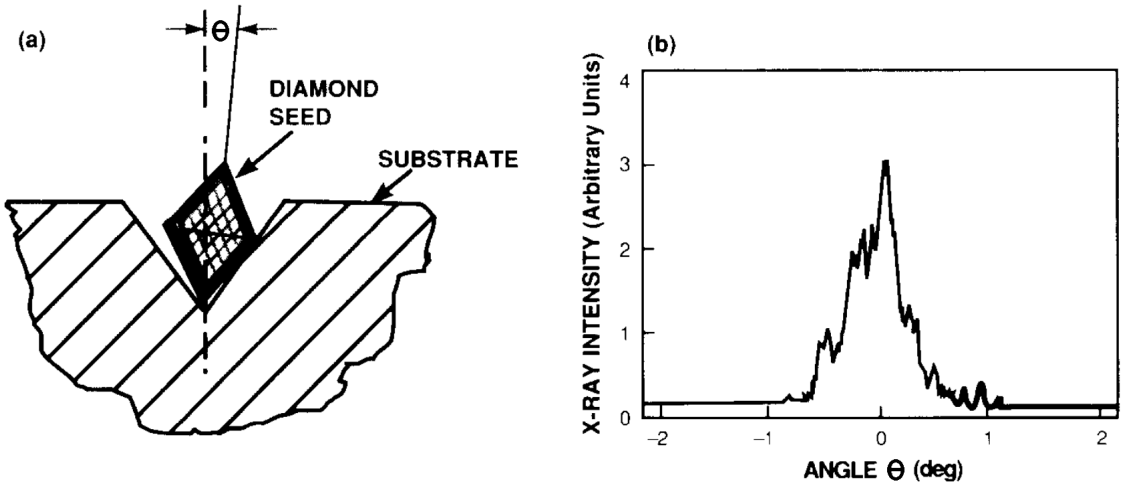

Figure 3.45: Schematic side view of an etched structure containing a diamond seed whose crystallographic axis is tipped by an angle Θ from the axis defined by the facets of structure in the silicon substrate. (b) Typical distribution of diamond seed orientations as a function of Θ [228].

X-ray, Raman, and electrical characterization of these mosaic films by means of fabricated diodes over this grown surface show that low angle grain boundaries tend to form between each micro-tile, as illustrated in Figure 3.46. These results, consistent for substrates up to 10 mm wide, are comparable in quality to homoepitaxial films grown over natural single crystal diamonds [228]. These benchmarks are not ideal for device fabrication, but these reports again confirm the mosaic concept is a valid path for substrate production.

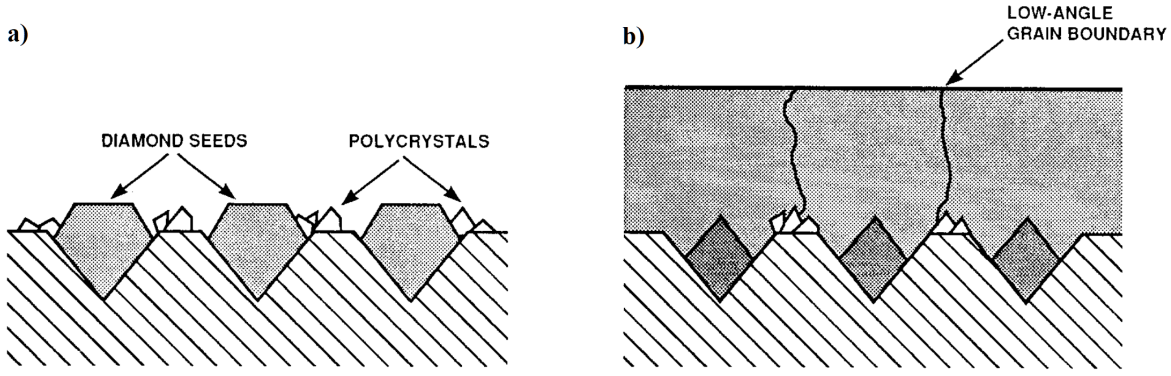

Figure 3.46: Schematic showing two growth stages on seeded Si substrates: a) before coalescence, and b) low-angle grain boundaries formed after longer term growth [228].

3.6.2 Single Source Mosaic Tiles

Research groups continued work on mosaic assemblies soon after the micro-tile reports. To reduce the influence of misalignment parameters between tiles, and to isolate the effects of an interface between two perfectly aligned tiles, the next step in mosaic research is sourcing both tiles from a single larger crystal. The approach is defined here as Single Source Mosaic Tiles.

Netherlands Mosaic

A group in the Netherlands produced the first report on this approach by laser-cutting two equal parts from a single type IIa natural diamond [224]. Each tile was cut to dimensions of 2 mm x 2 mm x 0.5 mm. Re-alignment was handled by soldering each tile onto a molybdenum substrate holder with a thin layer of high-temperature solder (melting point 1250°C). To prevent the plates from floating apart during soldering, a shallow tight-fitting recess was milled in the holder. The procedure was very effective, as it aligned the tiles within 0.2° in each of the three perpendicular directions, and reduced the gap between them to less than 1 µm. XRD measurements could not reveal double diffraction peaks, as this misalignment falls below the mosaic spread in natural type IIa substrates ($0.5 - 1°$) [224, 230]. The report includes two mosaic assemblies labeled Mosaic #1 and Mosaic #2. The main difference between them is the direction of a major wedge-type offcut polished in the top facet relative to the orientation of the interface. Both approximately 6°, one of them in the same direction of the interface, the other, perpendicular to it. Two distinct alignment facets were polished in each of their corners to identify offcut directions.

Grown layers of 14 µm and 40 µm were deposited on the mosaic substrates using the hot filament technique. The grown surfaces were smooth, and a number of large facets were developed with an orientation close to the exact (001) plane around the edges, as expected

from wedge type offcuts in the top surface due to step flow growth [176]. The resulting growth and surface effects, with corresponding diagrams showing the offcut direction in both cases is illustrated in Figure 3.47. Even though tiles were set close to ideal alignment conditions, both samples show what is described as a band of enhanced growth near the region directly over each interface.

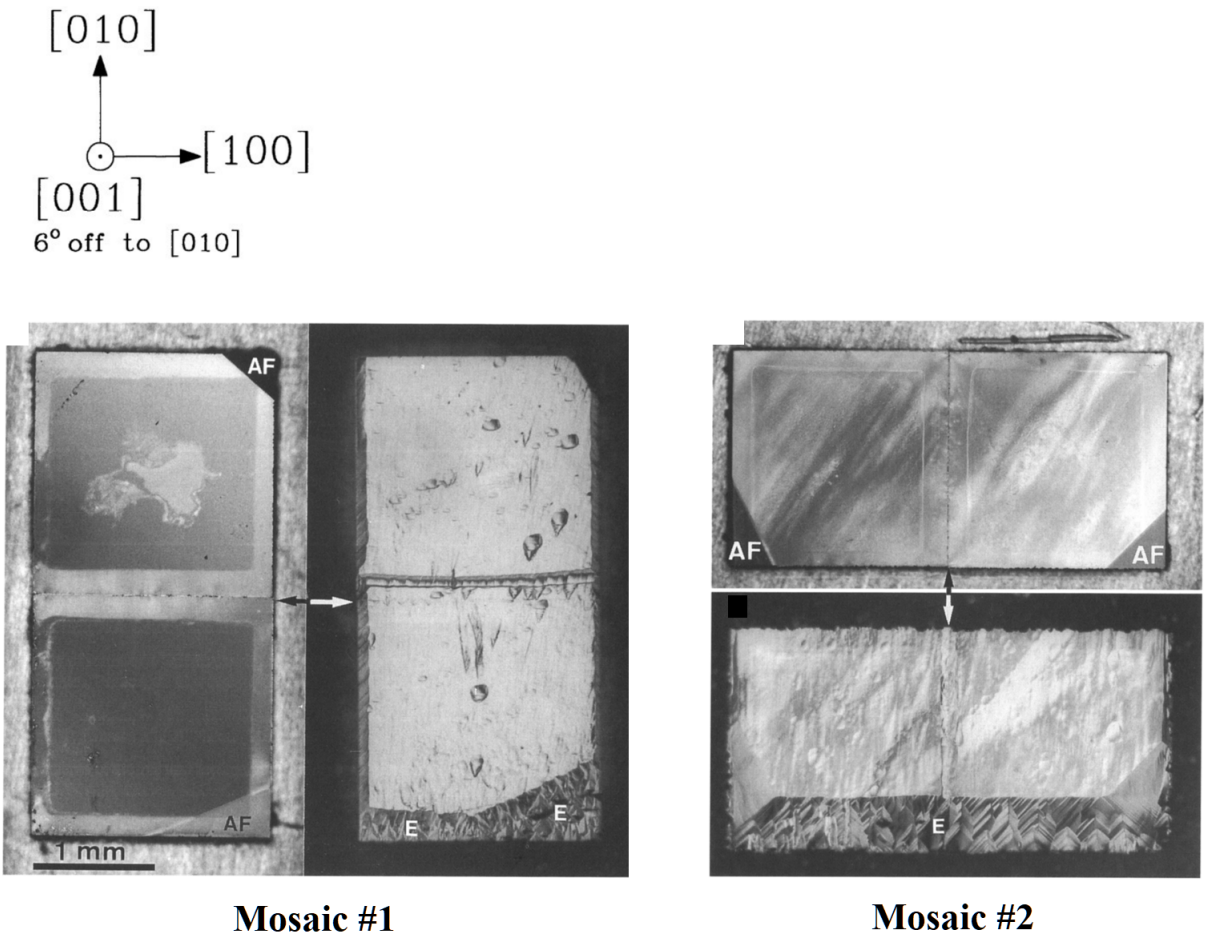

Figure 3.47: The direction of a wedge-type offcut direction depicted in the diagram applies for both mosaic seeds. The offcut in Mosaic #1 has a magnitude of 6°, and Mosaic #2 has a magnitude of 5.5°. Pictographs show how the band of enhanced growth on as-grown samples shifts in the offcut direction by comparison with the initial interface location. The label "AF" shows alignment facets polished to identify each tile and "E" shows exact facets as they emerged in alignment with vincinal (100) planes as expected from the step flow growth process [224].

The group concludes that this band begins to be formed as a low angle grain boundary inducing large numbers of screw dislocations and stacking faults act as step sources spreading in all directions. When this effect interacts with steps present from the offcut in the sample, step flow growth could either annihilate the process, or contribute to it. If the offcut is perpendicular to the interface direction, this effectively causes the grain boundary to propagate in the offcut direction. When the offcut is parallel to the interface direction, the authors mention propagation and slight broadening along the grain boundary itself, even though the effect was not clearly visible on the micrographs. In one case, the band is shifted by $115 \pm 10\,\mu m$, in the other, the band is almost exactly above the original interface.

The downside of this report is that many cracks were observed. These are either confined to the epitaxial layer, or could extend into seed crystals. Some of these cracks have zig-zag patterns along {111} planes, but most were situated near interfaces. The authors comment that its obvious the cracks formed after the cessation of the growth and they conclude that undesirable tensile stress was built up, but the source of the stress was not identified. They considered this issue, and determining the maximum allowable crystallographic mismatch as the main problems requiring further exploration. The main takeaway from this investigation is the clear demonstration that growth effects from mosaic boundaries can be controlled by careful regulation of the step flow mechanism.

We believe the source of this after-growth tensile stress is the process of soldering the tiles to the substrate. As the sample is cooled down after the deposition, the fixed structure with mismatched thermal expansion coefficients over relatively thin grown layers (15-40 µm) will result in cracks. Other experiments, including some in our own investigation, show that if the lattice mismatch is too high, this also leads to cracking. This confirms alignment is a critical issue with the mosaic technique and proposed solutions must be carefully evaluated.

Japanese Mosaic - Preliminary Experiments

The Japanese group at the Diamond Research Center of the National Institute of Advanced Industrial Science and Technology (AIST) in Osaka, Japan, have been the most successful at advancing the mosaic technique producing plates up to 2 inches wide. Their full process is discussed in more detail at the end of this chapter, but their project also began with a single source mosaic tile experiment to make sure initial crystal misorientations were reduced to a minimum and they could focus on observing the effects of grown material over a discontinuous mosaic substrate.

The plate used for the preliminary experiment was a single HPHT Ib-type substrate with 4 mm sides. The 0.4 mm thick sample was cleaved into two pieces [231], re-assembled as a mosaic substrate, then grown and polished, as illustrated in Figure 3.48.

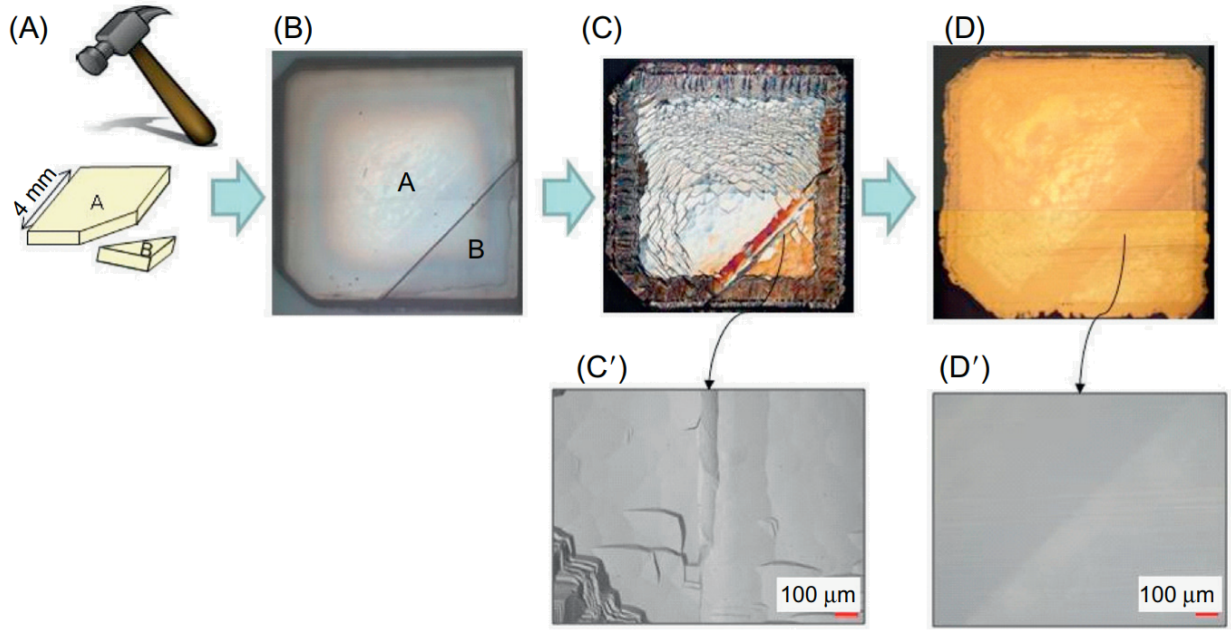

Figure 3.48: A) HPHT 1b type substrate, 4 mm wide, cleaved into two pieces. B) Optical microscope picture of the two pieces re-aligned into their original positions. C) Differential interference contrast microscope image of the as-grown sample. C') Magnified view of the boundary observed by laser microscope. D) Polished grown layer. D') Magnified view of the boundary region [208].

The resulting 200 µm growth fused smoothly, with no abnormal growth or pinholes observed along the junction, proving that epitaxy over sub-crystals with essentially the same orientation is very effective [231].

The next step is applying the ion implantation and lift-off technique, developed by the same group, over the polished grown surface as illustrated in Figure 3.49. The process produced a freestanding plate with a thickness of 0.3 mm. The authors reported how the junction can no longer be identified in the optical microscope image, but other types of measurements were not discussed in the publication.

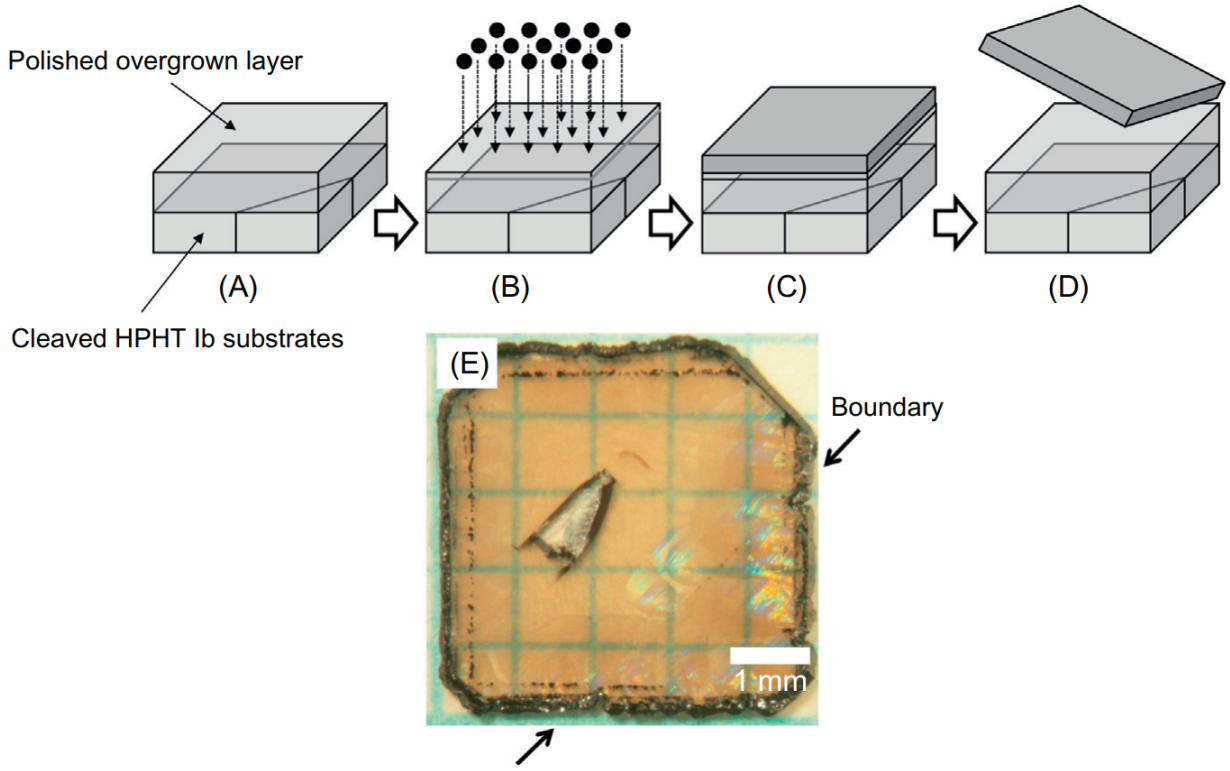

Figure 3.49: A) Polished growth over a cleaved mosaic substrate. B) Ion implantation. C) Growth over ion-implanted layer. D) Freestanding mosaic wafer from the applied lift-off technique. E) Photograph of the freestanding plate. The large crack at the central region was produced accidentally and is separate from the junction [208, 231].

3.6.3 Cloning Technique

The Japanese research group at AIST realized that if the ion implantation and lit-off process is repeated using the same seed, each produced plate would have identical crystal orientations. The group decided to proceed with developing mosaic technique by defining these produced planes as clones [231]. The process began with HPHT Ib-type seed ion implanted at 3 MeV. Each clone was grown by CVD, as well as the resulting mosaic layers. A schematic of the full process is shown in Figure 3.50.

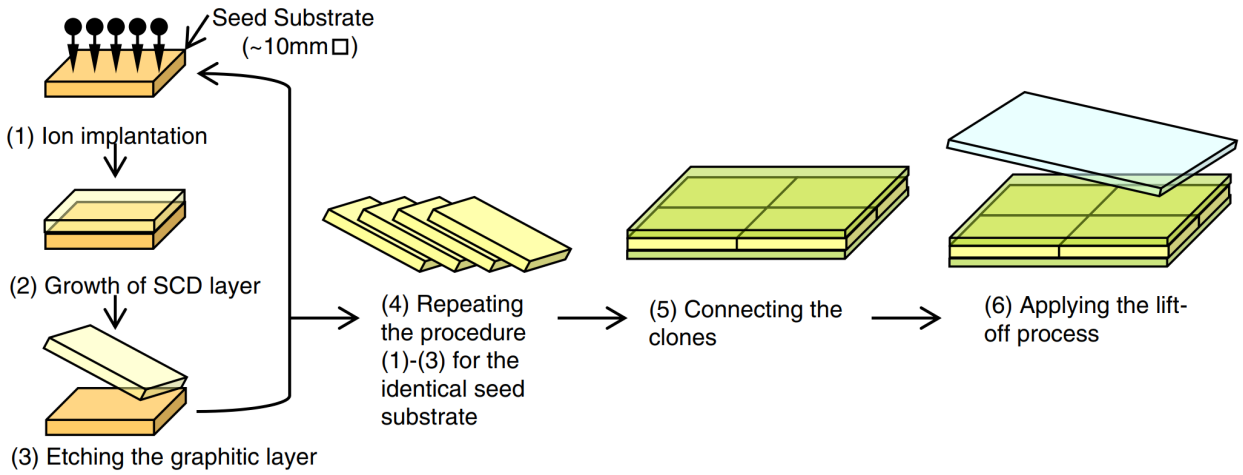

Figure 3.50: Production of cloned tiles by ion implantation, and large plate production by deposition over the ion implanted mosaic seed [232].

Each cloned tile has to be adjusted by laser cutting and polishing, including pre-deposition planarization. Not many details are discussed regarding these intermediate steps, but to get an idea of the resulting misalignments from the re-assembling process, each section on a six piece mosaic made from clones was measured after growth, and their {100} planes deviated by a maximum of 0.3° from the off-angle aveage of 2.9°. In terms of in-plane rotation, measured as relative deviations from the (110) planes, the misorientations were measured as high as ∼2°, which corresponds to the maximum threshold suggested by Findeling-Dufour [233].

The process was successful at the 1 inch scale by joining four tiles [211]. Pictures of the sample, illustrated in Figure 3.51 shows how boundaries above the original interfaces are barely perceptible with the naked eye. When imaging the cross section, and in particular when measuring birefringence in the region, as illustrated in Figure 3.52, it can be concluded that there is still a significant amount of stress developed over mosaic boundaries.

XRD Rocking Curve and Raman mapping over the final polished plate shows how the defective region is limited to a very narrow region, not wider than 200 µm.

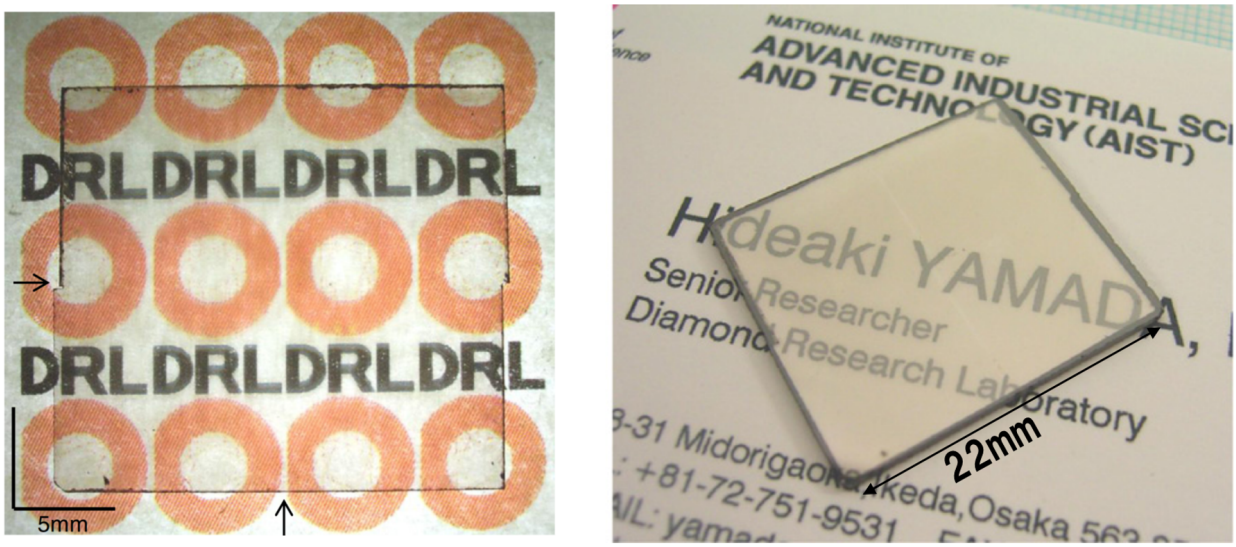

Figure 3.51: Polished mosaic plate 22 mm wide produced by the tile cloning method based on four underlying tiles [232, 234].

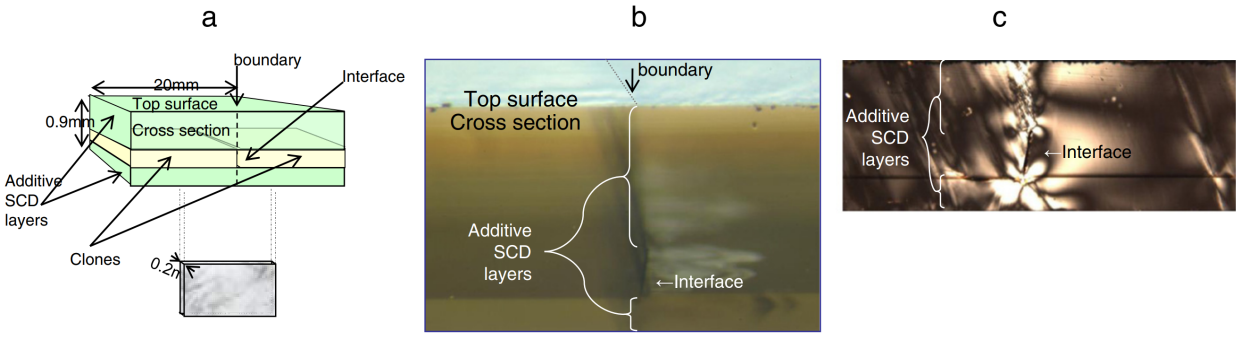

Figure 3.52: a) Schematic of a 0.2 mm thick cross-section taken from a boundary between two tiles on a 0.9 mm thick mosaic sample. b) Image of the cross-section of a mosaic boundary. c) Polarized microscope image of the cross-section of a mosaic boundary [232].

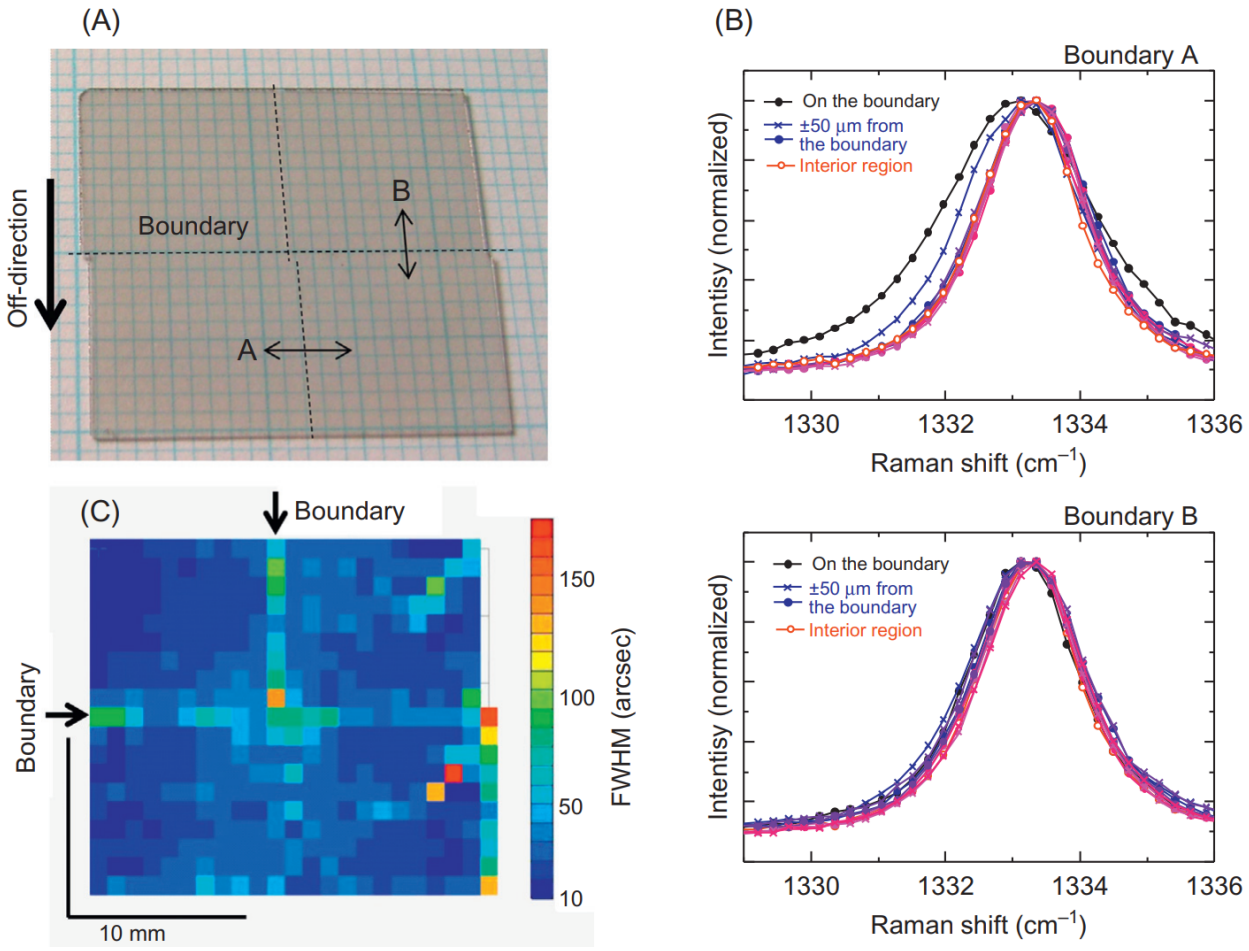

Figure 3.53: A) Photograph of a four tile mosaic plate with outlined and labeled boundary locations. B) Raman measurements near boundaries labeled "A" and "B". The black, blue, and red lines show the spectra obtained just above the boundaries, ±50 µm from the boundaries, and in interior region, respectively. C) XRD Rocking curve FWHM map. Each pixel corresponds to a region 100 µm wide [208, 232].

When the Raman spectra over each boundary is analyzed in greater detail, boundaries parallel to the off-cut direction are broader than those perpendicular to it. The cause of this anisotropy is cited in the study as probably caused by direction of the off-angle in the constituent clone substrates [232] . This observation reaffirms the conclusion by Janssen et. al. [224] where step flow overgrowth induced by a deliberate offcut direction over the top surface will effectively improve dislocation densities and defective regions near mosaic boundaries.

In terms of rocking curve mapping, it should be noted that the 2-D data presented from the study only covers peak widths, representing local mosaicity within the area covered by each spot measurement. Data corresponding to the peak locations was not discussed, therefore relative misorientations after growth were not disclosed for this particular plate for evaluating the accuracy of the initial assembly or any possible readjustments over grown layers.

If the process is repeated by using the produced plates as constituent tiles, the resulting area is amplified exponentially. Using this approach, the group expanded their final areas up to $20 \times 40\,\mathrm{mm}^2$, as illustrated in Figure 3.54.

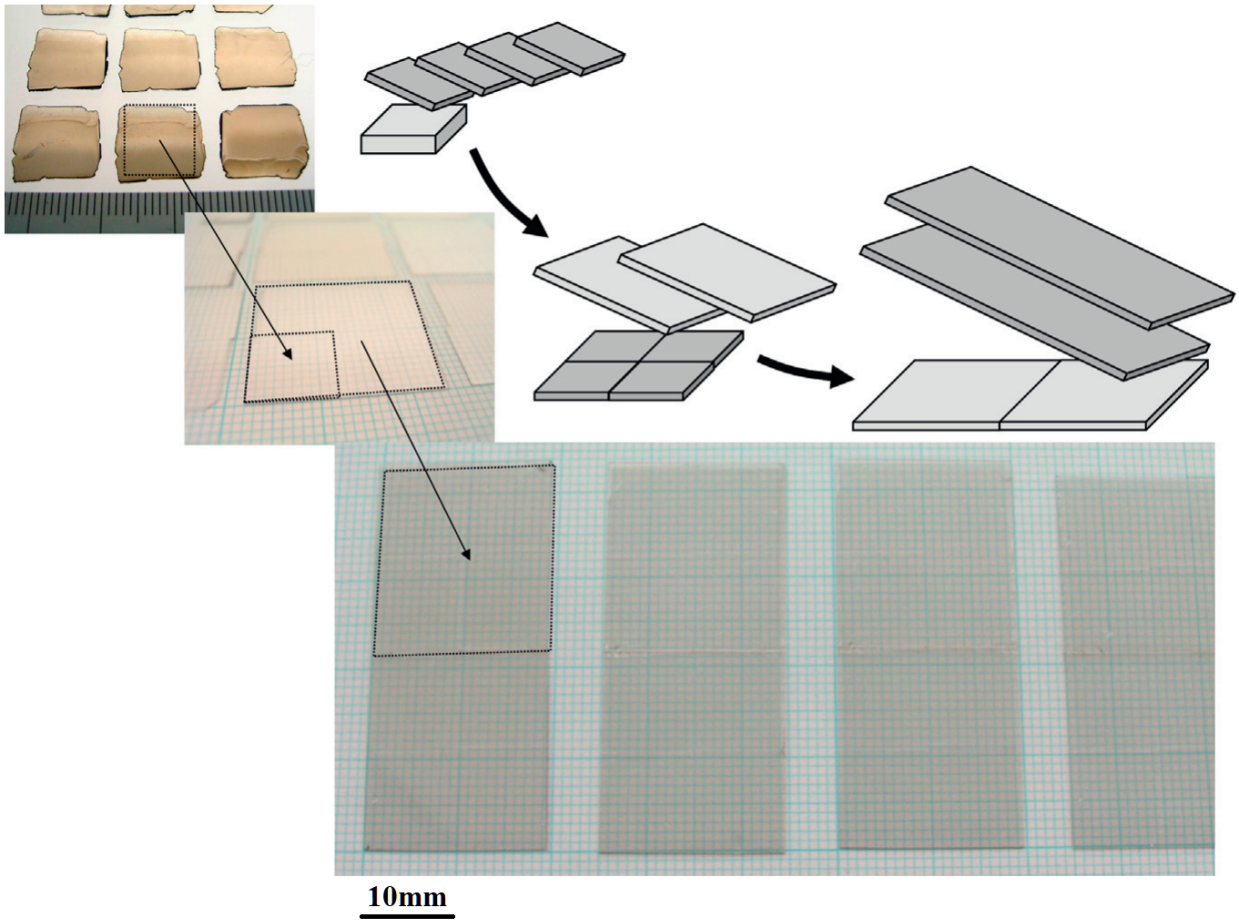

Figure 3.54: Repeating the process using produced plates as constituent tiles led to a final product measuring up to $20 \times 40\,\mathrm{mm}^2$ [208, 234].

The group expanded the efforts by attempting a 2 inch wide wafer, which is the benchmark size for semiconductor materials. A mosaic substrate with dimensions of $40 \times 60\,\mathrm{mm}^2$ was assembled by joining together twenty-four $10 \times 10\,\mathrm{mm}^2$ cloned SCD plates [235]. The as-grown sample with total thickness of 1.8 mm can be appreciated in Figure 3.55.

Figure 3.55: A $40 \times 60\,\mathrm{mm}^2$ as=grown mosaic wafer with thickness of 1.8 mm [235].

In this case, the first thing the authors noticed is how remarkably non-uniform the growth became at this size range. Cracking at the edges occurred after the growth of mosaic wafers larger than 1 inch. The authors conclude that cracks form during termination of the discharge, not during growth, and probably due to internal stress. A temperature difference between the center of the samples and the edges was measured to be as high as 100°C and the growth rate decreased by as much as 24%. This size limitation is attributed to the 2.45 GHz CVD reactor. The corresponding half-wavelength of 60 mm at this frequency implies that an alternative plasma source must be developed when approaching substrate sizes anywhere near this range.

The main conclusion from this study, other than highlighting the inherent size limitation when using a 2.45 GHz CVD system, is that other factors were confirmed to contribute towards the quality of mosaic growths. High quality seed crystals were cited as improving wafer qualities. Using appropriate crystallographic orientations, which includes selecting an effective off-cut magnitude and direction tilted with respect to the mosaic boundaries was confirmed to prevent cracking. Further control of these crystallographic parameters were left for future work.

3.6.4 Multiple Source Mosaic Tiles

The cloning technique is a relatively recent development, and is not necessarily a straightforward procedure, which is why most reports on the mosaic technique have not relied on this step for tile production. When cloning is not available, the only way to substantially increase substrate areas with the mosaic technique is by sourcing tiles from different crystals. This section will outline all the publications where the mosaic technique was applied using tiles assembled from multiple sources. This has been the main approach throughout the years starting soon after the first report. Each study focused their investigation on different parameters, and progress on the technique is shown to be incremental as most useful results and observations are taken into account in subsequent studies.

North Carolina Mosaic

In 1995, a few months after the MIT micro-tile mosaic [225, 227] was published, a group from the Research Triangle Institute in North Carolina published a technique where two commercially obtained natural type Ia tiles, polished within a 2° tolerance around the (100)-plane orientations, and very precise dimensional specifications at 3.00 ± 0.01 mm x

3.00 ± 0.01 mm x 0.250 ± 0.005 mm were used as tiles [236]. Under such rigorous geometric tolerance limits, the prominent issue is then tile alignment. The technique used by this group was to deposit a 2 µm thick Ni layer on the back surface of the tiles, then applying a compressive load for a few minutes under 900°C to bind them together into a silicon wafer, as illustrated in Figure 3.56.

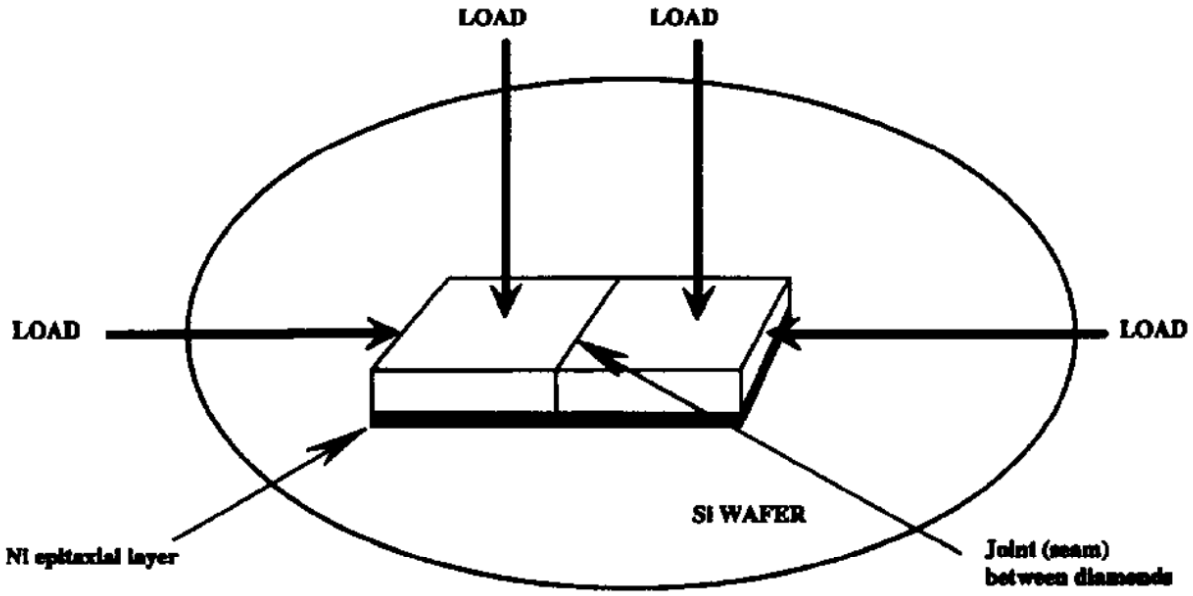

Figure 3.56: Schematic diagram showing the bonding of two Ni-coated diamonds in close proximity to each other on a Si wafer [236].

The multi-step process continued with a successful deposition of ∼75 µm layer over the mosaic substrate based on an RF driven plasma enhanced CVD process that utilizes water and ethanol to grow the homoepitaxial films. A process pioneered in their laboratory with a growth rate of $0.5\,\mu m\,h^{-1}$. The resulting topography was excellent, but both Raman and etch pit density analysis indicated a defect density of $>10^7\,cm^{-2}$ at a concentrated location limited to the dimensions of the original gap between the tiles. The defect density away from the interface was $10^6\,cm^{-2}$, typical for natural diamond. The transition in defect density near the joint is described as abrupt.

Propagation and reduction of this defective region was addressed as an issue that needs to be explored in future work on samples with tighter crystallographic tolerances and thicker growths. An interesting observation reported by this study is that the initial gap between the tiles is easily bridged with lateral growth. The worst case scenario explored in the study was an initial gap of 50 µm, which was overgrown with no problems. The outlined technique is able to achieve much smaller gap distances, but has not been reported as used by other research groups. Presumably, this can be attributed to the nature of their water and ethanol-based deposition system tolerating nickel impurities, while more common plasma-assisted CVD systems are not necessarily as compatible with the approach.

French Mosaic

A group in France summarized a significant advancement in the mosaic technique with a doctoral dissertation by Findeling-Dufour in 1998. The project explored how other factors such as height difference, step height direction, seed separation and crystallographic misalignment had a direct effect on the morphology of the interface region by using five or more tiles on each growth and collecting data on the resulting boundaries from each interface [233, 237]. Type IIa natural diamonds were used as seeds with dimensions of 2.00 ± 0.01 mm x 2.00 ± 0.01 mm x 0.500 ± 0.005 mm. The plates were assembled using high surface-tension liquid fixation on a silicon wafer previously covered with a polycrystalline diamond film. The gaps between adjacent diamonds were adjusted to less than 20 µm, and the height difference less than 5 µm. In terms of crystallographic alignment, the orientations were set within 1° of each other. Both the top and side facets were selected close to the {100} crystallographic planes as this orientation tends to favor lateral growth. The top surface was purposely misoriented by 2.5° to control the step flow growth mechanism over boundaries, and the growth was

carried out under 10ppm nitrogen and low temperatures to avoid the formation of twins. Tile assembly was fixed in place by using an carbon containing glue to keep the orientation in place within a silicon wafer used as the substrate holder, and to ensure thermal and mechanical contact between the seeds. A key contribution by this group to the mosaic approach was the application of an experimental technique used to accurately measure crystal orientations near interfaces based on Electron Back Scatter Patterns (EBSP) from a scanning electron microscope. The technique measured relative misorientations down to a very punctual zone within $1\,\mu m^2$ and with an accuracy of $\pm 0.5°$.

From the observed behavior of the resulting as-grown interfaces, Findeling-Dufour et. al. found that optimized growth conditions are not sufficient for growing a single crystal layer at the junctions. Other physical parameters along with the misorientation were determined to drastically influence the quality of the mosaic junction. Junction morphologies were categorized into three different types of structures with corresponding proposed mechanisms of overlap. These are described based on the behavior of the band of ehanced growth, as previously defined by Janssen et. al. [224], and on whether the growth led to epitaxial growth:

Type A: Layers grown on each diamond are completely merged. The band of enhanced growth is largely shifted in the misorientation direction. Interfaces of this type lead to epitaxial growth.

Type B: Similar to type A, but the band of enhanced growth is only slightly shifted, and for some cases in the opposite direction to the misorientation. Epitaxial growth is not guaranteed for this type.

Type C: One layer grows over the other, and a macro-step is observed on the whole layer. The band overlap is relatively small and shifted in any direction. This type of interface does not lead to epitaxial growth.

All types can be observed on the same growth, therefore, the main cause leading to different types was determined to be the structure of the original interface. When tiles were not well aligned (>2°), interfaces were always observed to be Type C. Assuming step flow growth over closely matched tiles, the parameter that was determined to distinguish whether interfaces would develop into Type A or Type B was the difference in step height direction. The layer growing on the highest diamond always overgrows over the layer growing on the lowest, regardless of top surface offcut directions. Type A mosaic interfaces would then require first of all close crystallographic alignment, and then a small height difference manifested as a macro step that points towards the same side as the expected step flow growth direction. Figure 3.57 shows a graphical representation of these geometric growth parameters.

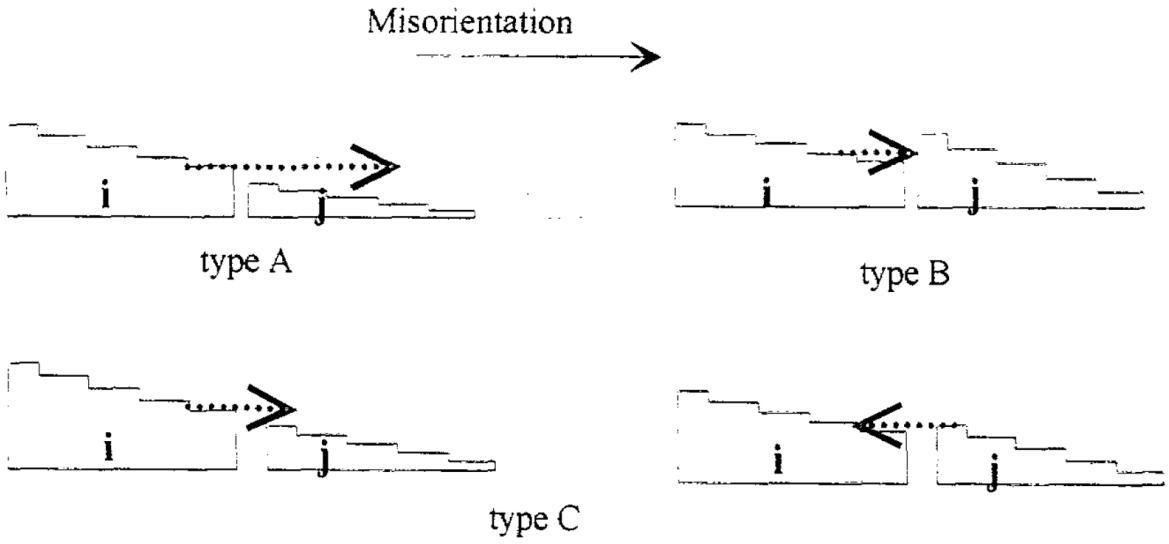

Figure 3.57: Misorientation defined by a deliberate offcut relative to the vincinal (001) planes illustrate as steps in each diagram. Step flow growth and the resulting shift and magnitude of the band of enhanced growth is represented by dashed arrows. The step flow growth process is compatible with the macro step direction at the Type A interface. Step flow growth progression is limited by the macro-step in Type B. The shift in direction for Type C is dependent on the direction of the macro step, but a low angle boundary will be developed as the relative misorientation is relatively high for both cases [233].

The success of this study in establishing a wide set of combinations for growth and alignment parameters, and furthermore cataloging different types of observed interfaces based on resulting behaviors is still unsurpassed in terms of disclosing full results on their methodical analysis of mosaic growth conditions. The study placed emphasis on the need for accurate measurement of relative orientations as this geometric condition was identified as critical. The main conclusion from this study is how multiple crystal assembly parameters are key factors, and demonstrated how sub-optimal deviations from these conditions easily degrade boundary quality. Specific conditions that need to be met for successful mosaic growth were explicitly listed. As a consequence of these conclusions, 12 years passed with no reported progress in the mosaic technique. The approach was only revived by the Japanese group at NIST with the application of new technological advancements such as the development of much higher growth rates, and the tile cloning technique.

Other studies have challenged the concept of necessarily close crystallographic alignment as covered case by case over the next sub-sections.

Russian Mosaic

A group led by Muchnikov at the Institute of Applied Physics at the Russian Academy of Science have presented the strongest case challenging the idea that initial orientations are critical. The group claims successful merging is definitely possible even with relatively extreme misorientations between tiles [238].

The project was based on multiple tiles ranging from 2.8 mm to 3.8 mm wide, and 310 µm thick Type IIa natural diamonds with random angle deviations from the (100) crystallographic axis ranging from 2° to 12°. Deviations from the crystallographic (110) axes were measured to be as far apart as 40°. Approximately 1 mm was grown by MPACVD on the mosaic substrate.

A macro-step formed on the interface during growth, and some strain was measured by Raman over the region. Figure 3.58 illustrates a schematic of the orientations of each tile, and an image illustrating the grown sample after planarization.

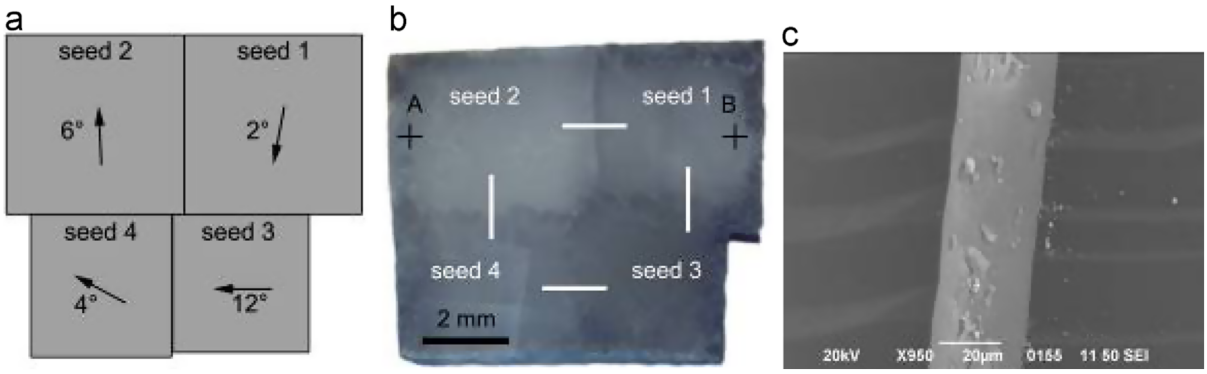

Figure 3.58: a) Schematic deflection of the (001) plane for each substrate on the four tile mosaic seed. b) Samples after planarization and laser cutting to process the edges. c) SEM view of boundary between tiles 1 and 2. [238]

Even though the top surface was grown together with no cracks present, XRD analysis shows how individual tiles inherit the orientation of their respective substrates. Stress levels close to the boundaries were measured to be in the range of 0.3-0.6 GPa. These values are not extraordinarily large for CVD growth, and the discussion contrasts this amount with stresses related to HPHT/CVD boundaries measured at 2.4 GPa. The stress level at the boundary is low, but not zero, in part attributed to indirect annealing from thermo-mechanical polishing.

The group affirms that the mosaic technique is viable regardless of orientation parameters, but XRD analysis, stress level measurements, and even high magnification microscope of boundary regions, as illustrated in Figure 3.59, show how each region can be interpreted as Type C interfaces, not fundamentally different from large scale grain boundaries.

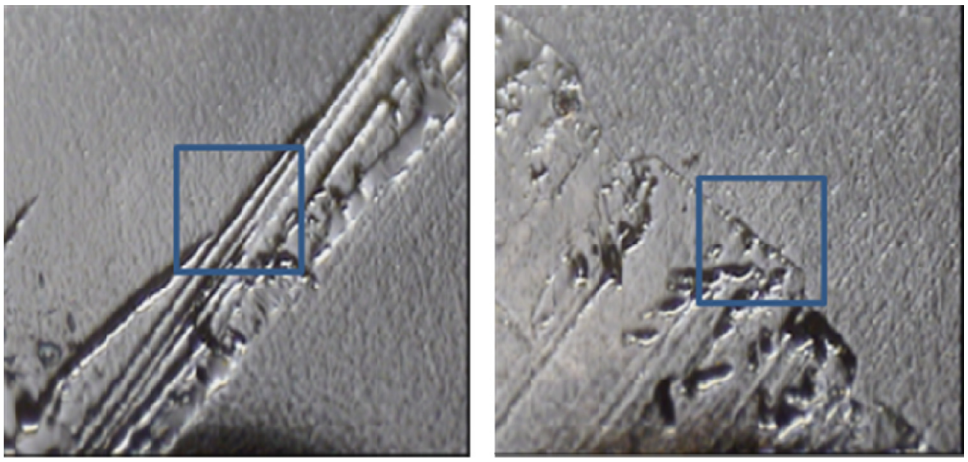

Figure 3.59: Images of two regions within the mosaic crystal after thermo-mechanical polishing. Each frame size is 800 x 800 µm, with the middle squares showing 150 x 150 µm regions over each boundary [238].

Wang Mosaic

Chinese groups are also exploring the mosaic technique. Wang et. al. at the State Key Laboratory of Crystal Materials in Jinan, China, are challenging the need for precise offcut alignment as well with this latest report on the mosaic technique in a report as recent as early 2020 [239]. The team is proposing how the main driving force for boundary propagation is their initial height difference, with the lateral growth direction being independent of the off-axis directions. Four HPHT tiles, each measuring 5 mm x 5 mm x 0.3 mm were grown in two steps up to a total thickness of ∼1.1 mm. Figure 3.60 shows the as-grown surface for both growth steps with an overlay illustrating the initial offcut directions for the four tiles.

The main argument for successful mosaic growth over misoriented tiles is the observation that step flow growth is clearly divided by regions where the surface morphology of the slightly thicker tiles tends to dominate and propagate towards lower tiles. Figure 3.61 shows the boundaries of these step flow domains are traced as they propagate relatively quickly over the as-grown surfaces.

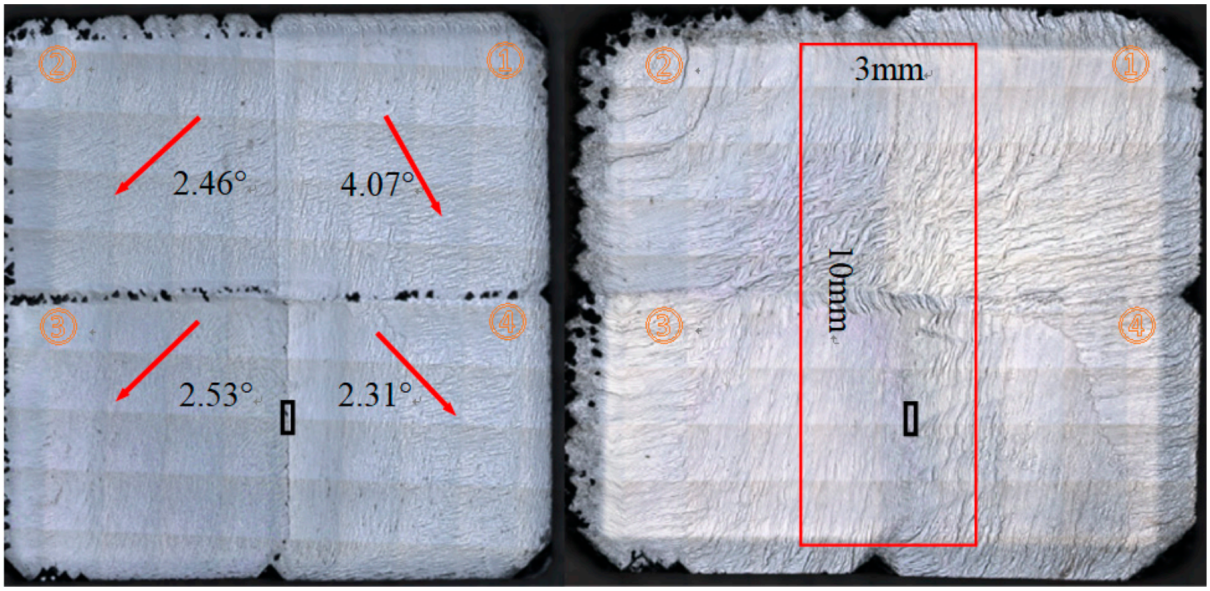

(a) (b)

Figure 3.60: Confocal laser-scanning images of the as-grown sample after growth of 24h and 48h. The red arrows correspond to the off-axis directions of the (100) planes [240].

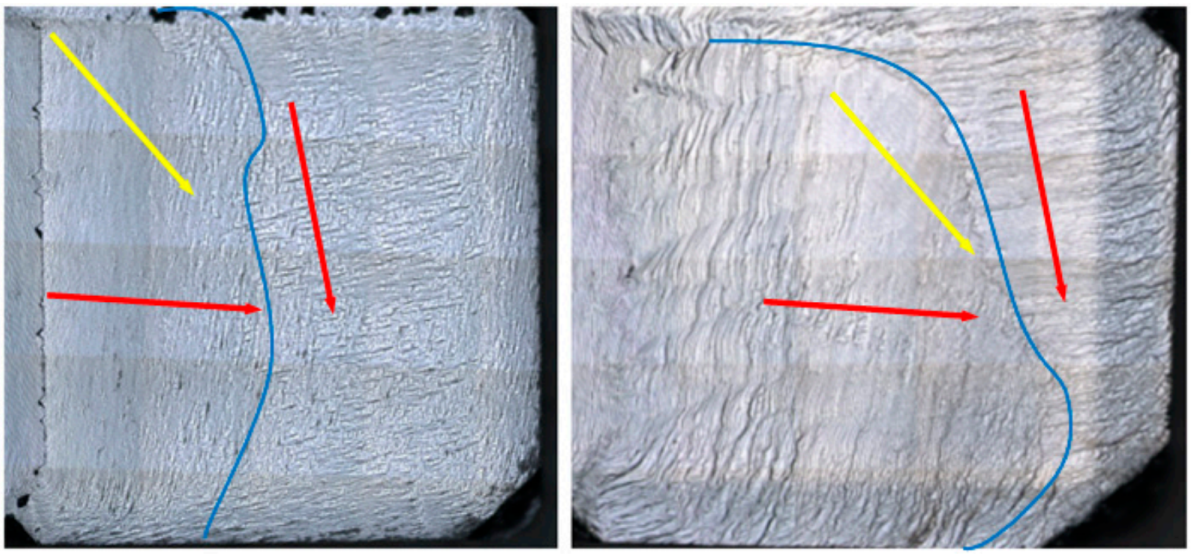

(a) (b)

Figure 3.61: Step flow surface morphology propagating over the top surface as observed at growths of 24h and 48h. Blue lines mark the boundary of the two surface domains with different step flow directions labeled by red arrows. The yellow arrows indicate the (100) off-direction of substrate 4 (lower right) [240].

Even though the step flow morphology is a compelling visual indicator of fast lateral overgrowth, XRD rocking curve measurements over the sample shows that the original orientation of each underlying seed is maintained over the grown layers. Raman mapping showed how the region directly over the interface is internally stressed up to 0.295 GPa. The stress field in the region was not constrained to the area directly above the original interface, but was observed to shift about 200-400 µm from one substrate to another.

XRD analysis showed almost no correlation with the behavior of the step flow growth movement direction, contrasting with the surface height distribution which was concluded to be the driving force on top surface morphology. The proposed mechanism for the junction interface formation and mosaic step surface morphology transformation is illustrated in Figure 3.62. Regardless of whether step flow and lateral growth is independent on the underlying orientation or not, this study demonstrates how height differences are yet another critical factor that must not be ignored when applying the mosaic technique.

University of Colorado Mosaic

A US Department of Energy program for growing and testing detector-grade single crystal CVD diamond sensors with areas $\geq$1 cm^2 was carried out in 2011-2013 by a team at the University of Colorado in collaboration with the Tallaire group at the LSPM in Paris. The terms of the project [241] agreed not to reveal too many details on the processes for preparation and growth of the single crystal CVD films, but in general was based on attaching multiple sourced HPHT tiles on a molybdenum sample holder. Dozens of (100) top surface oriented 3.2 mm x 3.2 mm Sumitomo seeds were purchased and sorted by height and corners closest to 90°. Tiles were aligned by multiple methods, including machining molybdenum holders, and/or preparing what they call "racks" (like cue-ball racks) to hold seeds together

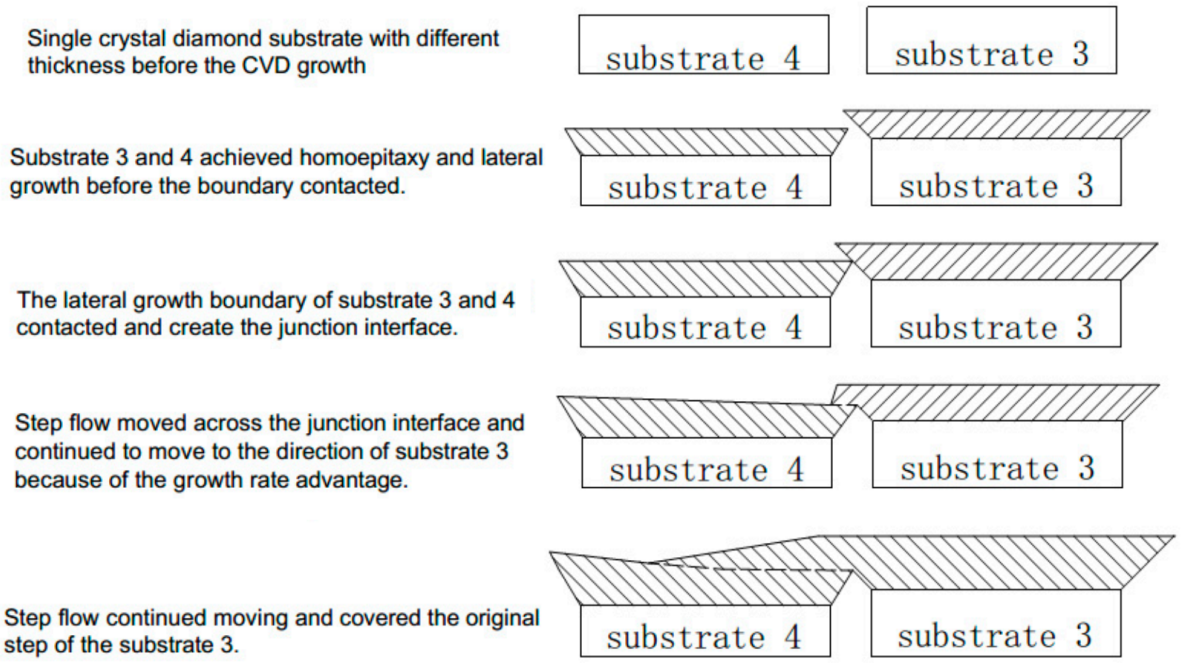

Figure 3.62: Mechanism of the CVD diamond mosaic junction interface formation and the movement of the surface step flow. Image adapted from [240].

as illustrated in Figure 3.63a made of molybdenum or high-quality graphite. Top plates were removed by laser cutting, or with the lift-off technique. Growth was prepared thick enough such that after kerf losses and polishing, the final framed and polished plates were set to be thicker than 500 µm.

A total of eleven mosaic assemblies were grown and their performance tested as charge collectors for sensing applications. Results were positive in the sense that some of the sensors were measured to have higher charge collection efficiency than 750 µm thick polycrystalline diamond wafers. The main problem on why the other mosaics had inferior performance, or failed altogether was the significant cracking observed in all samples. Results in Figure 3.63c were typical, where damaging cracks are mostly sourced at the junctions.

Unfortunately, it was only by the end of the project that the group had a chance to measure the crystallographic offcuts by XRD analysis and realize that they incorrectly assumed the

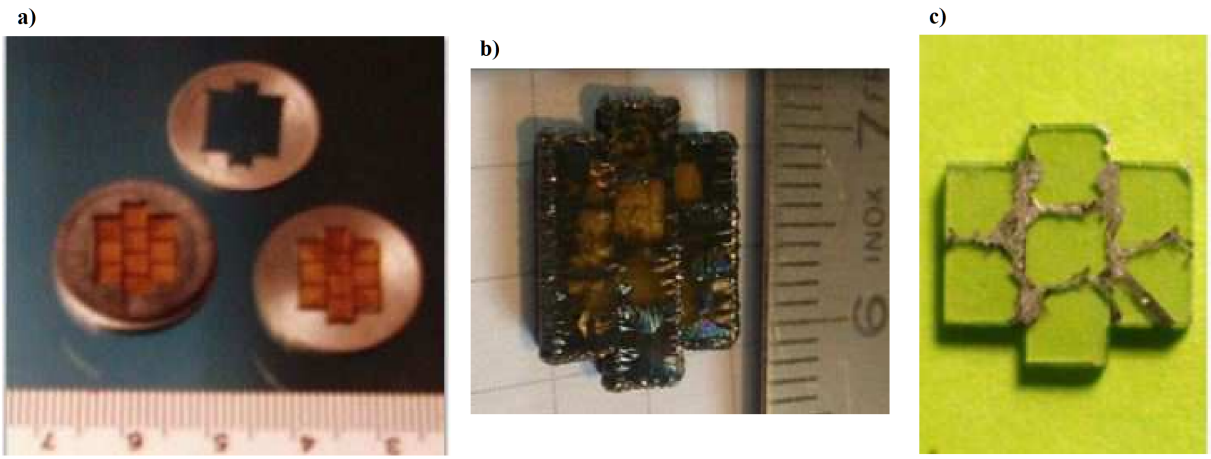

Figure 3.63: a) Mosaic substrate composed of ten tiles, kept together using a molybdenum "rack". b) As-grown substrate. c) Polished plate [241].

accuracy of the manufacturer's claim of {100} orientation for the top facet. In practice, these orientations vary by as much as 5°. These values made all mosaic substrates significantly more misoriented than originally expected. These joint-based fracture patterns are typically observed in highly misoriented (>2°) mosaic interfaces.

Matsushita Mosaic

A recent publication by a group from the School of Science and Technology in Kwansei Gakuin University in Hyogo, Japan, shares a CVD growth over HPHT seeds with no particular consideration for plate alignment during the fabrication process. The group did incorporate nitrogen as an added dopant to increase the growth rate and improve step flow growth conditions. The framed and polished plate can be seen in Figure 3.64a. The plate is slightly opaque as a product of the nitrogen addition, and a cross can be seen on the substrate directly over the original interface locations. Relatively small misorientations were measured, as identified and illustrated in Figure 3.64. These misorientation measurements are approximate quantities measured by electron backscatter diffraction. Crystallinity measurements by

Raman mapping show defective regions extending out to approximately 500 µm. The study is considered successful in the sense that no cracks are present, and the report is useful as it shows how careful adjustment of process parameters can lead to effective merging between plates. It must be mentioned that the relatively low misorientations should be considered a significant factor when analyzing the lack of crack formations in this sample.

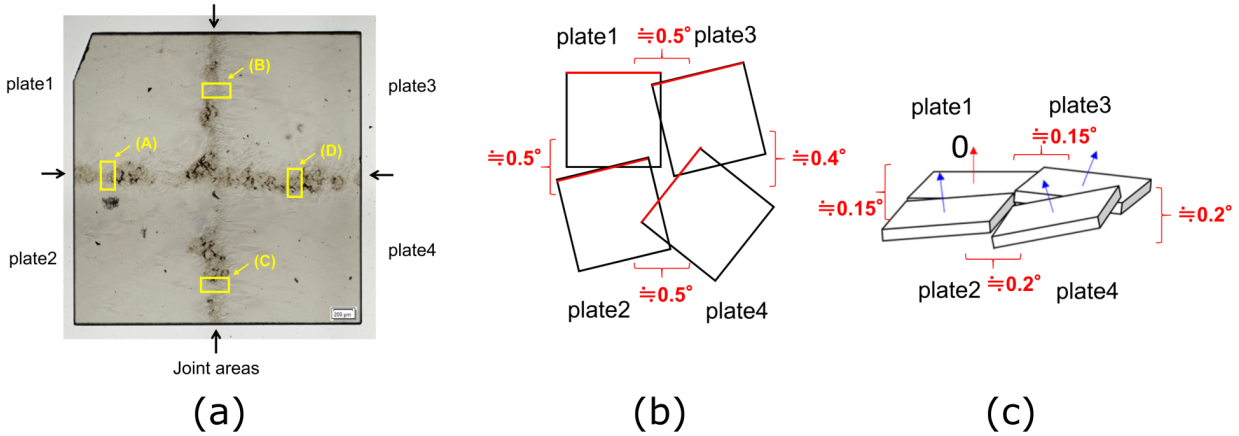

Figure 3.64: a) Mosaic sample with four $3 \times 3 \times 0.35\,\mathrm{mm}^3$ tiles. b) Twist rotation measurements measured below 0.5° c) Tilt misorientations measured below 0.2°. [242].

Shu Mosaic

A group led by G. Shu and B. Dai in a Chinese-Russian collaboration reported their mosaic project in 2017 by publishing a detailed analysis of a thick growth. The bulk of the analysis was confocal Raman measurements to obtain stress field measurements at different depths. The group used misoriented HPHT seeds as illustrated in Figure 3.65a.

Measurements show how a mosaic interface on a 2x1 mosaic that failed to merge resulting in defected and stressed zones consistently increasing in size and worsening as the sample is grown thicker [243]. The study was very systematic in the approach, and shows how misoriented samples might appear to grow together by inspection with an optical microscope,

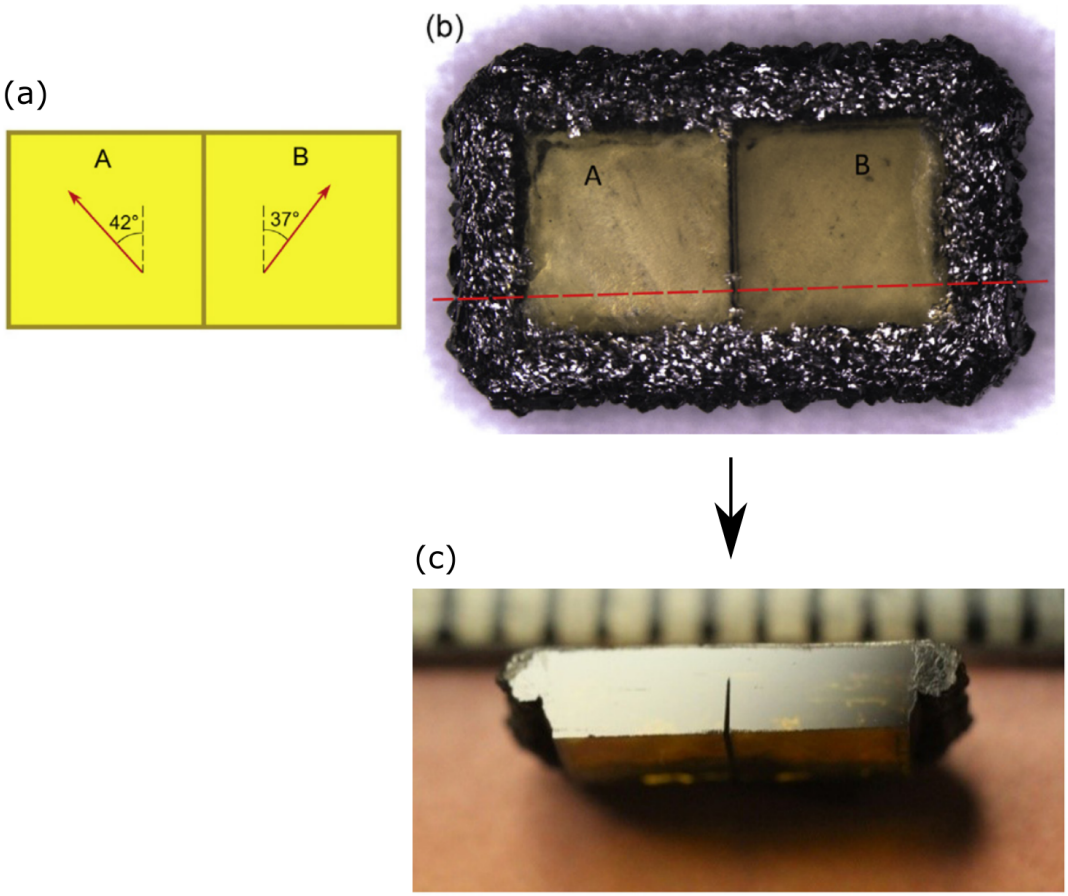

Figure 3.65: a) Initial seed misorientations. b) As grown sample with thick PCD rim product of an open holder configuration, but showing no signs of cracks forming at the interface. c) Polished cross-section showing no apparent signs of defective regions at the junction [243].

but there might be a stress field increasing within the region. Figure 3.66 shows how both the stress and the width of this defected zone were observed to increase with grown thickness. At this rate, it is natural to expect the internal stress within the region will eventually cross a threshold and crack the sample at the junction [244].

In 2018 the group reported results from what was defined as a 3D mosaic, in essence a T-shaped structure with tiles extending out both horizontally and vertically [245], with special focus on analyzing grown layers at different heights over a flipped tile [246], leading to better understanding of stress distributions across grown regions.

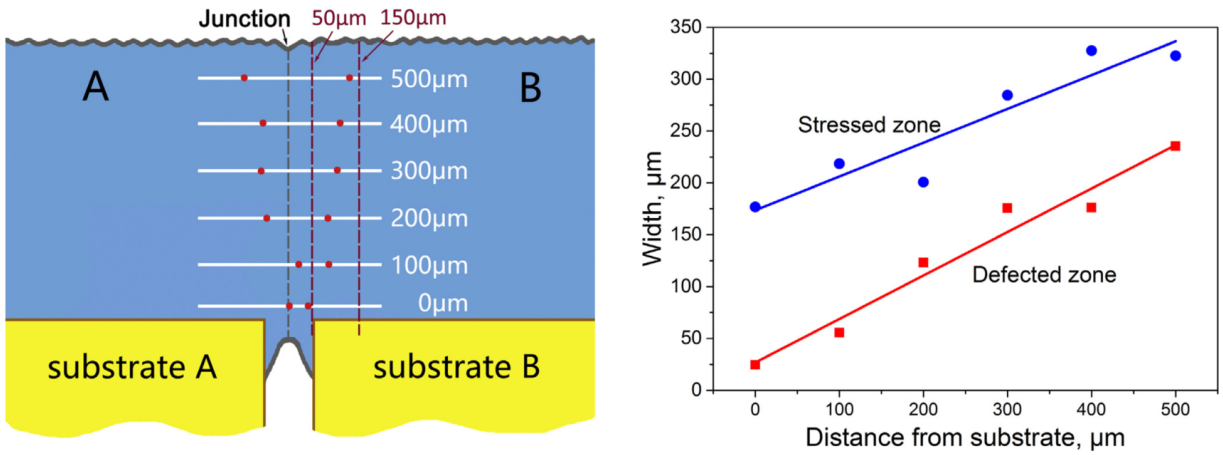

Figure 3.66: a) Expansion of the stressed and defected region near the junction as measured by confocal Raman spectroscopy. b) Width of defected and stressed zones vs grown thickness [243].

With respect to mosaic structures, after exploring growth conditions and analyzing interfaces, the group concludes that perfect crystals and perfect interfaces do not exist in reality. The group emphasizes that the possibility of complete connection with exactly the same orientation between tiles at atomic level is practically impossible and often has a relatively negative impact on crystal quality [247]. This does not mean that the group has discarded the mosaic approach. On the contrary, the group has made significant experimental and even theoretical advances on the technique. Their approach on analyzing the mechanism for interface formation is arguing that the Mosaic Technique has two components: Mosaic Assembly and Mosaic Growth.

Mosaic Assembly is the process of tiling together separate substrates, which even covers applications in sensor technologies where a working large area device can be assembled as a detection array with no material growth between each tile [248]. Mosaic growth, on the other hand, is regarded as a misnomer. The argument states that since it is not possible to bond diamond by traditional technologies such as welding or brazing, the only way to expand diamond in terms of volume is by means of nucleation and epitaxy. The underlying

mechanism for "mosaic growth" is then in no way fundamentally different from polycrystalline growth, nanocrystalline growth or even isolated island growth mode on single crystal diamond homoepitaxy. The only difference is the size of the initial diamond nuclei. In the case of "mosaic growth" the initial nuclei are large, monocrystalline and with approximately similar orientations. Diamond epitaxy in all cases, regardless of initial size, will necessarily nucleate, grow, as illustrated in Figure 3.67, and eventually make atomic contact with each other via a bridging carbon atom that could be sourced from either free radicals or diffused from either one of the two zones. The separate polycrystalline grains now in direct contact will extend vertically in competitive growth as illustrated in Figure 3.68. Resulting small angle grain boundaries lead to inevitable accumulation and expansion of defects and stresses in the surrounding region.

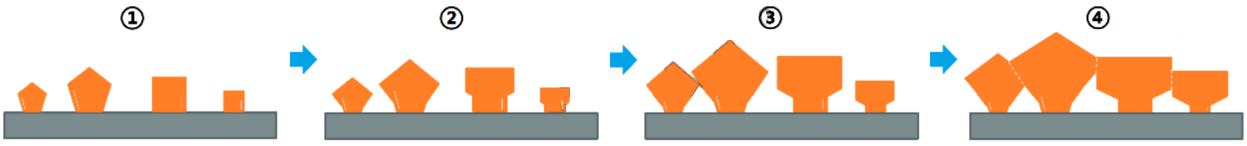

Figure 3.67: Schematic of epitaxial growth starting with nucleation up to atomic contact between independent grains. [247]

The influence of both nucleus size and orientation mismatch in the nuceli formation process and the dynamics that develop as the grains approach each other was explored theoretically in terms of Gibbs Free Energy. The thermodynamic conditions that need to be satisfied to achieve isolated nucleation instead of two dimensional spreading was expressed as a function of several terms, including the average nucelus radii as well as the surface energy of the substrate [247]. This framework has the effect of establishing a generalized growth process that covers a wide set of growth conditions ranging from heteroepitaxy up to mosaic seeding, as illustrated in Figure 3.69.

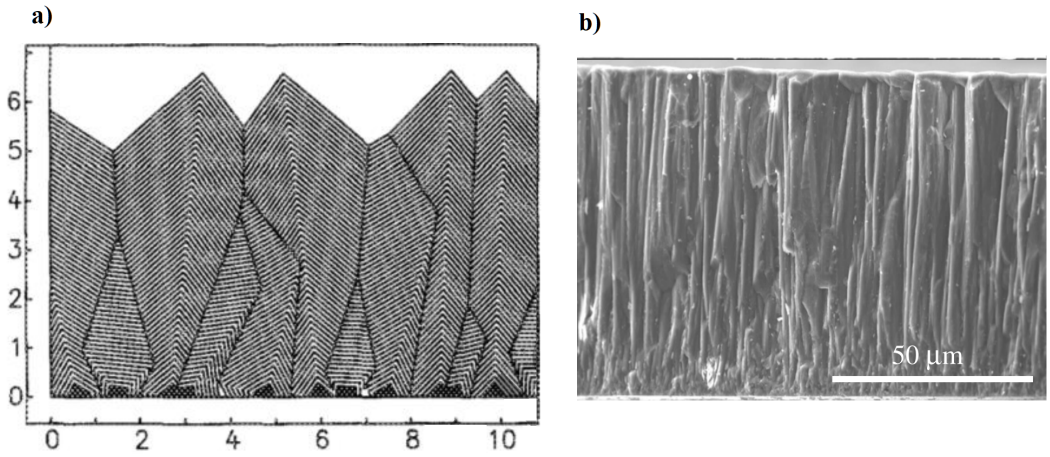

Figure 3.68: a)Schematic of polycrystalline growth cross-section with arbitrary units illustrating independent diamond nuclei which result in competing grain boundaries growing vertically and extending dislocation sites between them [247], b) SEM picture illustrating the growth process [249].

The universal concept which covers the full range of CVD-based diamond film growth and preparation is defined by the group as "Coessential-Connection" (CC growth). The term is proposed as a more suitable definition to describe and analyze the generalized process by which diamond expands in size. In essence, the term serves as a way to explicitly state that diamond grains will never merge, and at best will just remain connected under energetically stable thermodynamic conditions.

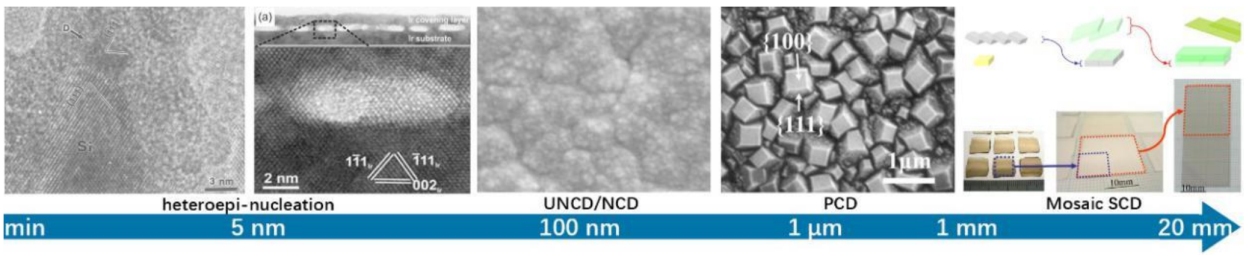

Figure 3.69: Grain size from smallest to largest within the framework of CC growth [247].

The latest developments from this investigation were first reported in the Chinese Journal of Nature back in 2019 [250]. The theoretical analysis was discussed in more detail and new pictures of their experimental results were published on a review paper in early 2021 [247].

As a result of years of growth parameter optimizations, including data analysis from different geometric configurations and addressing technical bottlenecks such as polycrystallization and stress concentration, the group has presented evidence of one inch polished mosaic plate, as illustrated in Figure 3.70, and even a two inch diameter grown sample assembled from dozens of underlying tiles, as illustrated in Figure 3.71.

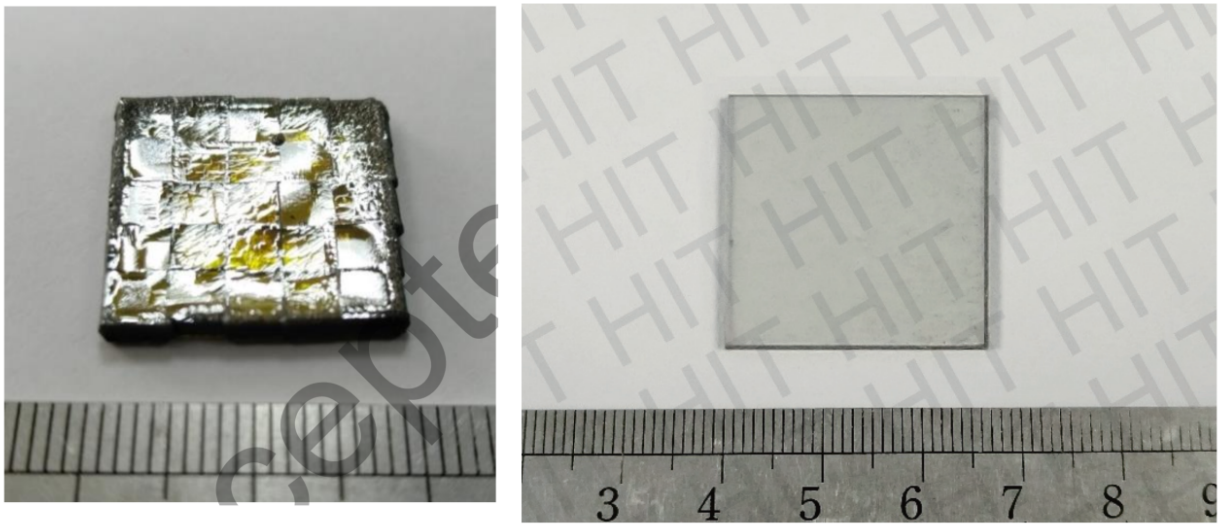

Figure 3.70: One inch as-grown sample [247], and one inch polished plate [250].

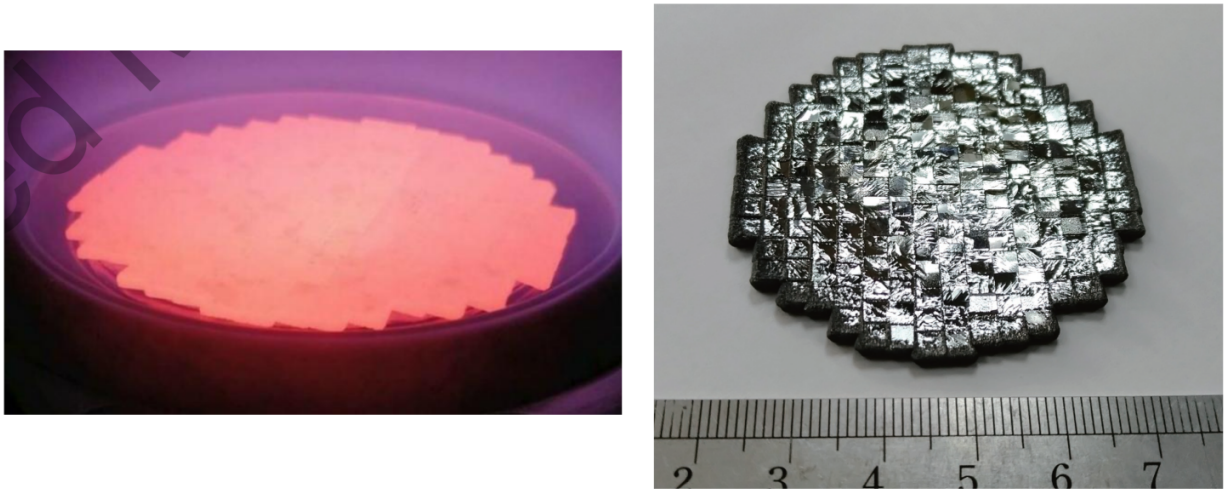

Figure 3.71: Two inch diameter sample during growth [247], and as-grown sample with thickness non-uniformity measured at a maximum of 25% [250].

Contrasting with the depth of Raman analysis used in the initial 2017 report [243], no additional measurements have been reported on these large area samples either on relative misorientations, mosaicity, or stress distributions for these large area samples.

This latest report is significant as they have not only reached the scale achieved by the Japanese group [234], they have also established a useful framework for analyzing diamond growth itself and how it can be applied to the mosaic technique. By the end of the last publication [247], despite all the reported progress, the group advocates for heteroepitaxy as necessarily being the indispensable way for producing ultra-large single crystal diamond wafers.

3.6.5 Strategies for Reducing Defects at Mosaic Boundaries

3.6.5.1 Tungsten Buffer Layer

If an additional thin buffer layer of metal-assisted termination (MAT) diamond layer using hot-filament CVD is applied to a grown sample, the tungsten (W) inclusions at this layer leads to significant annihilation of dislocations [251], as illustrated in Figure 3.72.

This technology, developed by Ohmagari et. al. at NIST, is illustrated in Figure 3.73. The dislocations sourced at the interface region were observed to be highly suppressed [252], reducing their densities by as much as two orders of magnitude. Schottky barrier diodes fabricated over these W-layered mosaic substrates were shown to have improved rectifying behavior with suppressed leakage current [253]. The MAT buffer layer technique has been recently applied by the same group to heteroepitaxial substrates and was also proven to be highly effective [254].

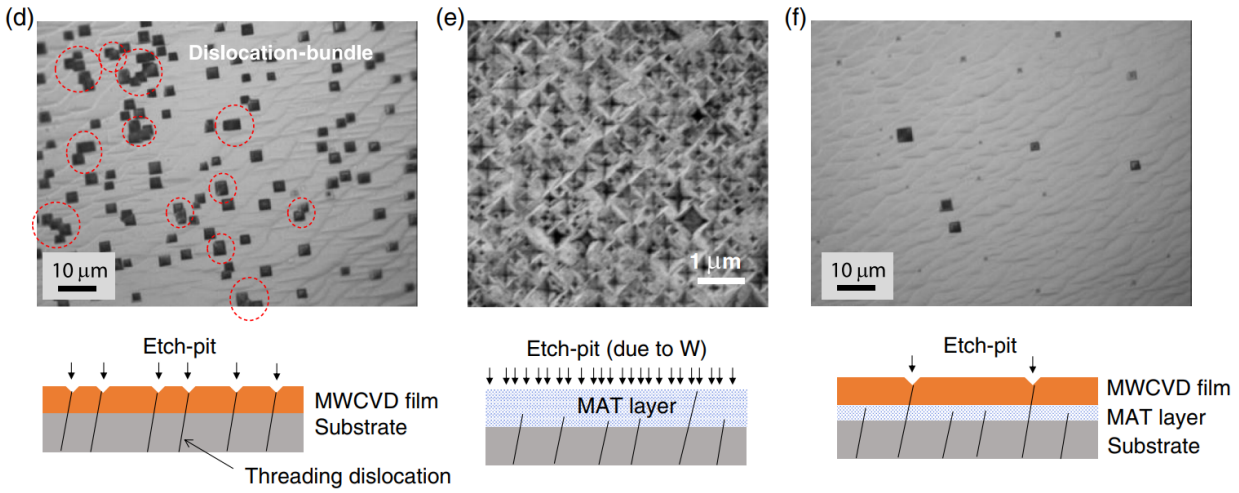

Figure 3.72: Etch pit analysis illustrating threading dislocation densities at the d) CVD substrate, e) MAT layer (10^9 - 10^{10} cm^{-2} etch pit density), and f) MWCVD overgrown layer with a MAT buffer layer inserted [252].

3.6.5.2 Interface Angle

Another technique also explored by the same group was first mentioned in one of the reports outlining progress in the cloning technique [234]. The observation that was later expanded as it was systematically studied in more detail [244], is to force a misalignment of the offcut direction with respect to the edges to suppress cracking at the boundary. Figure 3.74 illustrates the procedure used to adjust the angle of the off-direction relative to the interface between two tiles.

The off-angle direction was again confirmed to lead to better quality when the off-direction is perpendicular to the edges. Stress analysis, on the other hand, shows that an off-direction parallel or perpendicular to the interface direction results in the generation of large number of abnormal growths. It was mentioned that these defects may not even appear on the surface, but internal stress is generated within the layer. The authors note that the reason why this occurs is not exactly known. The resulting strategy to avoid cracking based on this observation is then to select an angle pointing in a direction between both extremes.

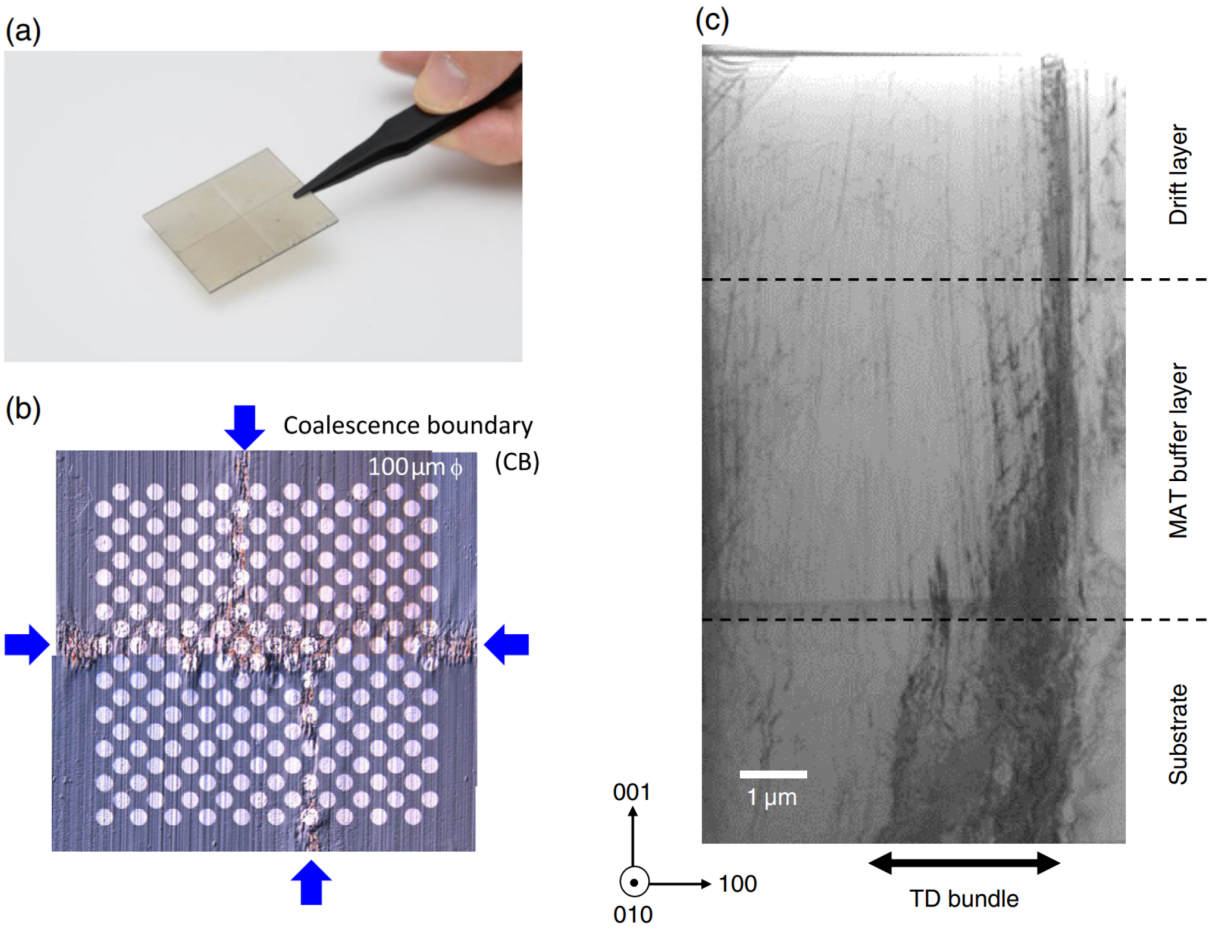

Figure 3.73: a) Photograph of a diamond mosaic wafers (40 mm x 40 mm) where freestanding plates are connected laterally by CVD growth. b) Optical microscopic image of Schottky barrier contacts fabricated near boundaries. Electrode diameters are 100 µm. c)Cross-sectional TEM image of Diode-B in the on-boundary region showing a reduction in threading dislocations (TD) [252]

Figure 3.75 shows improvement in boundary quality based on consistent step flow growth as this angle is varied.

It should be noted that based on the adjustment procedure used in this study two angles were being modified simultaneously: the (100) off-direction relative to the interface, and the {110} plane rotations. Analyzing the effects of changing this second angle was left for future work. The report that was published the previous year [235], on the other hand, does mention that the {110} direction was also varied against the boundaries and that no obvious

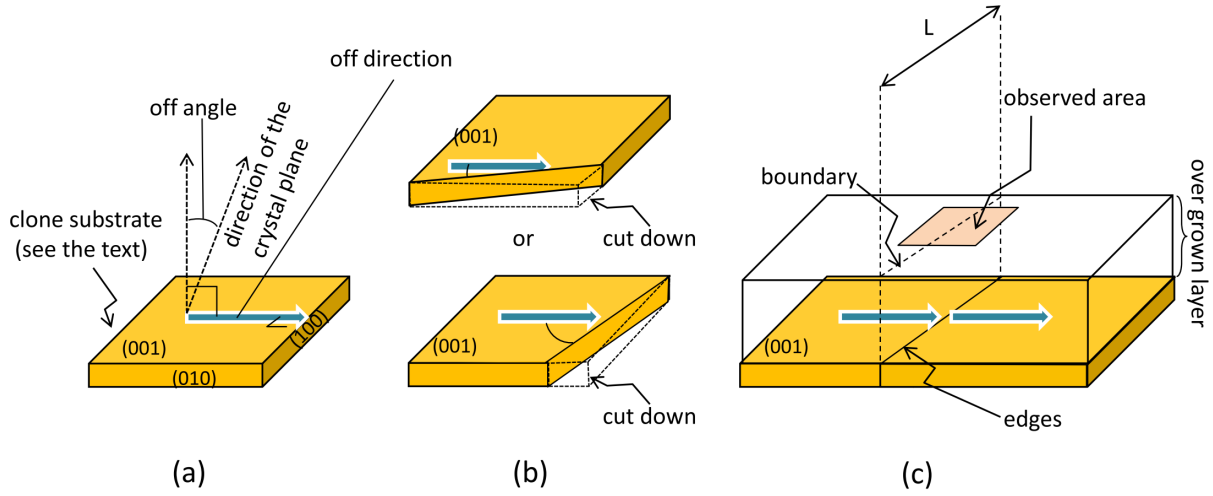

Figure 3.74: Schematic illustrating how crystallographic angles were defined with respect to sample edges, and the process used to adjust the off-direction angle [244].

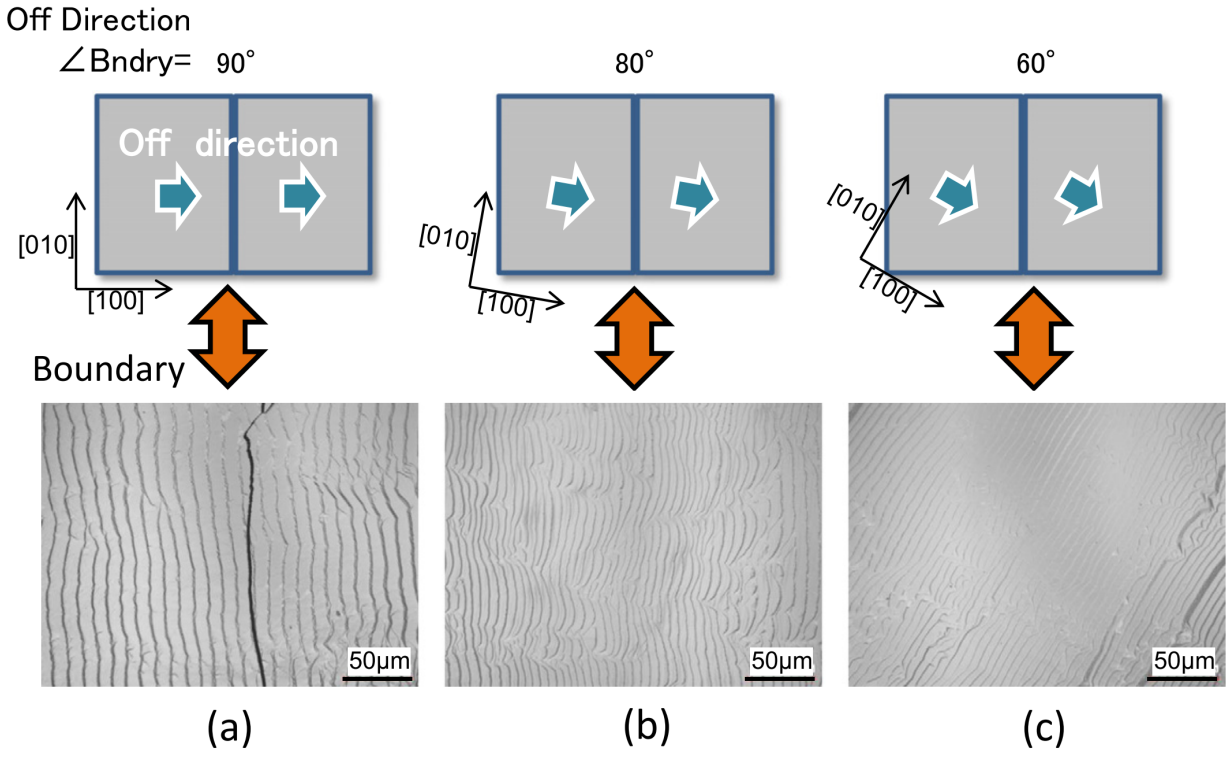

Figure 3.75: Surface morphologies around the boundary after the overgrowth for three cases where the off-direction was varied relative to the interface [244].

effects were observed on the growth. They only mention that this direction has no remarkable effect on step flow growth. It might be reasonable to conclude that with this new report, the authors are only clarifying that the condition that has not yet been systematically analyzed is change in stress in the grown layers by varying the {110} direction, only observations in step flow morphology.

Chapter 4

Experimental Setup

4.1 MPACVD Reactor

Two Microwave Plasma Assisted Chemical Vapor Deposition (MPACVD) systems were used in this investigation: DS3, a third generation, Type B reactor [255], and DS4, a fourth generation, Type C reactor [129]. These systems are the latest two iterations of a MSU patented design first developed in the 80's [256]. The design relies on a cylindrical applicator where electromagnetic modes are excited using a microwave source. When the cavity dimensions are well adjusted and the process gases are kept under controlled conditions, the resulting energy distribution induces a plasma discharge. The thermal energy within this region then generates free radicals that lead to the CVD diamond growth process described in Chapter 2.

Implementing this process requires a deposition system which is best described as a set of integrated sub-systems: (1) Microwave Power Delivery, (2) Cylindrical Cavity Applicator, (3) Process Gas Delivery, (4) Pressure Control, (5) Temperature Control, and a (6) Computer Monitoring and Control hub to integrate all components. A generalized summary of the diamond deposition system is illustrated in Figure 4.1. Relevant details for each sub-system are outlined in the following sections.

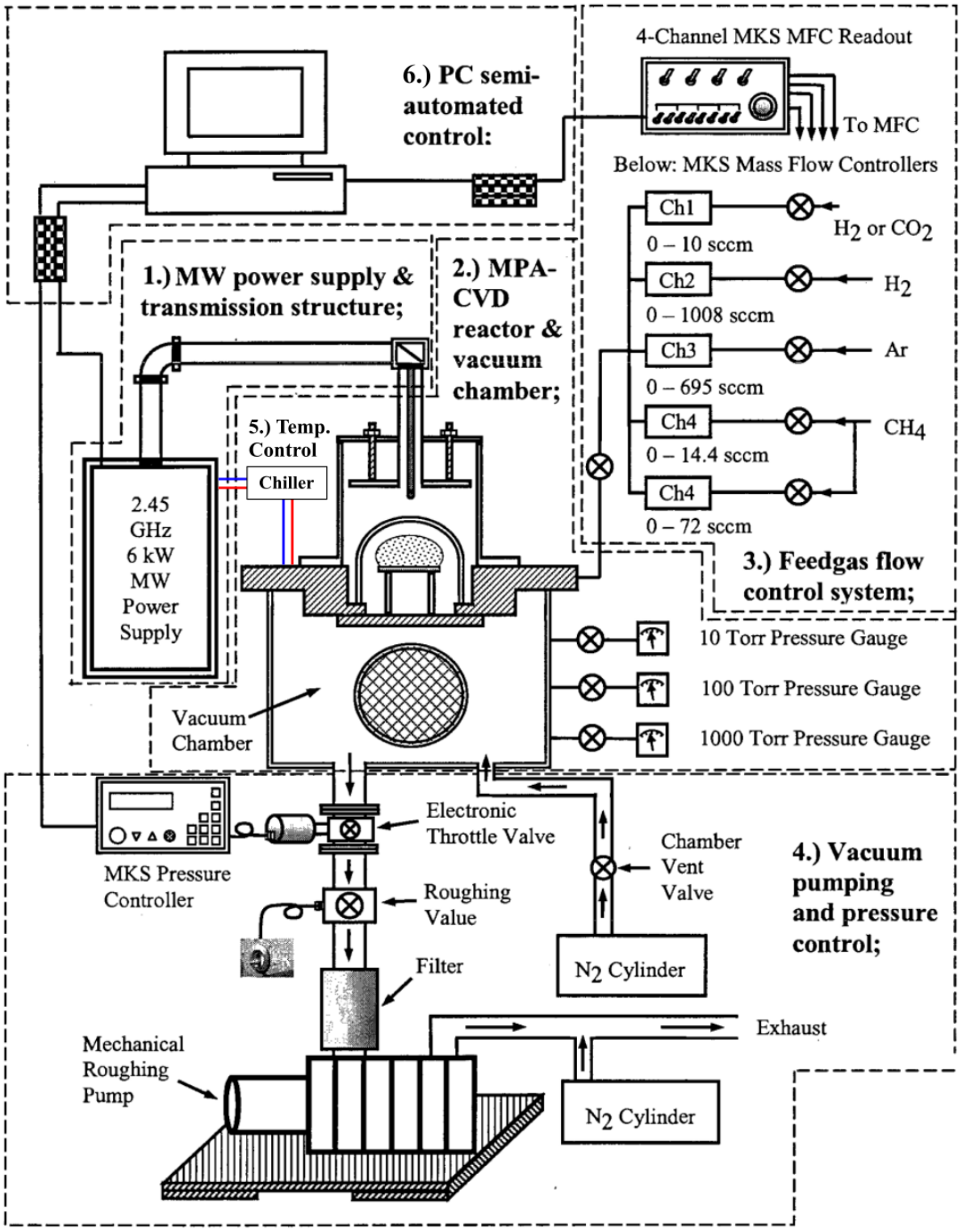

Figure 4.1: Schematic illustrating a generalized diamond reactor system, with main subsystems highlighted. Image adapted from [194].

4.1.1 Microwave Power Supply

The microwave power delivery sub-system in Diamond System 4 (DS4) is composed of a Muegge Power Supply model MS015KE-110DL and Magnetron Head model MH015KS-312CN operating at 2.45 ± 0.01 GHz, capable of supplying a maximum power output of 10 kW. Typical operation is set within the range of 1.8 - 3.4 kW. The output of this supply is connected to a circulator which redirects reflected power from the cavity to an impedance-matched and water-cooled dummy load as illustrated in Figure 4.2.

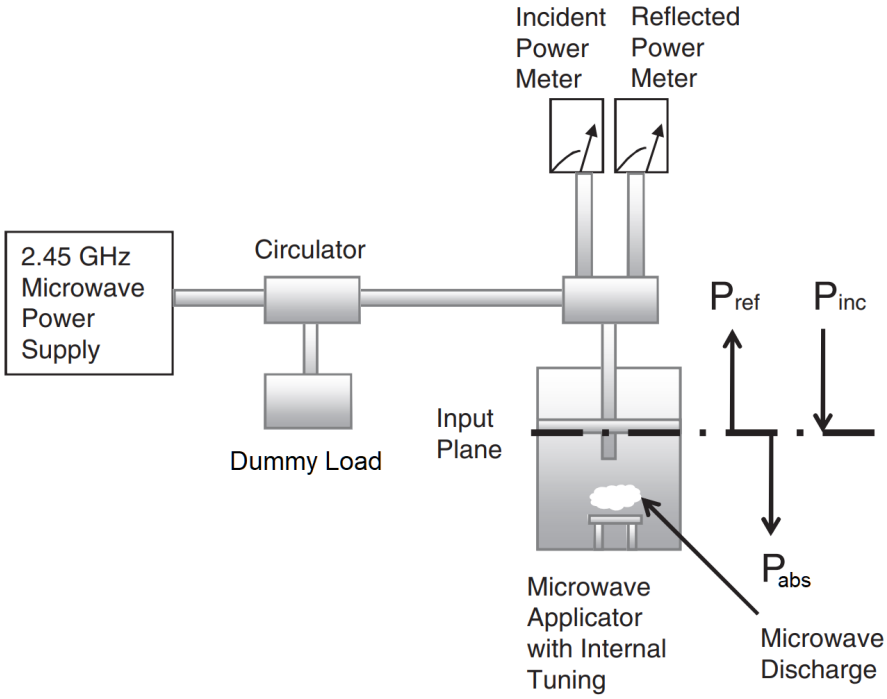

Figure 4.2: Schematic outlining the standard microwave power supply sub-system. At the input plane, defined as the interface with the cavity applicator, the absorbed power P_{abs} is measured with as P_{inc} (incident power) - P_{ref} (reflected power) [257].

Both incident and reflected power are computer monitored by sensors placed within the waveguides and programmed with set limits that trigger an interlock which shuts down the supply when the reflected power is too high. Standard operating conditions in DS4 typically operate within a reflected power ranging between 5%-15%. Exact values depend mainly on

geometric sample holder configurations, the operating pressure of the process gases, and the incident power. Specific details for the components of the power supply sub-system in DS3 are described in full detail elsewhere [258, 259], but the general operating principles are equivalent for the system and every other sub-system described in these sections.

4.1.2 Cylindrical Cavity Applicator

The cavity applicator for these reactors is composed of two main sections, a cylindrical cavity and a coaxial cavity. The design, used directly in reactor Type B, has dimensions adjusted such that the top cavity is excited with a TM_{013} electromagnetic mode based on the incident wavelength as illustrated in Figure 4.3. The bottom cavity, which results from the volume needed to accommodate the cooling stage used to control the temperature of the sample, behaves as a coaxial section producing a TM_{001} electromagnetic mode.

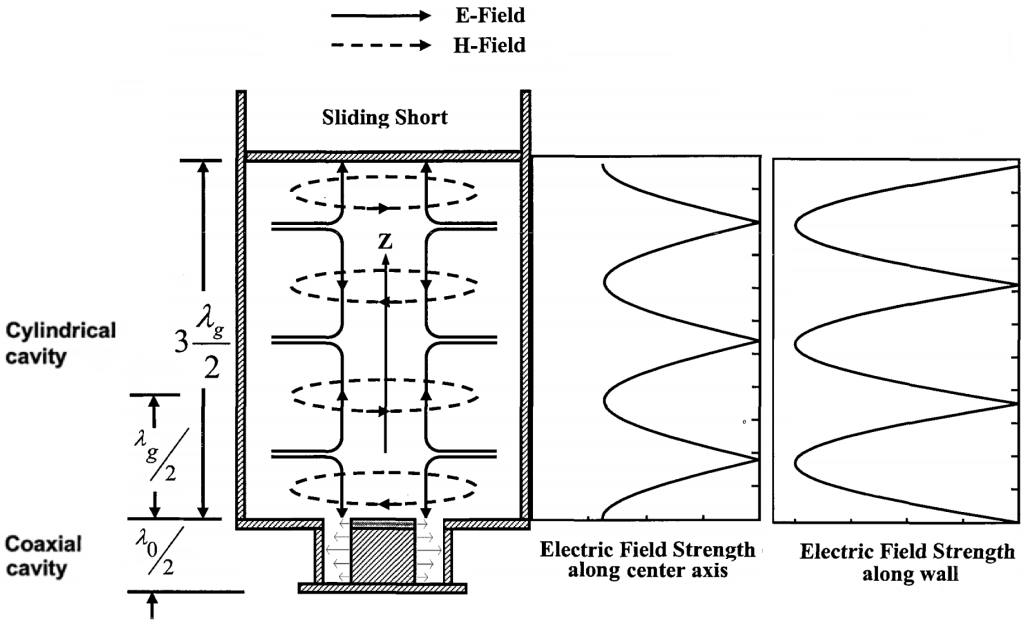

Figure 4.3: Sketch of the hybrid TM_{013}/TM_{001} electromagnetic resonant mode. A tuned cylindrical cavity has a height close to 1.5 times the incident wavelength λ_g. The height of the coaxial cavity corresponds to half of the wavelength in air λ_0 for the microwave frequency. Image adapted from [194].

Since several discharge regions would be generated from the excitation mode, the process gases are contained within a quartz dome. This only activates the node where the sample is placed, at the lower end of the cylinder. This addition of a new material within the region, as well as other factors to consider such as probe position, cooling stage and holder dimensions, all have an effect on the actual electromagnetic resonance within the cavity.

One of the main factors that can be adjusted is the height of the top cylindrical cavity. This value can be set by adjusting the location of what is defined as the sliding short, named this way as it slides freely within the fixed cylinder walls. Electrical contact between both surfaces is maintained with finger stocks, ensuring a closed volume in terms of electromagnetic microwaves enclosed by a Faraday cage. The short position is measured relative to the sample, and defined as L_s, and the energy is applied to the cavity through a probe with length L_p measured relative to the position of the sliding short. Figure 4.4 shows the location of these quantities as well as a comparison of the electromagnetic cross-sections for Reactors Type B and C.

The vast majority of the growth runs during this investigation were performed on DS4, a type C reactor. This relatively newer configuration designed with dimensions of $R_1 = 15.24\,\text{cm}$, $R_2 = 10.16\,\text{cm}$, $R_3 = 1.84\,\text{cm}$, $R_5 = 12.07\,\text{cm}$, $L_1 = L_2 = 6.12\,\text{cm}$, and fixed dome dimensions of $2R_D = 21.6\,\text{cm}$, and $h = 10.86\,\text{cm}$. The probe and sliding short lengths are variable parameters set at typical values of $L_p \approx 3\,\text{cm}$ and $L_s \approx 16.25\,\text{cm}$. As observed in Figure 4.4, this configuration does not correspond to the TM_{013}/TM_{001} electromagnetic mode quite as directly as the Reactor B. This modified Type C reactor design with a larger dome, and larger cavity employs a "non-classical" electromagnetic TM_0/TEM_{011} plasma excitation applicator mode [128]. This hybrid approximation allows control of plasma position, size, shape and intensity. Figure 4.5 shows an example of the flexibility provided by this reactor as the shape

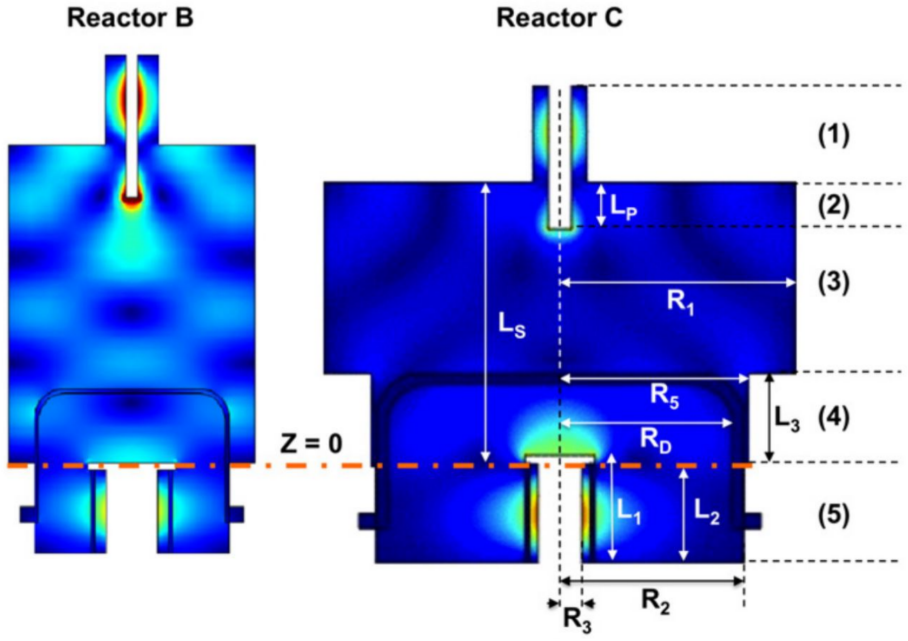

Figure 4.4: Comsol simulations of electromagnetic cross sections for reactors Type B and C. Reactor design for Type C has an increased cavity and dome diameter which results in a mixed TM_{012}- TM_{013} mode. The five main regions are identified on Reactor C as (1) coaxial input section, (2-3) main cylindrical applicator with additional section (4) with reduced diameter and (5) fixed coaxial cavity. [128]

of the discharge region and corresponding electric field distribution can be fine-tuned by making height adjustments on the sample holder/cooling stage configuration. This reactor design allows for faster growth rates, high power density discharges, and provides robust diamond synthesis up to 300 Torr [128].

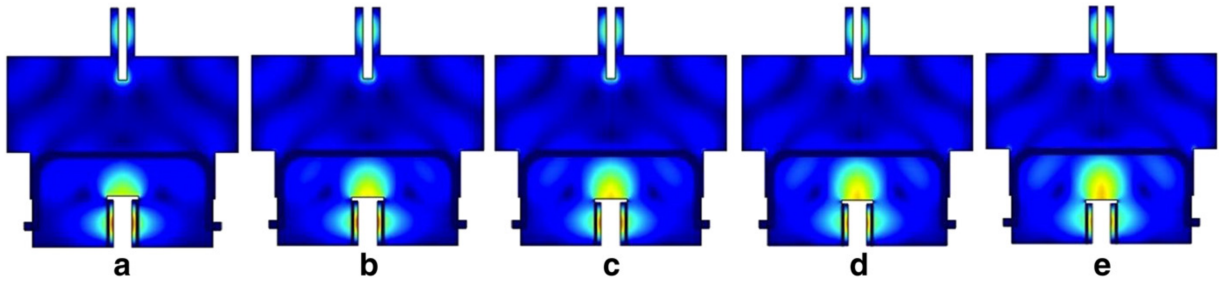

Figure 4.5: Electric field strength variation in the cavity applicator with varying Z_S=$L_1 - L_2$. Z_S=+4 mm, +2 mm, 0 mm, –4 mm, –6 mm for image (a) … (e) [128].

4.1.3 Process Gas Delivery

A mixture of H_2 and CH_4 process gases are needed for diamond epitaxy, as discussed in previous sections. These are supplied with research grade purity (99.9995% or <5 ppm for hydrogen, and 99.999% or <10 ppm for methane). General purpose MKS Type 1179A mass flow controllers are used to regulate gas flow rates, typically set to 400sccm H_2, and 20sccm CH_4 at a ratio of 20:1. No nitrogen is intentionally added to process gas mixtures. Safety protocols are critical when handling the outflow of process gases. Nitrogen is used as a purging gas with a flow rate automatically set at 10 times the hydrogen input rate to reduce exhaust line concentration rates to non-flammable levels.

4.1.4 Pressure Control

Plasma discharge conditions under this configuration requires pressure in the range of 10-300 Torr. The operating pressure set point must be maintained while flowing a continuous supply of process gases. The only vacuum source used in the DS4 sub-system is a TRIVAC D 16 BCS, a two-stage rotary vane mechanical vacuum pump. The pressure level is regulated by a MKS Type 153D/1253D throttle valve, and measured by three pressure gauges operating at different ranges: MKS Type 141A Baratron Absolute Pressure capacitive based sensor operating at 0.1-1000 Torr, a MKS Type 623 Baratron Capacitance Manometers operating at the same range, and a more recently installed MKS Series 910 Dual Trans Micropirani/Absolute Piezo Transducer with a wide net range of 1×10^{-5} - 1500 Torr. This manometer is used for base pressure sensing and external monitoring during normal operation. This lower limit is still above the base pressure achievable in the system, reachable in less than three hours under current conditions.

Vacuum and gas flow lines are all protected and computer controlled by pneumatic valves. The leak rate in this system is regularly monitored and usually found to be between 5 - 12 $\mathrm{mTorr\,h^{-1}}$. Any value higher than this implies the main leak source, the dome o-ring set, should be cleaned or adjusted. Based on the total vacuum chamber volume of 3.41×10^4 cm, if we follow calculations previously outlined [129], the updated estimate for the leaking gas flow rate is 7.5×10^{-3} sccm, equivalent to a residual nitrogen content in the system of approximately 20 ppm.

The system is kept under vacuum when not in active use, and the same nitrogen line used for purging is redirected for venting the system to limit prolonged exposure to atmospheric gases.

4.1.5 Temperature Control

An IRCON Ultimax monochromatic infrared pyrometer operating at 0.96 µm was used for measuring substrate temperatures. The pyrometer is fixed in place just outside the cavity and pointed at substrates through an inlet in the cavity wall. The emissivity of the pyrometer was set to 0.1.

The thermal energy generated in the process requires active cooling for several components, including most of the power supply sub-system, beginning with the dummy load, the magnetron, magnetron head, the probe, sliding short and the base plate. The sample itself needs to be cooled down in both Type B and Type C reactor configurations to achieve higher power densities. These components need to be maintained at a minimum temperature of 20°C to prevent condensation. The temperature is regulated by a water conditioning system operating as an active heat exchanger off a main cooling line servicing multiple reactors in the building.

In terms of air cooling, two air blowers are used to cool the quartz bell jar through an inlet in the cavity wall. This air flow is designed to circulate within the cavity to maintain temperature uniformity outside the bell jar to prevent thermal stress. An additional air blower cools the magnetron head. If the temperature increases above a certain threshold, an interlock is tripped shutting down any active process. The cavity itself is cooled from the outside with a simple air fan pointed at its external walls.

Figure 4.6, included here for reference, shows a generalized MPACVD reactor cavity illustrating many of the sub-components directly related to this section of the reactor, including elements designed for thermal control.

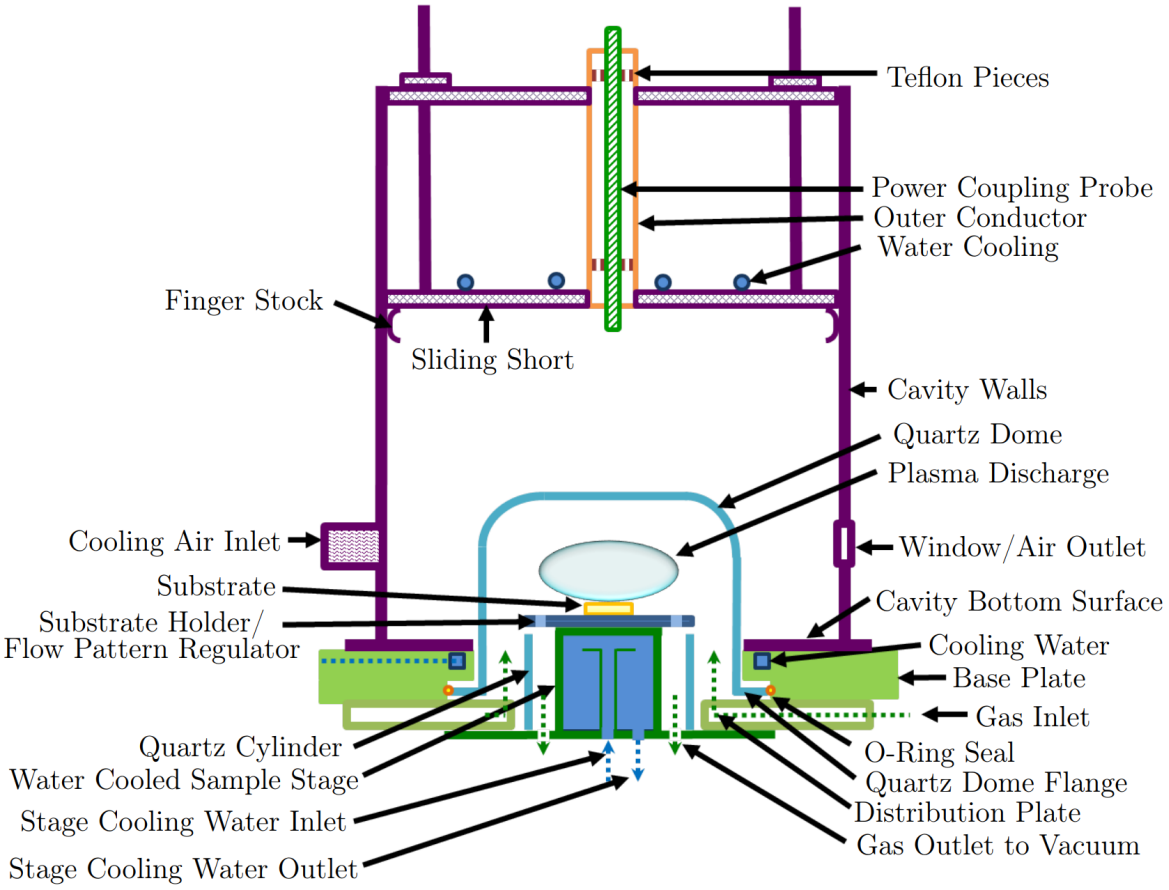

Figure 4.6: Shematic illustration of a general MPACVD reactor with supporting components [260].

4.1.6 Computer Control

The computer control sub-system in DS4 is a Windows-based closed-source software designed to monitor and control all components through a Beckoff I/O bus. The user is able to monitor all parameters including temperature, pressure and flow rates. All values are logged with a sampling rate of 3 seconds, with data stored in a standard tab-delimited text file. With this software, the user has full control by digital input of location based parameters, such as the short and probe positions, which are mechanically adjusted by stepper motors. The user also has direct digital control of pressure, flow rate and power set points. The user is only limited by hard coded physical limits, and includes multiple digital interlocks for safety. The system can be operated manually, or programmed to follow editable sequences defined as recipes. The user retains control of any ongoing process as long as the current step carried out in the recipe is a pre-programmed delay. Recipe steps can not be modified or extended during an active sequence.

4.1.6.1 Closed Loop Control

The system was designed for semi-automatic control, where the process is safely self-sustained, as long as the steps are able to be reproduced with no need for user input. However, in many cases the growth process requires active feedback. For example, when a diamond substrate is grown thicker and the top surface approaches the discharge region, its temperature naturally increases. During the standard growth sequence, designed for expanding rimless surfaces, the user must maintain a constant temperature throughout the process. This has been achieved by constantly monitoring the temperature, and manually lowering the incident power as needed to regulate the measured temperature within the desired set point [7, 192].

Efforts have been directed towards upgrading the system with a closed loop control

mechanism. The main software is not open source, and disconnecting the power control signal from a system well equipped with plenty of interlocks and pre-programmed recipes is not an option. The approach has been to complement the computer control with external components to effectively mimic the feedback steps an operator would follow during a growth process. This extension reduces human error, and the need for constant monitoring over long processes that could potentially last several days.

The extended computer control system, illustrated as a block diagram in Figure 4.7 is based on a Raspberry Pi 3 Model B+ used in part to monitor the temperature signal from the pyrometer, the only component not directly connected to the main Beckoff bus.

The temperature signal from the pyrometer is converted using a 10-bit model ADS1115 analog-to-digital module. At this resolution, temperature is measured with an effective precision of 1.4°C. An additional digital-to-analog module, model MCP4725, relays a scaled signal into the Beckoff bus. With this new data line installed, the log file in the main computer now includes continuously updated temperature measurements.

A Python script in the Raspberry Pi monitors the measured temperature, and determines when power adjustments are needed as temperature deviations exceed set thresholds. Power adjustments are sent back into the main computer by emulating keyboard strokes corresponding to new power set points using an Arduino Leonardo. It should be noted that the Beckoff module which sends the power set point signal to the power supply only has an 8-bit resolution to cover the full 10 kW range. With this resolution, the minimum power adjustment corresponds to approximately 40 W. At typical operation ranges, this difference corresponds to temperature adjustments of at least 6°C. This sets how wide the temperature thresholds should be established on each run. When operating at relatively low power ranges, with values close to 2000 W, the minimum temperature adjustment can be as high as 20°C.

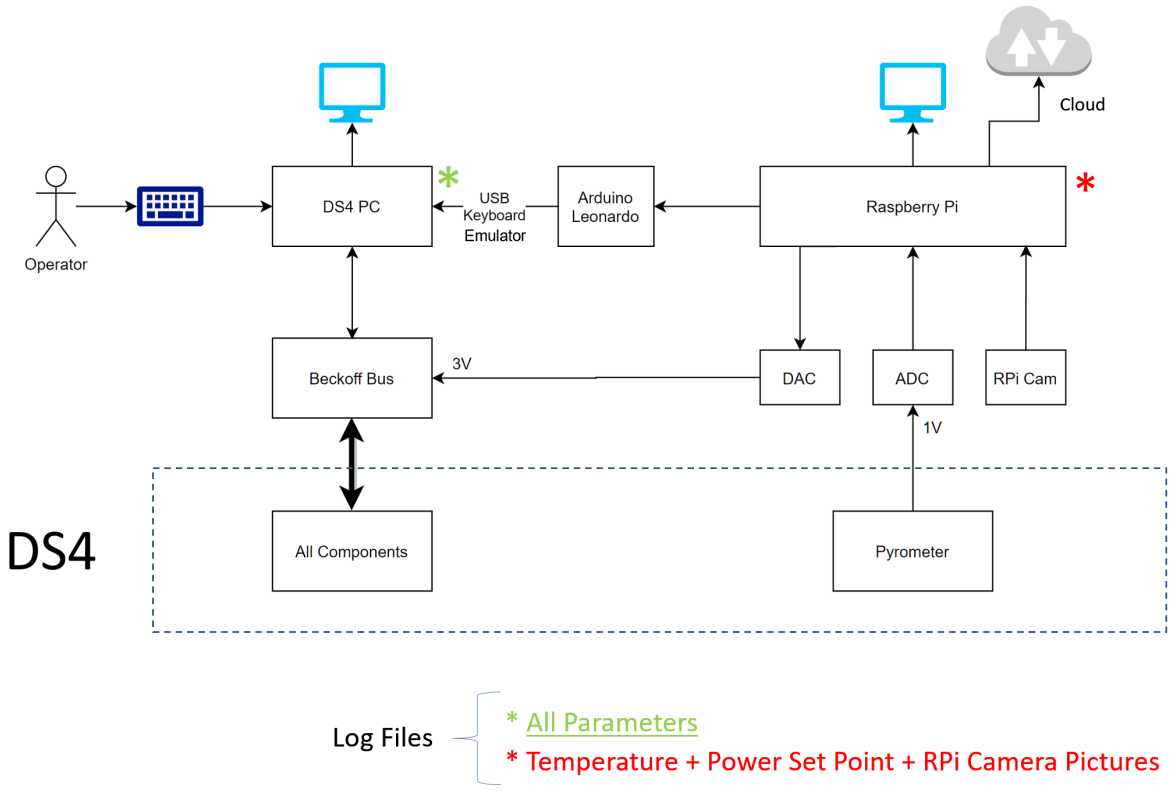

Figure 4.7: The main computer (DS4 PC) handles most of the components in the system through the Beckoff control Bus. Temperature measurements from the pyrometer are measured at the Raspberry Pi using an analog-to-digital module (ADC) and relayed to the Beckoff bus using a digital-to-analog module (DAC). Power adjustments from the Raspberry Pi are sent to the main computer through an Arduino Leonardo. Camera pictures are taken with a Raspberry Pi camera (RPi Cam). Both the main computer and the Raspberry Pi have separate monitors and keyboard inputs. Data from the Raspberry Pi can be uploaded to external cloud servers for real-time monitoring during long runs.

This limitation is set from the Beckoff bus and power supply interface, therefore the same effect also applies when making direct manual adjustments and is not related to any of the closed loop components. Figure 4.8 shows typical temperature curves during a growth process demonstrating how substrate temperature levels are kept as close to the set point as possible given current hardware limitations. Resulting power profiles are similar to previously reported curves [193] for this system and growth process.

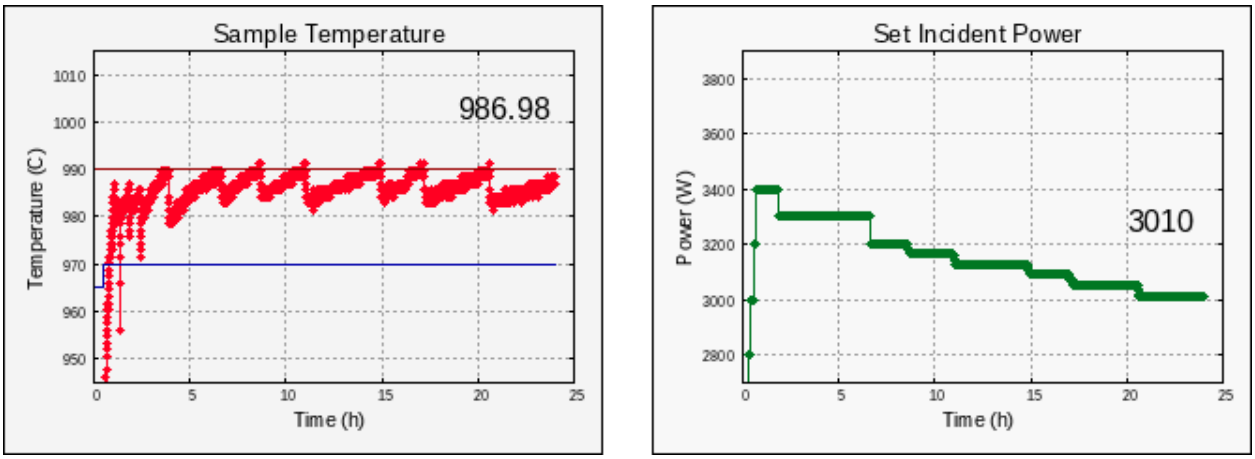

Figure 4.8: Figures showing Temperature measuremetns and corresponding Power Set Points vs. time for a 24h+ run under typical operation at relatively high power. During the first four hours, the system was controlled by manual power adjustments, and the automated power control mechanism was activated during the rest of the run. In this case, power levels were lowered when the temperature exceeded the maximum set threshold of 990°C.

4.1.6.2 Timelapse Pictures

The photographic sub-system previously described for DS4 [7] has been upgraded from a stand-alone DSLR camera to a native controlled Raspberry Pi Camera Module v2, based on a Sony IMX219 8-megapixel sensor paired with a Pixco 50 mm F1.4 lens to limit the field of view to a small region not wider than half an inch across the substrate. As camera pictures are now directly available, a short timelapse can be compiled and continuously updated, serving as a real-time monitoring and diagnostic tool. Figure 4.9 shows the updated camera setup, and Figure 4.10 shows a picture of a sample taken during a growth run.

Now that all components have been covered, Figure 4.11 shows a picture of the front facing panel, cylindrical cavity, and user interfaces for both the main computer and extended control systems in DS4.

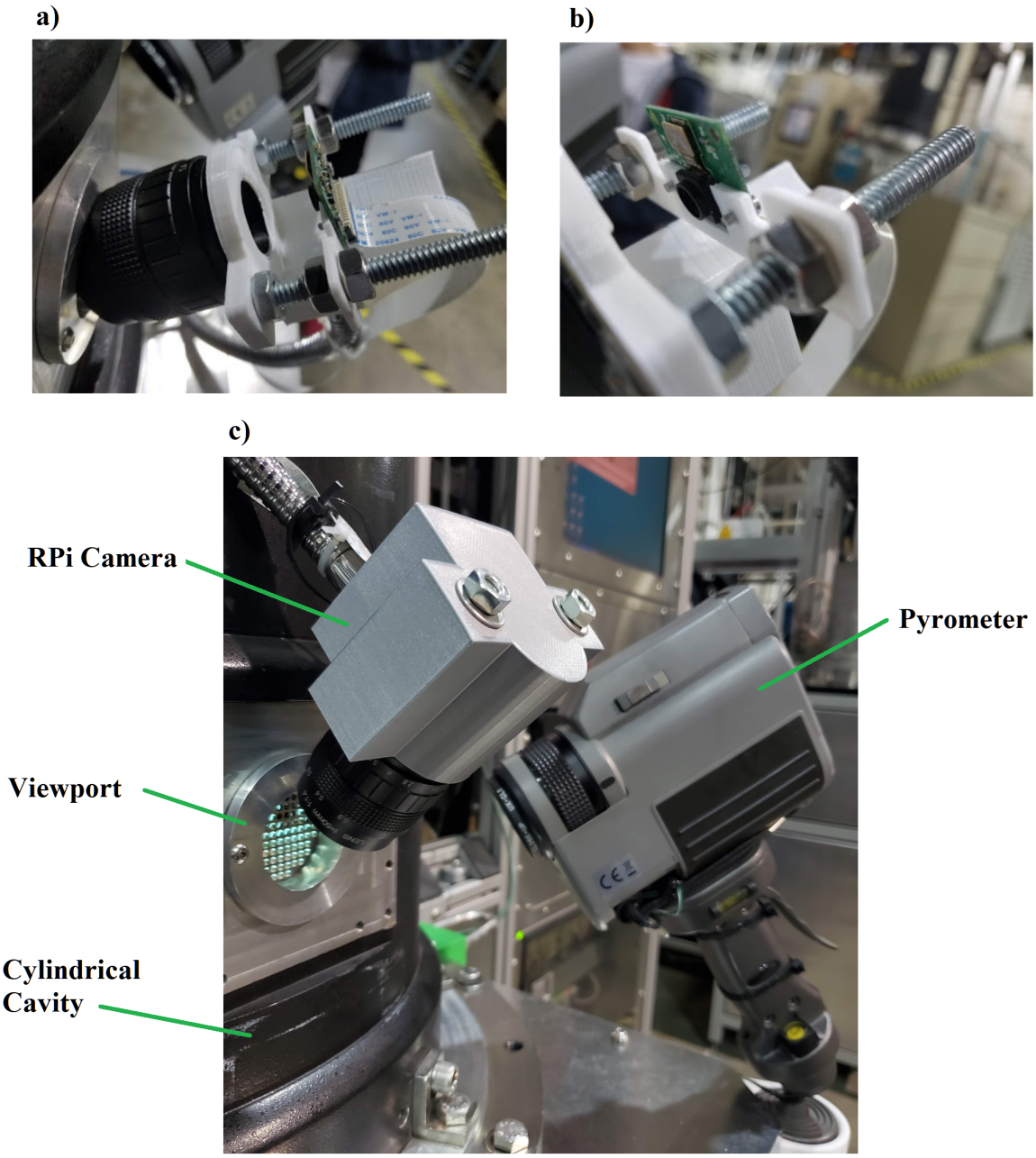

Figure 4.9: a)Raspberry Pi camera and lens combination. b) Factory lens removed from camera module. c) Focused setup enclosed in a 3D printed case. Both the camera and the pyrometer focused at the sample through view ports in the cylindrical cavity.

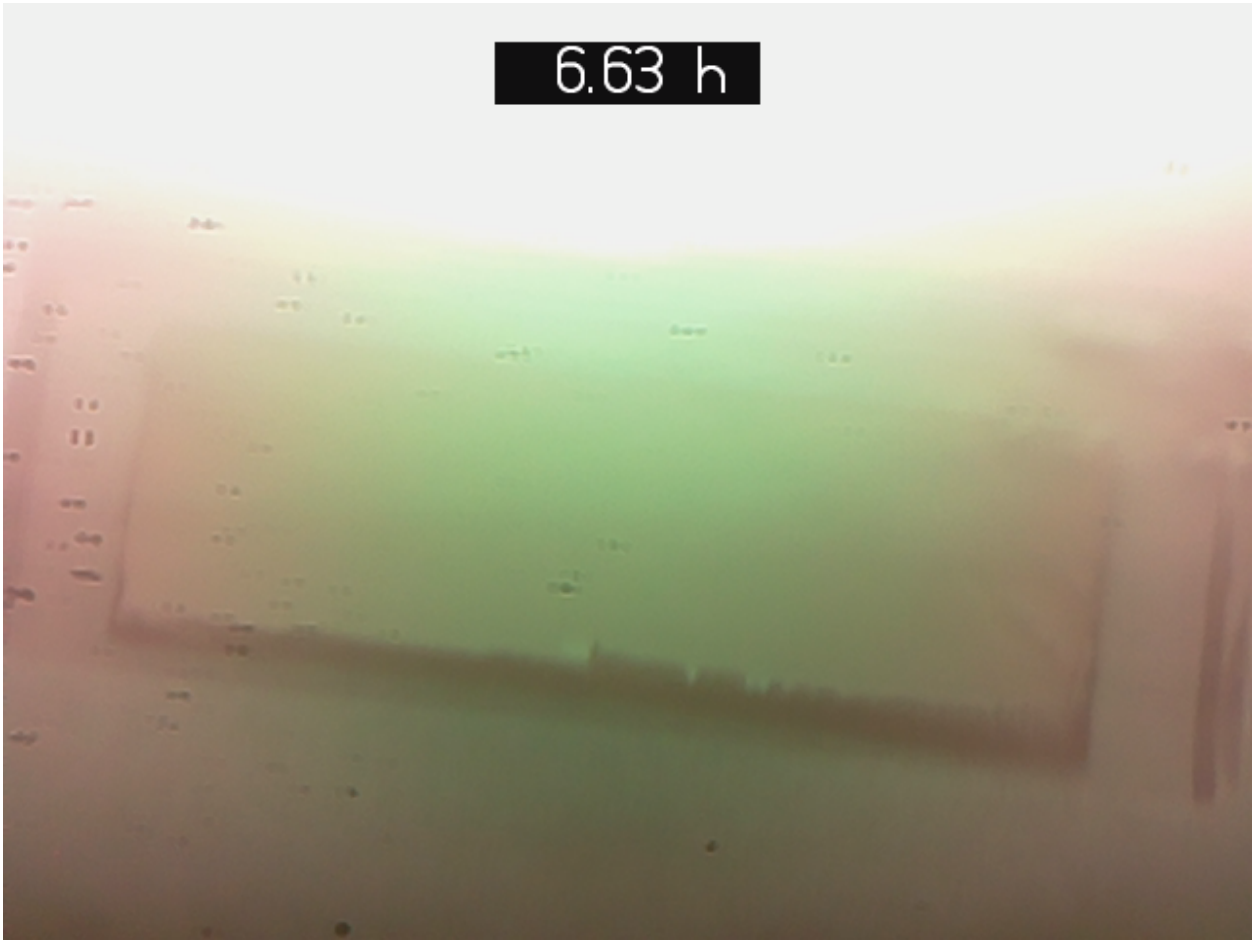

Figure 4.10: Picture taken during a mosaic seed growth process. This sample was composed of two separate tiles, each measuring approximately 5.5 mm on each side. Details can be appreciated such as interface location, size, edge roughness and surface quality as they develop during the growth run. The green hue is typical for discharge regions with methane concentrations, and the red hues on the image are an effect sometimes observed when camera sensors are saturated.

Figure 4.11: Diamond System 4 (DS4) during normal operation.

4.1.7 Substrate Holder and Sample Holder

The setup used to hold samples can be described as a set of three components. The base is a fixed cooling stage, critical for operation at higher pressures and temperatures. Its relative position within the cavity assembly is drawn to scale in Figure 4.12.

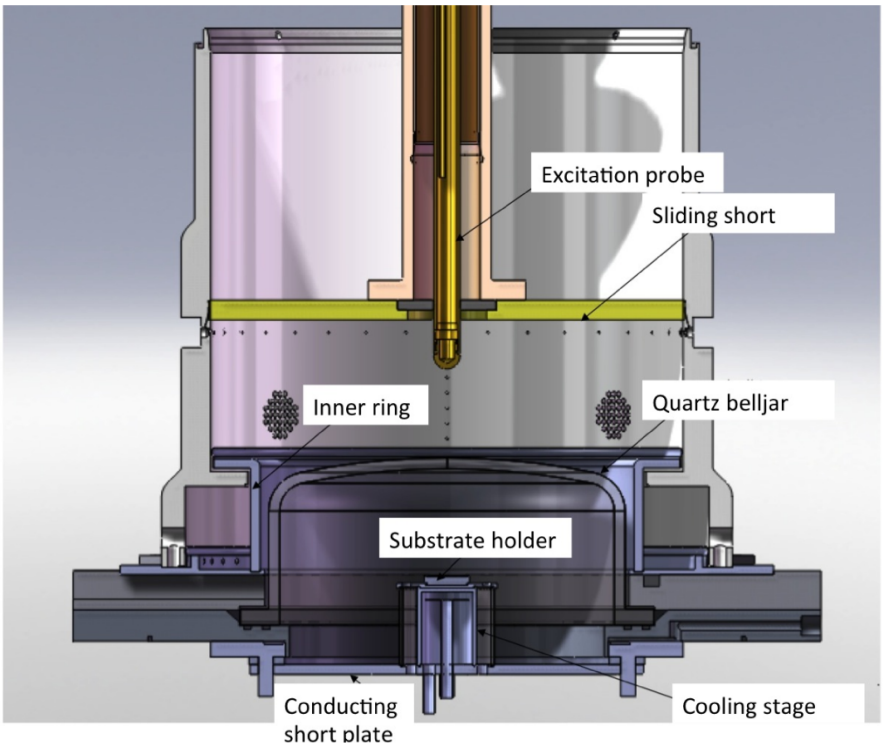

Figure 4.12: Cross-section of the applicator cavity for Reactor Type C [129].

Stacked over the cooling stage, as illustrated in Figure 4.13, are two molybdenum components. The source material for both is obtained from Ed Fagan Inc. and milled by the Physics Machine shop at MSU. The first component is called a "Substrate Holder", which consists of a 64.7 mm diameter flat disc with multiple holes drilled to allow exhaust gases to flow out of the system through the underlying quartz tube. The full dimensions of this component are described elsewhere in more detail [259], as it is based on the substrate holder used in DS3, reactor Type B. The name "susbtrate holder" might sound misleading in the current setup, as substrates are not directly loaded on this surface, but the term has

remained unchanged since early reactor prototypes designed to grow polycrystalline diamond over silicon substrates [127]. In case of Single Crystal Diamond growth, the seeds need to be enclosed from the sides to promote a uniform thermal environment, as discussed in Chapter 2, therefore an additional component called the "Sample Holder" has been incorporated into the design.

The sample holder, sometimes also referred to as the pocket holder [7] due to its geometric design, is also machined from molybdenum. The sample holder, with full standard dimensions [129] illustrated in Figure 4.14, is placed over the substrate holder, as seen in Figure 4.15, and the single crystal seed is placed within the pocket.

All pocket dimensions and total thickness of this sample holder design have an effect on diamond growth conditions and final outcomes. If the pocket is too wide, sample edges eventually exhibit uncontrolled polycrystalline (PCD) growth as the setup approximates an open holder configuration, illustrated in Figure 4.16. If the pocket is too narrow, the PCD layer grown on the inner edges of the pocket eventually encroach onto the sample from its sides, limiting lateral expansion on the single crystal seed, as illustrated with an example in Figure 4.17.

Sample holder design is not a straightforward process as any parameter will have an effect on the growth. Different configurations have been explored on a recent investigation based on the DS4 reactor [7, 193] to explore how these conditions can be optimized toward large areas with minimal PCD formation around sample edges. Figure 4.18 shows one of the trends obtained from this study, where wider pockets led to faster lateral growth rates, but resulted in jagged edges.

In this present investigation, when the option of designing a new sample holder was available, the design parameters were based on pocket dimensions equivalent to widths of

6.6-7.0 mm, as these values were observed to yield a balance between significant lateral growth, and edge quality.

This study was followed in terms of deposition times as well, as Figure 4.18 also shows how effective as-grown areas are time dependent [7]. Holder design parameters, including

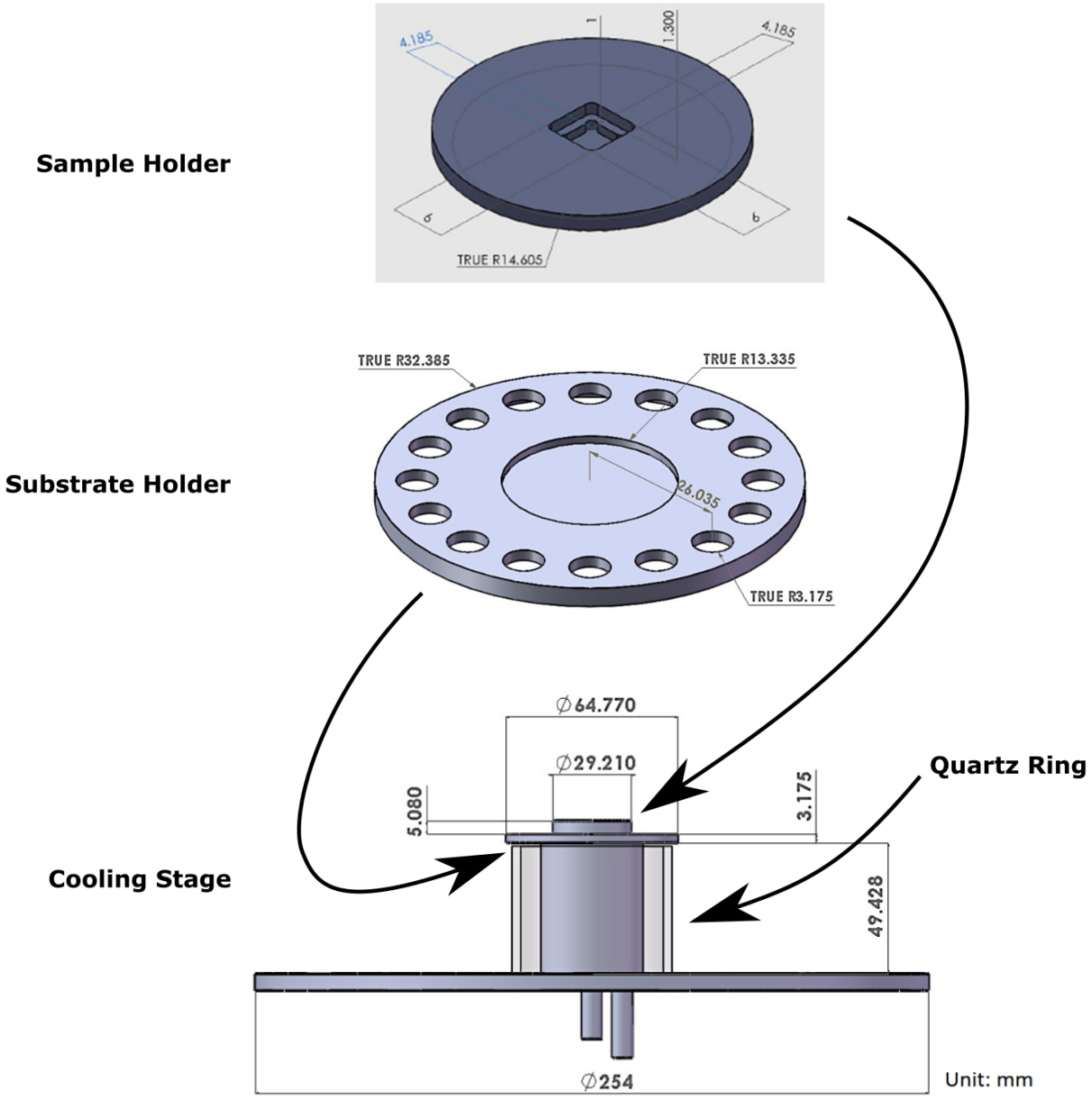

Figure 4.13: Cooling stage dimensions including isometric views of the substrate holder and sample holder. Image adapted from [129].

depth and shapes discussed in more depth the study were also applied. Similar results were obtained in terms of linear and lateral growth rates as well as top surface morphologies.

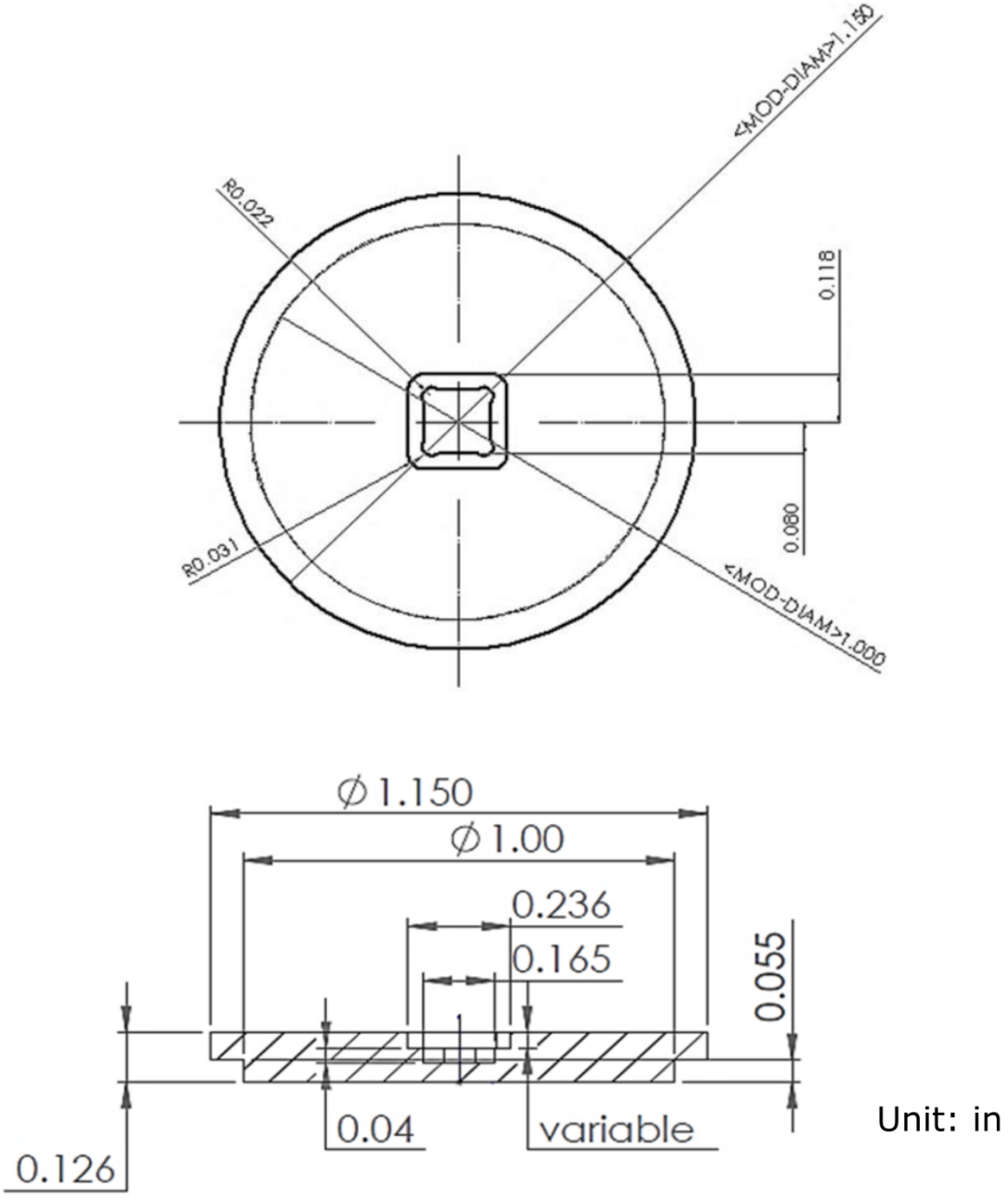

Figure 4.14: Standard dimensions for the sample holder design [7].

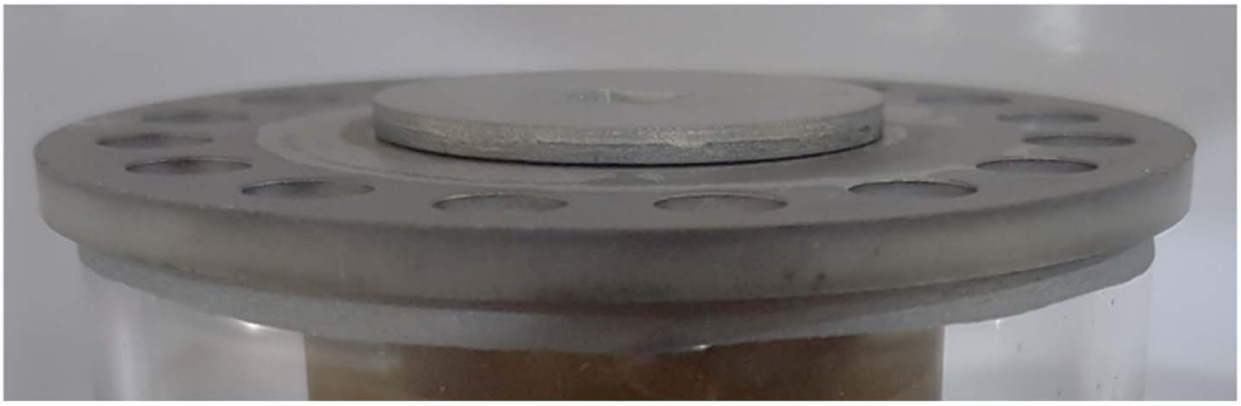

Figure 4.15: Assembly of a sample holder and substrate holder over the cooling stage [193].

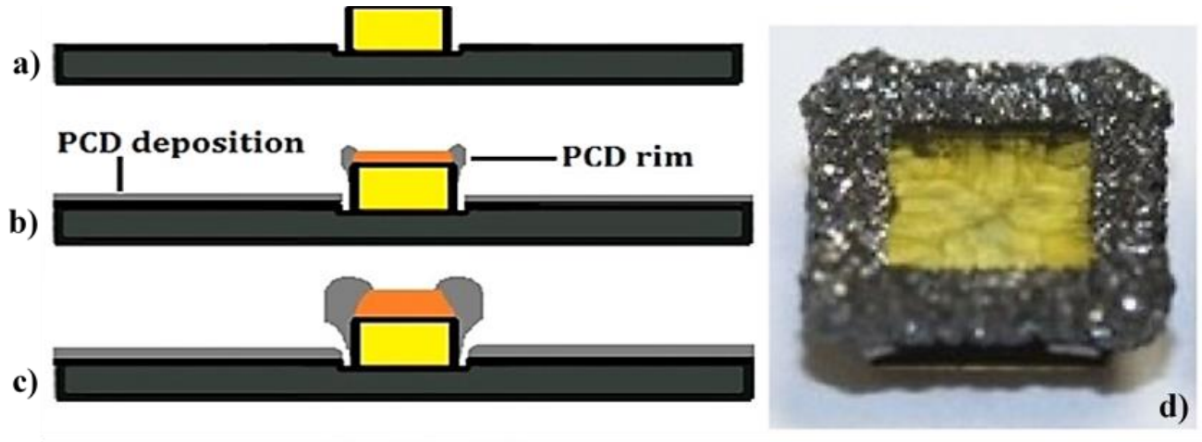

Figure 4.16: a,b,c) Cross-sectional view of diamond synthesis over time in an open holder configuration. PCD is grown over the top surface of the sample holder and exposed sample edges. d) Diamond grown on an open holder exhibiting thick PCD rims [7].

4.1.8 Holder Conditioning

To achieve intrinsic growth, sample holders need to be free of contaminants that might incorporate into the grown lattice. Contaminants could be present in the holder due to several reasons, for example, a new holder will inevitably be covered in oil and other foreign materials due to lubrication used in the machining process. Solvent cleaning is not necessarily enough to get rid of these contaminants. The high temperatures at which the holder is exposed to during a growth run will result in outgassing of any absorbed materials.

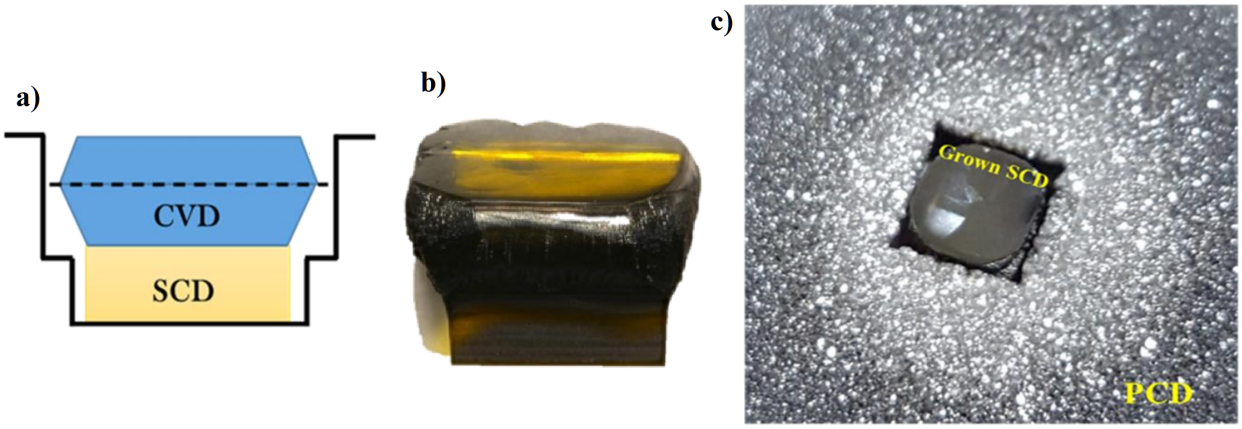

Figure 4.17: a) Cross-sectional view of CVD grown layers with reduced area, as PCD from the sample holder encroaches on the grown surface. b) As-grown sample with reduced area. c) Top view showing how the top surface of the Single Crystal Diamond (SCD) sample is limited by PCD growth from the sample holder [7].

Another source of contaminants results from the sandblasting process, which is sometimes needed when PCD fails to delaminate from the holder after a deposition. The sandblasting media is usually composed of silicon dioxide, which is also not cleared from the holder with standard ultrasonic solvent cleaning.

The solution for this contamination issue is to first clean the holder with methanol for 15 minutes, rinse with DI water and dry at 100°C for an hour. After this preliminary cleaning, the holder is exposed to a hydrogen plasma similar in incident power and pressure as the process it was designed for prior to the actual run. The length of this conditioning process can be as short as one hour for typical contamination levels found in new holders, but could last as long as 12 hours depending on the type of sandblasting media used. During this conditioning process, the observed plasma color might be blue or orange depending on the contamination type and it gradually fades to the expected purple hue from a pure hydrogen plasma.

The criteria used to establish the length of each conditioning process is to wait until the measured temperature of the holder stabilizes into a constant value, ensuring there is no

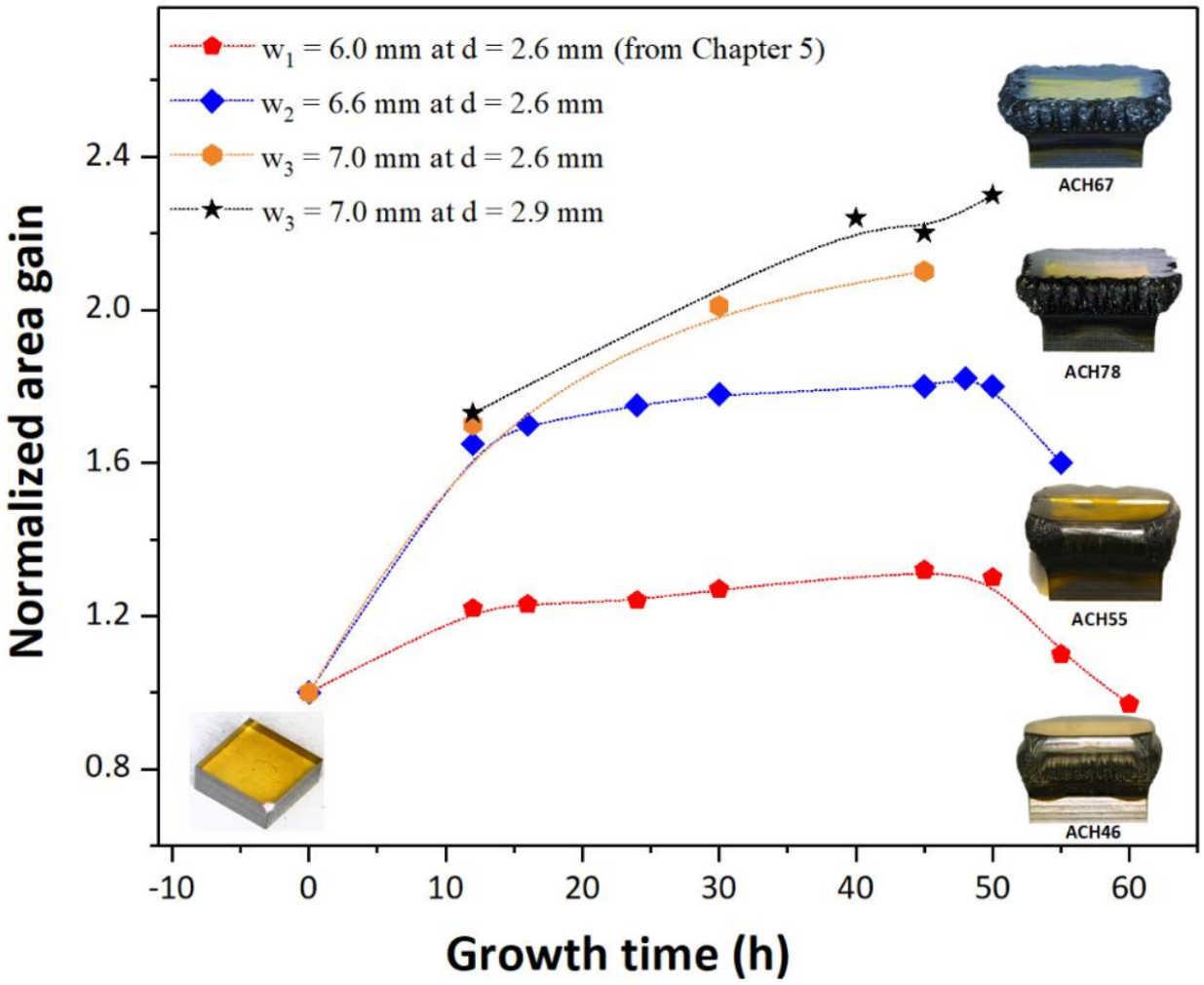

Figure 4.18: Experimental data summarizing normalized area gain versus growth time for several pocket configurations [7].

material left to outgas under current conditions.

4.2 Seed Preparation

4.2.1 Sample Polishing

Sample surfaces set for growth need to be as flat as possible to promote a smooth step flow process during deposition. Macroscopic defects are flattened out by diamond polishing, a

purely mechanical process which has in essence been unchanged for centuries. Since diamond is the hardest material, the only way to produce abrasion on its surface is with diamond grit over a rotating cast iron disk called a scaife. The diamond grit size can range from 1 µm up to 20 µm and is spread thin throughout the scaife using olive oil to contain the powder. The diamond surface is pressed against the flat surface with force in excess of 10 N, and the scaife rotates at an angular speed of 3000rpm, equivalent to a linear velocity of approximately 50 m/s. The process results in material removal rates in the order of tens of nm/h, and can achieve average surface roughness levels below 1 µm [261]. The diamond polishing process was carried out throughout this investigation with a Coborn PL3 planetary lapping bench. The planetary movement in this equipment limits the effect of scratching due to uneven roughness in the scaife.

If the sample holding jig used to control the pressure applied to the sample is equipped with micrometers, then small angle corrections below 0.1° can be performed on surfaces during the polishing process.

4.2.2 Laser-cutting

One way to prepare seeds for deposition is to ensure the edges are also as flat as possible, as any rough edges tend to favor uncontrolled growth that could lead to undesirable PCD formation. Irregular edges are also not ideal, as it would make experimental results difficult to replicate. Producing flat edges or removing large quantities of material for either framing or large angle corrections would be impractical by direct polishing. The method used for sample preparation in these cases is laser ablation, which has in principle already been discussed in section 3.3.1. The system used for all laser cuts during this investigation was a Bettonville Ultra Shape 5xs-IR system, with a continuous wave Nd:YAG Laser system from CSI Group

operating at 1064 nm. The power output on the sample is 18 W with a laser spot size below 20 µm in diameter. Cut planes within the sample result with a roughness of $R_a = 180$ nm, and $R_{zdin} = 1100$ nm when using this equipment. After polishing, these values can be reduced to $R_a = 2.5$ nm, and $R_{zdin} = 17$ nm, as measured by surface profilometry [199]. Both values for polished samples are in the typical range measured for commercial substrates.

4.2.3 Seed Cleaning Procedure: Wet Chemistry

Before every diamond deposition, the seed itself should be as free from surface impurities as possible. This is achieved with a wet chemical cleaning procedure to remove metallic, graphitic and organic contamination. The steps are standardized and proceed as follows for pre-deposition to remove all contaminants, and post-deposition to remove graphitic residues deposited during the ramp-down process.

4.2.3.1 Pre-Deposition Cleaning

1. Nitric Acid (40 mL) and Sulfuric Acid (40 mL) mixture boiling at 300°C for 20 minutes.
2. Rinse in DI water.
3. Hydrochloric Acid (40 mL) boiling at 300°C for 20 minutes.
4. Rinse in DI water.
5. Use DI water beaker to transport sample to solvent fume hood.
6. Ultrasonic cleaning with sample in Acetone (30 mL) for 5 minutes.
7. Ultrasonic cleaning with sample in Methanol (30 mL) for 5 minutes.
8. Dip sample in Isopropanol (30 mL). (Store in isopropanol jar if the sample will not be loaded into the system within a couple of minutes.)
9. Dry sample with nitrogen.

10. Transport sample using a new covered pietri dish for immediate loading into the deposition system.

4.2.3.2 Post-Deposition Cleaning

1. Nitric Acid (40 mL) and Sulfuric Acid (40 mL) mixture boiling at 300°C for at least 1 hour, and up to 3 hours. The acid mixture can be discarded and replaced as needed until the sample is free from graphitic residue.
2. Rinse in DI water.
3. Use DI water beaker to transport sample to solvent fume hood.
4. Ultrasonic cleaning with sample in Methanol (30 mL) for 5 minutes.
5. Dip sample in Isopropanol (30 mL).
6. Dry sample with nitrogen.

4.2.4 Hydrogen Plasma Etching

An optional step before proceeding with diamond deposition is hydrogen plasma etching. When no carbon containing reactants are included in the CVD process, only the desorption components of gas-surface interactions apply. As carbon atoms are removed from the lattice at a given rate, the process is known as Hydrogen Plasma Etching. This process is isotropic at a given rate as long as the crystal lattice is uniform, but if the surface is defective in terms of impurities, roughness, or lattice dislocations, these will tend to be preferentially etched.

One application from this effect is forcing a controlled etching condition, such that counting and locating etch pits can be used as a direct measurement of defects and lattice dislocations. This application will be discussed in the following chapter as it was actively used as an analysis technique.

This hydrogen etching step can be performed as an independent process, or performed immediately before the deposition in a continuous transition toward the growth step. The process, performed for an hour at 700-850°C tends to reduce any remaining polishing damage at a rate of approximately $5\,\mu m\,h^{-1}$ and has been reported to improve dislocation densities in grown samples. During this investigation, the hydrogen etching process was not always applied, as removing material would result in wider gaps. This effect will be discussed in chapter 6.

4.3 Summary: Diamond Growth Process

A detailed outline on the steps followed to operate the DS4 reactor is described elsewhere [7]. The steps on that investigation have been followed closely on this project in terms of system operation, with the addition of activating the closed loop control once the system is under normal operation during a growth run. This section will serve as a summary of all the steps that need to be followed, with references to sections where each concept is discussed. Most of the steps during the growth process are automated, but this sequence will outline the updated list of what the operator is expected to carry out to complete the process.

4.3.1 General Diamond Growth Steps

1. Design sample holder for a given application (Section 4.1.7).
2. Sample holder cleaning and conditioning (Section 4.1.8).
3. Optional Substrate Adjustments: Polishing (Section 4.2.1), Framing (Section 4.2.2) or Angle corrections (Section 6.3).
4. Clean Substrate (Section 4.2.3.1).

5. Load sample into the deposition system.
6. Wait for system to achieve base pressure (Section 4.1.4).
7. Set up data logging and recipe in main computer (Section 4.1.6).
8. Set up monitoring and power control system in Raspberry Pi (Section 4.1.6.1).
9. Synchronize Raspberry Pi monitoring with recipe start time in main computer.
10. Wait for plasma ignition.
11. Align pyrometer with sample position.
12. Wait for system to achieve programmed operational pressure.
13. Optional hydrogen Etching: Adjust power as needed to achieve desired etching temperature (Section 4.2.4).
14. Wait for activation of methane gas input.
15. Adjust Power as needed to achieve desired deposition temperature.
16. Activate power control system in Raspberry Pi.
17. Monitor system during the deposition.
18. Wait for deposition to near completion time.
19. De-activate power control system in Raspberry Pi.
20. Wait for ramp-down process as programmed in the recipe.
21. Shut down power supply, gas and cooling sub-systems (Section 4.1).
22. Unload sample.
23. Clean Sample (Section 4.2.3.2).

Chapter 5

Analytical Instruments and Analysis Techniques

5.1 Sample Dimensions: Linear Encoder

Sample thickness for seed preparation, and growth rate estimates for all plates and samples were measured using a linear encoder Model Solatron DR600, with maximum resolution of 0.05 µm. Each thickness measurement was determined by averaging at least five measurements on top surfaces. One measurement at the approximate center of the sample, and four measurements close to each of the four sides as shown in Figure 5.1. With this approach, any height difference will determine if the top surface is not polished parallel to the back side. When the sample is measured against a flat surface, for example a silicon wafer, and the position of the silicon wafer is controlled with a micrometer positioning stage, top surface slopes can me measured within fractions of an arcsec on 3 mm wide samples.

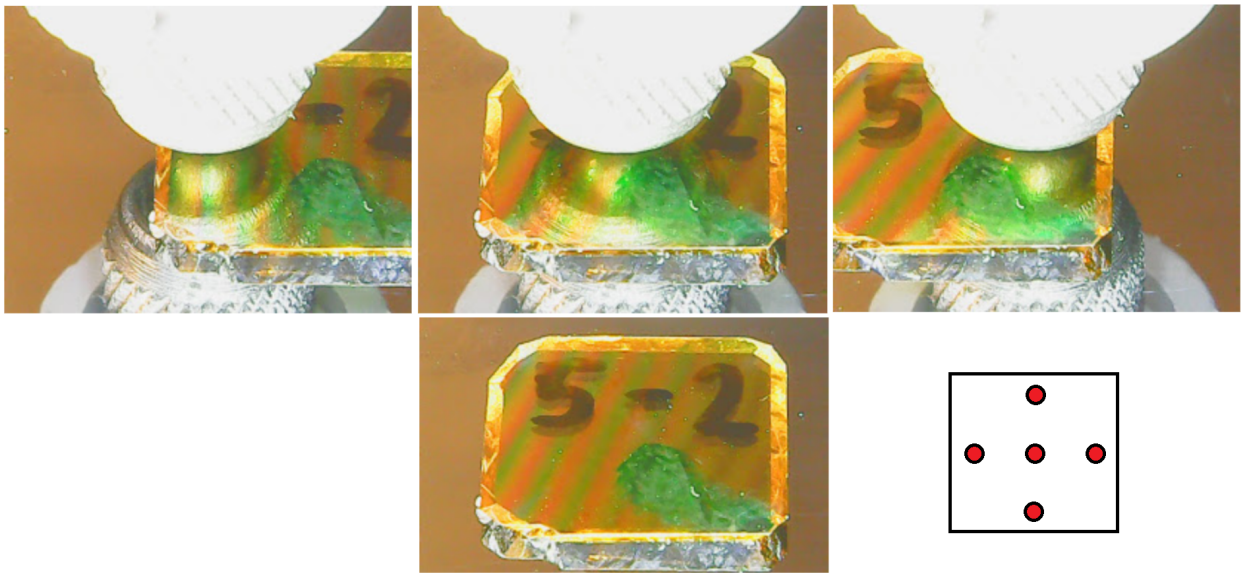

Figure 5.1: Three horizontal measurements over an sample that has not been framed yet. One corner of the sample has been marked with a temporary marker for reference. The top surface is labeled with a short-hand ID to identify the top surface. The sample is placed over a silicon wafer, which shows a reflection of the profilometer tip on its surface. The small square inset shows the location of five typical measurement points.

5.2 Surface Quality

5.2.1 Optical Microscopes

Two microscopes were used to capture surface images. A low magnification (20x) Stereomicroscope was used for close up work such as confirming alignment of mosaic samples and pictures of larger samples and assemblies requiring a wider field of view. For more detailed study of surface morphologies, a Nikon Eclipse ME 600 optical microscope, illustrated in Figure 5.2, was used in several operation modes, including reflection mode, with or without Differential Interference Contrast (DICM) mode, and transmission mode which highlight internal features within the sample such as depth and shape of crack formations. When polarized light is used in this transmission mode, birefringence measurements can be performed, as discussed in the following section.

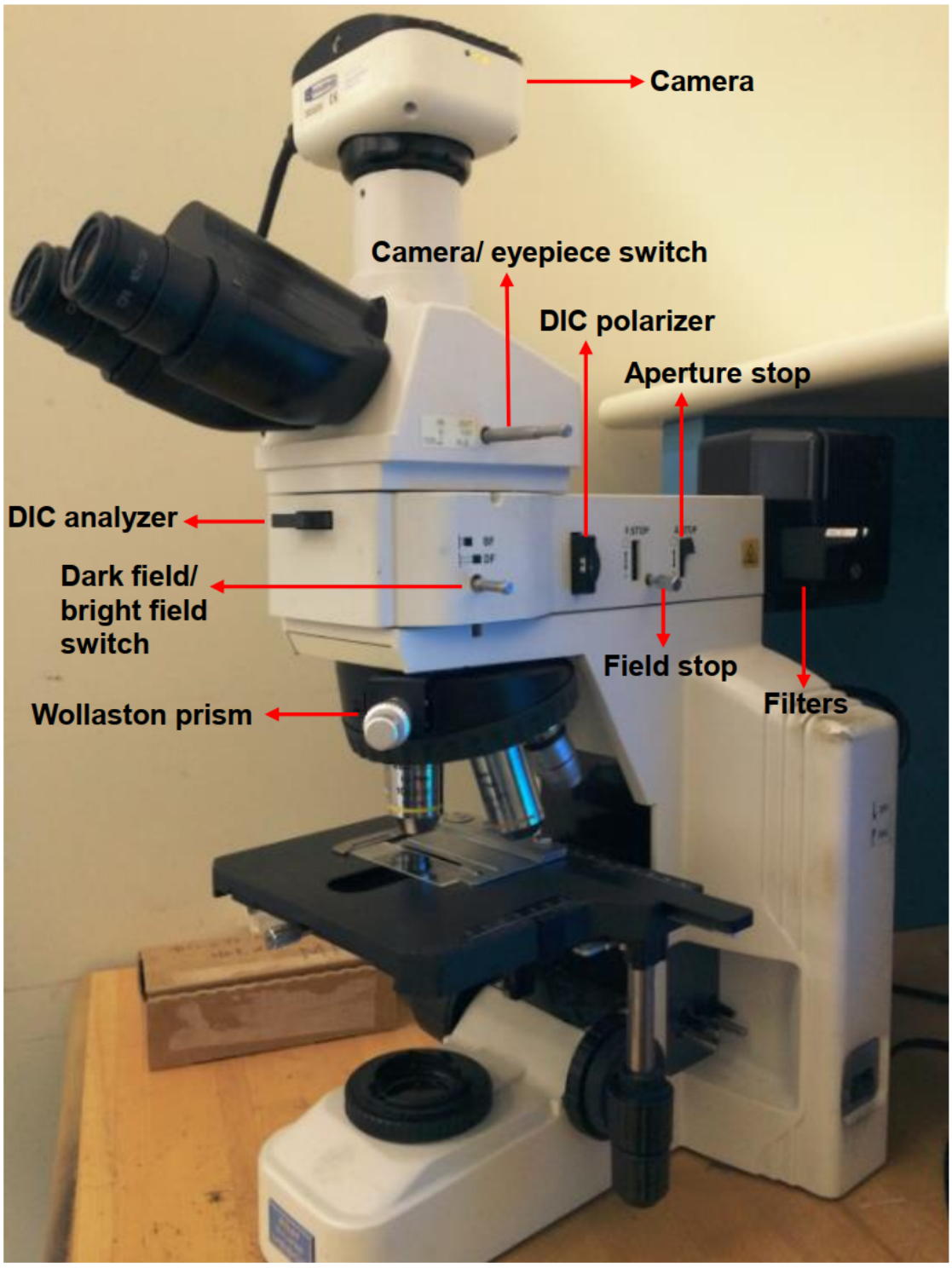

Figure 5.2: Components of the Nikon Eclipse ME 600 optical microscope [259].

5.2.1.1 Birefringence

This technique is based on a custom built setup [145] which sets two cross-phased polarization filters in the optical path of the microscope. The first filter polarizes light, and the analyzer is set at 90° rotation such that no light is transmitted between the set. When a sample polished on both sides is placed between the filters, any internal stress within the crystal will cause anisotropic rotations of the polarization vector of the transmitted light. The observed image, after crossing the analyzer, shows a 2D projection of the stress distribution within the sample. The process is straightforward and the resulting image will display slight variations in stress levels with clear contrast, but the current setup is only qualitative, as corrections due to incident light intensity, exposure time, or sample thickness are not taken into account, making comparisons between samples uncertain. Nevertheless, the current setup clearly shows how stress is relatively distributed within any given sample at a resolution only limited by the range of the optical microscope.

5.3 Sample Composition: SIMS Analysis

Secondary Ion Mass Spectrometry (SIMS) is an analytical technique used to measure low dopant concentrations. A focused ion beam (O^+ or Cs^+) generated by an ion gun is used to sputter the sample. Secondary ions formed during the process are extracted and analyzed with a mass spectrometer. Measurements were carried out by the Evans Analytical Group (EAG) where their system can measure trace amounts with a dynamic range covering six orders of magnitude, and is capable of measuring sub-ppm precision trace levels. Figure 5.3 shows a general schematic of a SIMS system.

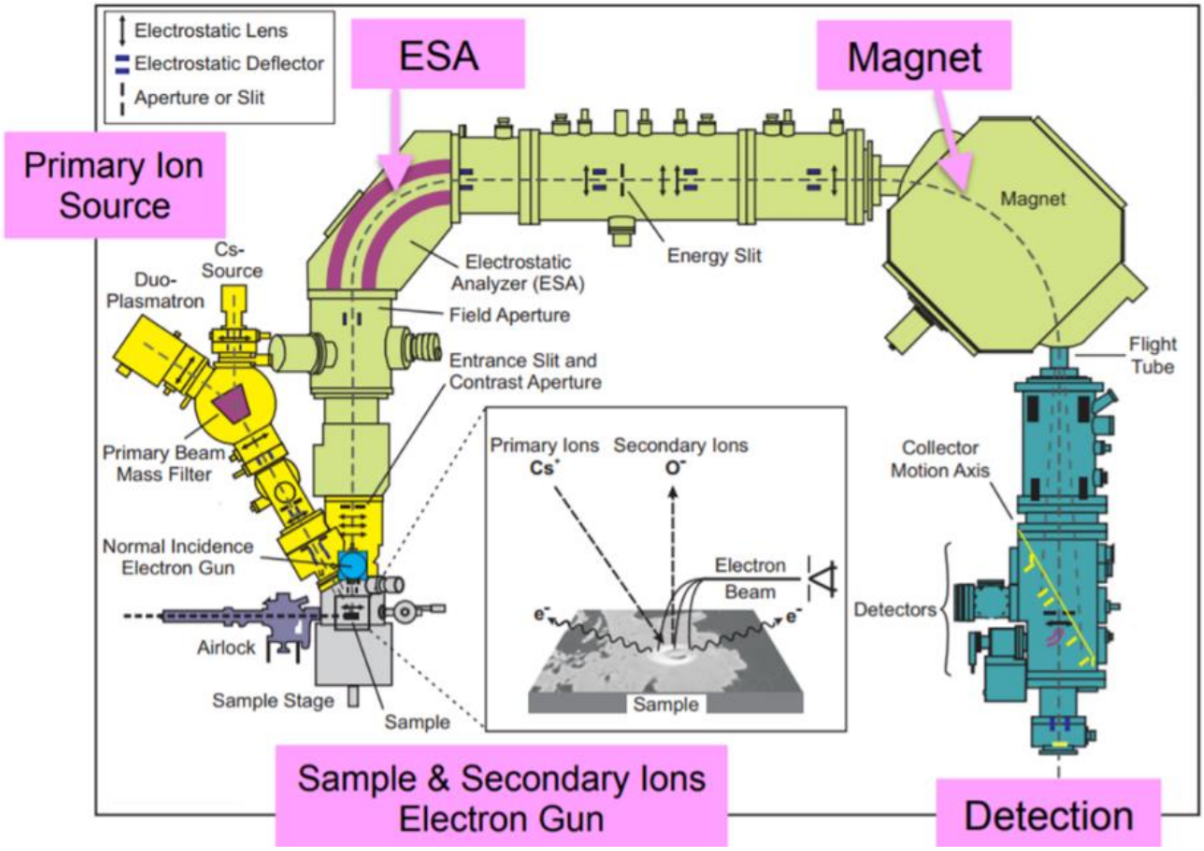

Figure 5.3: General schematic of SIMS system [7].

5.4 Dislocation Density: Etch Pit Analysis

The tool used to measure dislocation densities within the lattice structure extending to the top surface is Etch Pit Density Analysis. As discussed in section 4.2.4, etch pits are generated from exposing the surface of the sample to a hydrogen plasma. Hydrogen radicals will etch away carbon atoms from any exposed diamond lattice, but the process has a more prominent effect on the weaker chemical bonds found around defects and dislocations. The two main defects targeted by this process are sourced by either (1) Polishing Damage, or (2) Dislocation defects in the bulk of the substrate that manifest as stacking faults or threading dislocations on the top surface. One way to isolate the dislocations as the only defect source

is to pre-apply a Reactive Ion Etching (RIE) process to uniformly remove a few microns over the top surface corresponding to the region affected by the polishing process. A typical etch pit is illustrated in Figure 5.4.

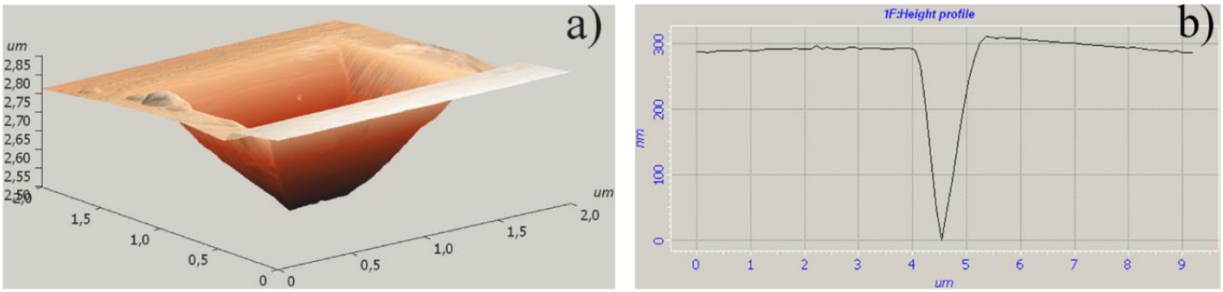

Figure 5.4: (a) A 3D image reconstructing an etch pit from an AFM measurement, and (b) height profile of a typical etch pit as measured by AFM [259, 262].

The typical way to perform Etch Pit Analysis to estimate dislocation densities over an entire surface of a sample is to perform RIE, then expose the sample to a hydrogen plasma for at least one hour. The duration of this process is extended until etch pits can be easily identified using low magnification microscope images as illustrated in Figure 5.5.

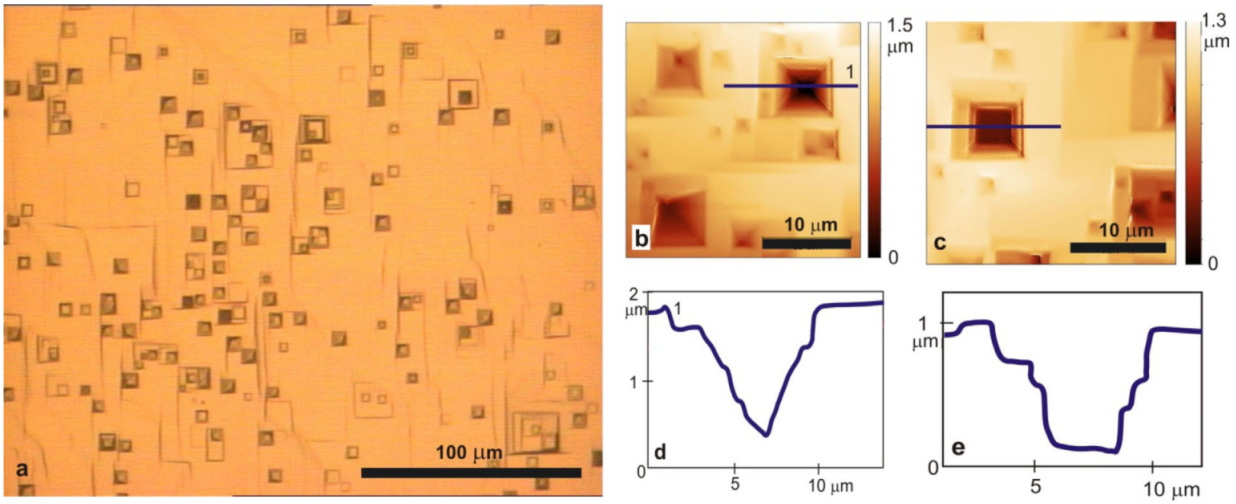

Figure 5.5: (a) Optical microscope image illustrating etch pits on a diamond surface. (b,c) Optical profilometer images after etching in H^2 for 5 h illustrating typical shapes of etched pits: point-bottom (b) and flat-bottom types (c), with their respective cross-sectional line profiles (d,e) [263].

Assuming a uniform distribution, a statistically significant typical region is selected, etch pits are counted within the area, and the ratio is used as an estimate for the overall etch pit density, and therefore the dislocation density on the sample. Our group has developed MATLAB software in previous projects to help facilitate these steps using image processing, but the present project required additional development, as the dislocations are not evenly distributed across grown surfaces.

5.4.1 Regional Etch Pit Density

It has been frequently reported how mosaic samples tend to have a much higher dislocation densities at the joint regions between tiles [224, 233, 235, 252], as expected from low angle grain boundaries. One way to quantify this effect is by following the standard process for etch pit density analysis, but performing an enhanced approach that considers the expected dislocation distributions on two-tile mosaic samples. The same concept of averaging over smaller areas can be applied, but the regions can be reduced to a rectangle where the length that runs parallel to the original boundary covers the entire sample, and the width is reduced to a smaller window. The dislocation density is expected to increase as the region is measured closer to the interface. Figure 5.6 illustrates a diagram of the approach.

As a way to characterize how the density gradually increases as the area approaches the boundary, the procedure is to first identify etch pit locations, then etch pit densities are calculated across a small window on the edge of the sample. The process is repeated with the window shifted across the full region while maintaining a fixed width, effectively compiling a moving average as the density is measured across the interface. The resulting Etch Pit Density vs Position curve and measuring technique has been defined as Regional Etch Pit Density Analysis.

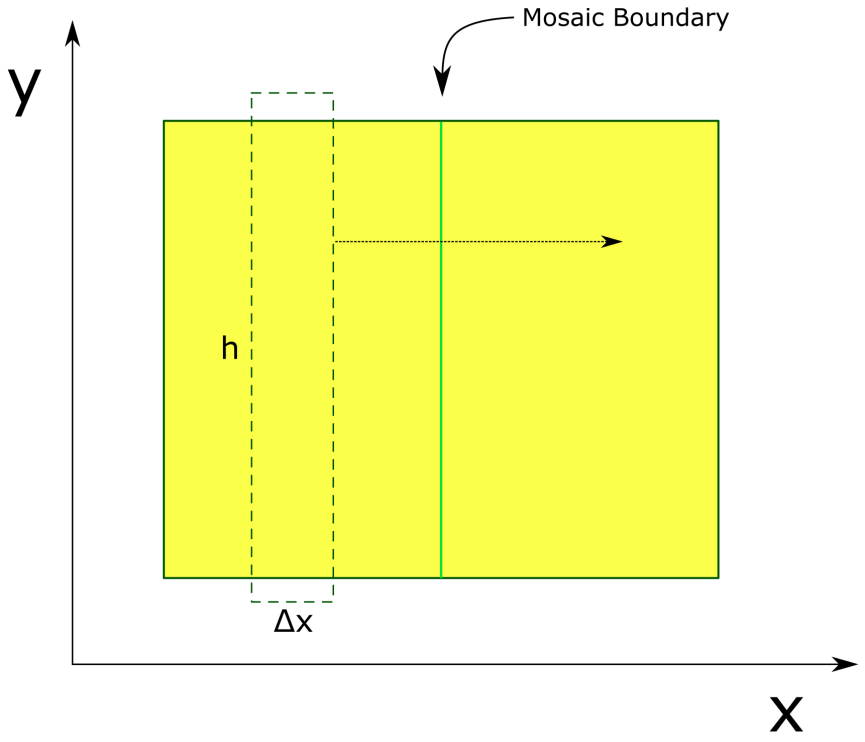

Figure 5.6: Diagram illustrating the Regional Etch Pit Density approach. The yellow rectangle represents the top surface of a measured sample grown from two underlying seed tiles and the green line represents the location and direction of the original mosaic interface. Etch pit densities are calculated for a small area with dimensions h and Δx. The process is then repeated, storing regional densities across the sample as a function of position (x).

5.5 Orientation Measurements

Lattice orientations are a critical component in the mosaic technique, as lattice mismatch is one of the fundamental parameters that need to be considered during seed assembly. Two methods to measure orientation were explored and developed in this study, but before the analysis techniques are described, preliminary definitions have to be established. Previous literature and standard orientation measurement terminology did not provide the concepts needed for a full description of mosaic sample alignment conditions.

5.5.1 Definition: Relative Misorientation

Crystal lattice misorientations on two-tile mosaic samples are frequently represented as a pair of standard lattice tilt measurements, where each tile is measured with offcut and direction, but for the purpose of this study, misorientation measurements have been explicitly defined relative to the boundary location.

If we consider three orthogonal axes based on the top surface of the sample, Tilt is defined as the angular difference in rotation of the normal vectors corresponding to the (001) planes in each tile along the rotation axes aligned with the boundary direction. Torsion is defined as the difference in rotation along the orthogonal component of this rotation axis on the top surface, and Twist is defined as the difference in rotation along the third component, the normal vector to the top surface, using the alignment of (111) planes in both tiles. With these definitions, illustrated in Figure 5.7, a full description of lattice misorientations can be described covering all three degrees of liberty in misorientation measurements using the boundary along the top surface as the main reference.

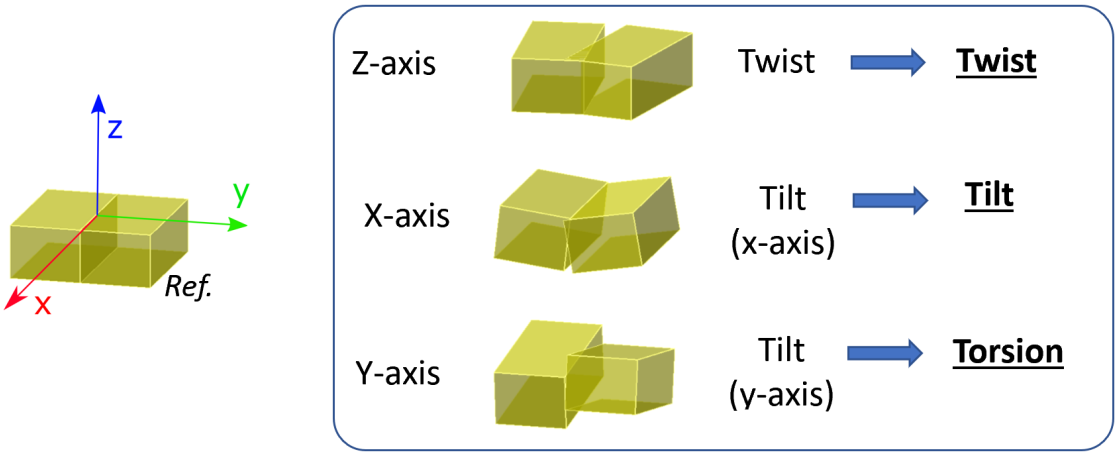

Figure 5.7: Three defined relative misorientation measurements. In this case, the 'x' axis of rotation with respect to the reference diagram corresponds to the Tilt-type misorientation, the 'y' axis corresponds to Torsion, and the 'z' axis corresponds to the Twist-type of misorientation.

5.5.2 Xray Topography

White beam X-ray topography (XRT) is a measurement technique typically used to observe the effects of dislocations, stacking faults and other types of imperfections and deformations in crystal lattices. The concept is based on applying a high intensity collimated X-Ray beam with enough intensity to transmit through the sample and a range of wavelengths wide enough to satisfy the Laue condition on different crystal planes simultaneously. The diffracted beams, illustrated in Figure 5.8, are captured on photographic film as individual topographs detailing lattice features as projected from each crystal plane.

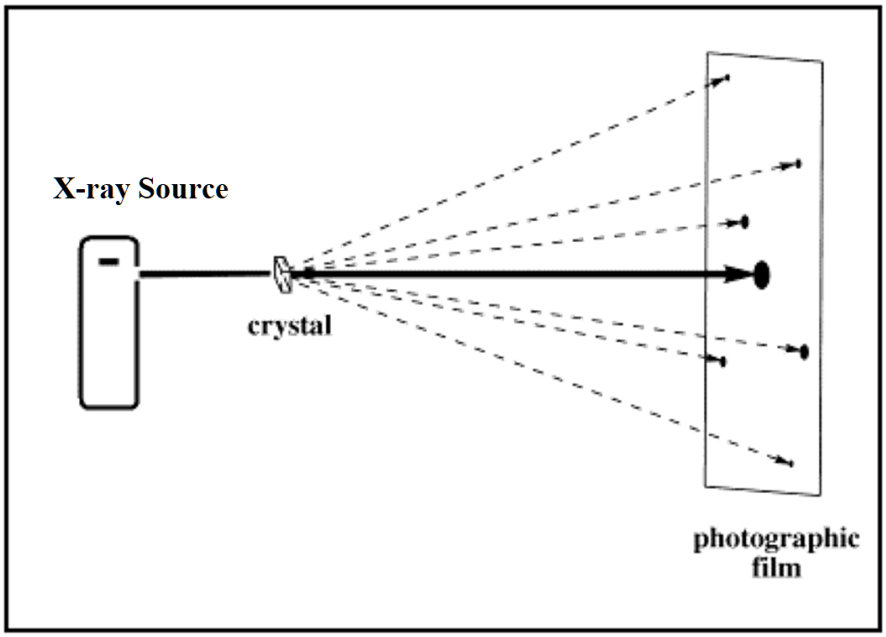

Figure 5.8: Laue Pattern based on white beam topography [264].

In this investigation, the technique was not used to measure topographical features within the lattice. The beamline setup was used to design a new method for measuring relative misorientation. The process is detailed in the following sections. All XRT measurements were performed at the 1-BM-B Optics Testing Beamline of the Advanced Photon Source at Argonne National Laboratory [265].

5.5.2.1 XRT Sample Holder Design

Samples polished on both sides were positioned by 3D printed sample holders, illustrated in Figure 5.9. The XRT holder was designed to have three adjustable rotation axes so that the top surface of the sample can be set approximately parallel to fixed X-ray photographic films in transmission geometry. One holder was printed and adjusted per sample, as the size and shape of each plate can vary significantly. Spatial alignment with the beamline can be set with standard optical table components. This setup allows for effortless loading as every sample in queue was pre-adjusted in its holder and was able to be swapped in on the optical path, maximizing the available beamtime for actual measurements.

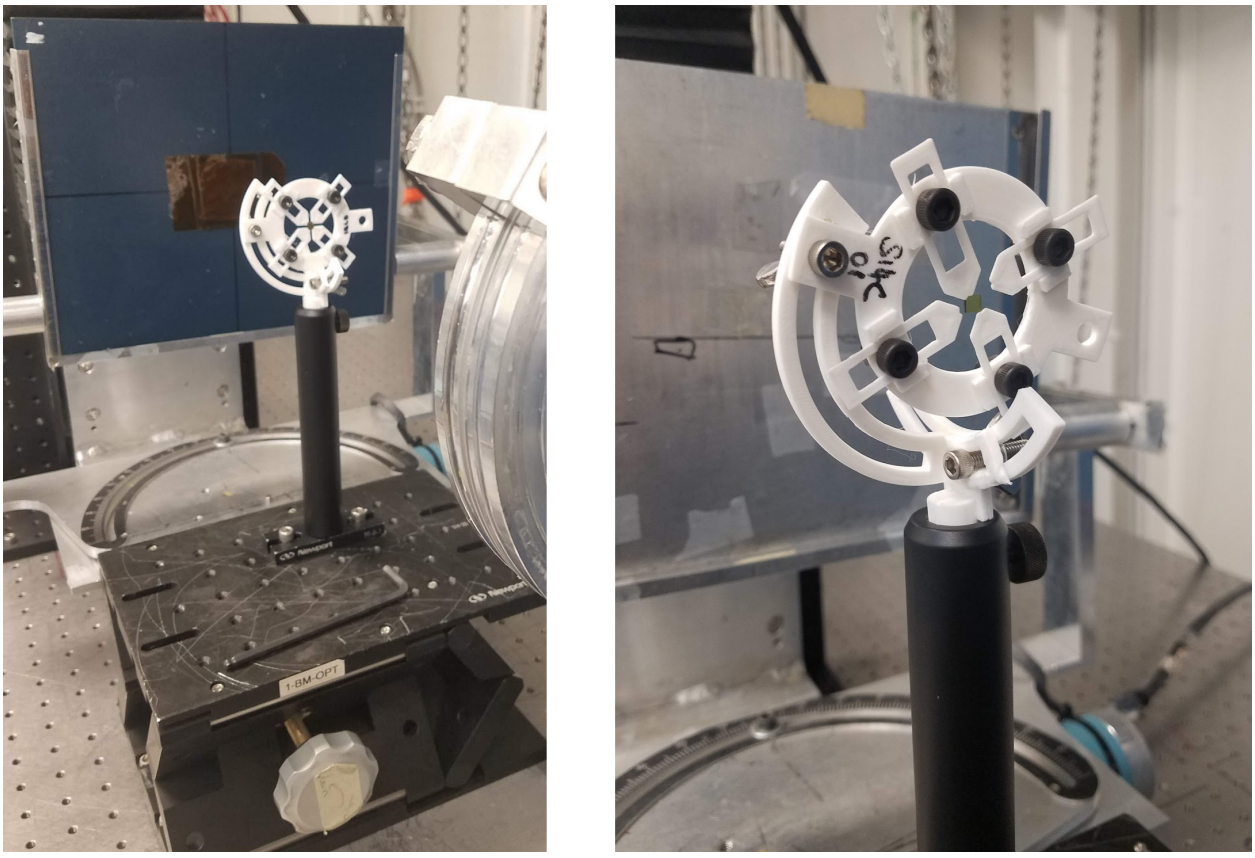

Figure 5.9: 3D printed sample holder design positioned with standard optical table components. Three rotation axes can be readily adjusted for sample alignment with respect to the photographic film.

5.5.2.2 Topograph Indexing

Photographic films set with the transmission geometry at approximately one meter from a single crystal diamond will show Laue patterns which typically include topographs corresponding but not limited to {311}, {151} or {220} planes. The process of indexing the topographs is carried out by scanning the photographic films and analyzing the images with a specialized software designed for this purpose, called LauePt [266]. With this software, the user inputs the crystal structure and lattice constants, in addition to the approximate distance from sample to film as illustrated in Figure 5.10.

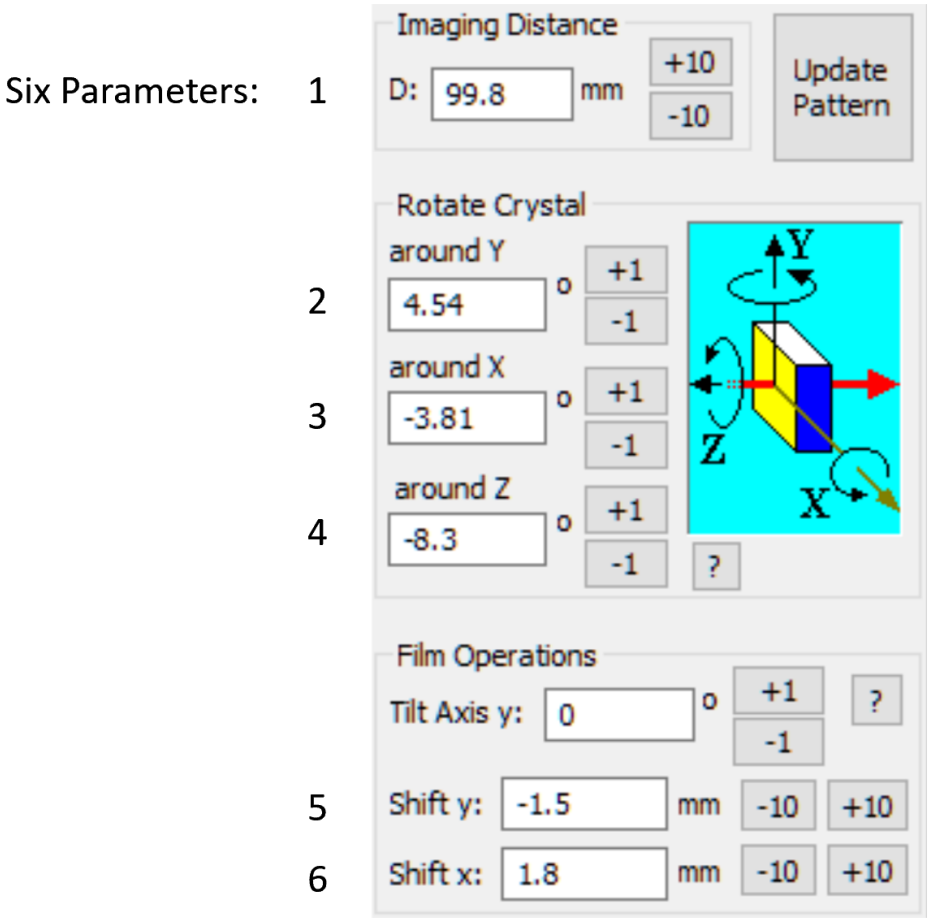

Figure 5.10: Input window in the LauePT software where six degrees of liberty can be set by the user as three rotation parameters, and three spatial parameters to produce a simulated Laue diffraction pattern [266].

By making manual adjustments on relative sample location and crystal rotations in all three axes, the user can compare simulated topograph locations with the measured films. When the simulated diffraction pattern are closely matched with the scanned film based on user input, then the simulated pattern will have effectively indexed each topograph, as shown in Figure 5.11.

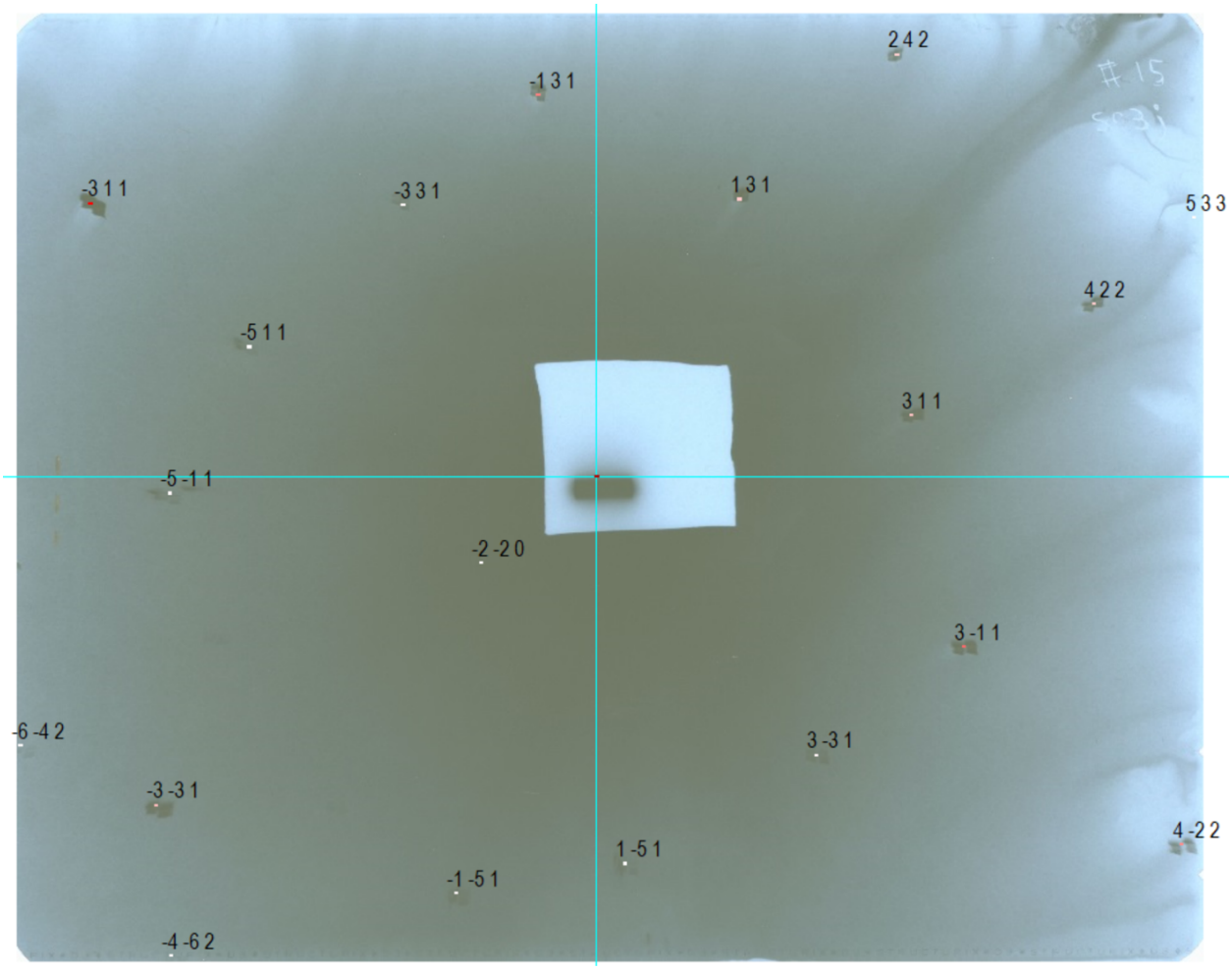

Figure 5.11: Scanned X-Ray topography photographic film where the topographs have been indexed with the LauePT software.

5.5.2.3 Measuring Lattice Misorientation with XRT

In the case of mosaic samples, the lattice misorientation between underlying tiles across the boundary region will produce significantly shifted patterns, as illustrated in Figure 5.12

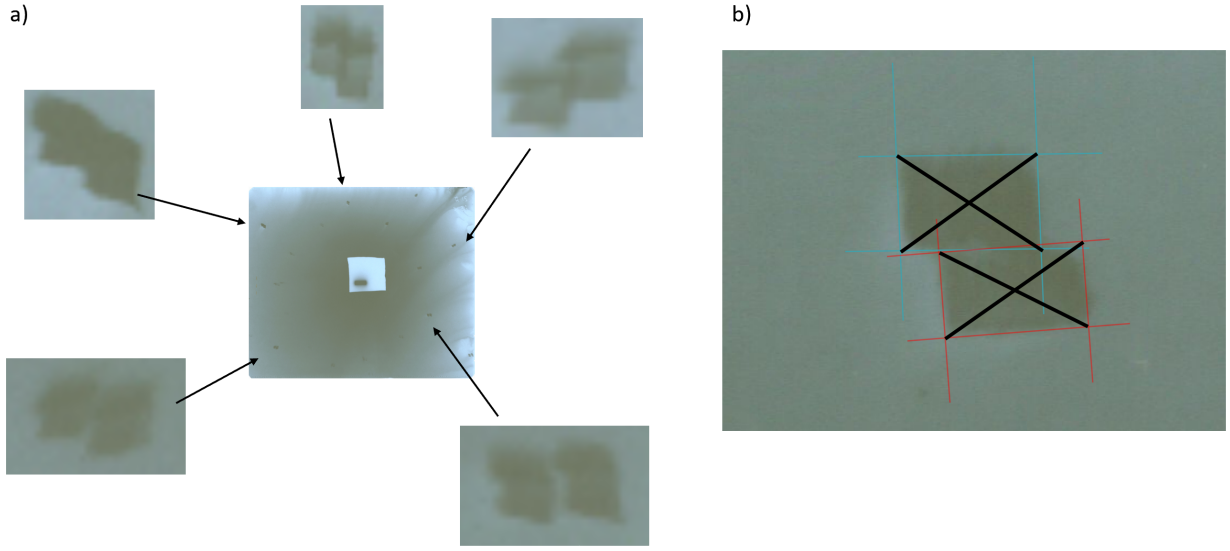

Figure 5.12: a) Constructed example of how topographs measured from mosaic samples can be significantly shifted depending on both lattice misorientations and relative rotation of each crystal plane. b) Centroids can be identified in each individual tile for every topograph.

The relative separation between each tile is measurable, but adjusting six parameters manually is not trivial because on closer inspection, the simulated diffraction pattern does not necessarily match topograph positions with exact precision. This generates uncertainty and bias in manual estimates. Additional development was needed to quantify the relative misorientation for each mosaic sample. The process can be summarized as follows:

1. Index and list available topographs (Software: LauePT). Figure 5.11.
2. Measure relative location of centroids for each tile (Software: Inkscape). Figure 5.12b.
3. Predict topograph locations based on listed planes (Software: MATLAB) Figure 5.13.
4. Find optimal parameter set which minimizes the average distance between measured and predicted centroid locations for one tile (Software: MATLAB). Figures 5.14 - 5.15.
5. Find optimal parameter set for second tile.
6. Relative misorientation for a given sample is the difference in optimal rotation parameters for each underlying tile. Figure 5.16.

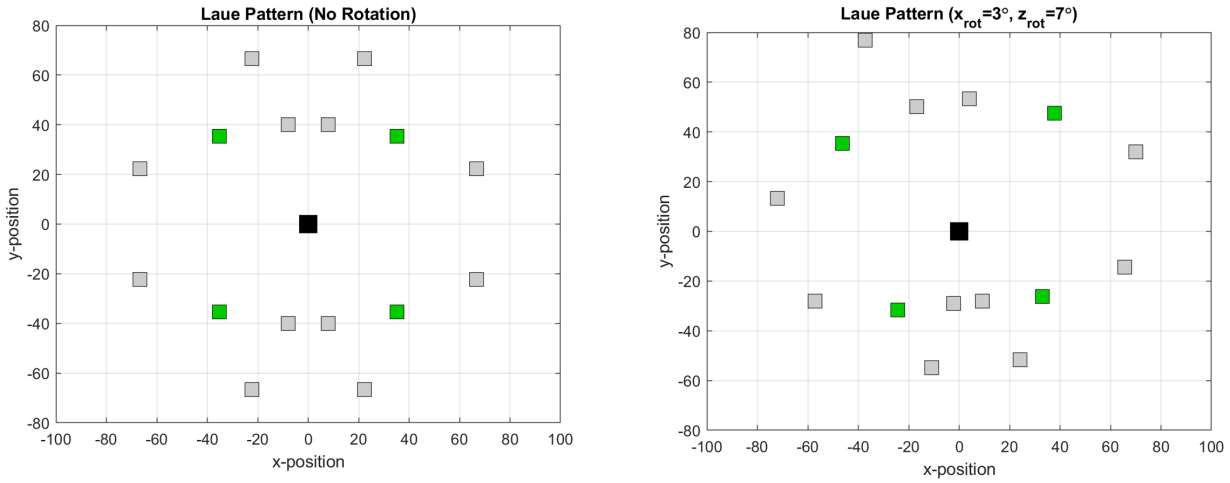

Figure 5.13: Predicted effect on Laue pattern when sample is rotated on two axes. Green markers highlight the topographs generated from the {311} plane family.

The optimal parameter set is defined as the set of position and rotations (D, x, y, r_x, r_y, r_z) that will minimize the deviation from predicted to measured position on the photographic film $\varepsilon_i = \left|\vec{f_i} - \vec{p_i}\right|$ as illustrated on Figure 5.14. The average deviation considers all available topographs i for one of the two tiles.

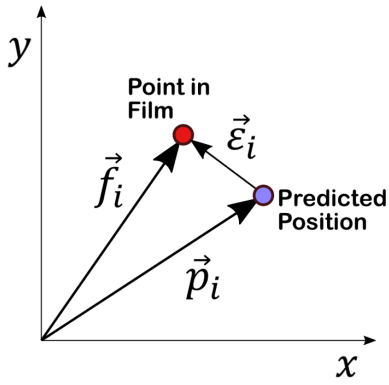

Figure 5.14: The xy plane represents position on the scanned photographic film. The red dot is the measured position of a given tile on topograph i, and the purple dot represents a predicted position given a set of parameters.

The average deviation is minimized in this six dimensional parameter space by successive approximation where the average deviation eventually converges to a minimum as illustrated in Figure 5.15. The process is repeated for the second tile, and the net difference is effectively

the relative misorientation for all three axes in one mosaic sample, as shown in Figure 5.16.

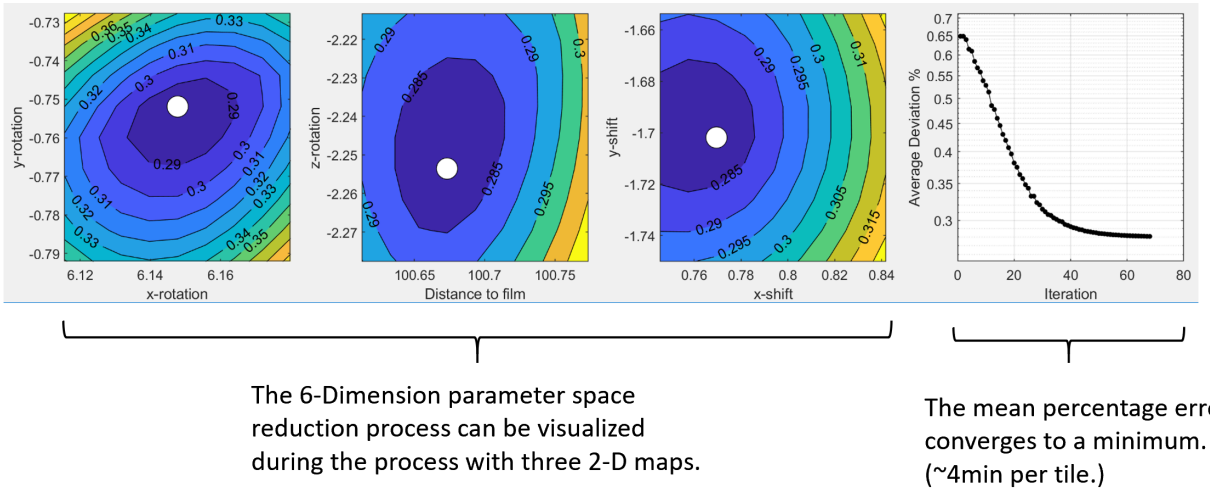

Figure 5.15: Visualizing the process of finding the optimal 6-Dimensional parameter set for one tile.

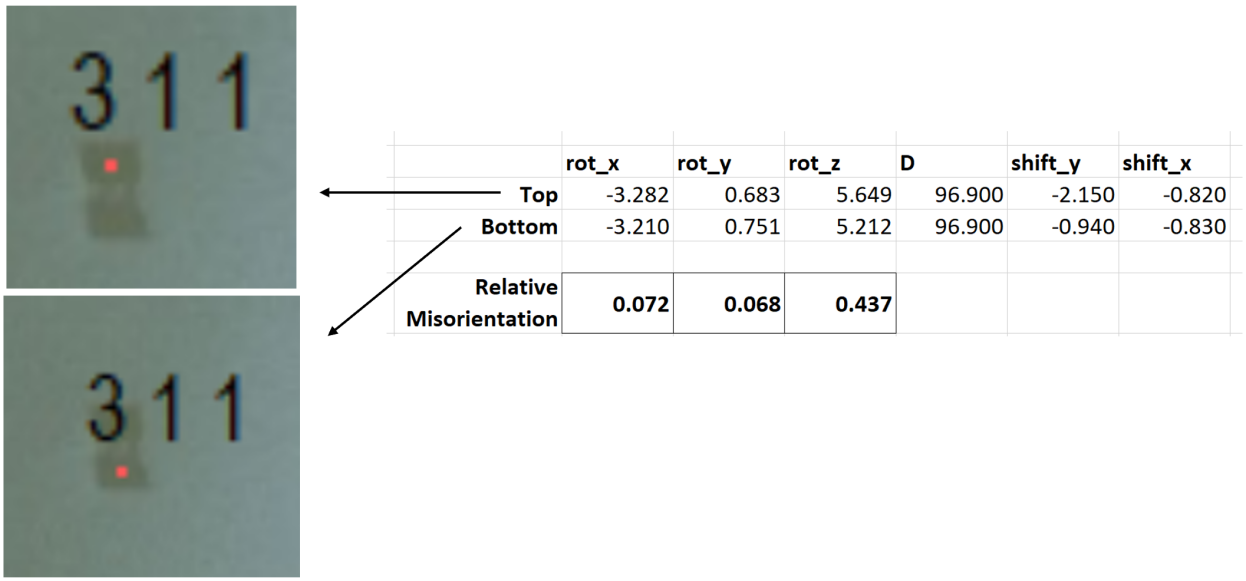

	rot_x	rot_y	rot_z	D	shift_y	shift_x
Top	-3.282	0.683	5.649	96.900	-2.150	-0.820
Bottom	-3.210	0.751	5.212	96.900	-0.940	-0.830
Relative Misorientation	0.072	0.068	0.437			

Figure 5.16: Relative misorientation measurements calculated from the net difference in optimal rotation parameters between both tiles.

The uncertainty of these misorientation measurements is based on the effective shift in rotation corresponding to the width of the diffused edge along each topograph, as illustrated on Figure 5.17, therefore the precision of this analysis method is limited by the resolution of

the scanned films.

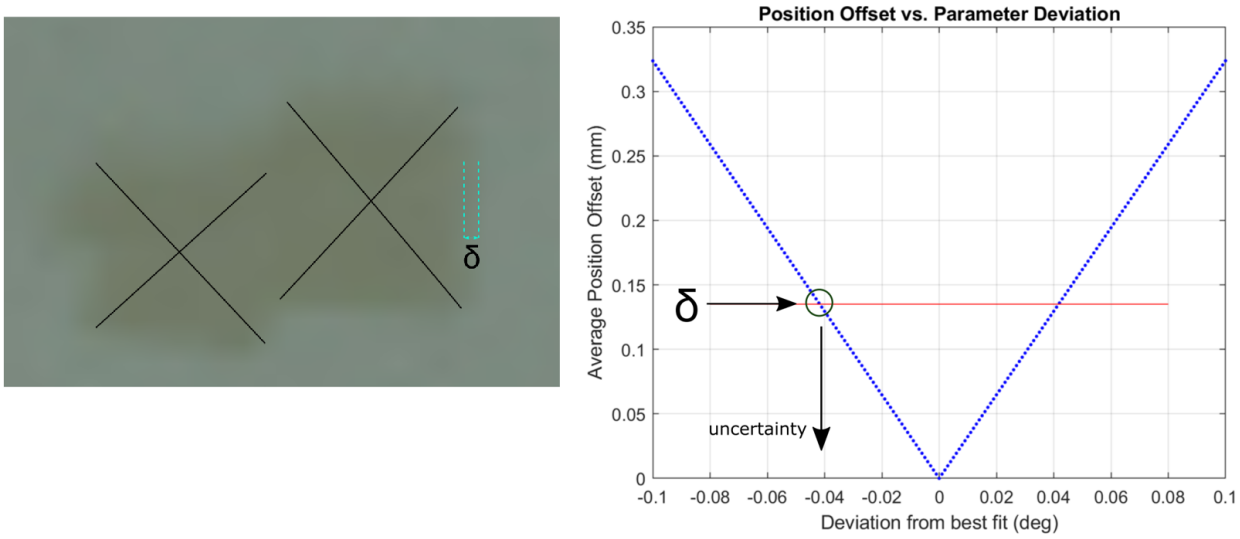

Figure 5.17: Calculating the effective uncertainty in the XRT misorientation measurement.

5.5.3 X-ray Rocking Curve

One method to evaluate lattice quality and orientation is by Xray Rocking Curve (XRC) measurements. The process is an extension on the standard $\theta - 2\theta$ diffraction technique where both the source θ_S and the detector θ_D are swept until the Bragg diffraction condition is met and a peak is observed. Lattice spacing is deduced based on peak locations, and crystalline materials can be identified in the sample. The experimental setup is similar to the XRC technique, but the process begins with a material that is already known, in our case single crystal diamond with an expected $2\theta = \theta_S + \theta_D = 119.51°$ for the {004} plane family when using a Cu Kα1 x-ray with wavelength of $\lambda = 1.541$Å. When the angle between source and detector is fixed, a new measurement can be performed by rocking the sample back and forth by ω as illustrated in Figure 5.18. XRC data from this measurement is stored as a 1D vector representing Intensity vs ω. Values are typically shaped like a single peak

where the intensity of the diffracted beam is highest indicating the sample rotation that corresponds to the average crystal orientation. In a perfect crystal, the width of this peak would be very narrow, but real crystals will be composed of an aggregate of many crystal domains with varying degrees of rotation and small angle boundaries between them. As these variations are pointed in random directions, it is reasonable to suppose that unlike $\theta - 2\theta$ XRD measurements, the resulting shape of XRC data is best described by isotropic Gaussian distributions [267]. The width of this peak is typically measured as the Full Width Half Max (FWHM), the width of the peak measured where the intensity is half its maximum value. This measurement is defined as the Mosaicity of the sample as it describes the statistical mosaic spread of the individual domains. The theoretical width of a perfect single crystal diamond is 3.1 arcsec for {004} planes [268]. The highest quality samples available have been known to be measured within an order of magnitude of this theoretical minimum.

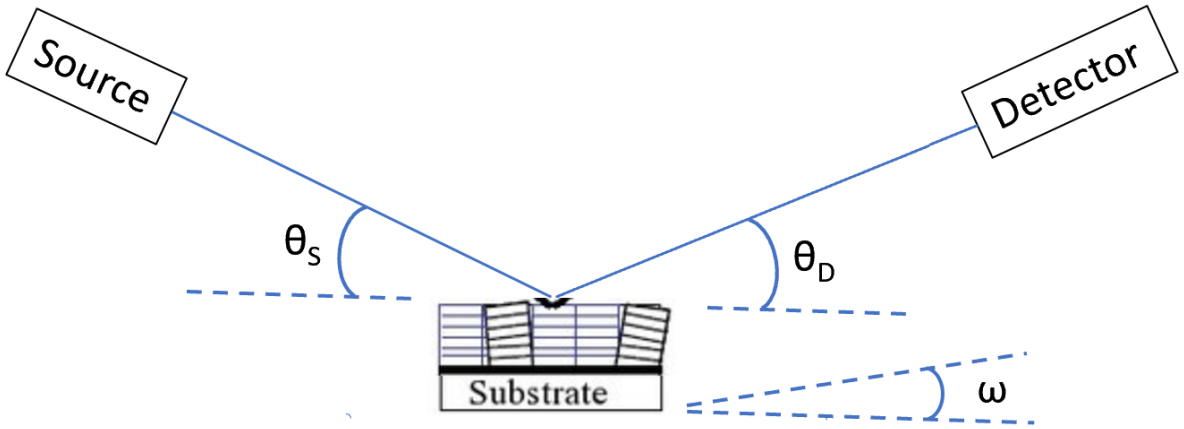

Figure 5.18: Diagram illustrating the XRC measurement setup.

With this XRC measurement, the data not only shows crystal quality, but also average orientation. If the system is set up with a beam spot size smaller than the area of a sample, multiple measurements can be performed on the surface, effectively mapping variations within

the crystal structure, making this measurement technique ideal for analyzing samples grown by the mosaic technique.

The system used to make all XRC measurements was a Rigaku 4 kW rotating anode source with Ge(220)x4 monochromator and 0.5 mmϕ collimator illustrated in Figure 5.19. Rocking Curve scans of the (400) planes with resolution of 0.002° were measured at step sizes as small as 0.1 mm.

Figure 5.19: a) Stock photo of the Rigaku Smartlab system [269]. b)System performing a wide angle $\theta - 2\theta$ scan.

Relative misorientation measurements can be performed directly by comparing peak locations on one tile or the other. The three types of misorientations defined as Tilt and Torsion can be evaluated by performing ϕ=90° rotations, as illustrated in Figure 5.20. Twist-type misorientations are measured by performing a ϕ-scan and comparing the relative rotation

needed to detect {111} peaks in each tile. A wide variety of tools were developed to analyze XRC data measured for mosaic samples, and diamond sample quality in general. These tools will be outlined in detail in Chapter 7.

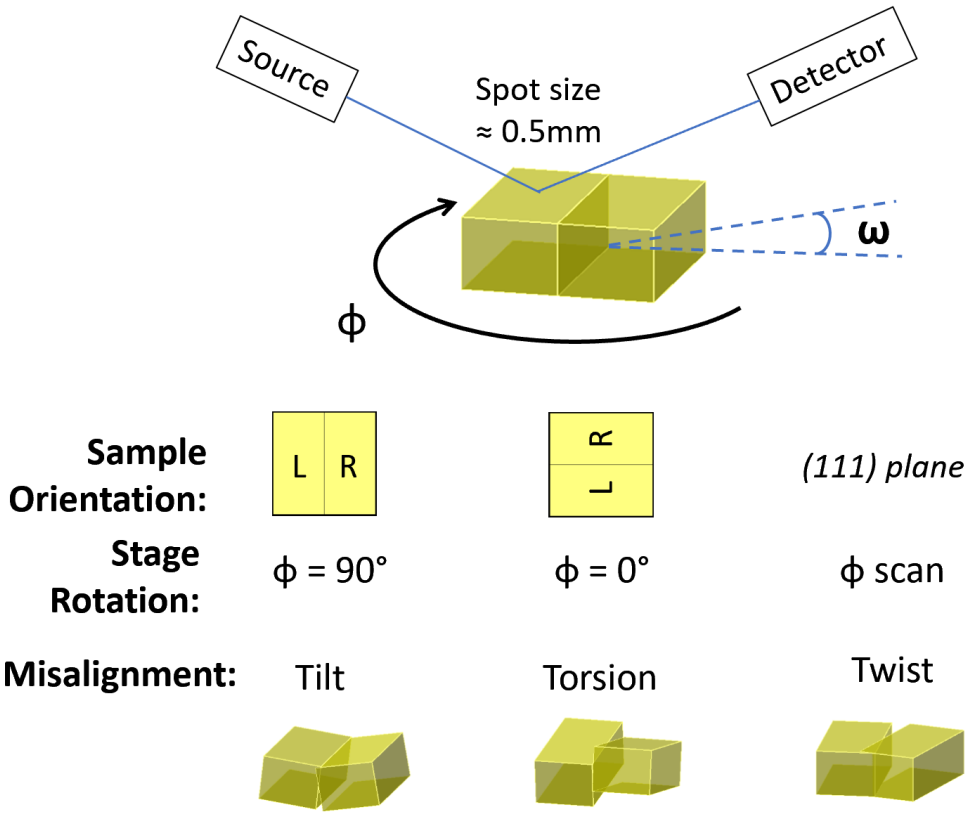

Figure 5.20: a) XRC measurement configurations corresponding to the three defined relative misorientation directions: Tilt, Torsion and Twist.

5.5.4 Offcut Measurement Precision

Relative misorientation measurements are straightforward, as the process only requires measuring the difference in peak locations on a single mosaic sample, but for this project, if two separate substrates were to be tiled together, their orientations must be measured independently.

The ideal offcut measurement process required for this project should be able to reproduce

ω-scans with precision below the width the sharpest peaks observed in single crystal diamond lattices. Samples with the highest crystallinity tends to be observed in high quality HPHT substrates, where (004) peak widths are measured in the range of 30". This corresponds to a resolution of approximately 0.008°. The XRD system used in this project operates with an ω-scan resolution of 0.002°, well below the required range, but the main problem in measuring offcuts with any degree of empirical precision is establishing a set of consistent reference axes.

There are a few factors that need to be taken into account, for example, when the XRD system is initialized, standard steps include a sample and optics alignment process which yields 2θ and ω offsets that will vary as much as a few tenths of a degree if any component in the beam path, including the sample holder, are slightly rotated when swapped or replaced. These offsets are expected to vary between measurement sessions as the system is used frequently by many operators for a wide set of different measurement techniques.

Even if two measurements are taken in the same session, sample placement on XRD holders are also subject to significant variation, in particular when measuring azimuthal rotation. Out of several techniques available which help counter these uncertainties [270–272], the methodology developed for this investigation is based on measuring diamond samples with respect to a silicon wafer back plate. The sample mounting process, illustrated in Figure 5.21, is straightforward. The sample and silicon wafer are both solvent-cleaned, and the diamond sample is pressed flat against the silicon wafer. No adhesives are used between both surfaces. Instead, a clear adhesive tape pressing down on the diamond is stable enough to keep the sample fixed in place. The location is chosen close to the reference orientation notch on the silicon wafer, and the lower edge of the sample is left exposed to measure the angular position of the sample. The pixel density on pictures taken with the available microscope

described in section 5.2.1 can produce measurements with angular precision up to 0.03°.

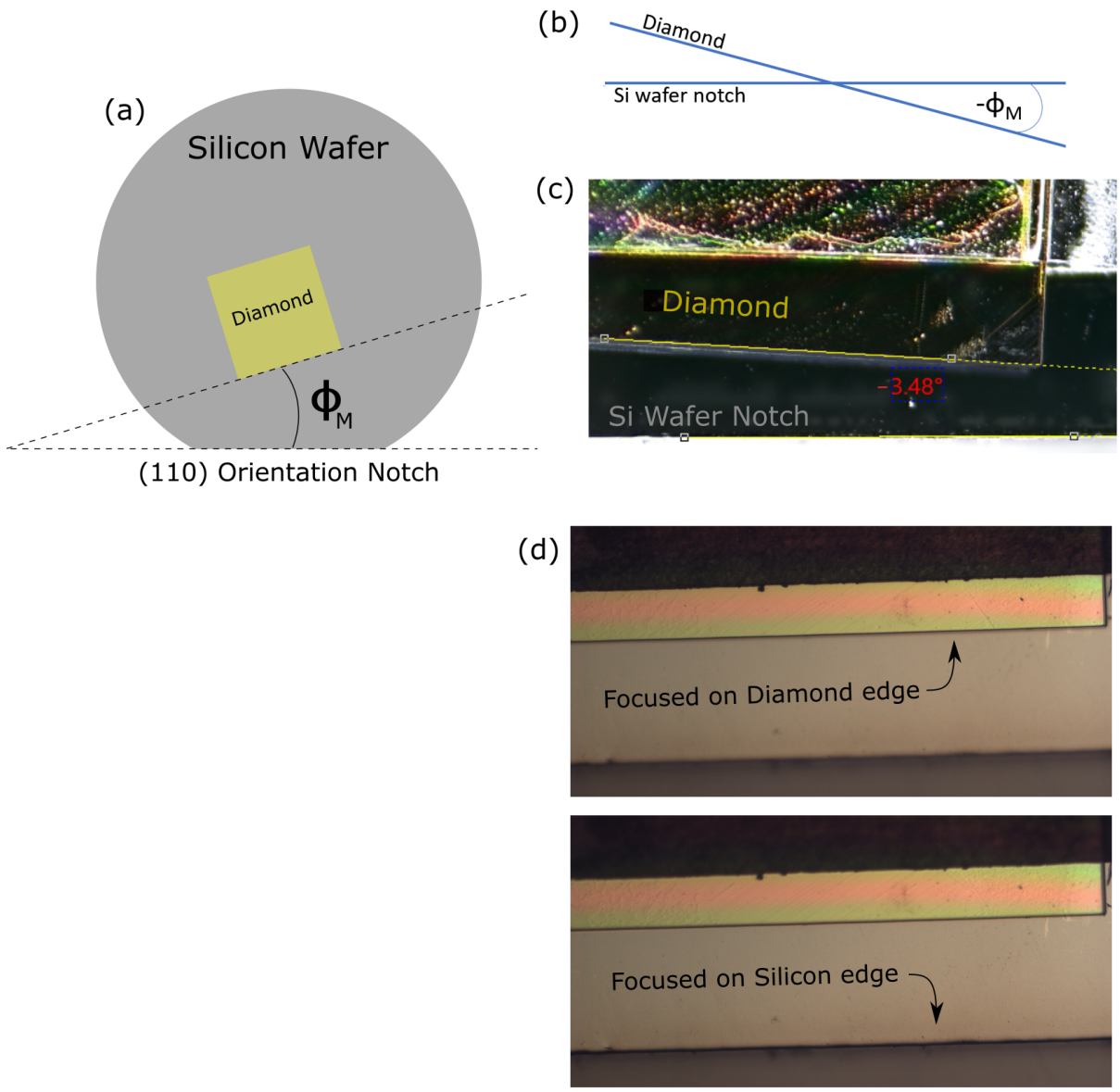

Figure 5.21: a) Diagram showing edge of sample measured relative to the (110) orientation notch on the silicon wafer. b) Reference defined using the standard phi coordinate system. c) Low resolution image illustrating $\phi_M = -3.48°$. d) Actual measurement pictures focused independently on both edges for maximum resolution.

The orientation of the silicon wafer is established by measuring four omega scans of the (004) planes at $\phi = 0°, 90°, 180°, 270°$ to cancel offsets in individual measurements. This

measurement is repeated by rotating the wafer itself in 45° intervals around a full circle. A sine fit over the oscillation of the calculated offcuts with respect to to ϕ was used to find any tilt on the XRD sample holder. The thickness of the wafer was measured to confirm its top and back surfaces are parallel within 0.005°. All these adjustments are combined to establish the silicon wafer (400) planes as fixed and known within a conservative error tolerance of 0.02°. Sample measurements are then as simple as measuring four (004) plane ω-scans for both the wafer and the diamond. The rotation of the (110) planes in both the diamond and the wafer are found by performing two ϕ-scans and solving for the location of the planes relative to the sample itself as illustrated in Figure 5.22 and a screen capture illustrating the MATLAB software designed to automate the process of this calculation and necessary adjustments is shown in Figure 5.23.

Several improvements on this measurement process are being developed which may improve the resolution up by an additional order of magnitude, but the guaranteed precision of the current process is currently below the tolerance limits of the offcut correction step. With these XRD measurement techniques, at their current point in development, orientation measurements are effectively not considered a limiting factor in mosaic sample growth and production.

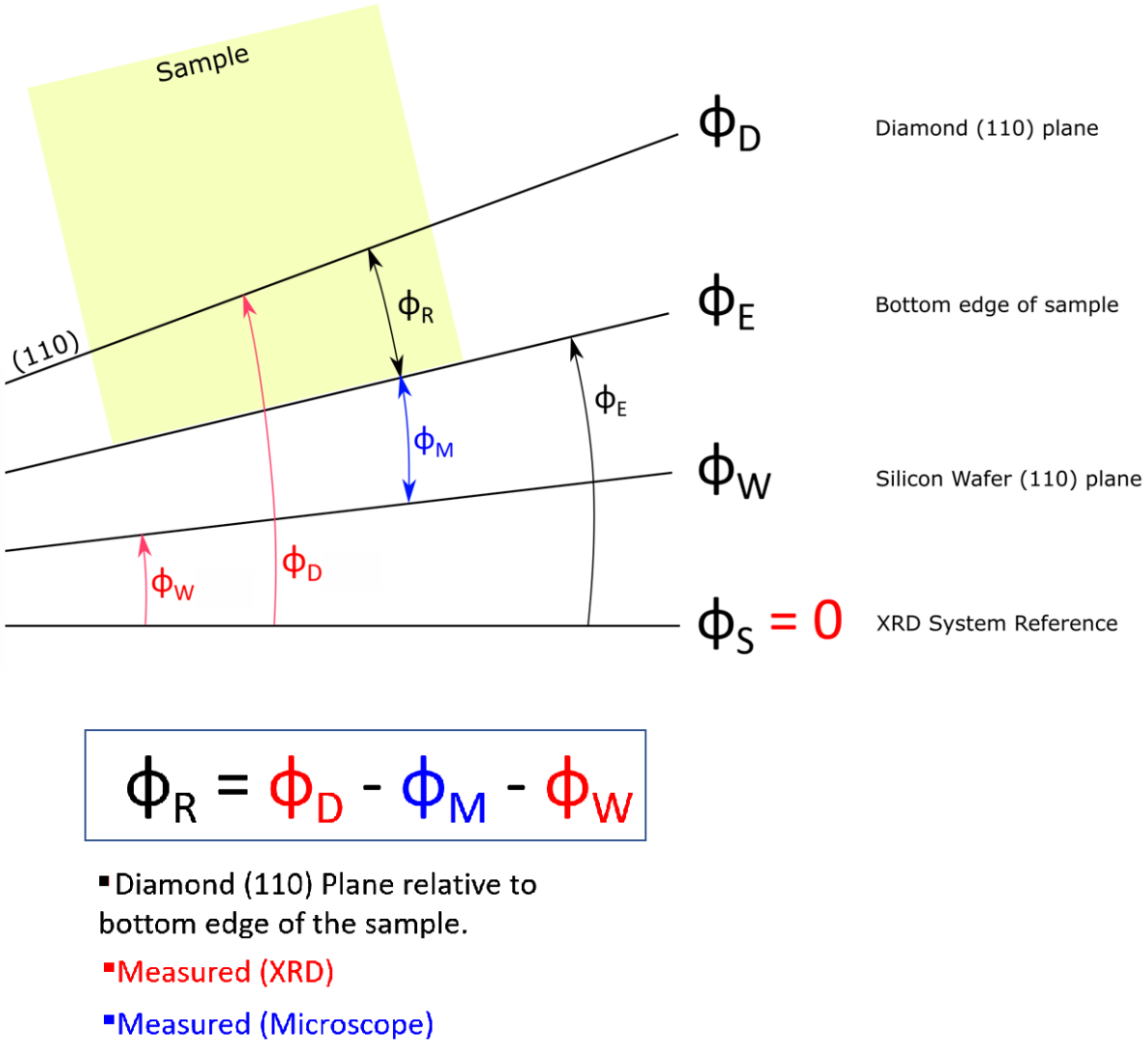

Figure 5.22: Definitions used to solve for the angular position of (110) diamond planes relative to the edge of the sample based on microscope and XRD measurements.

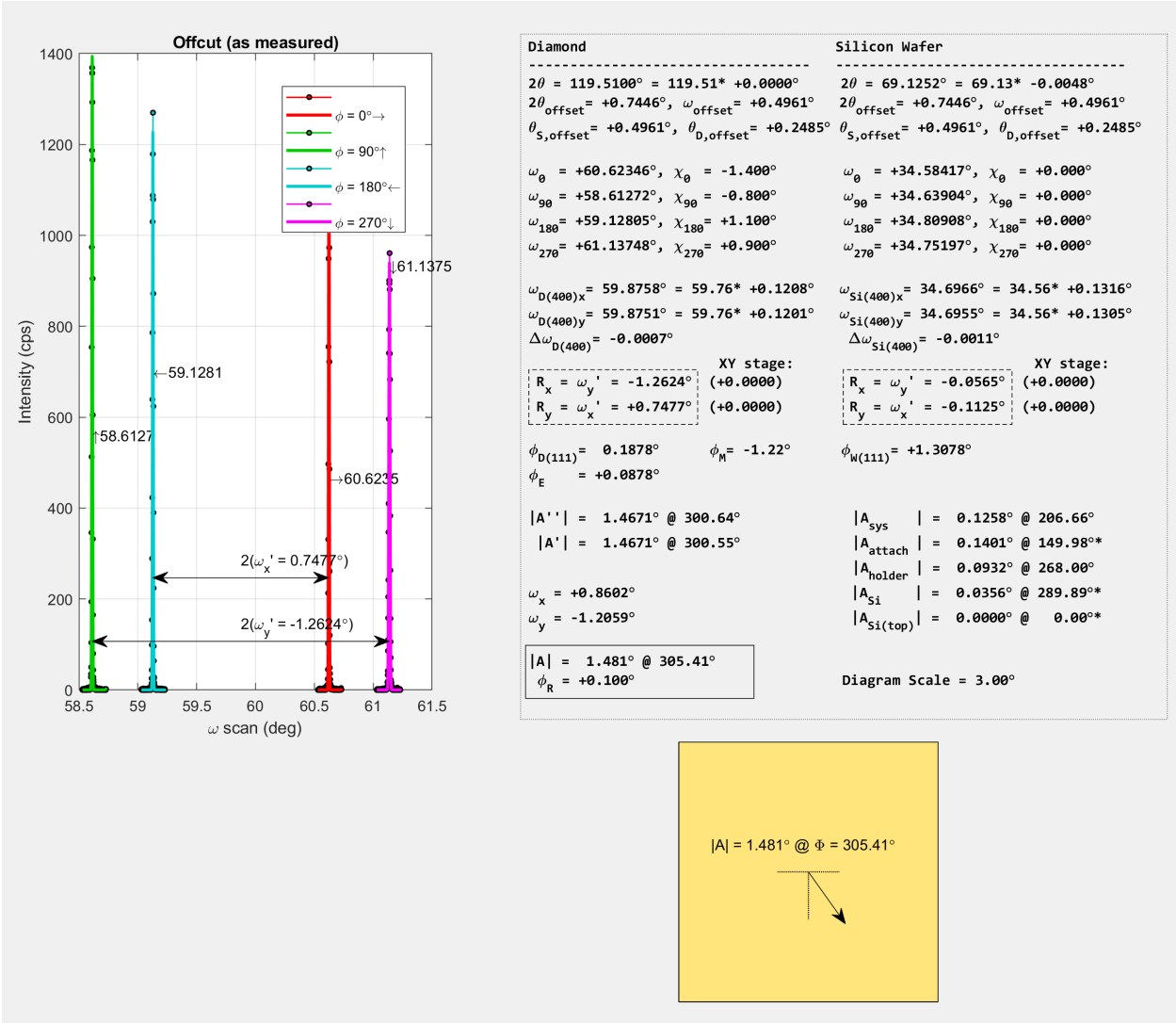

Figure 5.23: Screen capture of MATLAB software developed to measure offcut measurements in single crystal diamond samples based on a silicon wafer back plate.

Chapter 6

Mosaic Seed Assembly

6.1 Mosaic Seed Challenges

If an immediate increase in area is expected from the mosaic technique, the mosaic seed used must be composed of at least two plates not directly produced from the same source. Even when cloning is used to source each tile, they must still be processed to fit together. This includes rotation and height adjustments. When the cloning approach is not available, additional alignment considerations become critical when assembling a mosaic seed.

Before issues with growth parameters are even considered, and before lattice merging mechanisms are explored, the first step is assembling the mosaic seed. This chapter covers the issues that need to be addressed for effective mosaic seed assembly in three main sections. First, lattice orientations must to be defined, followed by a discussion of the process used to modify these orientations in individual tiles. After individual tiles have been adjusted to match both in size and lattice orientation, the last challenge that must be addressed is designing a method to join the tiles together while conserving their alignment. The alignment must be maintained during sample loading on the deposition system; while pumping the system down from atmospheric pressure; and must not be affected by extreme temperature changes as the seed will be ramped up to $\sim$1000°C in a matter of minutes.

6.2 Offcut Definition

A full representation of lattice orientations must require three quantities. Two of these are expressed as angles in the standard notation of defining θ as the maximum tilt of the vector $\hat{n}_A$ normal to the (001) plane relative to the back surface of the sample, and ϕ as the azimuthal direction at which the plane is tilted, as illustrated in Figure 6.1. The third quantity defined for this investigation has been the in-plane rotation of the lattice, represented as ϕ_R and best described as the position of the (110) plane relative to the side facet.

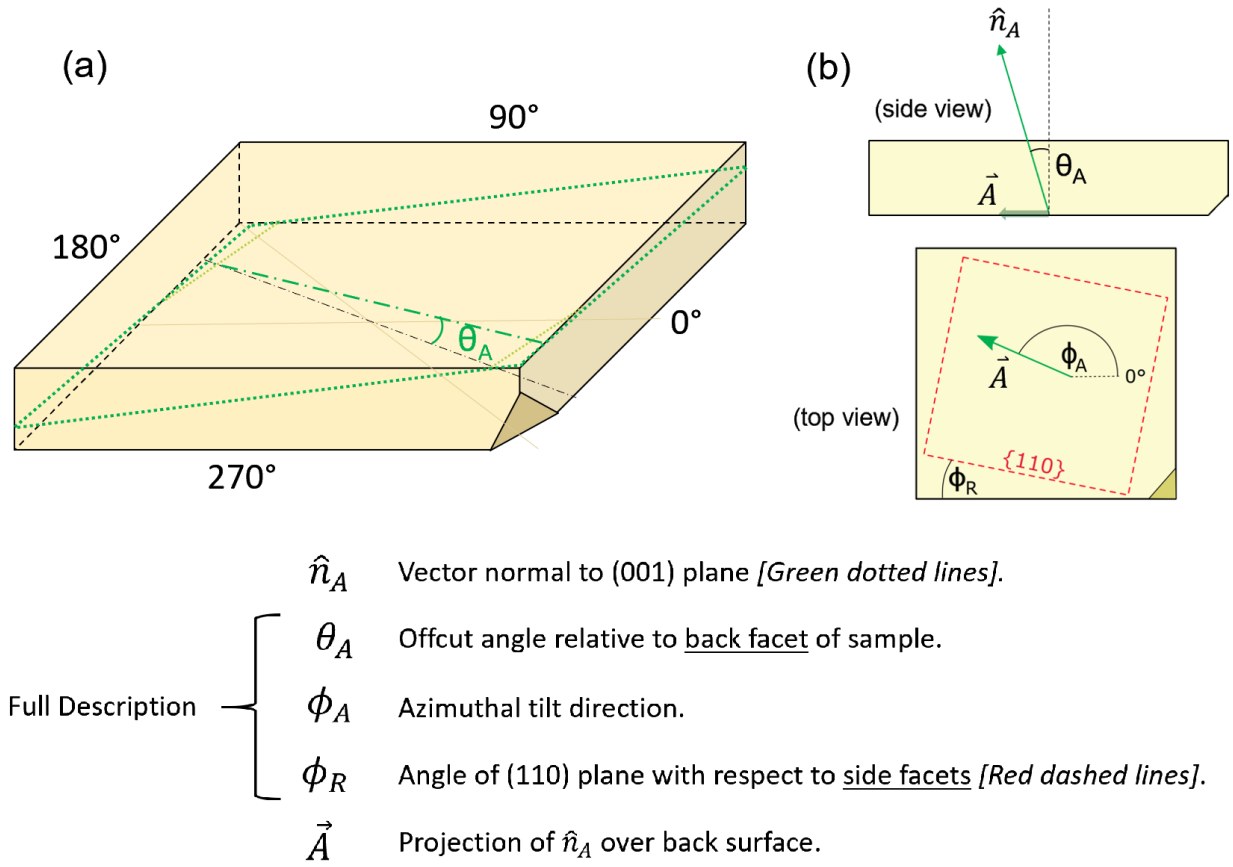

Figure 6.1: a) The green dotted line represents the (001) lattice plane tilted by a magnitude of θ_A in the ϕ_A direction. b) Side view: Cross-section along the phi direction of greatest misorientation. Here, $\hat{n}_A$ is defined as the normal vector corresponding to (100) lattice planes, where $|\hat{n}_A| = 1$ and is tilted by θ_A from the normal vector corresponding to the back side of the sample. Vector $\vec{A}$ is then defined as the 2D projection of $\hat{n}_A$ onto the sample surface, resulting with a length of $\vec{A} = sin(\theta)$. Top View: Illustrates both ϕ_A and ϕ_R.

Note how the standard practice is to cut a corner mark on the back surface to both distinguish it from the top surface and to define the rotation reference as well. Multiple samples can be identified by a combination of two or more corner marks.

This angle rotation of the lattice with respect to the back surface of the sample is defined as the offcut. Note how the offcut is then independent of the angle polished on the top facet. The distinction must be made since this top surface facet is often the angle referred to in some published reports [224, 233]. The convention of using the top facet is not ideal, and could lead to inconsistencies, as it assumes that the back facet is aligned with the lattice. In practice, seed manufacturers provide (100)-oriented samples, but within a tolerance often reported to be as high as 5°. When using the back facet as reference for the lattice, the magnitude of the top facet angle is technically irrelevant.

Figure 6.2 shows a typical example of an offcut measurement. This type of diagram contains all the information needed to communicate the state of the sample when either framing or angle corrections are needed.

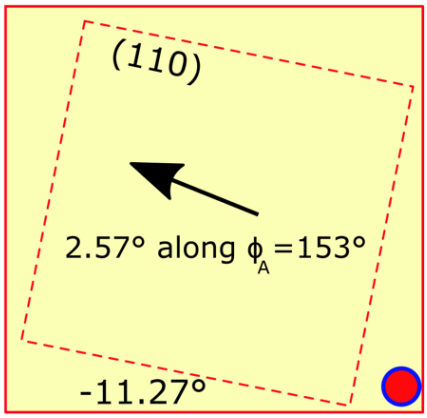

Figure 6.2: Typical diagram depicting all three measurements in a single image. The magnitude and direction of vector $\vec{A}$, as well as the rotation of ϕ_R, can be drawn to scale when comparing two tiles. The red circle in the bottom right corner is used for reference, representing the location of the sample corner mark in the back surface.

6.2.1 Step-flow Growth Direction

Step bunching, as discussed in Section 2.3.3.2 clearly shows that the lateral step flow growth direction will proceed in the direction of the relative inclination of the top facet. It must be noted, however, that given the offcut definition used in this study, the direction of the step flow growth will effectively progress in the opposite direction of the offcut vector $\vec{A}$ as illustrated in Figure 6.3.

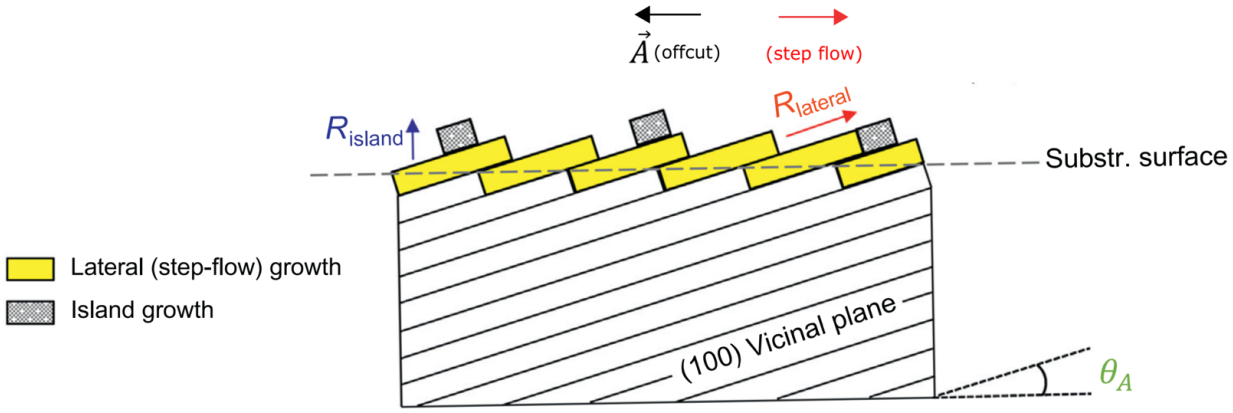

Figure 6.3: Diagram illustrating how the step flow growth proceeds in the direction opposite to the offcut. Image adapted from [208].

6.3 Orientation Adjustments

6.3.1 Offcut Adjustments

The next step after completing offcut measurements on multiple samples is adjusting the orientation on at least one of the tiles to match the other. Following the offcut definition, offcut adjustments can only be produced by removing material from the back side of the samples. The hardness of diamond implies that the only ways to achieve this is by either laser cutting, or by extending the process normally used for polishing diamond substrates.

Target orientations are obtained as the product of vector addition calculations. Figure 6.4 illustrates a visual summary on the steps that must be performed to produce desired changes in offcut directions.

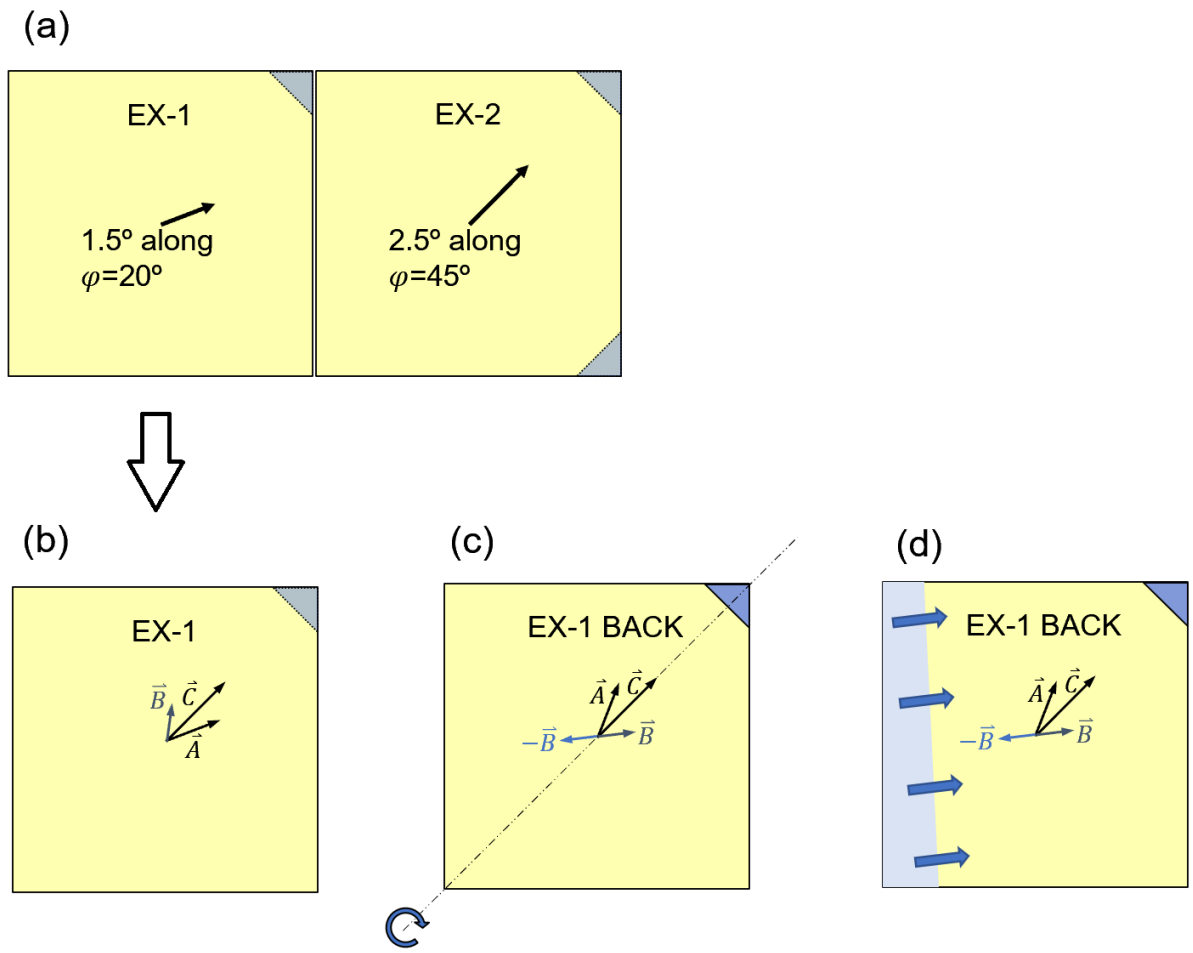

Figure 6.4: a) Surfaces of tiles EX-1 and EX-2. The offcut adjustment operation in this example consists of polishing the bottom surface of EX-1 to crystallographically align it with EX-2. b) Vector $\vec{A}$ represents the existing offcut of EX-1, and vector $\vec{C}$ represents the target offcut of tile EX-2. Vector $\vec{B}$ is then the correction operation that must be applied to the back surface. c) Tile EX-1 flipped over at its diagonal. d) Progression of new facet as observed during the polishing process.

6.3.2 Phi Rotation Adjustments

Phi rotation corrections are more efficiently carried out by laser ablation. One strategy explored in this study, as discussed in section 3.6.5 to avoid cracking on the interface, was to deliberately rotate the lattice relative to the interface direction. A typical adjustment based on a sample framing step is illustrated in Figure 6.5

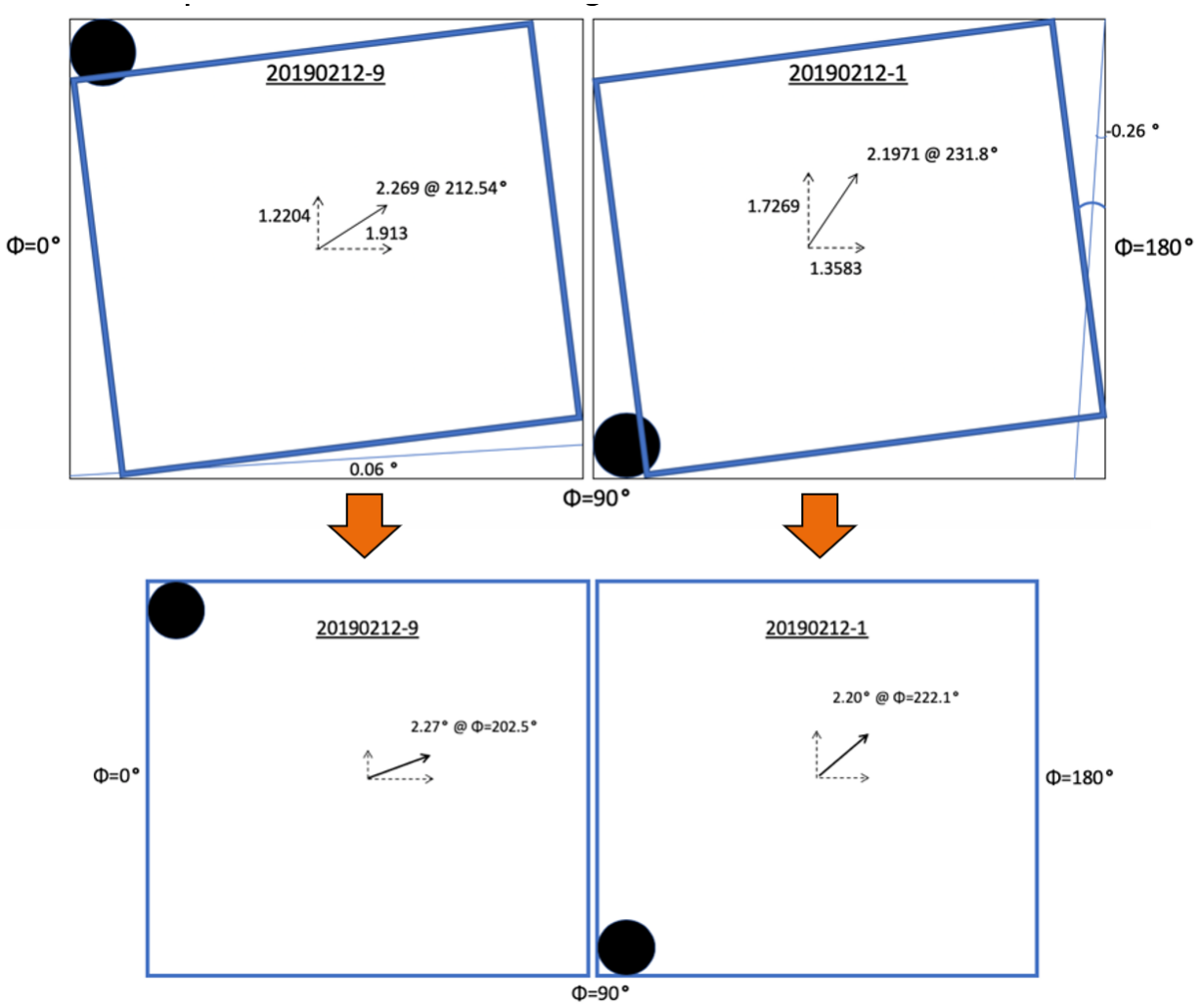

Figure 6.5: Typical rotation correction on two samples. The rotation angle is selected such that both offcuts are better aligned, and the (110) plane is significantly misaligned from the interface.

The (001) plane orientation offcut is mainly affected by adjusting the back facet, and the (110) rotation is mainly affected by framing, but as defined, both transformations are not

orthogonal. Adjusting the offcut will rotate the direction of the (110) plane, and rotating the sample by framing, will affect the offcut direction. Another factor to consider is when the side facets are not polished at 90° from the back or top surface. This condition has the effect of translating the reference angles as illustrated in Figure 6.6.

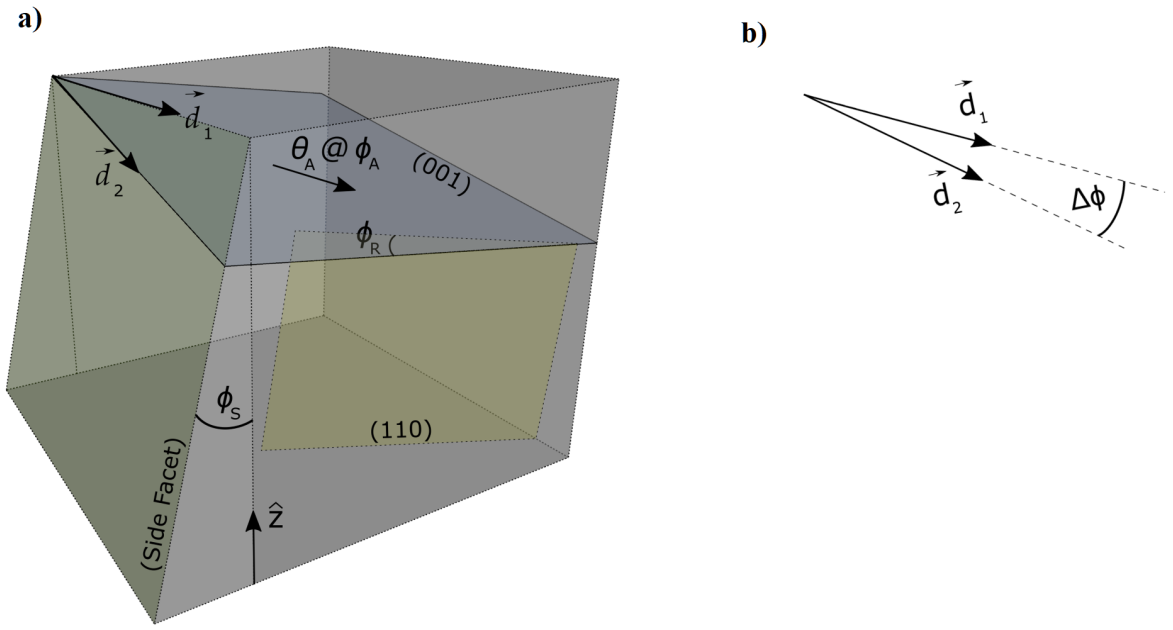

Figure 6.6: a) Angle and vector definitions using a 3D model using the back facet as reference. This figure adds a new angle ϕ_S to describe a potential tilt on side facets. $\vec{d_1}$ and $\vec{d_2}$ represent the top edge direction, and the intersection of the side facet and (001 plane) respectively. b) Projection of these two vectors as observed from the -$\hat{z}$ direction. This offset will affect measurement interpretations for both ϕ_A and ϕ_R and must be considered for high precision adjustments.

Offcut adjustments typically require several iterations of measurements and corrections, but by applying the definitions and list of corrections discussed in this chapter, the seed adjustment process has been established as a streamlined set of clearly outlined steps.

6.3.3 Precision in Offcut Corrections

Standard diamond polishing systems are not equipped to control angle corrections with fine precision. The modification needed to be able to make the small corrections required for this project was upgrading the coarse adjustment screws in the sample holders with micrometer screw gauges to allow fine-tuning. This back side polishing process has been refined over time such that net adjustments can be consistently achieved within 0.1° of target orientations.

Additional improvements are being developed to increase the precision of this process even further, but the level of control obtained with the current setup is still greater than the tolerance limits achievable in current frame production capabilities. Offcut adjustment techniques at their current point in development, just like the XRD measurement process, are not considered limiting factors in mosaic sample growth and production.

6.3.4 Facet Corrections

In addition to offcut and rotation corrections, other adjustments need to be considered when preparing tiles for mosaic assembly.

6.3.4.1 Framing

Framing, for example defined as applying a rectangular cutting profile to remove unwanted edges on a potential seed is another typical adjustment. Framing is usually needed for the first step to establish a clear reference angle, and as the last step to eliminate side facets generated during the offcut adjustment process. Figure 6.7 shows an example of tile framing after a growth step.

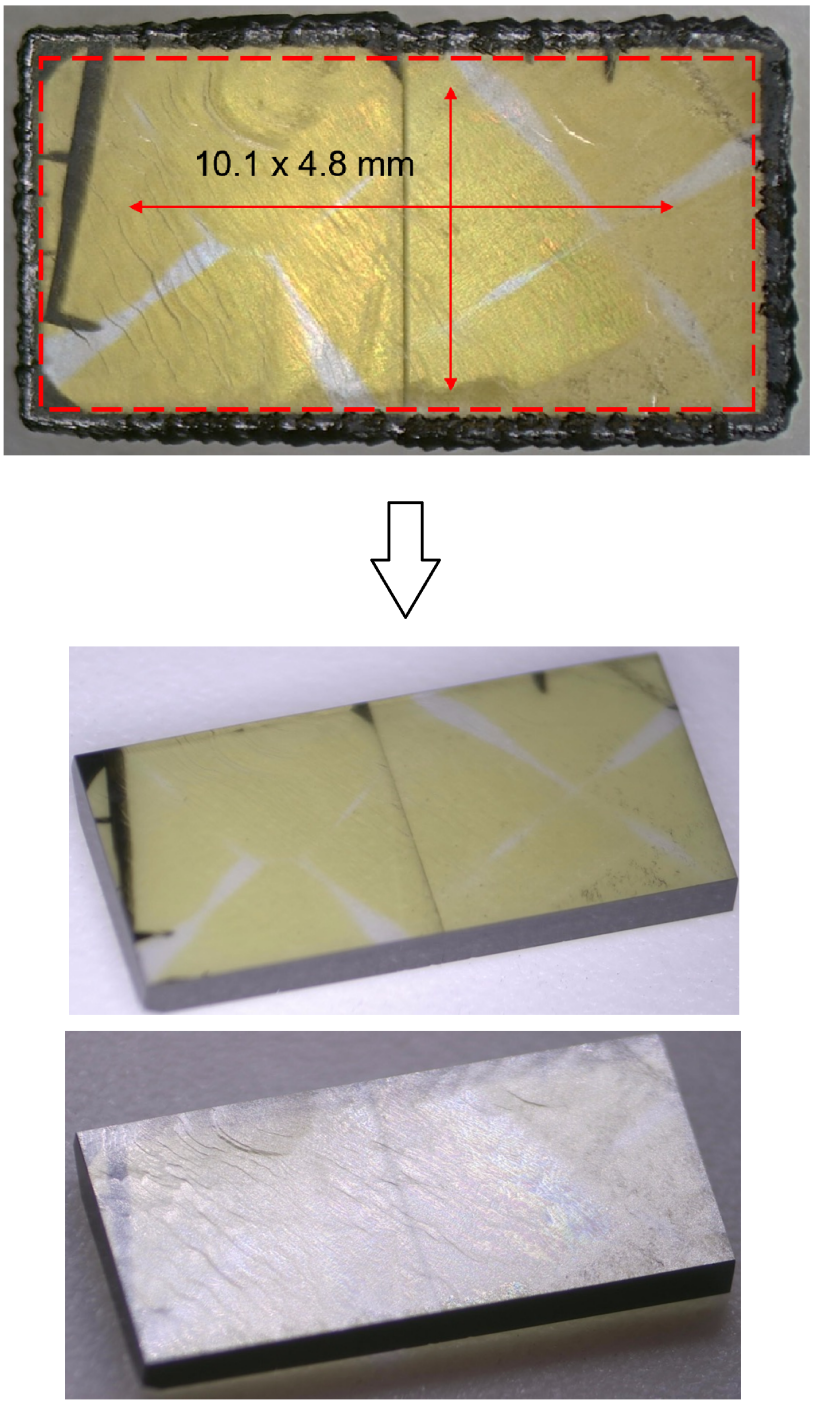

Figure 6.7: As grown mosaic sample with rough edges framed as outlined with the red dashed rectangle. Two pictures of the framed plate under different lighting conditions show the resulting state of the sample, ready for regrowth.

6.3.4.2 Tapering Inner Edges

The inner edges are typically polished with a taper, such that the point of contact between the tiles is ensured to be on the top surface as shown in Figure 6.8, with the end result showing smooth top edges in Figure 6.9.

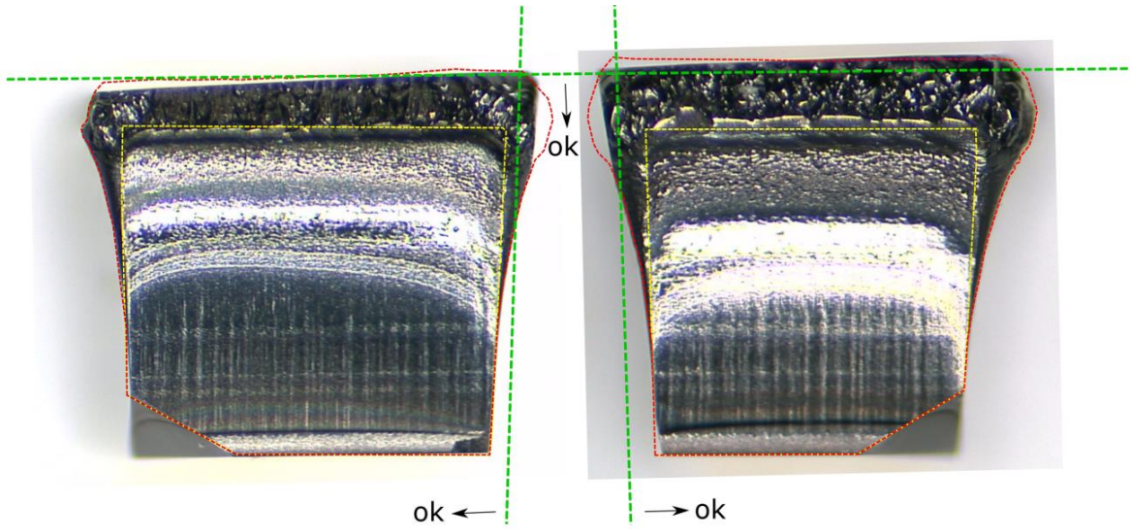

Figure 6.8: Side view of two tiles being prepared for mosaic assembly. Green lines show planned polishing planes and polishing directions. Arrows indicate a wider taper is expected. The yellow and red line overlays indicate sample outlines under previous seed, growth and polishing steps.

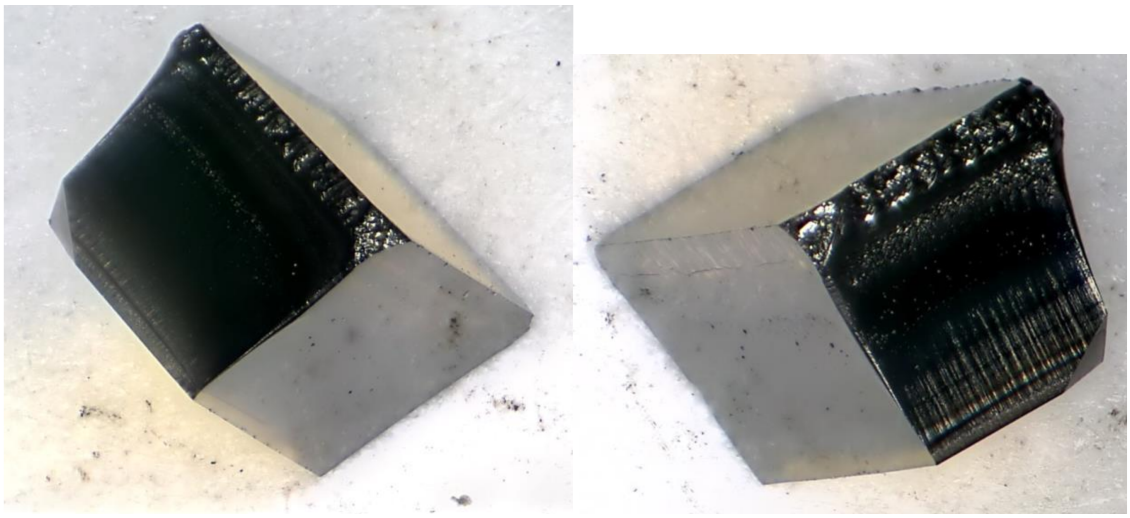

Figure 6.9: Smooth inner facets and top edges for both tiles.

6.3.5 Planarization

Before assembling the offcut corrected tiles, care must be taken such that all adjacent tiles have the same height, or at the very least, if tiles are not perfectly parallel, they should have the same height at their interface. The step used to achieve this result was to fix both tiles together in the polishing holder so they can be planarized simultaneously. Figure 6.10 captures the standard UV-curing step used to fix samples together for planarization.

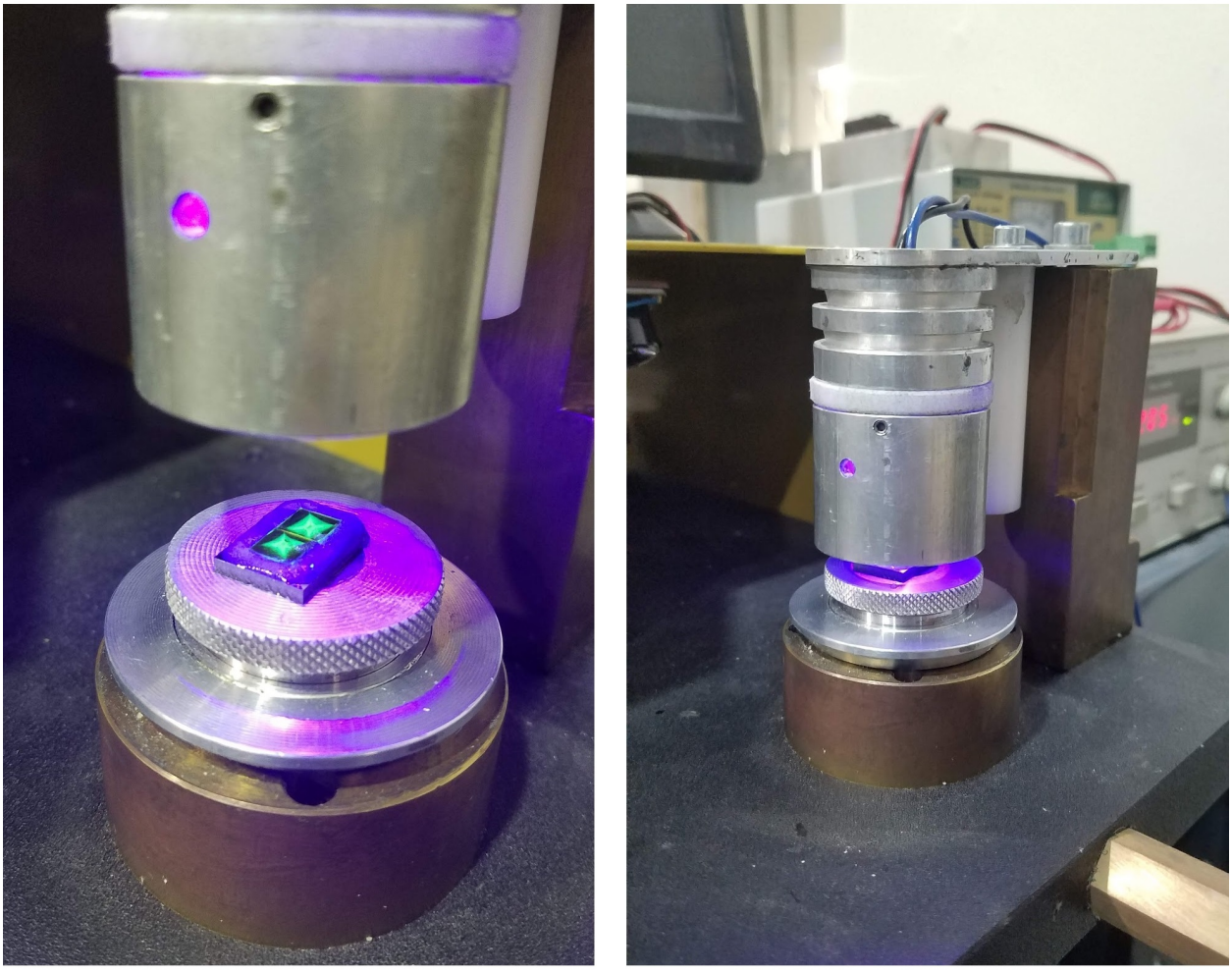

Figure 6.10: Two tiles held together as the resin is hardened with UV light in preparation for the planarization step.

6.4 Seed Alignments

Once individual tiles have been adjusted, a mechanism has to be developed to constrain all tiles together. This mechanism should be rigid enough to maintain all tiles together during sample loading and it should remain stable during ramp up, where the temperature is programmed to increase by hundreds of degrees per minute. The structural integrity of this assembly should be able to stay consistent during the process.

6.4.1 Polycrystalline Frame and Plate Assembly

The strategy developed for this investigation has been to prepare a laser cut frame to exact dimensions such that all tiles are held together as illustrated in Figure 6.11. This frame does not have to be thick. Most of the frames cut for this investigation were sourced from 50 µm thick plates. The inner dimensions of this frame should match the width of the mosaic tiles, and the outer dimensions should fit inside the molybdenum sample holder. The material selected for this frame is polycrystalline diamond to avoid potential issues of thermal mismatch as the temperature increases, and to avoid introducing any foreign elements into the pocket or deposition chamber.

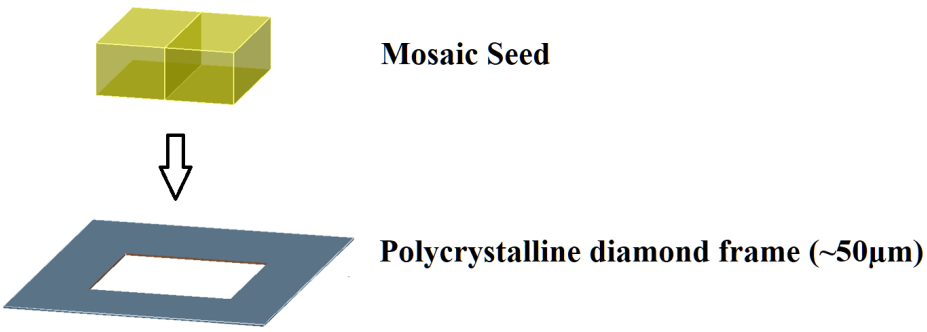

Figure 6.11: Polycrystalline diamond frame used to hold together two mosaic tiles.

Figure 6.12 illustrates an example of a frame with graphitic residue near recent cuts. Figure 6.13 shows a frame with an oversized pocket after acid cleaning.

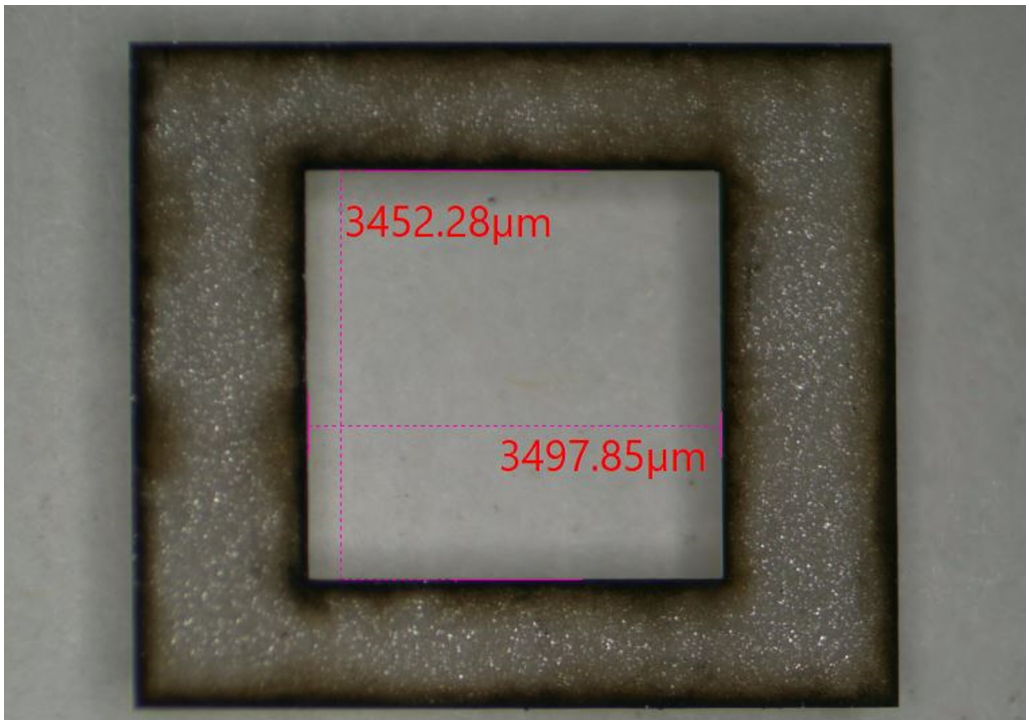

Figure 6.12: PCD frame with graphitic residue from the laser cuts.

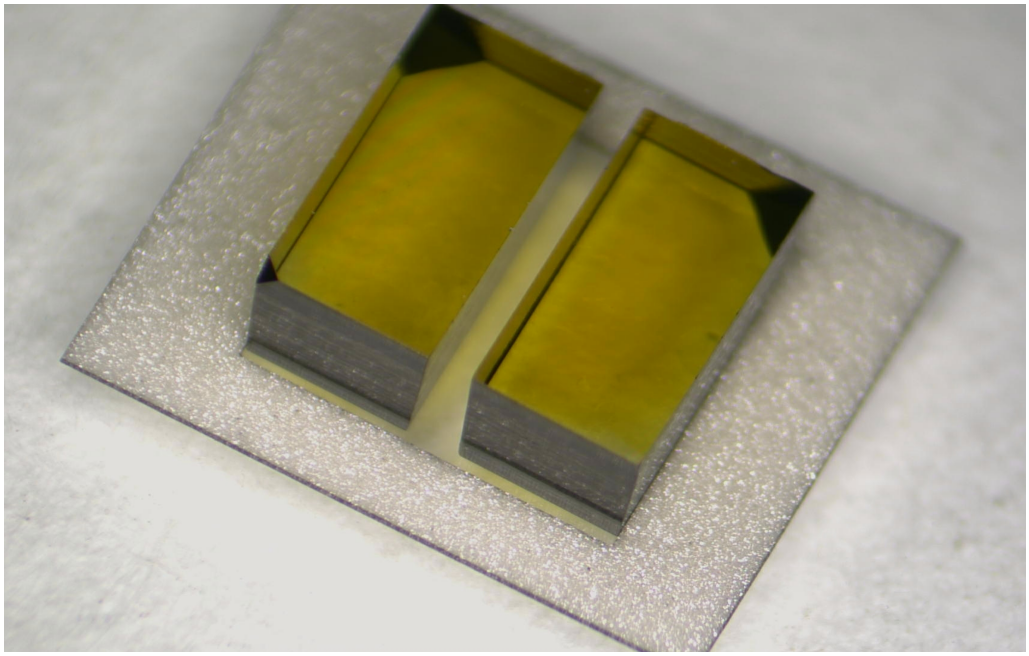

Figure 6.13: Two tiles measured on an oversized pocket used as reference.

The size of the inner pocket can be controlled with considerable precision after a few iterations and precise measurements. Gaps as small as 5 µm are achievable, as illustrated in Figure 6.14.

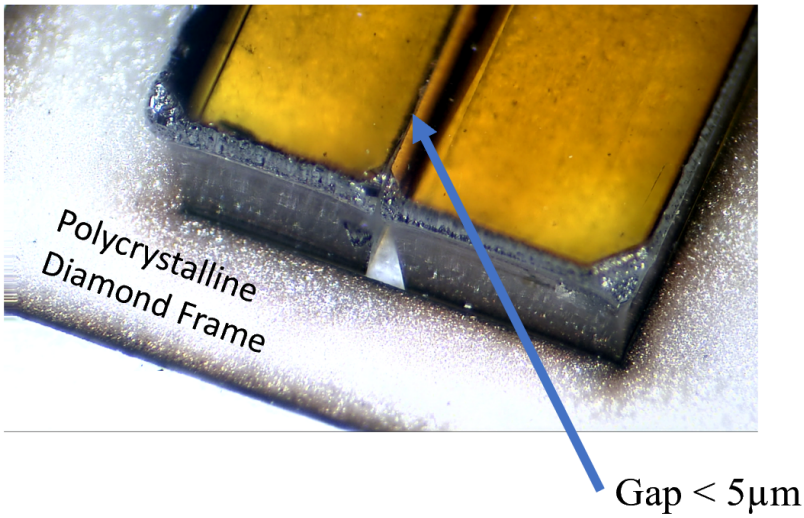

Figure 6.14: Diamond frame cut to precision, where the gap measures less than 5 µm.

The final component in the mosaic seed assembly is needed to address the problem of how the bottom surface in the molybdenum pocket holder is not guaranteed to be flat. The solution to this issue has been to add an additional polycrystalline plate below the frame. When this assembly is considered in terms of the three types of misorientation, the bottom PCD plate minimizes the risk of Tilt and Torsion, while the PCD frame minimizes the risk of Twist-type misalignments between individual tiles, as illustrated in Figure 6.15.

With the samples secured by the PCD frame and plate, the mosaic seed is ready for deposition. An example ready to be loaded in the system is illustrated in Figure 6.16. Given how this approach for handling mosaic assemblies has proven very effective, an international patent has been filed with MSU which covers this and several other technologies developed during this project to manufacture large area single crystal diamond substrates [273].

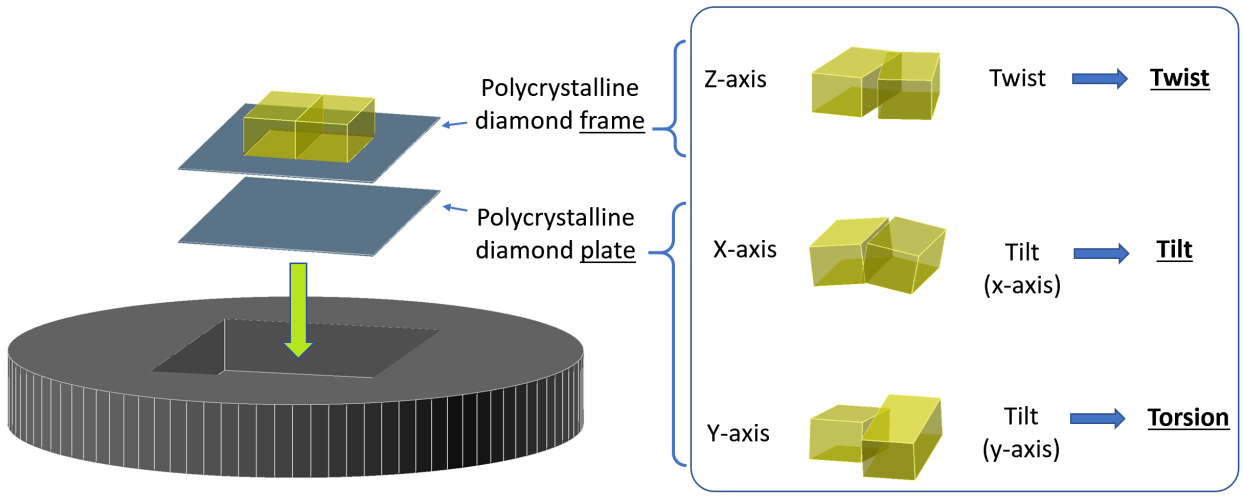

Figure 6.15: Three misorientation types on mosaic samples under control by a polycrystalline diamond frame and a polycrystalline plate.

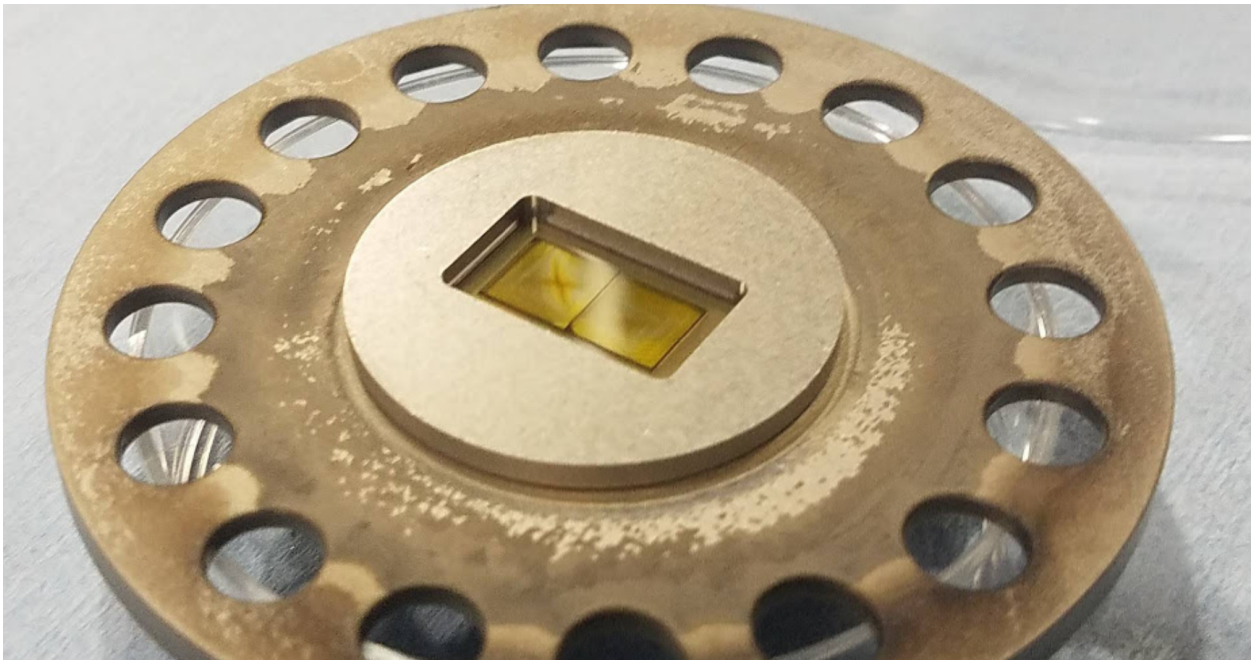

Figure 6.16: Mosaic assembly ready for loading into the deposition system.

Chapter 7

X-Ray Diffraction Analysis Tools

7.1 Introduction

Lattice orientations are expected to remain constant under ideal diamond epitaxy, but preliminary experiments show that this is not always the case. Orientation measurements on grown samples have been observed to be much more dynamic than originally expected. Studies covering this behavior have been very limited in both detailed descriptions or how these changes take place as new layers are grown.

The first observation over mosaic grown layers is how relative changes in orientation tend to differ from one tile to another within the same substrate. In addition to this effect, orientations and even overall mosaicity of each measured point is highly dependent on the position relative to mosaic interfaces. Additional factors need to be taken into account when areas are increased, such as lattice bending due to temperature non-uniformities during the deposition process. All these interactions and dynamic boundary mechanisms must be explored in greater detail. This chapter outlines the software tools that have been developed during this investigation. These tools were mainly designed to quantify some of the effects related to lattice merging dynamics. This information has been used to improve procedures leading towards smooth boundaries in mosaic samples.

Collected data from experiments frequently required additional definitions, analysis, and measurement techniques. This chapter is structured such that each section can be considered a series on how each tool and underlying concept was developed.

7.2 Multiple Peak XRC Analysis

X-ray Rocking Curve (XRC) measurements, as discussed in Section 5.5.3, quantify the statistical mosaic spread of individual domains as a direct measure of how their orientations randomly deviate from a macroscopic average. Measured XRC curves tend to follow standard Gaussian distributions as would be expected from random deviations from a perfect crystal structure. If the examined region contains two or more dominant orientations, then multiple peaks are distinguishable on XRC scans. Some examples of this effect can be found when:

- A crystal is cracked.
- There is a small angle grain boundary from an underlying defect or dislocation.
- Early stages of uncontrolled polycrystalline growth emerge from a single crystal seed.
- The measured region covers two separate single crystal seeds simultaneously.

When measuring grown mosaic samples, all the conditions listed above can generate multiple peaks. Surface measurements shows some of these effects can gradually increase as boundary regions or any sample edges in general are approached. Therefore, after criteria are established to determine when wide peaks can be deconvoluted into separate crystal orientations, this section covers additional analysis needed to quantify XRC data containing multiple peaks.

7.2.1 Peak Deconvolution Parameters

When a curve fitting algorithm is applied to experimental data, and multiple peaks are a possibility, some constraints need to be applied to find reasonable peak deconvolutions. The Gaussian curve fit model is based on the MATLAB peak fit function [274]. Applied to these XRC measurements, the peak width ranges have been set at a minimum of 10", or approximately 0.0028°. This value falls just below the highest quality HPHT diamond samples measured in the project, and also covers peak widths on standard quality silicon wafers used for reference orientations. The maximum peak width was set at an arbitrarily large number, but XRC peaks on diamond very rarely exceed a mosaicity larger than 0.5° with significant intensity. The maximum number of peaks was set at $N = 6$ to cover the possibility of multiple cracks on the central region of four-tile mosaic samples.

The next parameter that must be considered is establishing the criteria at which a wide peak should be deconvoluted into separate peaks. This threshold was set at a minimum peak separation larger than the smallest width of two adjacent peak fits. Figure 7.1 shows the significance of this parameter by illustrating the effect where two identical peaks with arbitrary intensity shifted by fixed peak separations (ps) ranging from 0.1 to 1.2 peak widths are convoluted to show a single curve. When an arbitrary minimum peak separation is selected, any peak fit pairs below this range are considered a single peak with wider mosaic spread.

The peak fitting algorithm proceeds by assuming a global maximum number of peaks, and if any adjacent pair are closer than their individual peak widths, the number of peaks is reduced until all peaks fit within the set range, and have sufficient separation between them to be considered two or more distinct crystal orientations.

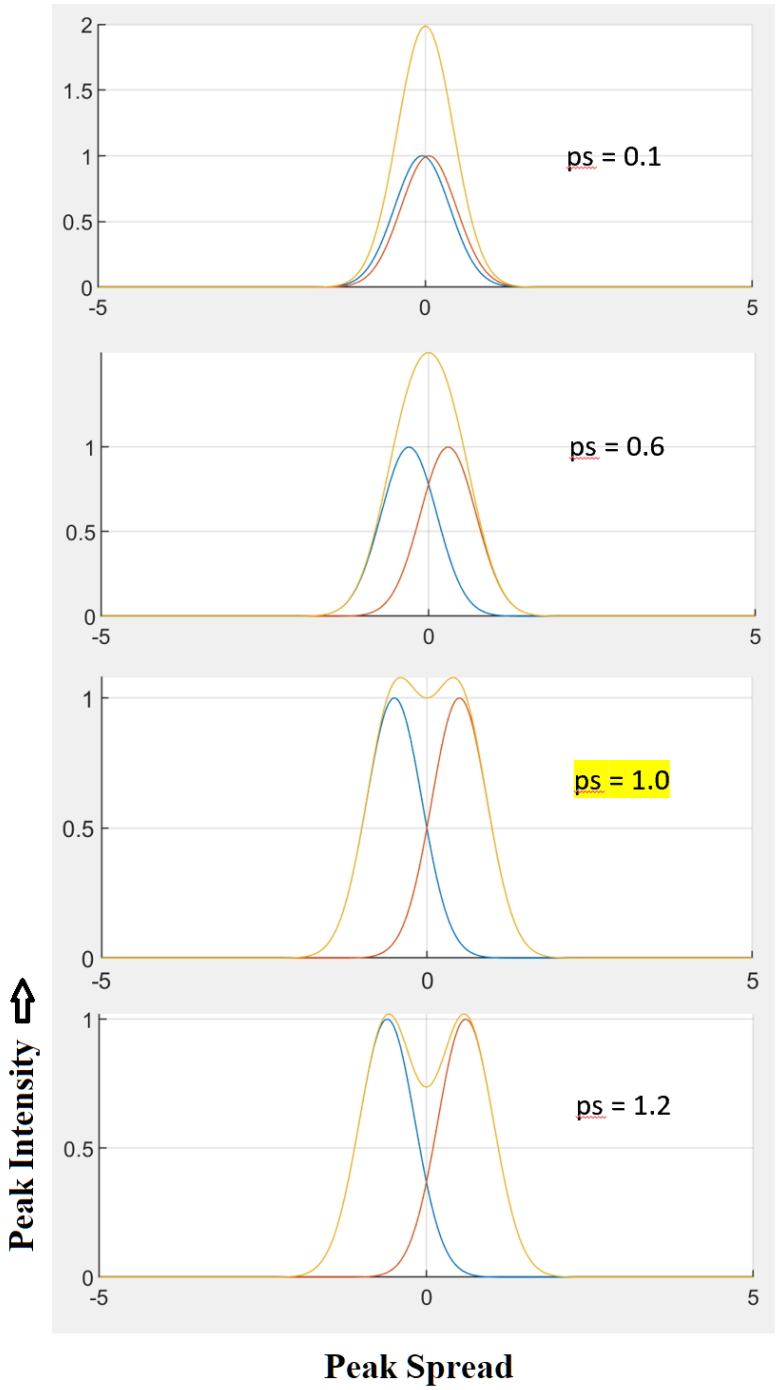

Figure 7.1: Illustrating the effect of selecting a minimum peak separation (ps) based on two identical convoluted Gaussian distributions. The x-axis shows arbitrary peak spread measured as Full Width Half Max (FWHM) units. The y-axis measures arbitrary peak intensity. A highlighted peak separation of ps = 1.0 FWHM units has been selected as the threshold at which wide peaks can be considered two or more separate orientations on XRC measurements.

7.2.2 Definition: Local Misorientation

The simplest application in XRC data analysis is calculating relative misorientation. The condition for this measurement is making sure the spot size is large enough to measure both sides of a mosaic boundary simultaneously. Two peaks are deconvoluted from the measured curve in the region, and the separation between them corresponds to the misorientation. The relative intensity of each peak will shift from one to the other as nearby regions are measured, but in principle, the separation between the peaks will not. This measurement is not necessarily considered a general misorientation measurement because in some cases, especially when samples are grown thicker, the misorientation within a single point will vary depending on the position. This direct measurement is therefore defined as the Local Misorientation, as it will only correspond to regions as small as the XRD spot size used to perform the scan. Figure 7.2 illustrates an example of this measurement near the boundary of a grown mosaic substrate.

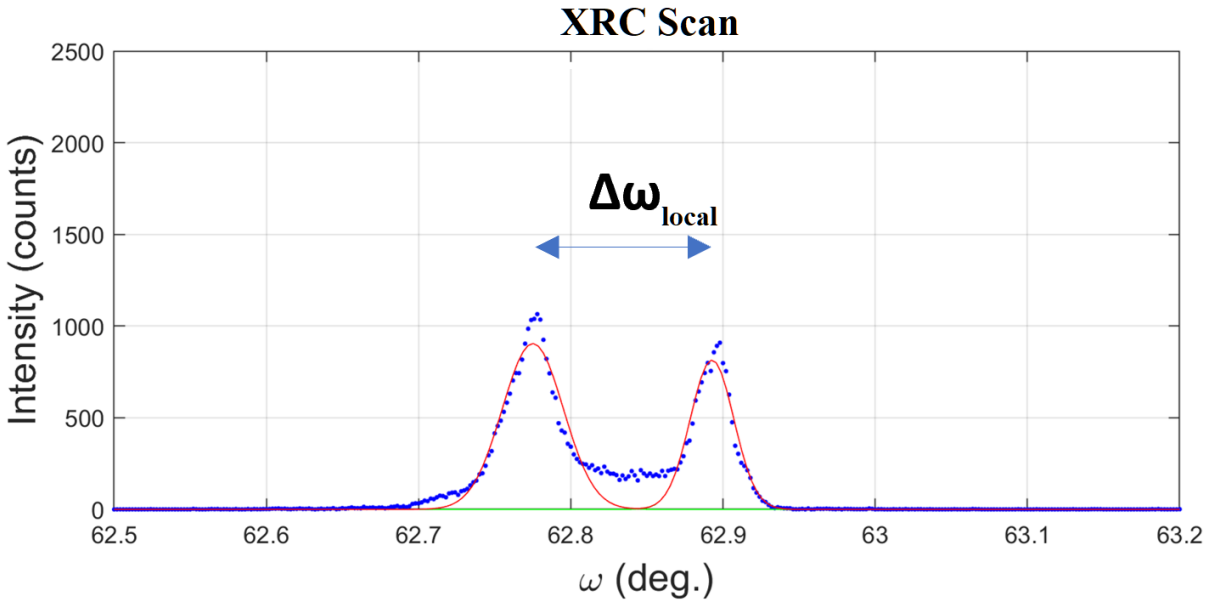

Figure 7.2: XRC measurement used to calculate local misorientation. In this case, the number of peaks has been limited to a maximum of two for simplicity.

The three local misorientation types: Tilt, Twist and Torsion can be measured for each point by adjusting the relative rotation of the sample as illustrated in Figure 5.20.

7.2.3 Definition: Aggregate Mosaicity

As boundary effects over an interface are not necessarily confined to a small region, or fixed in place as the sample is grown thicker, a new problem during analysis arises when two distinguishable peaks progressively shift closer together when scanned away from an interface. The two merging peaks will eventually be misinterpreted as a single broad peak when the peak separation parameter is reached.

When this pattern is observed, tracking peak behaviors along a surface will inevitably show discontinuities when comparing either the number of detected peaks, or the individual peak widths. One solution is defining a new Aggregate Mosaicity metric. The concept takes into account both the largest local misorientation, and half the width of each outlying peak, as illustrated in Figure 7.3. The final value is not heavily dependent on selected criteria for peak deconvolution parameters since the aggregate mosaicity of a relatively wide peak yields a similar result to a convolution of multiple peaks to characterize the same curve. This new Aggregate Mosaicity metric then leads to smooth transitions when measuring surfaces that include both single and multiple peaks. The metric is convenient in the sense that it serves as a direct extension on the definition of Mosaicity for cases where the underlying domains are significantly misoriented to any arbitrary degree.

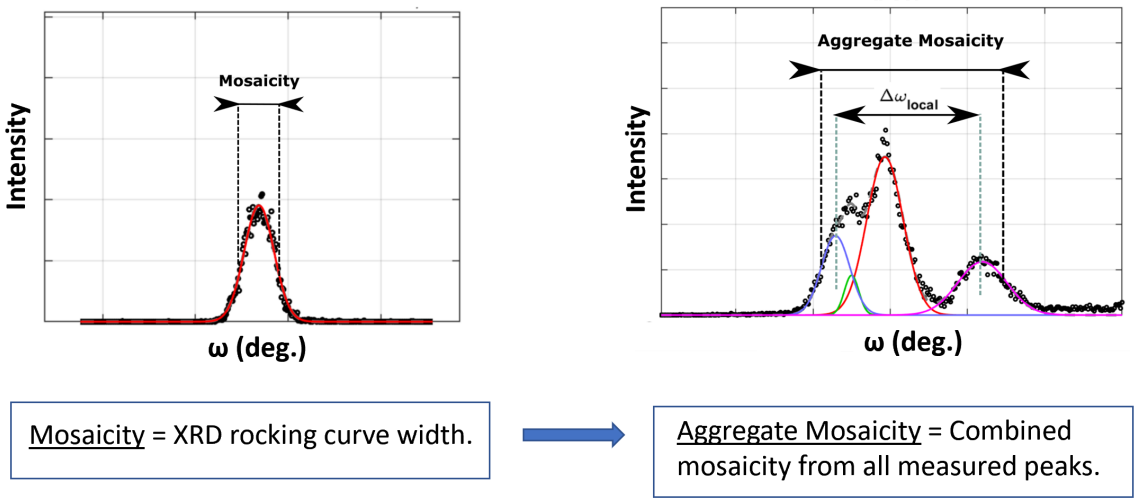

Figure 7.3: Standard definition of Mosaicity as the FWHM of a rocking curve scan, and the new concept of Aggregate Mosaicity defined as a combination of local misorientation plus half the mosaicity of each outlying peak.

7.3 XRC Mapping

The XRD system described in Section 5.5.3 used to measure samples is equipped with an XY moving stage where the position of the spot size can be controlled with a precision of 5 µm. The optimal grid size when measuring multiple points over larger sample areas is given by the effective spot size of the XRD system. Sampling substrate areas with a grid size of 0.5 mm is theoretically sufficient to cover all sample features.

7.3.1 Batch Curve Fitting

The analysis software, developed and written in MATLAB for this and other analysis projects, reads the rocking curve measurement taken at every point. Depending on selected fit parameters, the software performs a batch peak fitting on all points. Figure 7.4 illustrates the process, where each point covered in the area only needs a few seconds to find the best fit and store the output parameters. Figure 7.5 shows the process after successful completion.

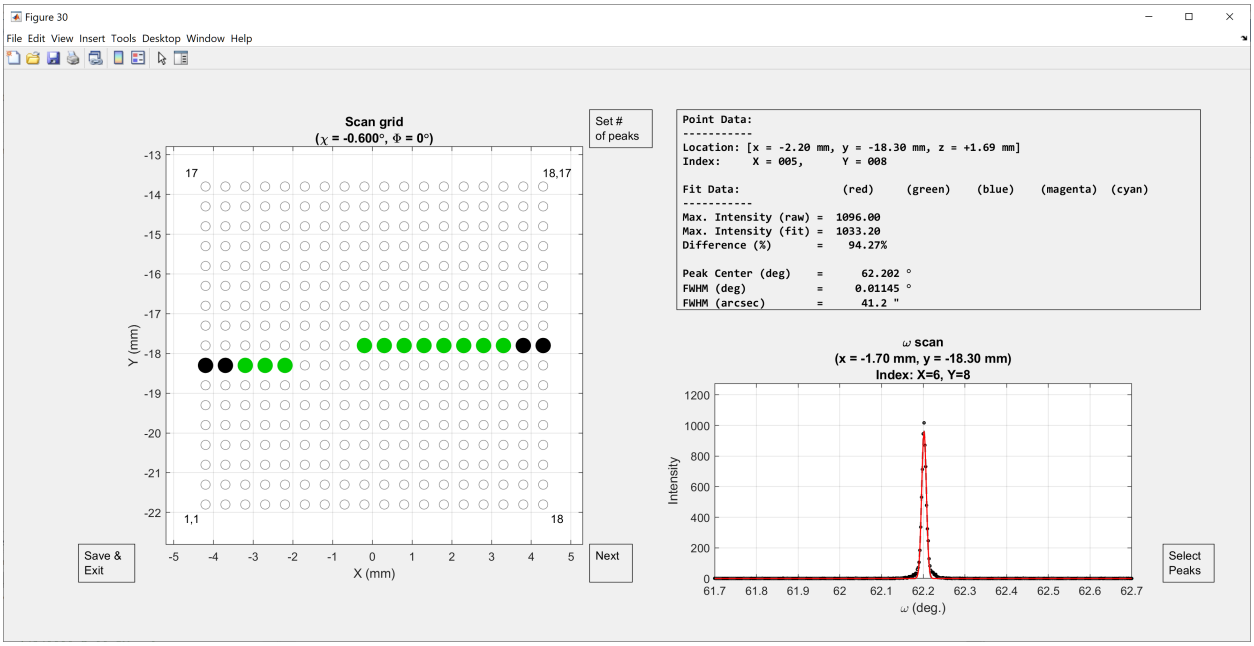

Figure 7.4: Batch curve fitting process in the XRC Analysis software.

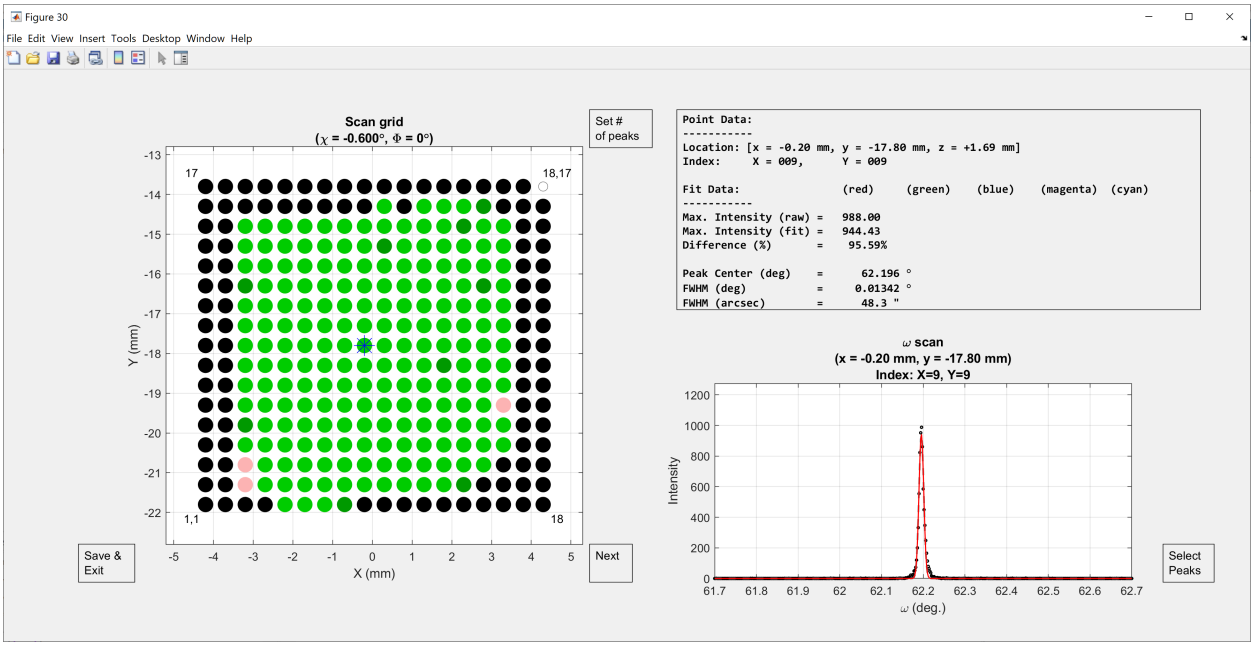

Figure 7.5: Curve fitting process complete. Each point is color coded for the number of peaks detected in each scan.

7.3.2 Map Types

Once all peaks have been identified, the software provides multiple ways to visualize the 2D data corresponding to the resulting fit parameters. The interpreted parameters can be illustrated with two styles, either contour maps or with a discrete grid. Available map types refer to the parameters obtained from curve fits, such as intensity, position and width as interpreted from the technique. The following six map types can be generated from a data set based on single peak measurements:

1. Peak Intensity
2. Integral
3. Peak Width
4. Orientation
5. Deviation from Average (Highest Peak)
6. Deviation from Average (Average Orientation)

The list continues with more map types generated from data sets that include scans with two or more peaks:

7. Number of Peaks
8. Local Misorientation
9. Relative Intensity
10. Deviation from average (left peak or right peak only)
11. Peak Width (left peak or right peak only)
12. Intensity (left peak or right peak only)
13. Aggregate Mosaicity

Each type is described in the following sections with examples for both contour and discrete maps in each case.

7.3.2.1 Peak Intensity

Measures the maximum peak intensity for each point. Units are arbitrary. The maximum value depends on the scan speed and slit sizes used during the measurement process

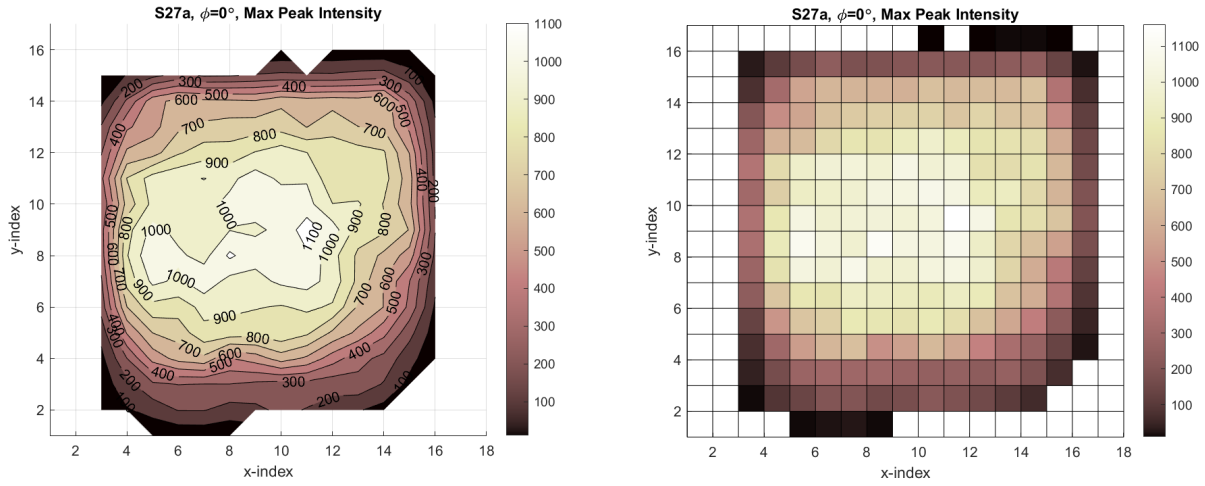

Figure 7.6: Peak Intensity maps.

7.3.2.2 Integral

Another scalar quantity measuring the total diffracted intensity of each scan at all angles.

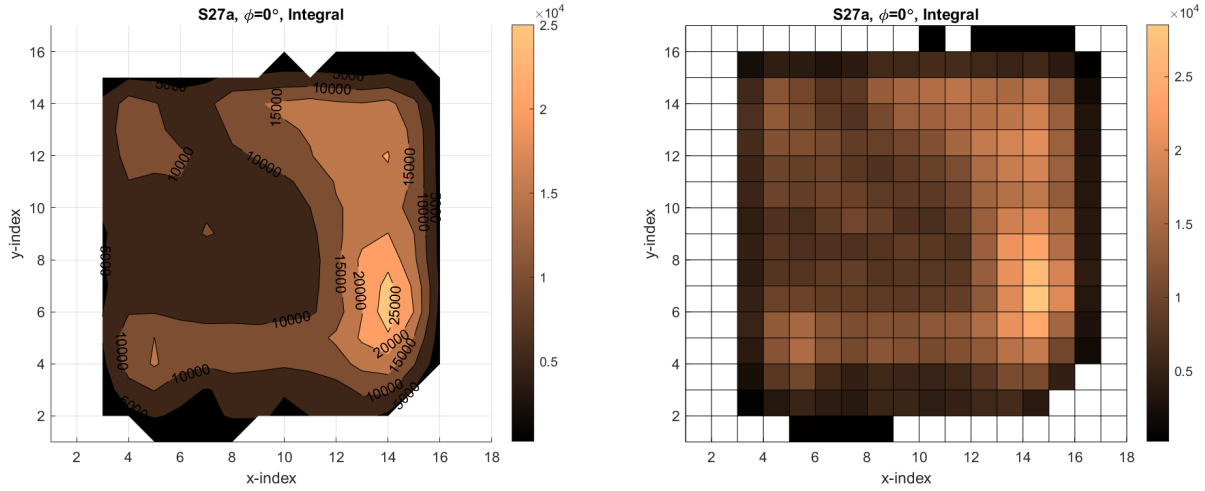

Figure 7.7: Total Intensity maps.

7.3.2.3 Peak Width

Full Width Half Max (FWHM) measurements for each point. This quantity is defined as the Mosaicity of the region. If multiple peaks are present, only the highest intensity peak

is considered. The units are expressed in arcsec, where the upper limits can be set at user defined levels for maximum resolution in areas with highest crystallinity.

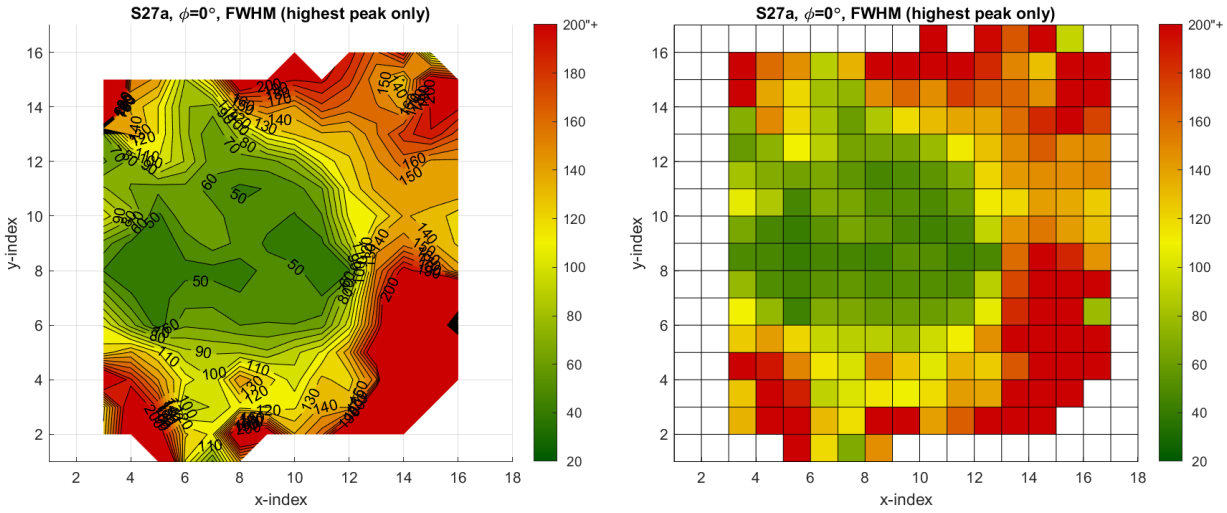

Figure 7.8: Peak Width maps.

7.3.2.4 Orientation

Orientation displayed as an as-measured absolute ω value, or relative to the average orientation. If several peaks are present, the user can select either the highest intensity peaks, or a weighted average of all peak orientations for each point. A Phi angle of $\phi = 0°$ corresponds to inclinations in the horizontal direction, and an angle of $\phi = 90°$ corresponds to inclinations in the vertical direction. The direction of a potential mosaic interface would make these measurements correspond to either Tilt or Torsion. Twist measurements can also be visualized with this type of map, where the scale could be interpreted as in-plane rotations.

7.3.2.5 Number of Peaks

A smaller mosaic sample is used here to illustrate maps showing how many peaks are detected per point. The discrete map type leads to a more intuitive interpretation of the data.

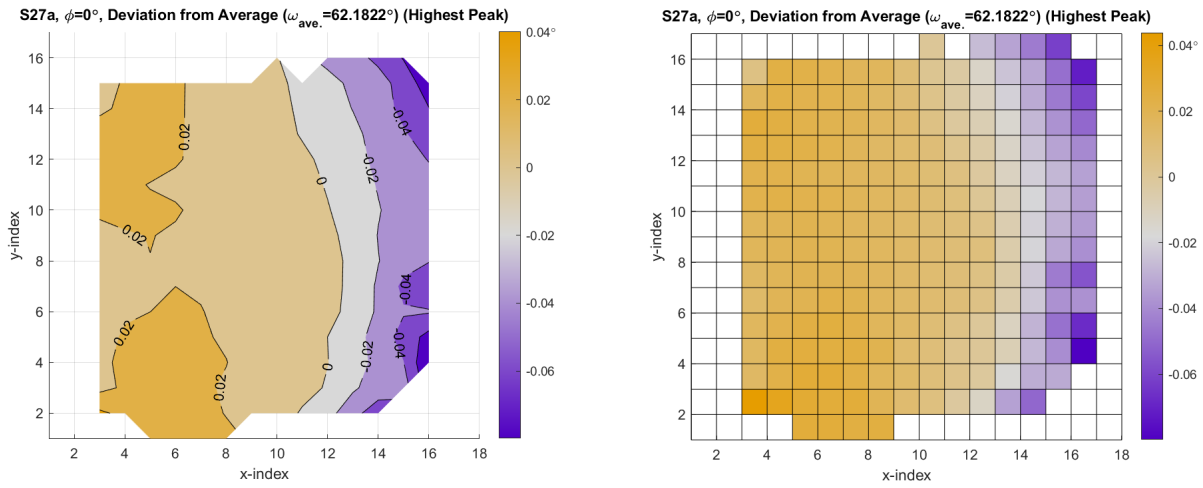

Figure 7.9: Orientation maps.

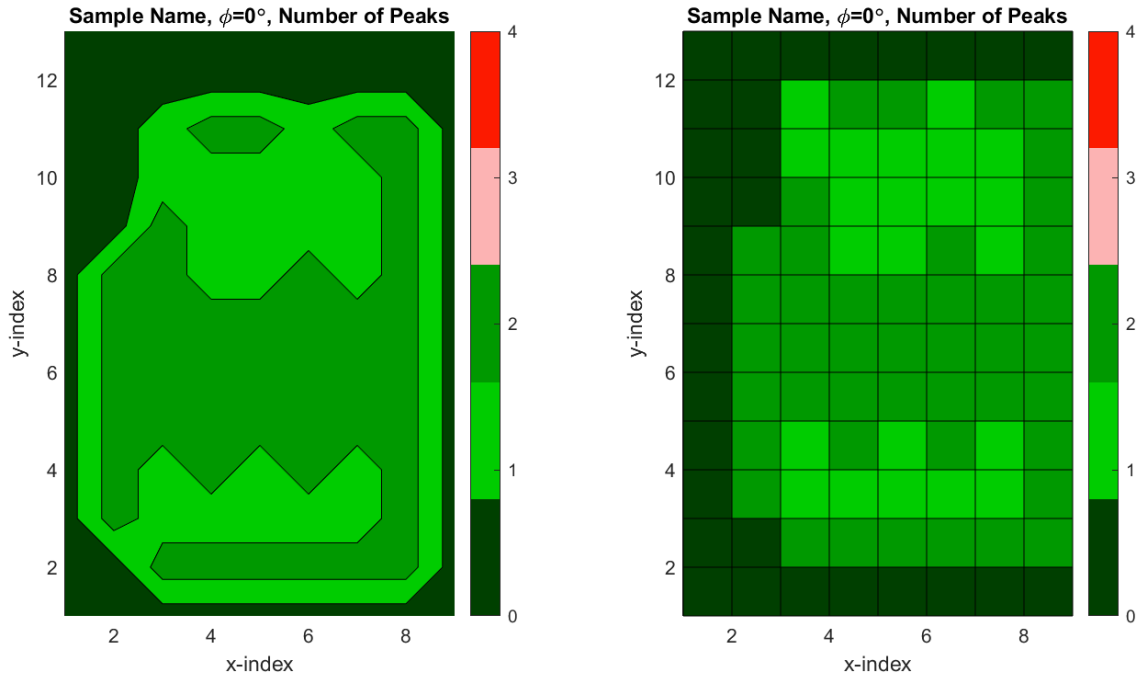

Figure 7.10: Maps illustrating number of peaks detected per scan.

7.3.2.6 Local Misorientation

Same mosaic plate shown in Figure 7.10 now illustrating the local misorientation between the detected peaks in each point in Figure 7.11. A local misorientation of $\Delta\omega_{local} = 0$ implies only a single peak was detected.

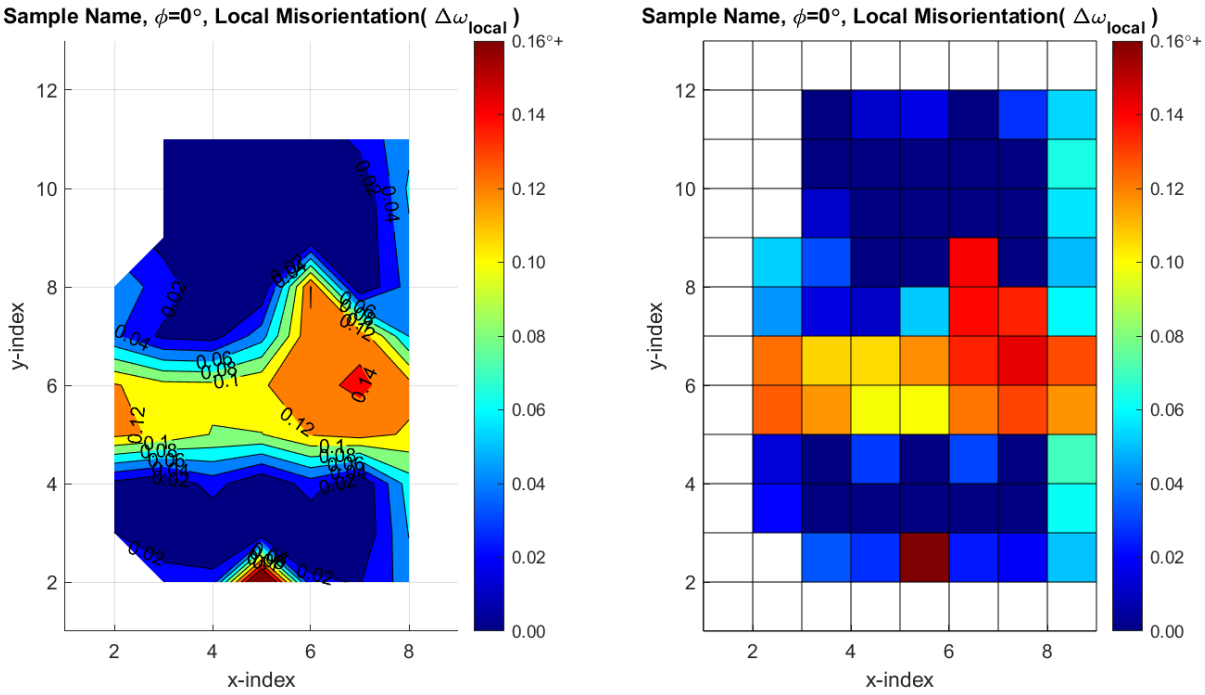

Figure 7.11: Maps illustrating Local Misorientation.

7.3.2.7 Relative Intensity

The relative intensity between two peaks for the same mosaic sample as the two previous examples is illustrated in Figure 7.12. This map type will show whether any of the two detected peaks is relatively weak with respect to the other which might affect how the data is interpreted and for tweaking initial peak fit parameters.

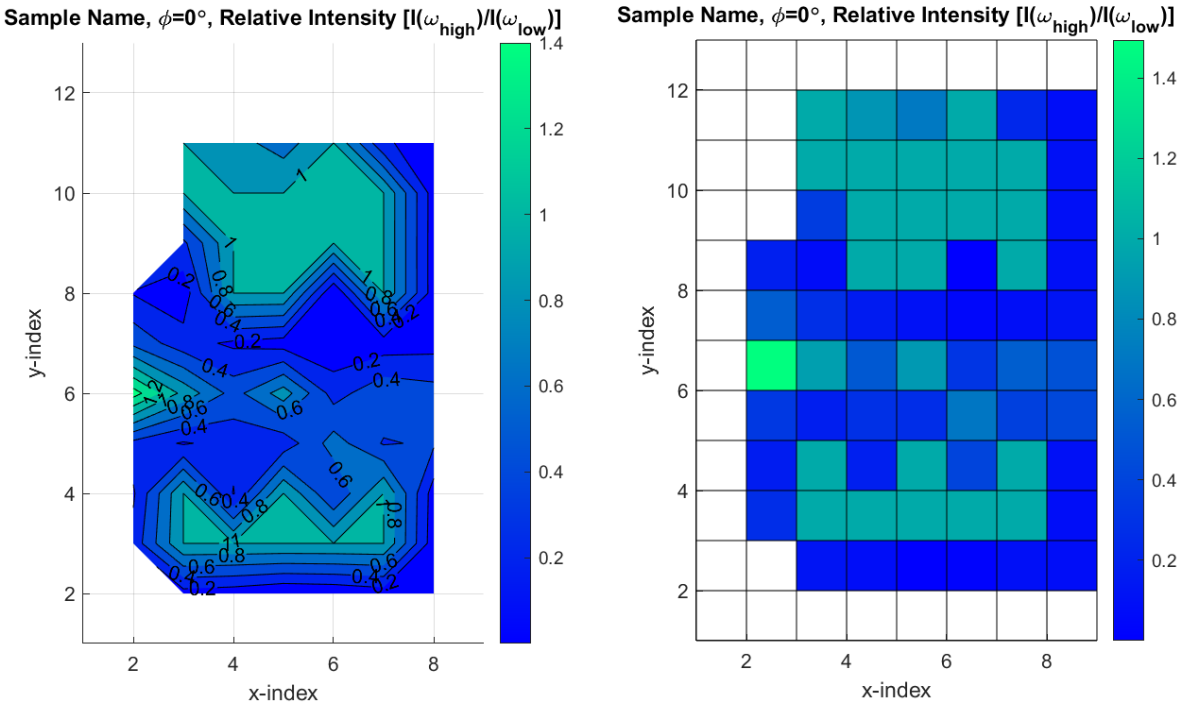

Figure 7.12: Maps illustrating Relative intensity between multiple peaks.

7.3.3 Isolated Peaks

If only two peaks are detected, the analysis software can distinguish between one peak or the other by considering the average orientation as the limiting threshold. Since peaks can be identified, figures can be selected to display a filtered set of one peak or the other. Figure 7.13 shows an example of peak widths filtered by orientation, but any other figure type discussed in the previous sections can be selected.

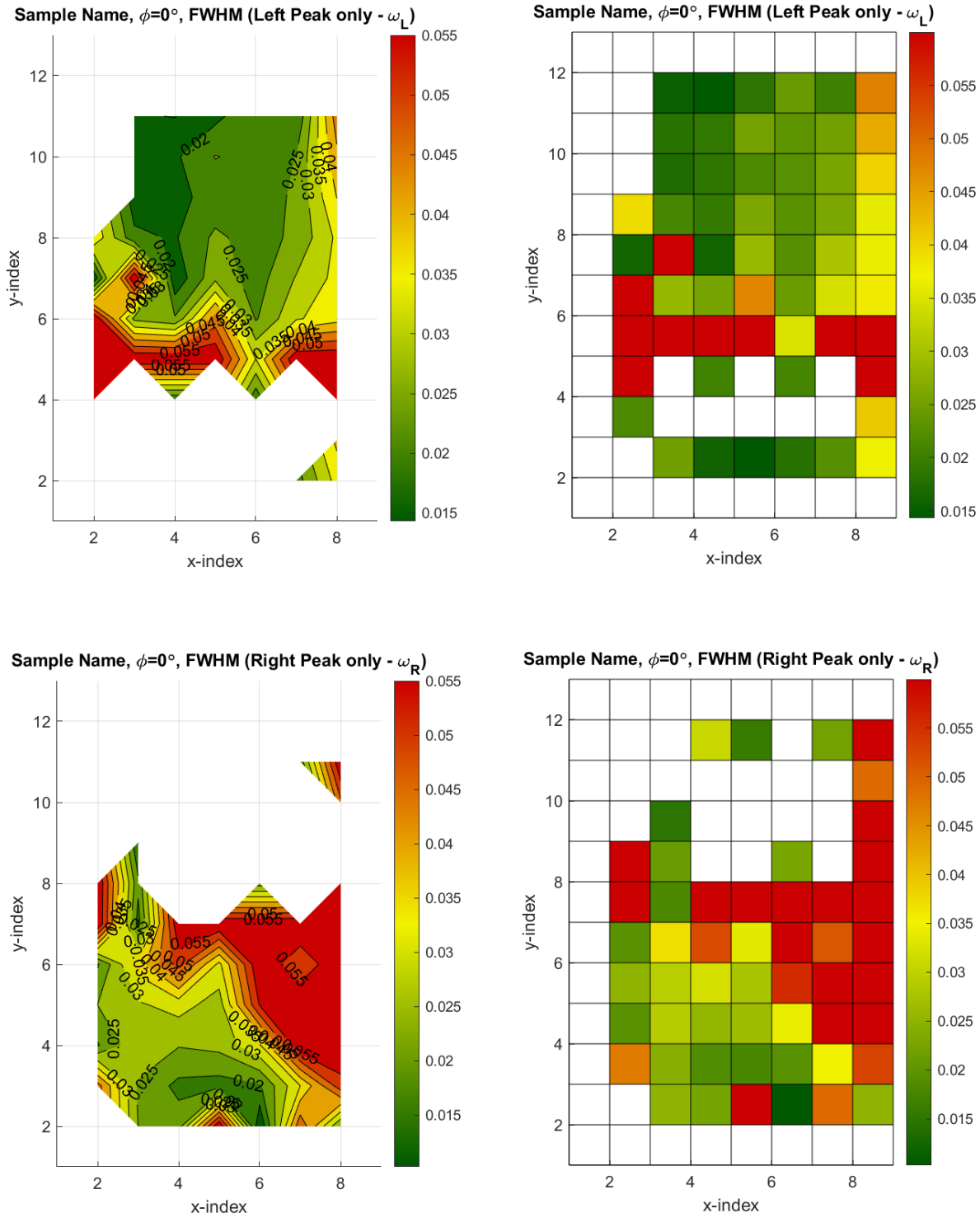

Figure 7.13: Maps illustrating peak widths after filtering the data based on orientation from each side of a grown mosaic substrate.

7.3.4 Aggregate Mosaicity

The new metric defined in section 7.2.3 is shown to be a combination of mosaicity and local misorientation. Figure 7.14 shows both the contour map and the discrete map at different axis limits to show how lowering the maximum limit can show more detail in different regions of interest.

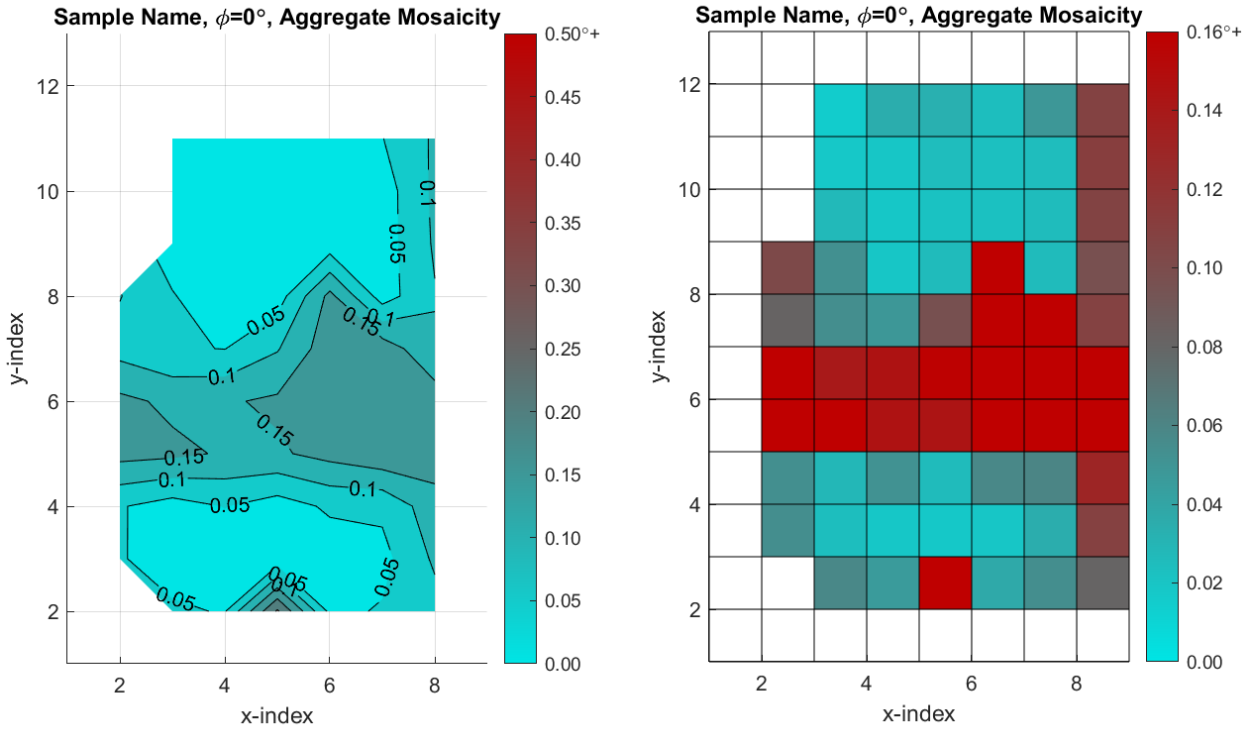

Figure 7.14: Aggregate Mosaicity maps.

7.4 XRC Line Scans

Mosaic boundary effects are sometimes confined to a relatively small region, as observed during this investigation as well as published by others, most notably by Yamada et al. [232], where they report stress limited to areas as small as 0.2 mm. This means that while data mapping is a useful tool, additional information can be obtained if more data points are

measured within grown mosaic boundaries. The first problem with acquiring additional data points is the spot size limitation on the XRD system. If points are measured too close together, it can be argued that the measurement set will contain redundant data. The second problem is logistics. Each XRC scan needs 2-5 minutes to complete a scan, therefore a high density map would need a prohibitively long time to complete as the XRD system is heavily shared by many users.

One solution is to assume symmetry over mosaic boundaries, and perform a high density scan over a single line across an interface, as illustrated in Figure 7.15. Measurements taken at step sizes of 100 µm over a typical boundary which only extends a few millimeters is a relatively fast operation. The output yields similar scans for adjacent points, but slight differences can be tracked point by point even though the spot size is at least five times larger than the step size.

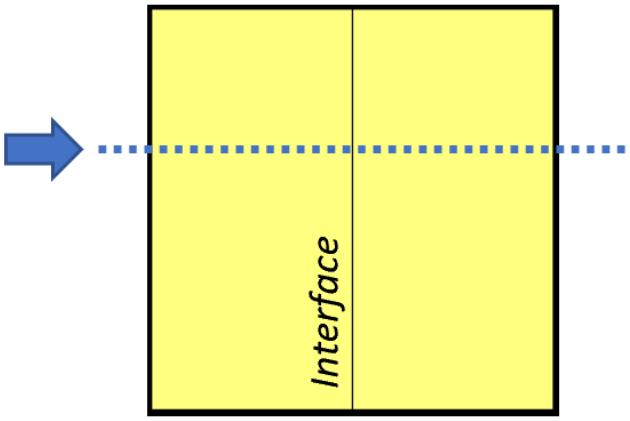

Figure 7.15: Linescan over a mosaic interface.

One example of this set of measurements is shown in Figure 7.16, where the line color from each scan is set by a gradient from black to blue corresponding to the orientation in one tile or the other at different sides of a mosaic interface.

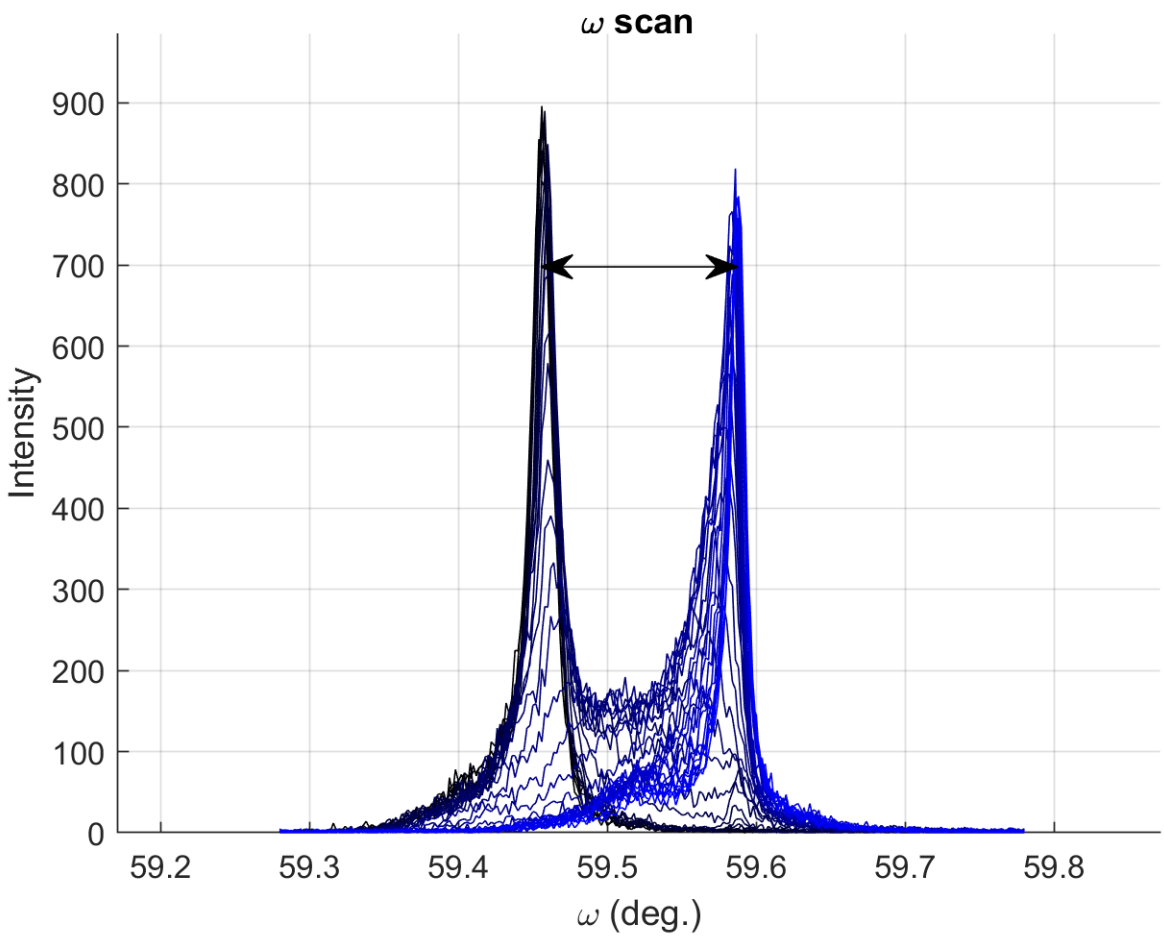

Figure 7.16: Overlay of multiple XRC line scans across a mosaic interface. The double arrow in this case represents the misorientation between the two points at the extreme ends of the linescan.

As can be seen in Figure 7.16, part of the challenge in analyzing X-ray Rocking Curve data is visualizing all the information regarding rocking curve peak intensity, location, width, and their dependence on position relative to each interface. Some effects such as peak shifting and broadening are frequently observed, and even third or fourth peaks can be detected over a two-tile mosaic as points are measured across the interface. Since some of these effects can be subtle and easily overlooked over stacked curves, a more meaningful way to visualize this information had to be developed. One possible way to condense all the relevant data from each linescan illustrated in a single plot is shown in Figure 7.17, where five quantities are

measured in a single figure where each marker represents a single peak. Multiple peaks can then be represented simultaneously, and their placement can be interpreted as follows:

- x-axis = Position across interface. $x = 0$ corresponds to the mosaic interface.
- y-axis = Orientation relative to the average orientation $[\omega - \omega_{ave.}]$.
- Marker size = Relative Peak Intensity.
- Marker bars = Peak FWHM.
- Dashed Line = Weighted average of peak intensities and orientations for each position.

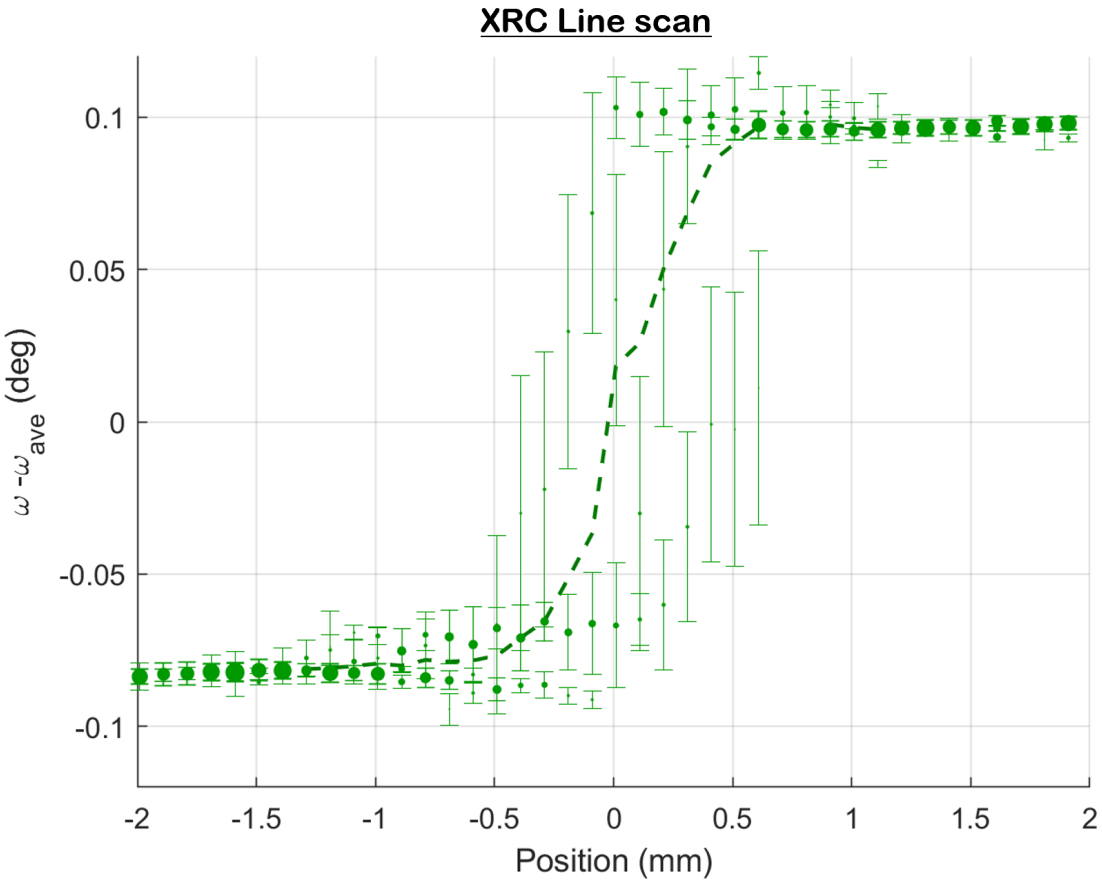

Figure 7.17: Measured Position relative to interface, relative orientation of every peak, their with and intensity, and a combined metric where peak intensity and location are taken into account as a weighted average, displayed here with a dashed line.

Linescans illustrated this way show how mosaic boundaries are not necessarily limited to small regions, and how the transition from one orientation to the other is not necessarily sharp. If we combine multiple peaks into a single value taking into account both the peak location and the peak intensity/orientation as a single weighted average metric, the resulting line is consistently smooth for all measured samples and misorientation types.

7.4.1 Back Side Line Scan Measurements

To appreciate a few immediate benefits of using this plot type, Figure 7.18 shows a scan of the back side of a grown sample. This makes sure both tiles have their initial orientations fixed in place as they were set in the sample holder assembly. By making this linescan measurement from the back side, the shift in orientation should be on display as an abrupt change in the figure.

Two features can be identified, first, this measurement leads to a more accurate way to measure misorientation, as the figure shows how consistent this value is across the boundary. A second effect is how the XRD spot size spread is now evident and directly measurable. The spot size demonstration shows how non-linearities in scans over grown surfaces are indeed boundary effects and not measurement artifacts. These back side measurements also showcase how the resolution of the XRD system is effectively increased when the full set of closely spaced measurements are taken into account.

Linescans can be used to measure all three misorientation types (Tilt, Torsion, and Twist) as each would produce a new set of figures with direct interpretations for each case.

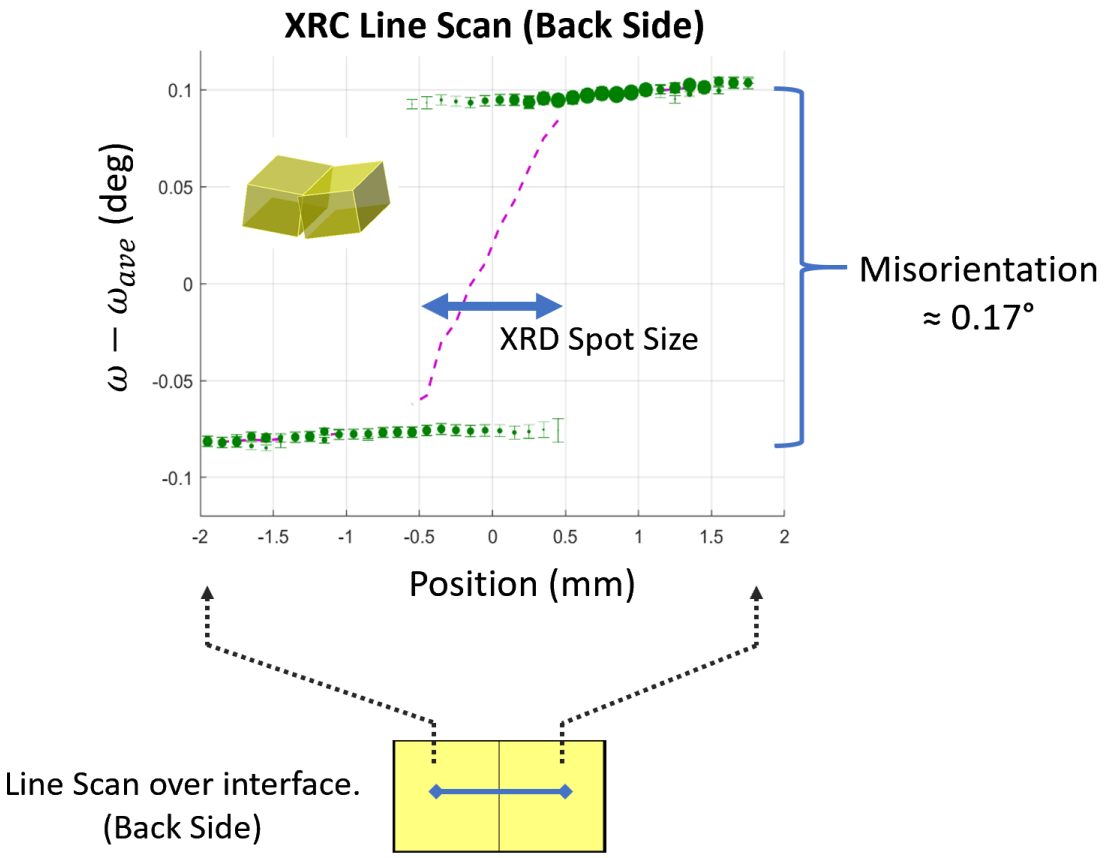

Figure 7.18: Back side line scan measurements.

7.4.2 Definition: Mosaic Boundary

Line scan analysis is currently a powerful tool used to evaluate boundaries over mosaic growths and several other effects, but the analysis needs to be extended even further in order to complete more quantitative comparisons between samples and grown layers.

The way to quantify both local misorientation and mosaicity in a way that leads to smooth transitions from single to multiple peak measurements is with Aggregate Mosaicity, as discussed in section 7.2.3. These transitions as linescans are measured over the original location of an interface can be shown as a function of position across a linescan. These Aggregate Mosaicity vs. Position curves have a characteristic shape, where linescans begin with relatively low single peak widths as measurements correspond to areas with an underlying single crystal

tile, then as the second tile is approached, the aggregate mosaicity starts increasing, when it drops back down again as the linescan measurements conclude with the second tile. An example of this Aggregate Mosaicity distribution along a line scan is illustrated in Figure 7.19 with the mosaicity of three points highlighted. Note how in this image, as coded in the analysis software, low intensity peaks can be ignored by setting user-defined thresholds.

The concept of a Mosaic Boundary can now be defined as a Gaussian distribution curve fit of Aggregate Mosaicity vs. Position measurements. From the curve fit parameters, three values can be extracted from the definition:

- Intensity of the Mosaic Boundary (fit height),
- Location (fit position),
- Spread (fit width).

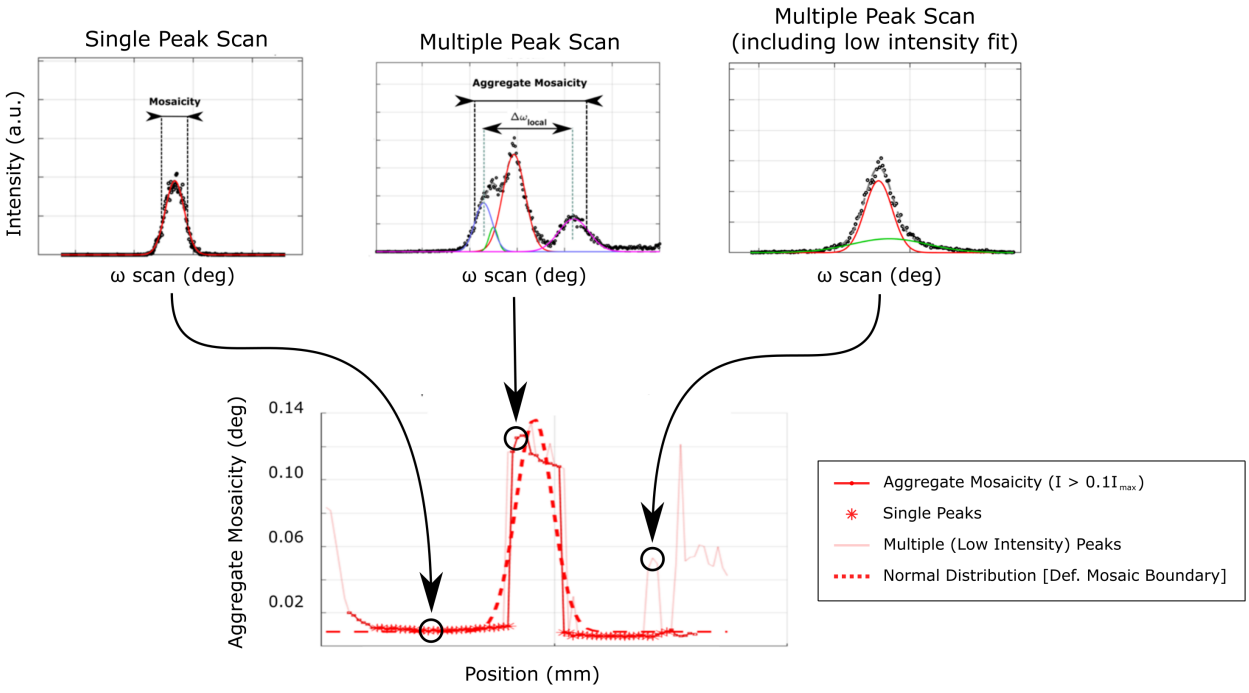

Figure 7.19: Mosaic Boundary at an interface with three highlighted aggregate mosaicity measurements. The main figure shows both filtered and unfiltered Aggregate Mosaicity curves along a scanned line.

The mosaicity of nearby single peaks can be averaged from the baseline reference in the curve fit. The intensity of the Mosaic Boundary as it extends above this baseline measures how the effective mosaicity in the region is affected regardless of the number of peaks detected by the deconvolution algorithm within each point in the region. Filters in this algorithm have been added since low intensity peaks emerging from sample edge effects can be more pronounced than effects from the mosaic boundary itself.

In terms of resolution achievable using this type of analysis, the Mosaic Boundary parameters can be tracked with arbitrary precision, as the best fit will find the intensity, location and spread of this fit by taking into account all points across the line.

If the intensity of the curve fit is reduced to zero, this implies the Mosaic Boundary region has become indistinguishable from single crystals in adjacent tiles. This is considered the ultimate goal with the mosaic technique, as it would not be possible to determine whether a substrate was sourced from a mosaic seed or not based on XRD measurements.

Chapter 8

Mosaic Tiling Results

8.1 Phase 1: Single Source Mosaic Tiles

This investigation began with the approach of reducing the wide set of parameters and conditions related to initial tile misalignments. In order to avoid complications from adjusting angle corrections, a single High Pressure High Temperature (HPHT) seed was cut in half and used as the mosaic seed. These initial experiments were focused on covering the first set of critical goals:

- Confirm lateral growth conditions.
- Develop the tile alignment process.
- Develop set of analysis tools.
- Confirm tiles are effectively merging.

Growth conditions for area expansion by direct lateral growth was explored by producing an initial growth on both tiles as separate units. The process of rejoining both enlarged sides with a smooth interface serves as confirmation that the proposed sample adjustment techniques are adequate for future tile alignments. Figure 8.1 shows the steps in the mosaic seed preparation process after growth from a preliminary deposition.

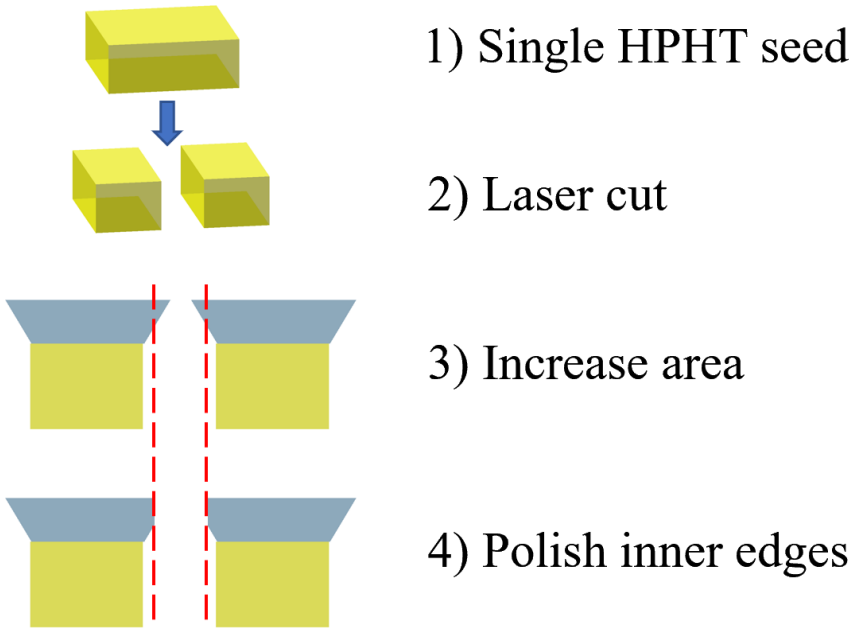

Figure 8.1: Diagram illustrating the process of generating a mosaic seed sourced from a single HPHT crystal after a preliminary deposition.

8.1.1 Preliminary Deposition

Mosaic tiles were laser cut from a single (100)-oriented Sumitomo (HPHT) seed into two corner-marked 3.6 mm x 1.8 mm x 1.4 mm substrates. The pair of mosaic seeds were placed on a custom holder with pocket dimensions of 7.5mm x 6.6mm and a depth of 2.3mm. The width is asymmetric such that both tiles can fit inside the pocket area while maintaining approximately the same distance from the pocket edges, and from each other. The relative position of the seeds within the plate during this preliminary growth were maintained by laser-cutting two seed size pockets on a commercially available 50 µm thick PCD plate shaped to fit inside the base of the pocket holder, as shown in Figure 8.2.

As an effect of reactor DS3 having an off-centered plasma, with its approximate position estimated in Figure 8.3, the sample was grown with non-uniform thickness, as observed in Figure 8.4. This first growth is referenced as (G1).

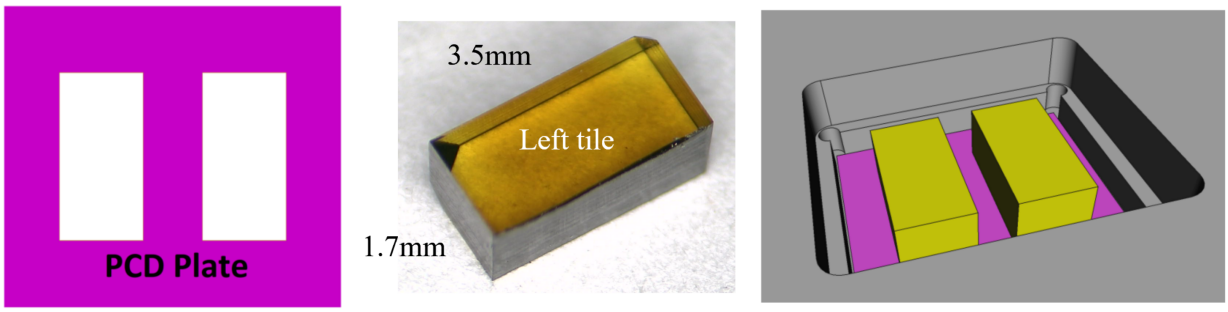

Figure 8.2: a) Laser cut PCD plate. b) Left tile, cut and corner-marked from HPHT seed. c) HPHT seeds in pocket configuration.

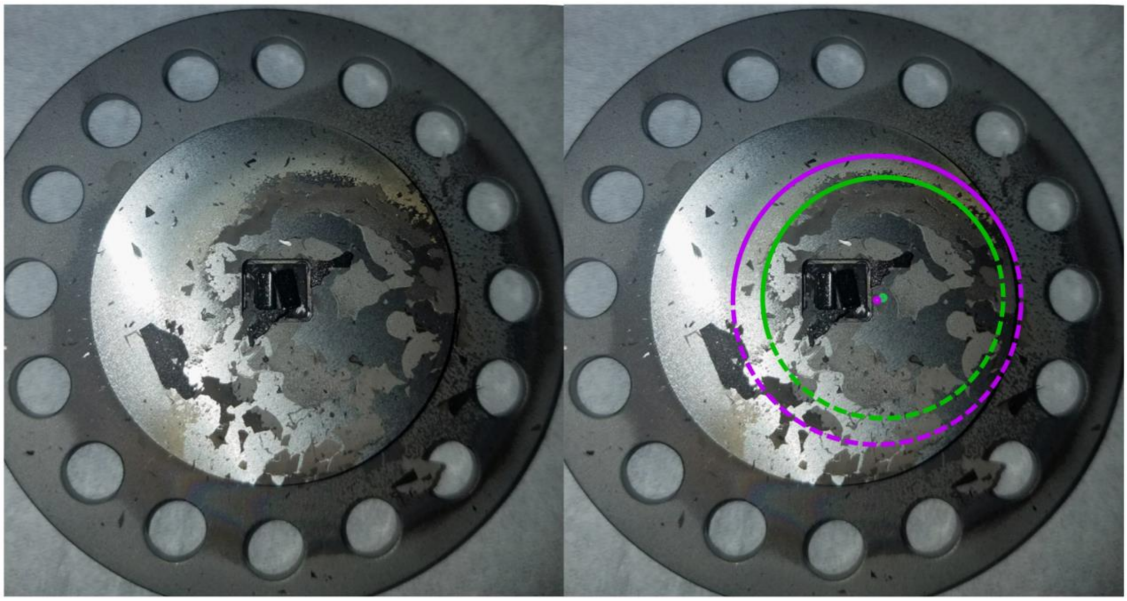

Figure 8.3: Locating the plasma center position. Two approximately concentric circles based on PCD grain size regions can be identified on the as-deposited sample holder. This location is off-centered by ∼4.8 mm.

The resulting off-angle from the deposition was maintained by planarizing a matching surface at an angle of approximately 2° making sure the macro-step between the tiles at the interface was directed from the highest tile to the lowest, and the height difference was not greater than 5 µm, as discussed by Findeling-Dufour [233]. The jagged inner edges were also polished with a taper during the process such that only the top inner straight edges in both tiles are in direct contact, as illustrated in Figures 8.4 and 8.5.

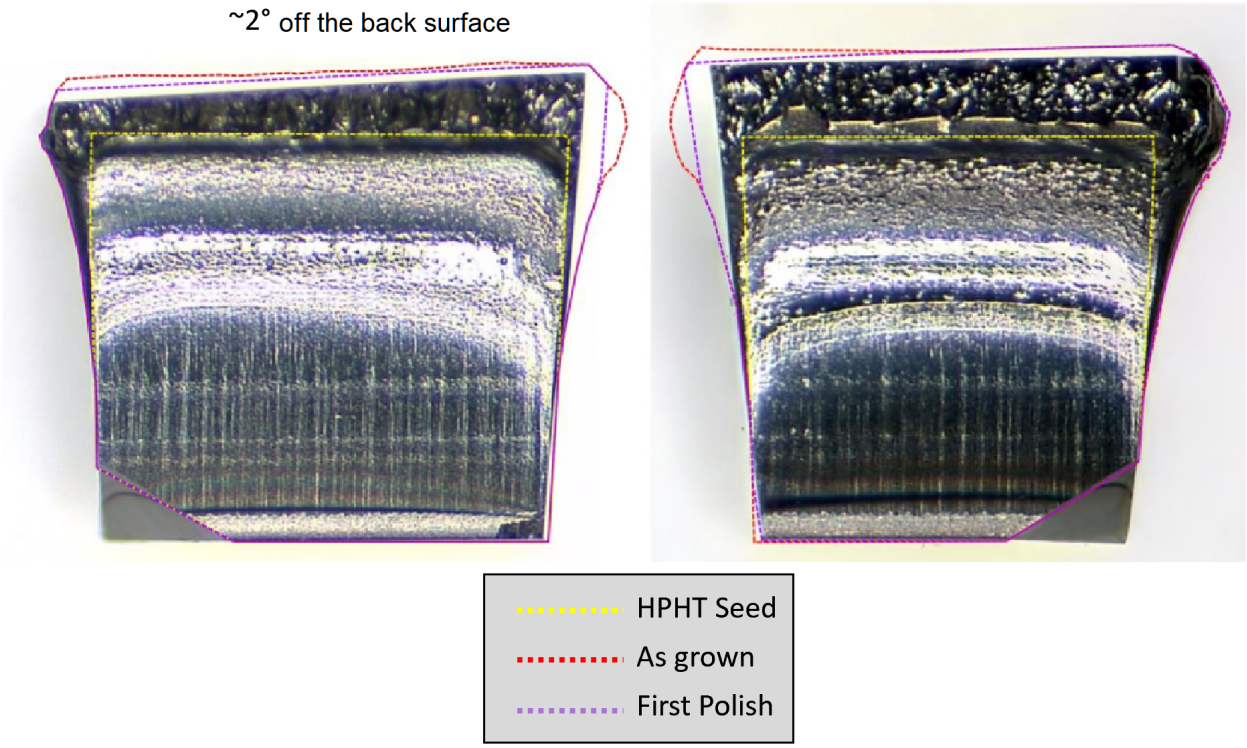

Figure 8.4: Side view with initial HPHT seed and as-grown outlines highlighted. Both tiles were planarized with approximately 2° off the back surface.

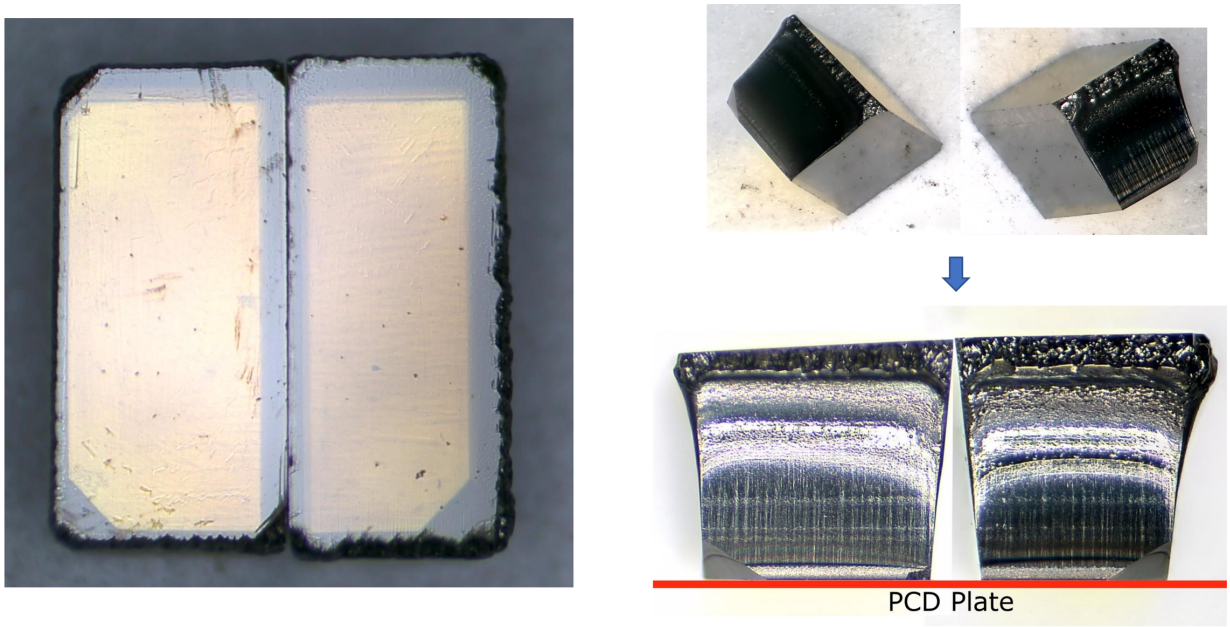

Figure 8.5: Top View illustrating net area enlargement from the initial growth process and a scaled side view of both tiles joined together.

8.1.2 Tile Alignment

Both tiles are assembled together and held in place as discussed in Section 6.4 and illustrated in Figure 8.6, where a combination of two PCD plates assembled at the base of the sample holder. The first plate is a rectangular frame cut out according to the area occupied by the base of the seeds when their top surfaces are in direct contact. The second PCD plate is polished and placed below the alignment frame so that the bottom facet of the mosaic seed sits on a known flat surface. The gap between the tiles is kept within 5 µm.

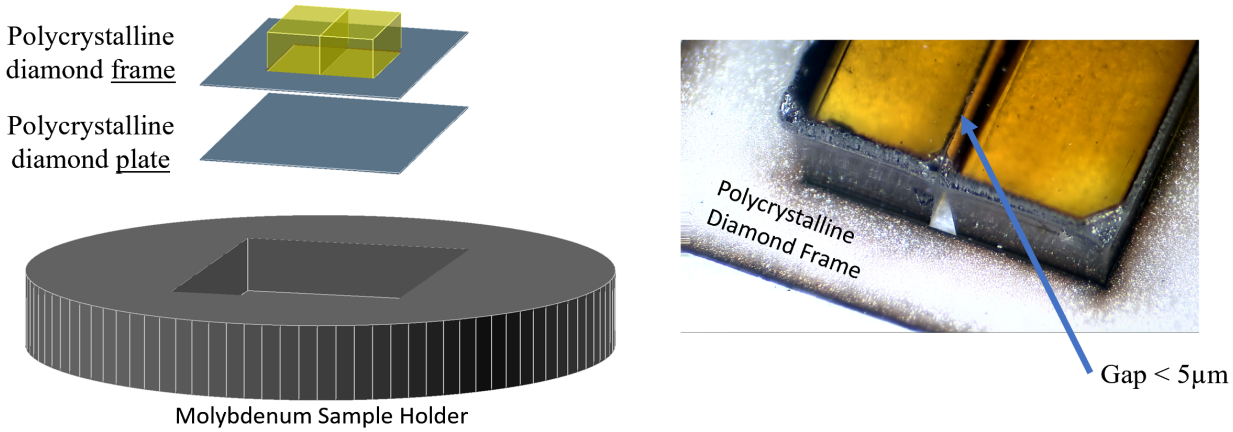

Figure 8.6: Mosaic seed held together by a PCD frame, and held flat by a PCD plate.

8.1.3 Mosaic Growth and Plate Production

The assembly of both aligned tiles are then used as a new mosaic seed and regrown (G2) under similar conditions. Figure 8.7 illustrates the resulting growth from a front view, and Figure 8.8 illustrates the top view, where the grown surface shows signs of surface migration and overgrowth across the mosaic interface.

After this mosaic growth, the back side of the mosaic seed is laser-cut such that the cut plane is parallel to the top surface, creating a sample with a resulting crystallographic

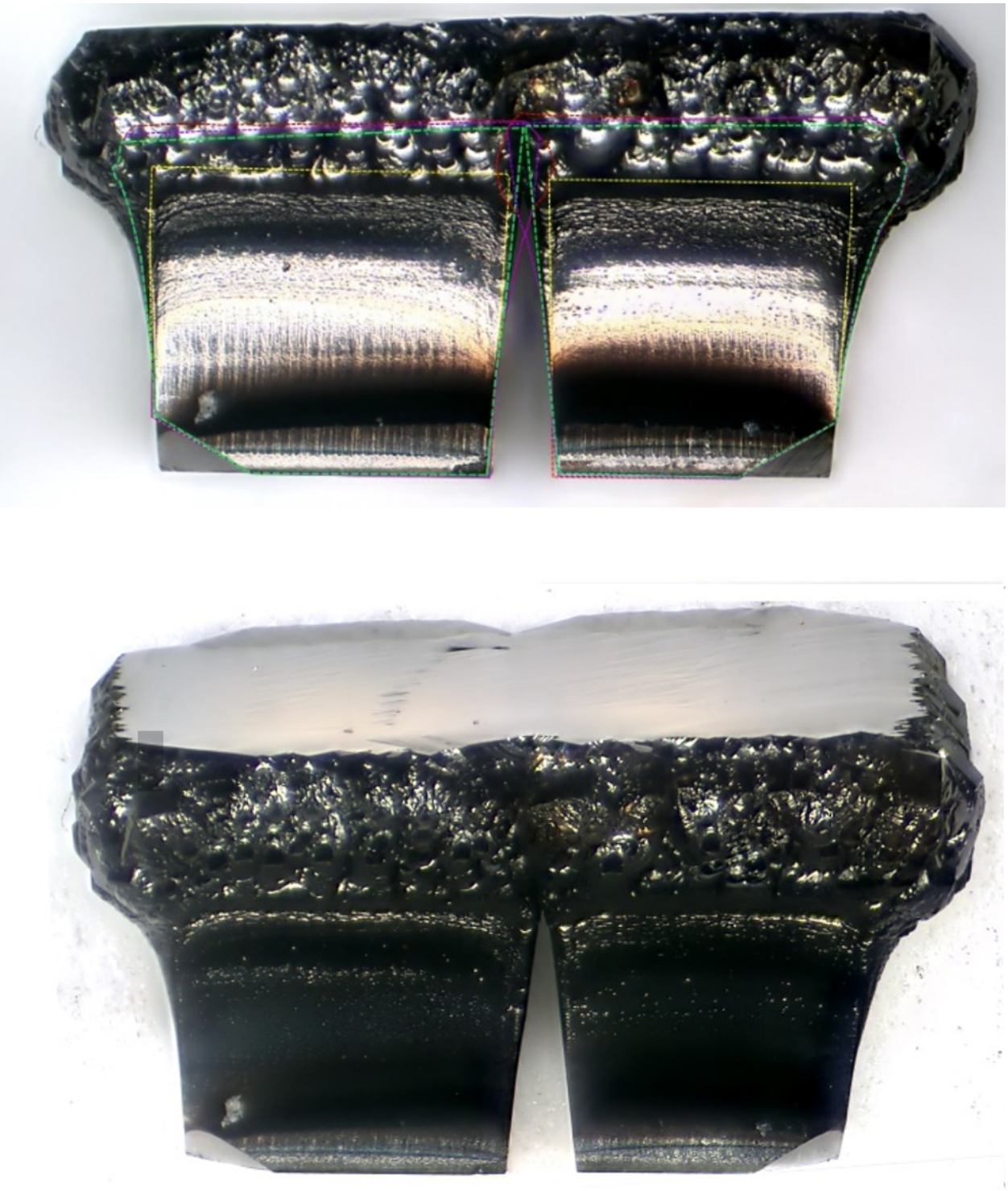

Figure 8.7: Front view of both seeds after the first mosaic growth (G2). The dashed outlines illustrate the original HPHT seed in yellow, the as-grown first layer in red, and the finally polished and assembled mosaic seed in green.

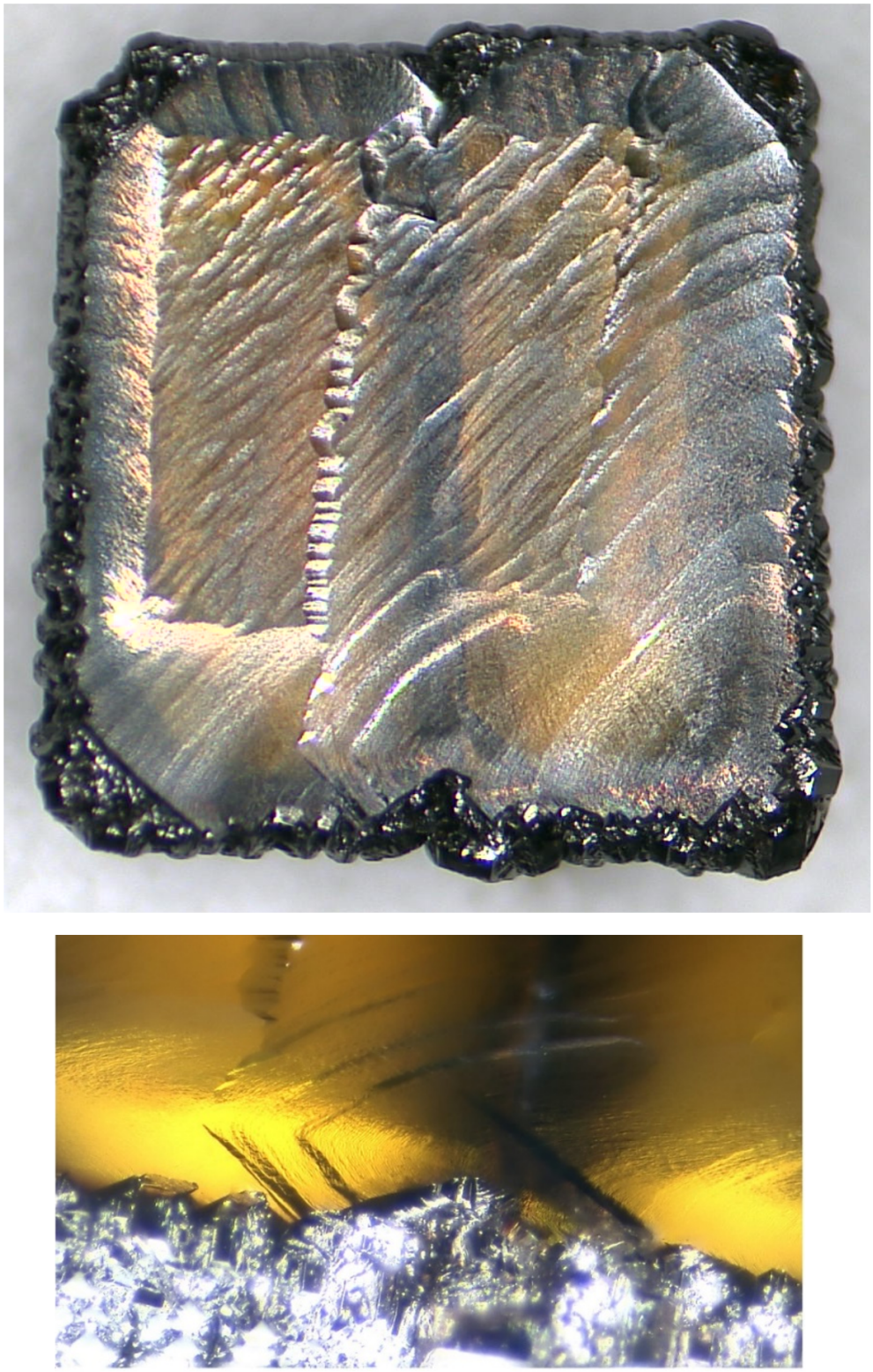

Figure 8.8: Top view of the as-grown diamond with a close up of the overgrown layer at the top surface.

off-cut of 3.1°, and with a total adjusted height of 1.4 mm, similar to the thickness of the original HPHT seeds. The new sample is re-grown (G03) and the first plate (A1) is produced. Both sides of this plate are polished to a total thickness of 620 µm, producing cracks during the process that were not present after the growth. After birefringence measurements, this polished sample with as-grown edges is used as a seed and grown on DS4, reactor type C [258]. The resulting growth was framed, and sliced in two separate plates, (A2 and B), where plate B was polished to a thickness of 620 µm. Some cracks were successfully limited from propagating to plate B after the slicing procedure, while others expanded to the new top surface during the polishing steps. This top plate was RIE etched to reduce polishing damage, where etch pit analysis was performed on both sides. The sample was re-grown (G5) under similar conditions up to a thickness of 1.30 mm. This thicker sample is yet again sliced into plates B and C, where both are polished on both sides and measured for birefringence. Plate C, with a resulting thickness of 560 µm is framed and used as a seed on a re-growth (G6). As a result of this growth, the final plate D with thickness of 350 µm was produced after slicing, again polished on both sides and measured for birefringence. This sample was deliberately cut as thin as possible to avoid cracks propagating from the back side of the plate. The sample thickness resulted in two cracked corners during polishing, but there are no identifiable cracks in the boundary region on plate D. All plates and their corresponding relative grown layer are illustrated in Figure 8.9.

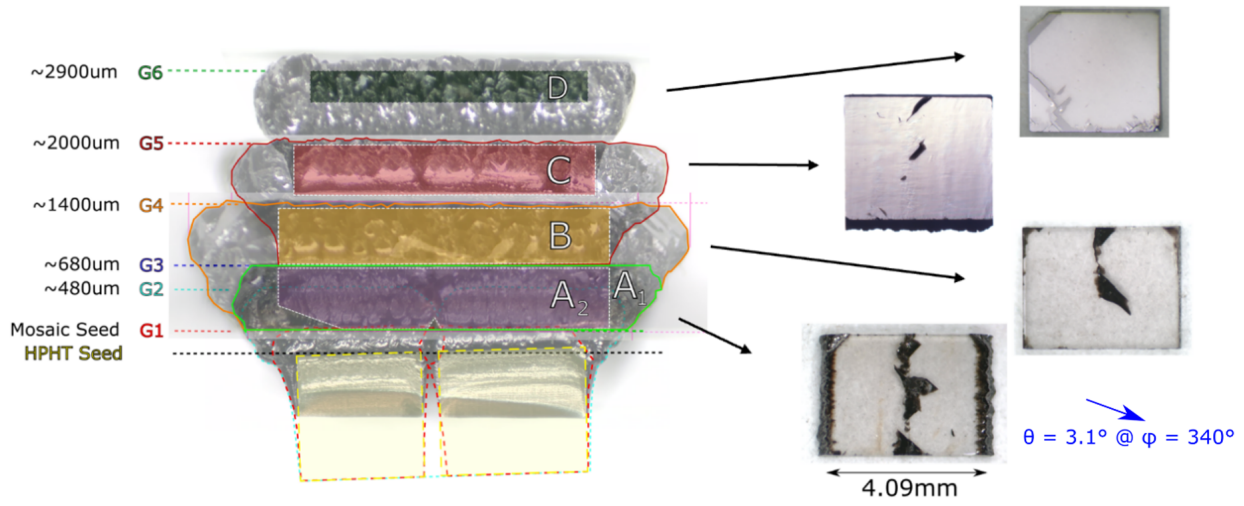

Figure 8.9: Image overlay drawn to scale illustrating the set of six grown layers (G1-G6) at cumulative heights relative to the original HPHT seeds and rotated to match the relative orientation of the four of the plates (A-D) produced during the process. The resulting offcut direction of the (001) planes is illustrated relative to the back surface of plate A.

8.1.4 Plate Analysis

All analysis methods discussed in Chapter 5 were performed on the four plates, which could be sorted in two main categories: Relative Misorientation measurements by XRC and XRT, and Boundary Shifting by analyzing Birefringence, Regional Etch Pit Density and XRC linescans.

8.1.4.1 Relative Misorientation

Figure 8.10 shows a few scans on each plate over the original interface. The relative separation between peaks for each point can be evaluated using different metrics, including measuring relative misorientation from points closest to opposite sample edges, local misorientation from scans close to the original boundary, or separation between integrated peak intensities along the full grid or single lines. All metrics yield similar values and are represented as XRC ranges in Figure 8.11.

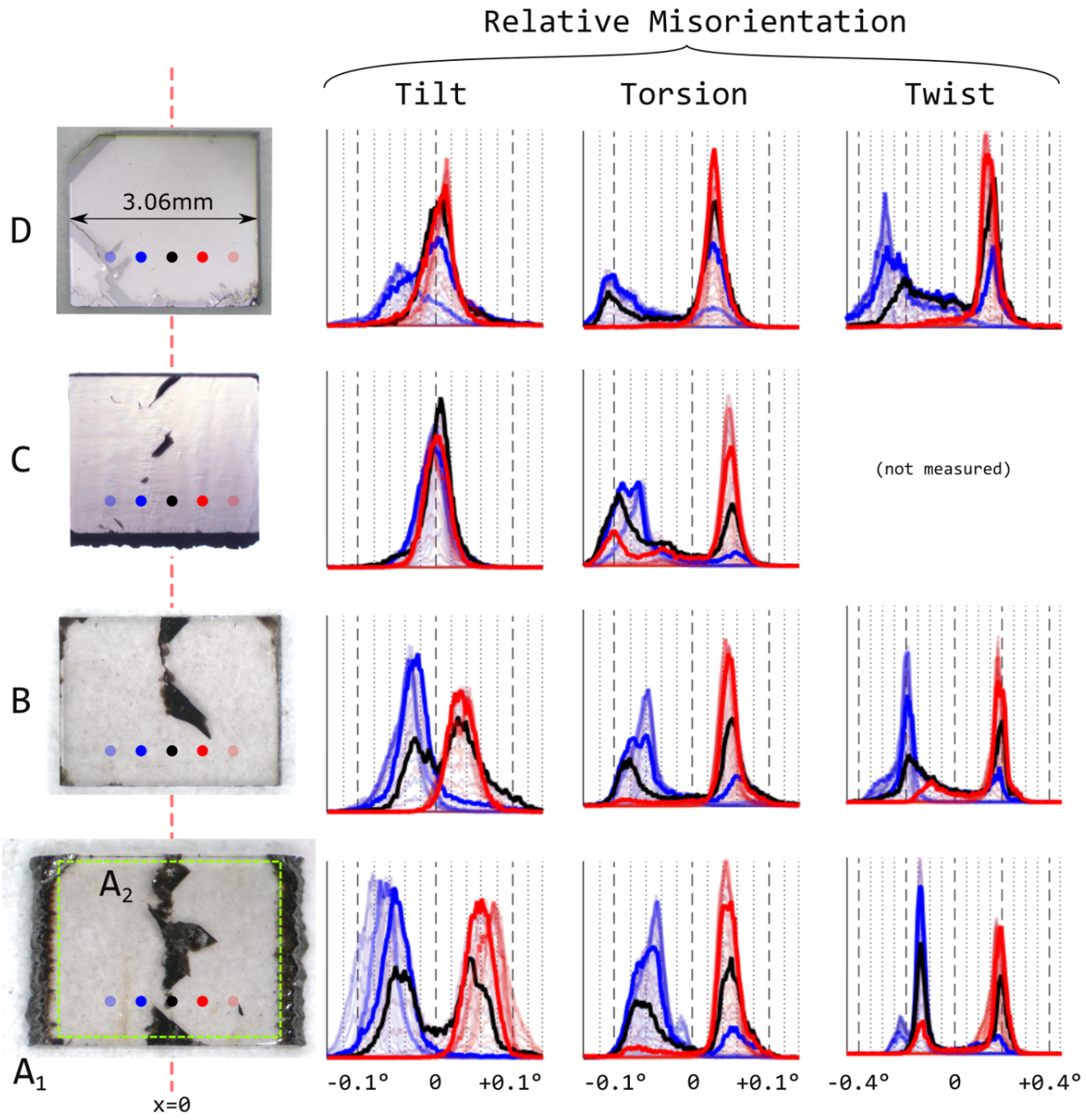

Figure 8.10: Series of grown plates. All images drawn to scale with plate positions aligned based on distinguishing features. The red dashed vertical lines are traced over the relative location of the original interface, defined as $x = 0$. XRC scans for the three misorientation types show all points across the illustrated lines over each sample, with highlighted scans color coded according to point positions at step sizes of 0.5 mm and 0.1 mm relative to the original interface. Peak positions along the x-axis are measured relative to the weighted average position for each plate.

Tilt and Torsion misorientation measurements closely match XRT data, where Torsion is approximately constant, but Tilt improves significantly with thicker growth. If the defective orientation ranges over phi scans for Twist measurements in Plate D were to be considered valid in the curve fitting algorithm, the Twist measurement would tend to yield decreasing misorientations, similar to XRT measurements. The average peak location for all three measurement directions is shown to be increasingly skewed towards the right side of the sample, suggesting the lattice orientation from the right tile tends to dominate over the left tile, as would be expected from a boundary shifting in position over the top surface, corresponding with the step flow growth direction.

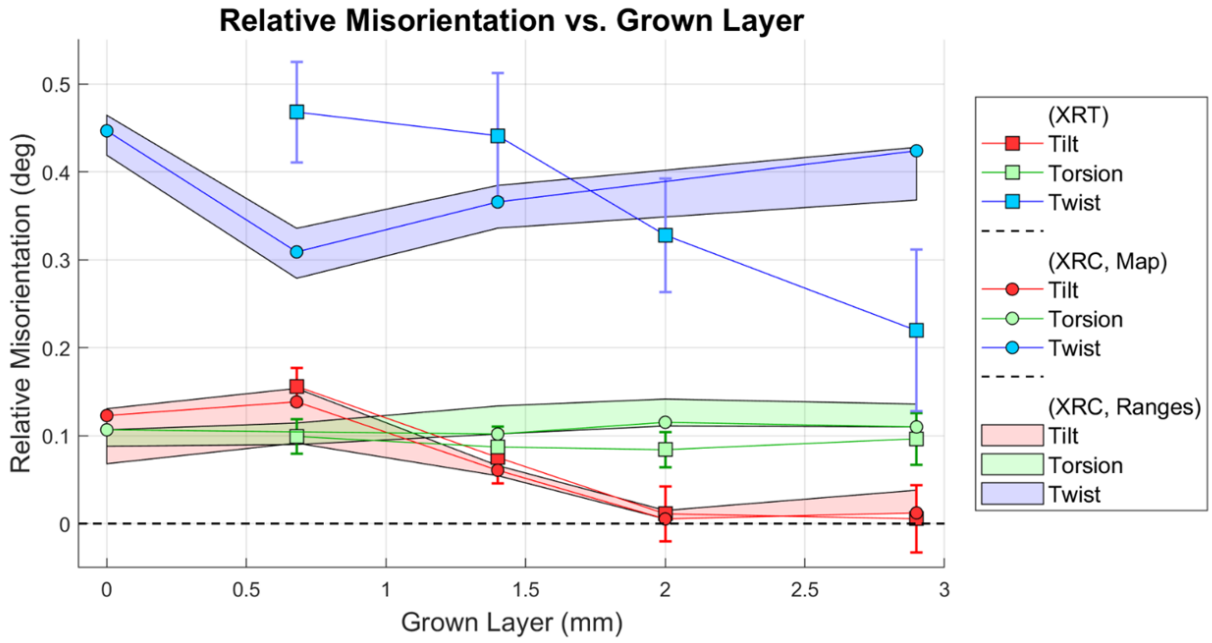

Figure 8.11: Relative Misorientation vs. Grown Layer. The shaded regions correspond to the observed range in relative orientation measurements across the sample. The highlighted rocking curve corresponds to the relative misorientation measured over the integrated intensity considering all points on the surface. This metric covers curvature and other lattice variations across the entire sample, more closely resembling data obtained from XRT measurements.

Figure 8.12 shows rocking curve maps over the four plates where the maximum overall misorientation follows the same pattern, a reduction in Tilt-type of misorientation and no change in Torsion with thicker grown layers. The maximum misorientation $\Delta\omega_{max}$ can be defined here as the maximum separation between any two peaks across the entire surface. The mapped measurement shows how tilt measurements in Plate D are very uniform while the maximum misorientation remained mostly constant for Torsion. The apparent shift in the boundary across the three plates especially notable in the Torsion measurements will be analyzed quantitatively in the following section.

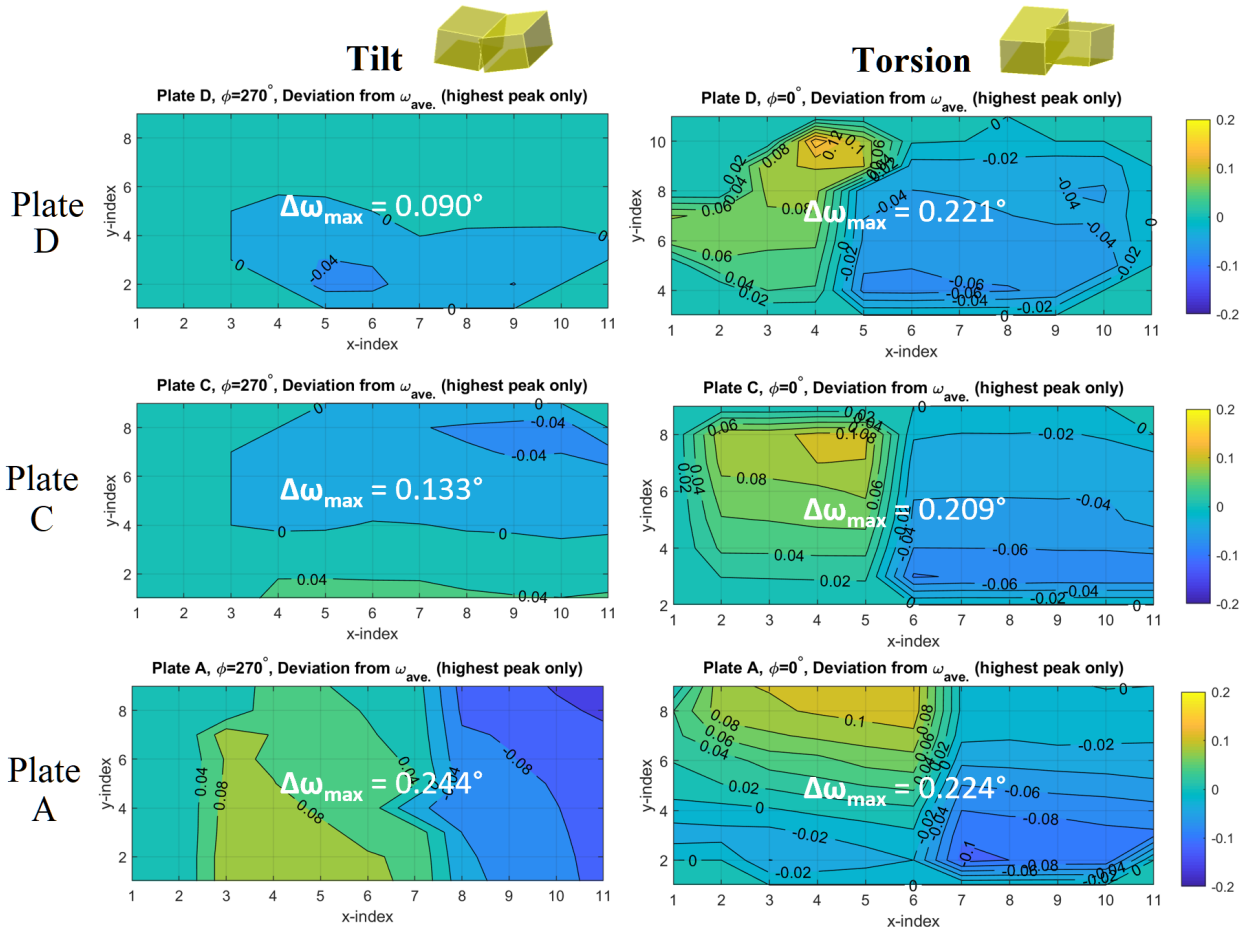

Figure 8.12: Misorientation maps for both Tilt and Torsion on Plates A, C and D.

8.1.4.2 Boundary Shift

Microscope pictures of the resulting four plates and intermediate steps were superimposed based on distinguishing features, such as sample edges and cracks, where the original interface location was identified relative to each plate and used as a single reference.

Birefringence

The result of this alignment on the four plates is shown as applied to their birefringence measurements, which were only compared qualitatively to show how there is an observed stressed region sourced from the interface which is propagating towards the direction of step flow growth, and appears to spread and diffuse over a wider range on all grown layers. An estimate of the onset of this stressed region was measured relative to the position of the original interface as illustrated in Figure 8.13.

Regional Etch Pit Density

Boundary propagation across grown layers was analyzed by performing regional etch pit density measurements as discussed in Section 5.4.1. A normal distribution curve measuring the regional etch pit density was drawn by curve fitting the data with respect to position. Plate B was analyzed on both sides based on a 50 µm moving average window with results are illustrated in Figure 8.14. The back surface of the plate shows an increasing etch pit density as the region approaches the interface. The top surface shows a more uniform etch pit density near the interface. The noticeable increase at the edges of this plate are caused by using a sub-optimal holder for this growth. The pocket size for this growth was relatively wide, promoting PCD formation at the edges. The shift in the center position of the curve fit closely matches the onset of the stressed region observed in the birefringence measurements.

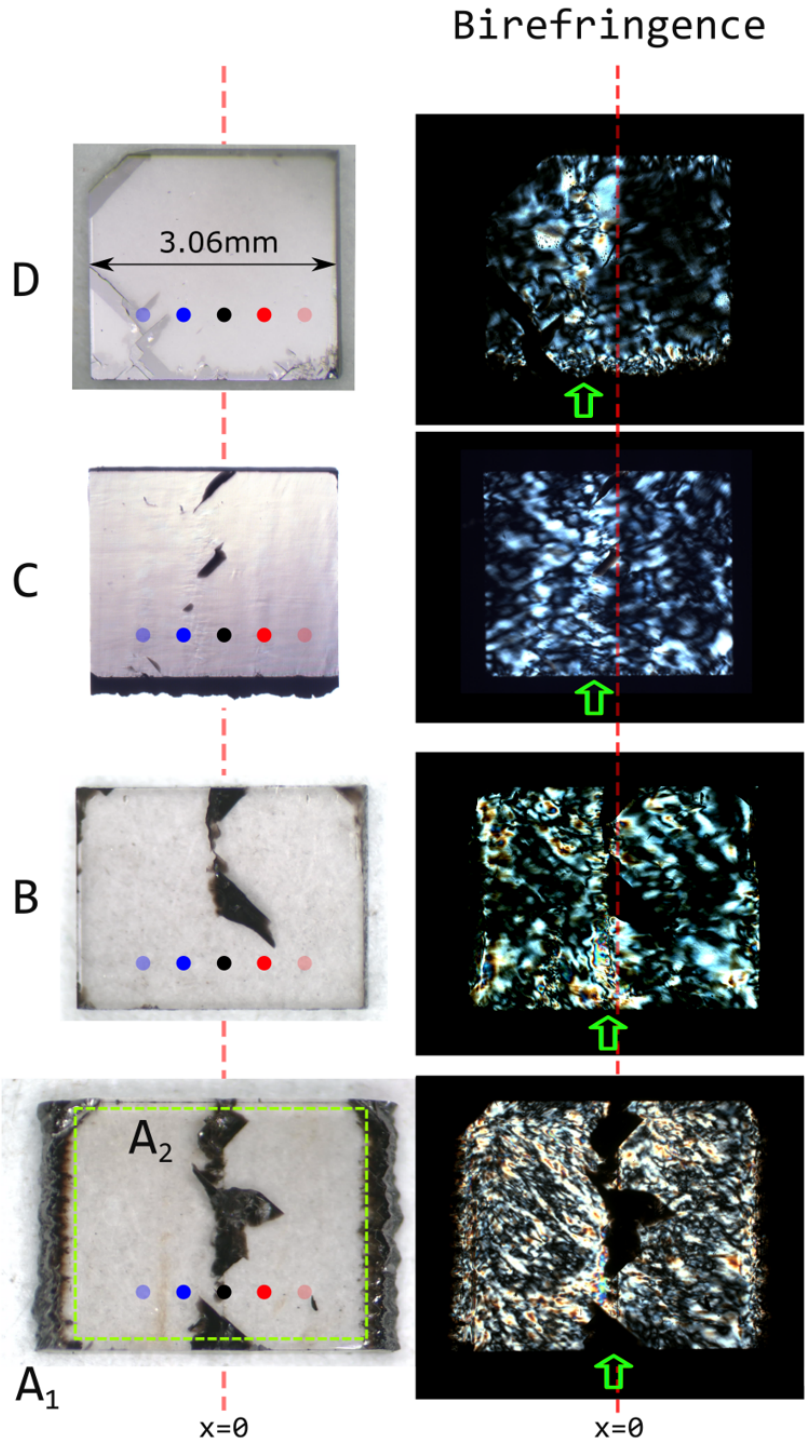

Figure 8.13: Series of grown plates and their respective birefringence measurements. All images drawn to scale with plate positions aligned based on distinguishing features. The red dashed vertical lines are traced over the relative location of the original interface, defined as $x = 0$. Green arrows over the birefringence images highlight how the approximate onset location of the stressed boundary region is shifting relative to the original interface.

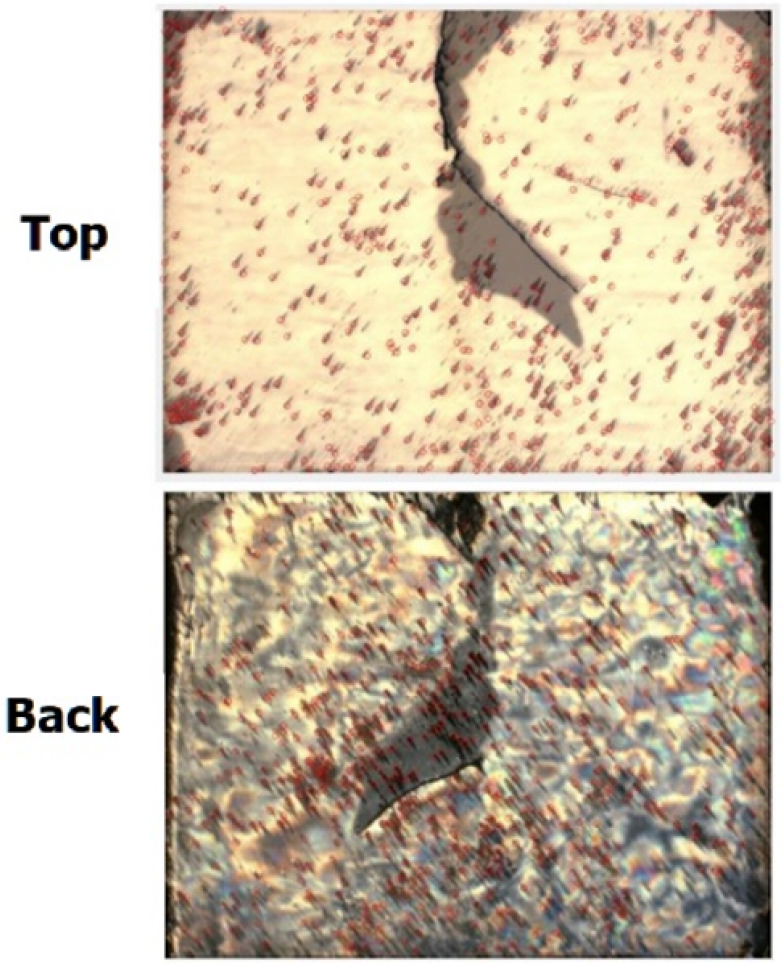

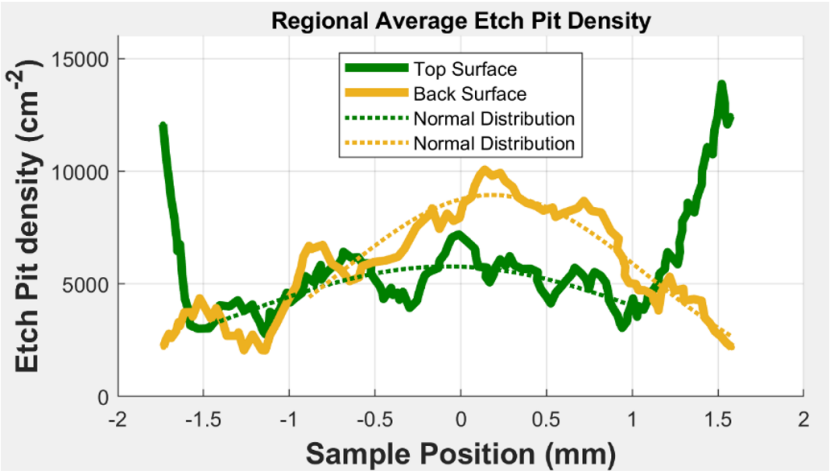

Figure 8.14: Regional etch pit density analysis based on a 50 µm window. The horizontal axis is defined with respect to the original interface location. Etch pits generated from surface cracks were ignored, as these effects were caused by polishing steps, not by the grown process.

XRC Line Scan Measurements

Boundary location and their spread as described in Section 7.4.2 were performed on all four plates including the back side of plate A. The Boundary position is observed to shift with respect to the original interface location as the sample is grown thicker at approximately the same rate as the stressed region on the birefringence measurements as well as the regional etch pit density measurements. The total shift of approximately 0.5 mm, pointed towards the direction of step flow growth as illustrated in Figure 8.15 is approximately constant over a cumulative grown layer of 2.5 mm.

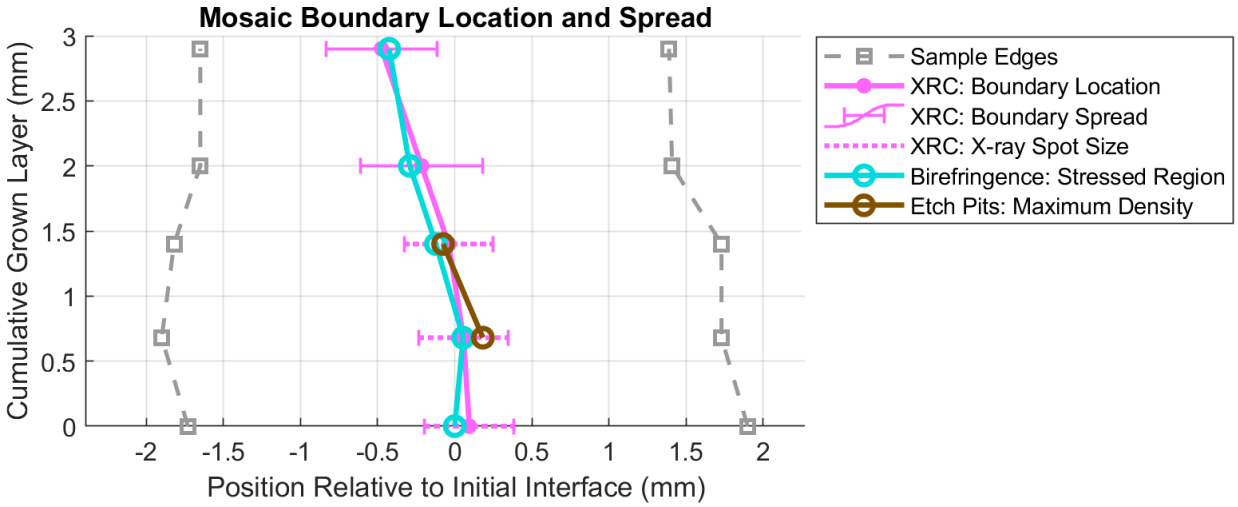

Figure 8.15: Boundary location and spread over cumulative grown layers as determined by XRC, Birefringence and Regional Etch Pit Density measurements

X-ray topography, and rocking curve measurements show how relative crystal misorientation decreases as the sample is grown thicker, but the effect is only observed over the Tilt-type rotation axis, one of the three orthogonal misorientation axes that had to be defined in order to describe this behavior. A possible mechanism for this effect is based on step flow growth over the interface induced by controlling the offcut direction on the mosaic seed. The Tilt-type misorientation between plates generates an effectively bent lattice at

the interface on which new layers are accommodated by the inclusion of lattice dislocations. Step flow growth across the interface has been determined to be necessary for this effect to extend across the grown surface. The two remaining misorientation axes, Torsion and Twist, are shown to increase slightly within an approximately constant range. When the average location of this highly defective and stressed boundary region is analyzed relative to the position of the initial interface, all three misorientation axes are observed to shift across the top surface at a relatively slow rate. Regional Etch Pit Density analysis, and Qualitative Birefringence measurements confirm the direction and rate of this shifting boundary. The overall spread of this defective region across the surface is also observed to increase slightly, but well within an approximately constant range.

8.2 Phase 2: Multiple Source Mosaic Tiles

After demonstrating how a single SCD plate can be grown from two tiles merged together, the next step in the approach is to repeat the process aiming for immediate increase in area by sourcing each tile from separate seeds. The project consisted of ongoing improvement on offcut adjustments, measurement techniques, analysis tools, and fine tuning of growth parameters. Instead of showing a series of experiments and parsing out individual results by partial success, this document will cover a long term experiment based on one 2x2 tiled mosaic substrate which covers a full set of observations and efforts related to this project. In this experiment, four 3.3 mm x 3.3 mm x 1.0 mm HPHT seeds were used as tiles. The offcuts depicted in Figure 8.16 were obtained on these four tiles. These misalignments were the closest that could be obtained with the as-developed technology, as the orientation adjustment procedures were not as well developed at the time this mosaic seed was assembled.

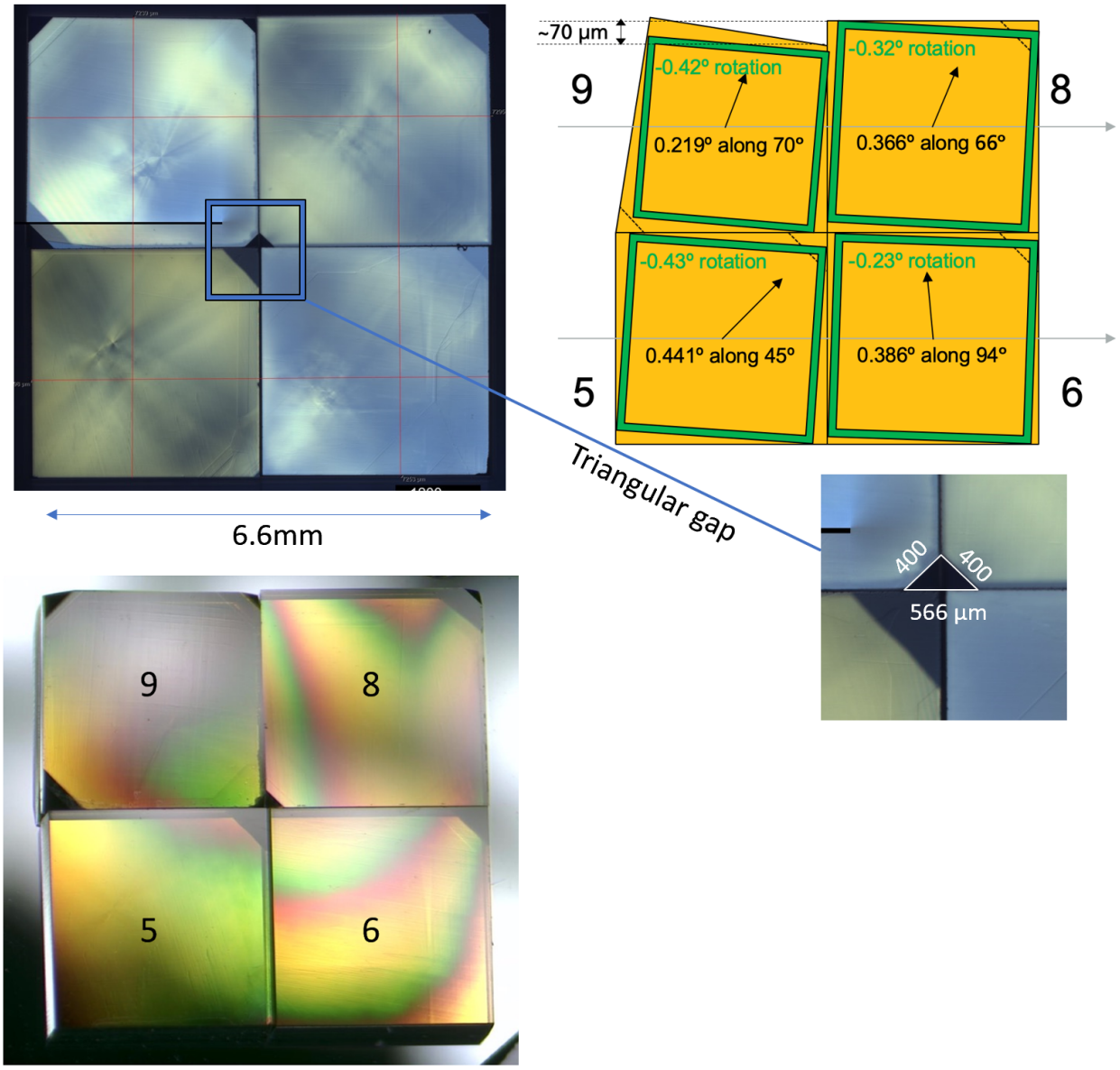

Figure 8.16: Four mosaic tiles and their respective lattice orientations. A 400 µm triangular gap can be identified between the four tiles.

Even though the values are relatively misoriented by current standards, the overall offcut was maintained towards one side of the sample as a way to analyze any potential effects of parallel or perpendicular step flow growth over tile interfaces. Figure 8.17 shows the resulting sample after growth under standard conditions with orientation measurements on both the original seed tiles, and the grown layer.

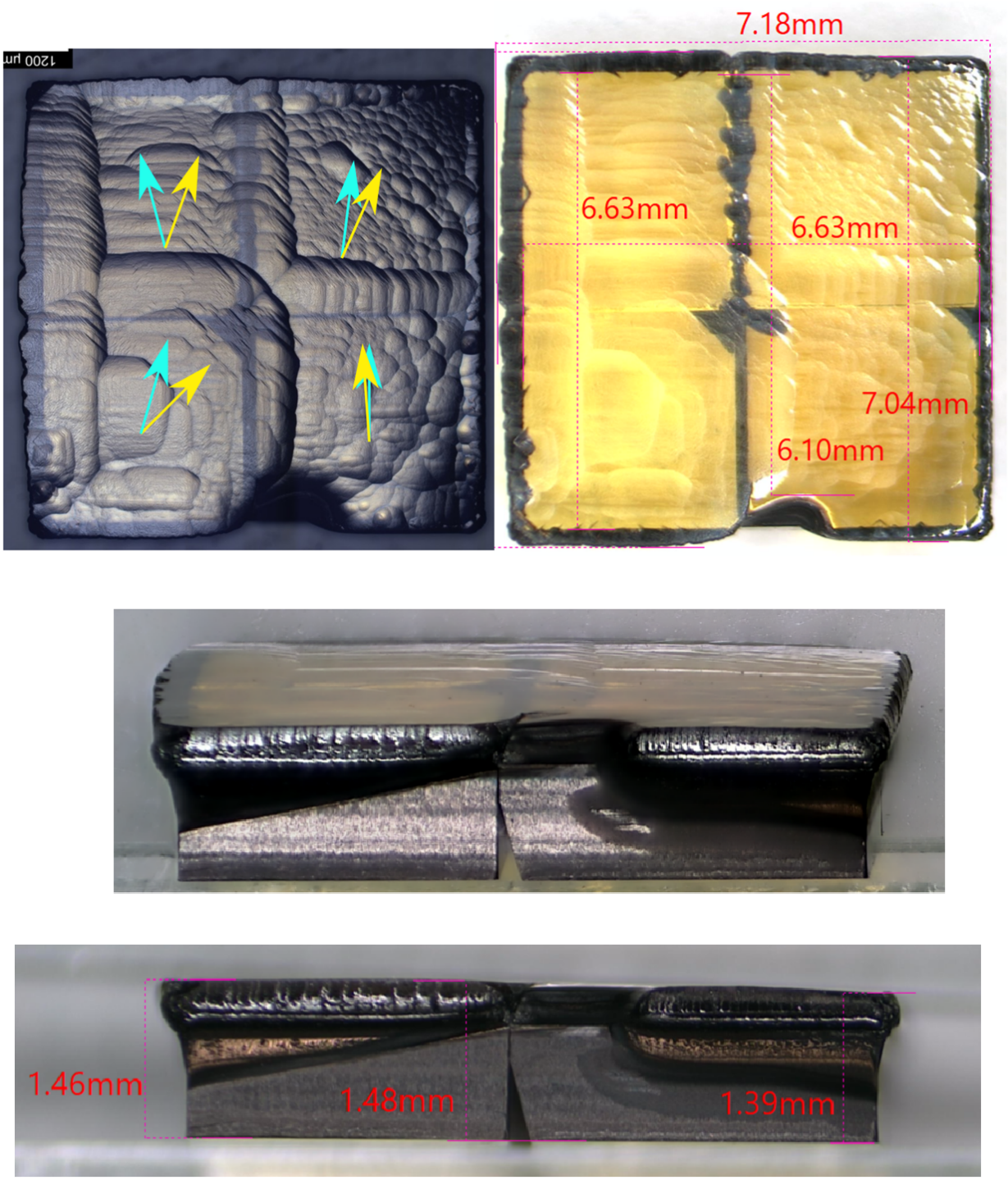

Figure 8.17: Smooth top surface and prominent lateral growth increasing the overall area of the mosaic seed. Yellow arrows represent single central point orientation measurements for each tile, and blue arrows represent the orientation of the grown layers.

The significant shift in orientation after a growth of just 400 µm is an indication of how lattice reorientation can be dynamically affected by multiple tiles. The effect is also highly dependent on the position relative to each interface. There are additional factors at play which only become more prominent as sample areas are increased, such as lattice bending due to temperature non-uniformities during the deposition process. These interactions and the boundary shifting mechanism had to be explored in greater detail. Analysis methods and tools developed so far were improved, as discussed in Section 7.4, as a critical approach when moving forward with this investigation.

Figure 8.18 shows the resulting linescans for illustrating XRC measurements at 100 µm spaced intervals as superimposed peaks with color-codes based on surface locations.

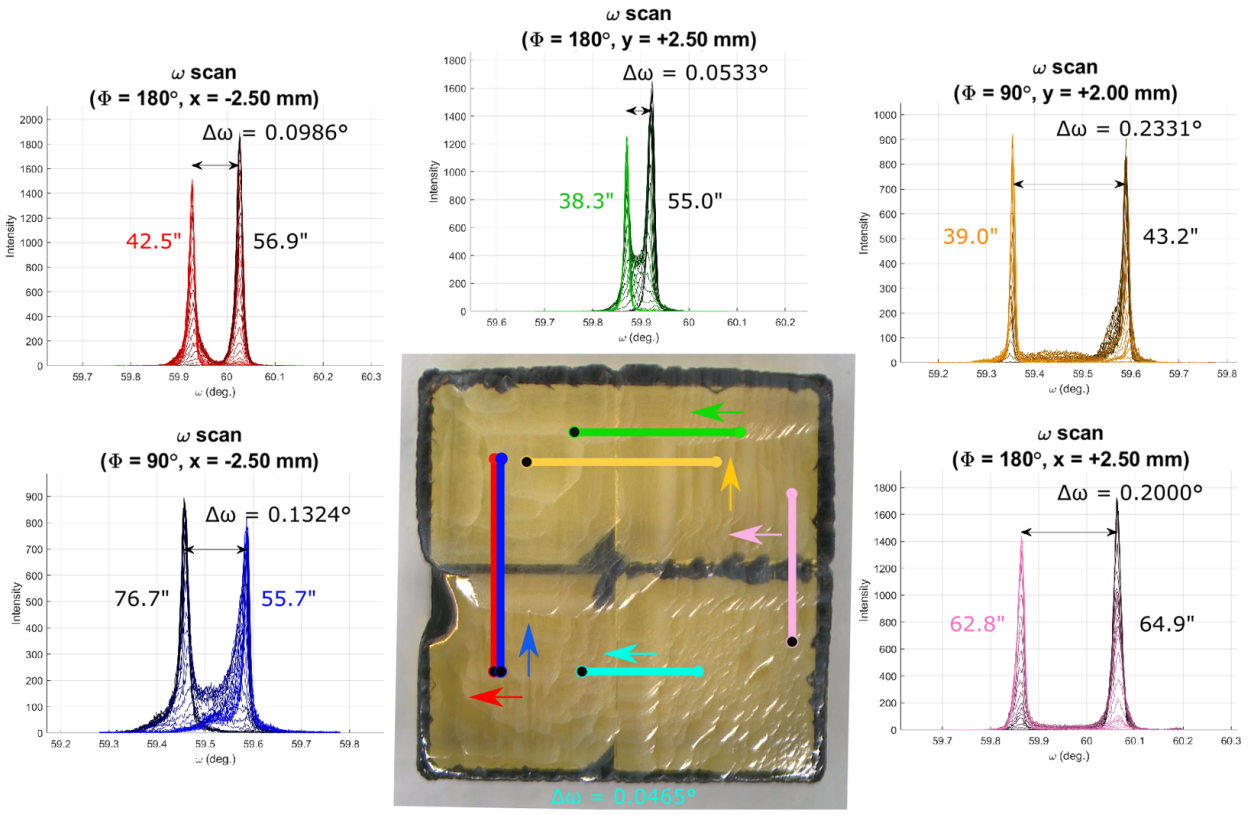

Figure 8.18: Linescans over grown sample color coded by location, arrows representing scan directions, and color gradients identifying which end point correspond to each peak.

The Mosaic Boundary quantitative analysis outlined in Section 7.4.2 was applied to this sample after each increase in total thickness as it was re-grown a total of five times. This sample was affected by multiple cracks during the process, but Figure 8.19 shows how the boundaries show significant improvement on at least one of the boundaries when analyzing the Mosaic Boundary Intensity, Location, and Spread.

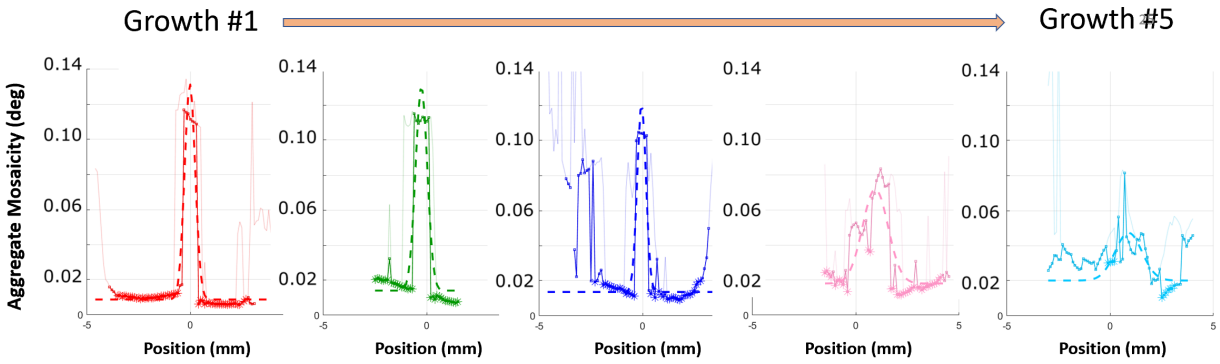

Figure 8.19: Mosaic Boundary measurements over multiple growths on line 'a' as identified in Figure 8.20.

A significant takeaway from these measurements is how the intensity of the boundary, a value most impacted by relative misorientation given the conditions of the mosaic seed, decreases for both Tilt and Torsion. In the case of line 'c' and line 'd' for the Tilt measurements of the last growth, as identified in Figure 8.20, the intensity of the boundary is decreased to a level indistinguishable from nearby single peaks. Another significant takeaway is that boundary shifting for Tilt type misorientations is again shown to be dependent on the offcut direction. In case of the boundary measured from a torsion perspective, all four boundaries appear to be shifting as well. Data from this sample shows how these lattice interactions can be very dynamic and there may be factors that still need to be considered, but the tools developed for this project have proven to be very effective in describing and quantifying behaviors observed when merging mosaic tiles.

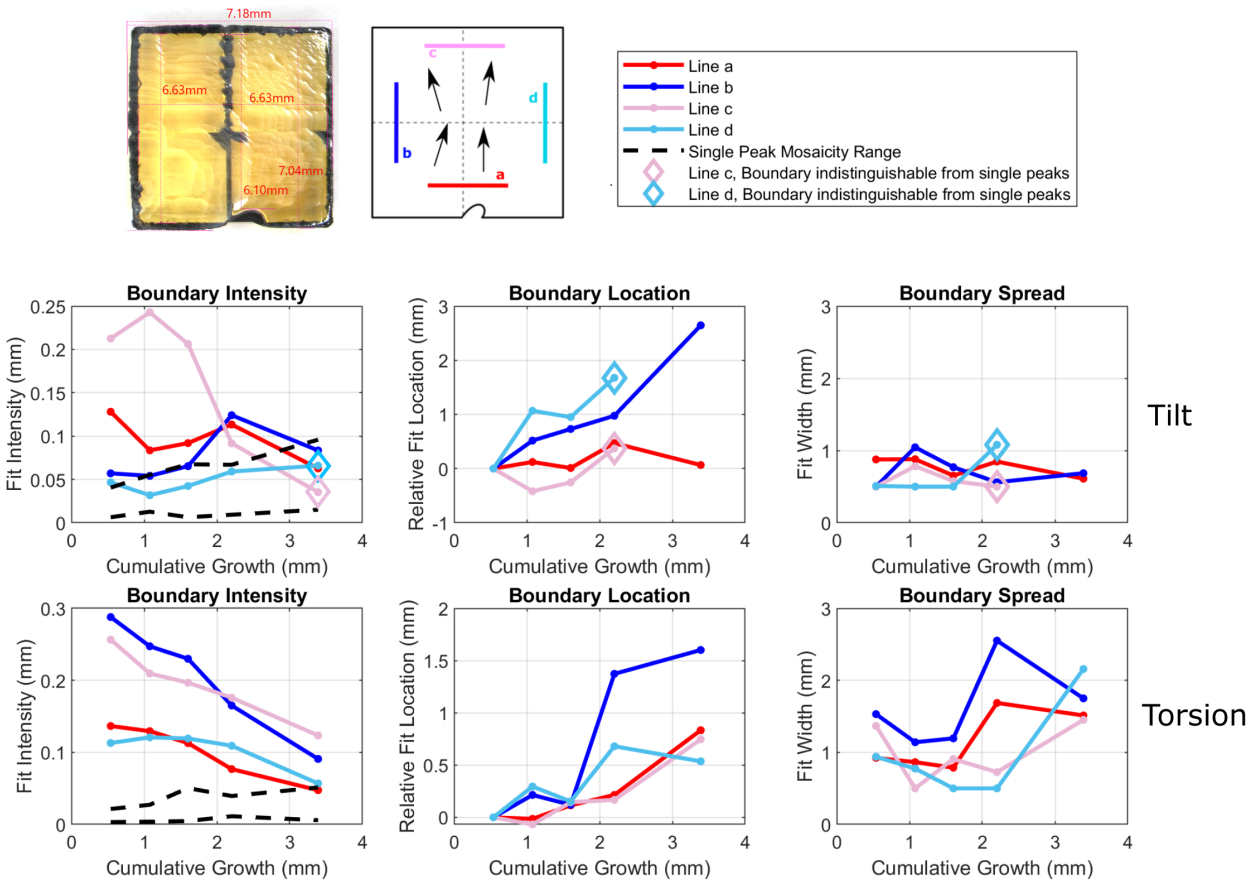

Figure 8.20: Parameters obtained from the Mosaic Boundary definition (Intensity, Location and Width) for both Tilt and Torsion type measurements on four interfaces over multiple growths. The intensity in Boundary Intensity for lines 'b' and 'c' is indistinguishable from adjacent single peaks in the Tilt-type misorientation after growth #4.

8.3 Phase 3: Large Areas

8.3.1 Approach

The most pressing problem on mosaic grown samples is cracking, as shared by every other report in the literature review. One source clearly identified as cause for cracks during this investigation is misorientation at the interface. The stress threshold for when this occurs is not yet determined, but evidently, the misorientation must be decreased as much as possible in the mosaic seed. One way to reduce the seed preparation process is to only attempt 2x1

tiles. This reduces the effort required for offcut adjustments as only one tile needs to be polished instead of three or more tiles. Figure 8.21 shows an example of the largest size 2x1 mosaic seed prepared for the project with area of 5 mm x 10 mm. The process parameters have also been developed and optimized for growth uniformity and lateral expansion. Figures 8.22 and 8.23 illustrate the as-grown sample. Figure 8.24 shows a higher magnification image where seamless growth has been obtained over the interface region.

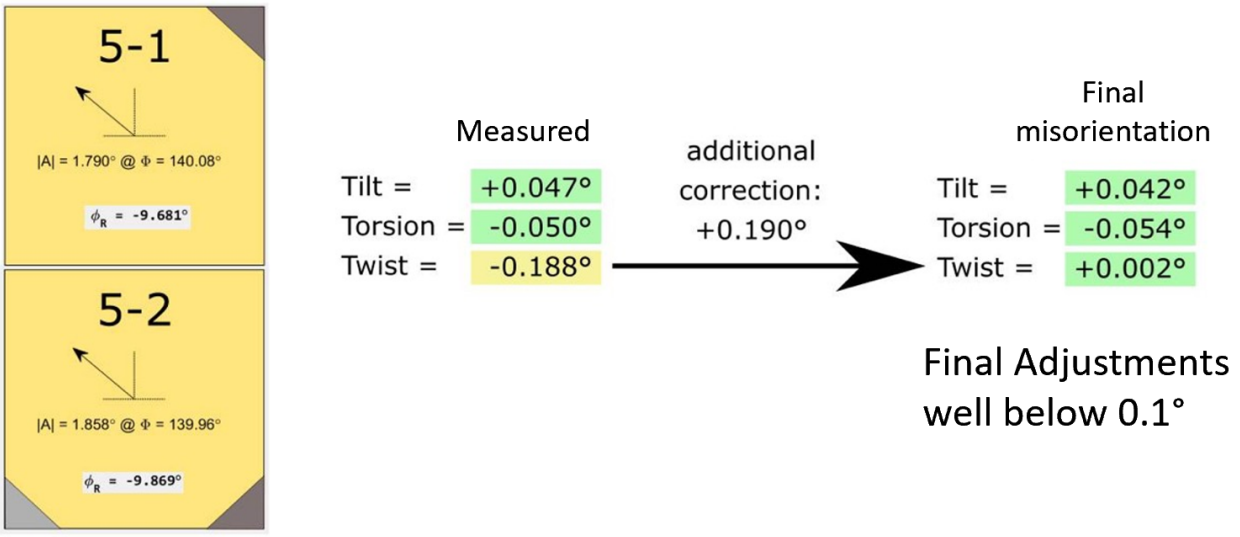

Figure 8.21: Diagram illustrating the final corrections on a closely aligned pair of tiles.

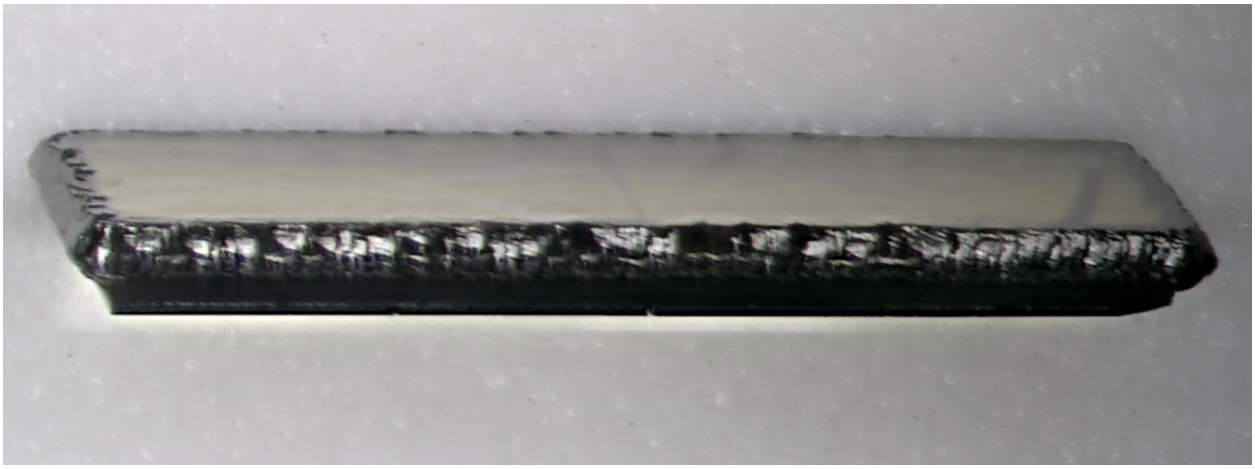

Figure 8.22: Low angle side view of as-grown sample.

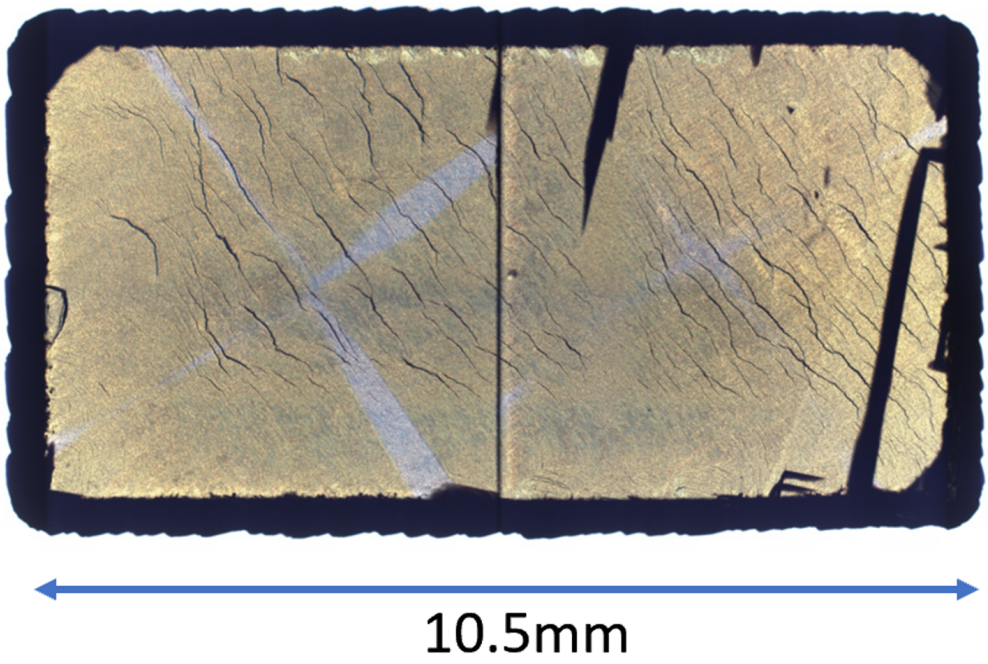

Figure 8.23: Top view of as-grown sample.

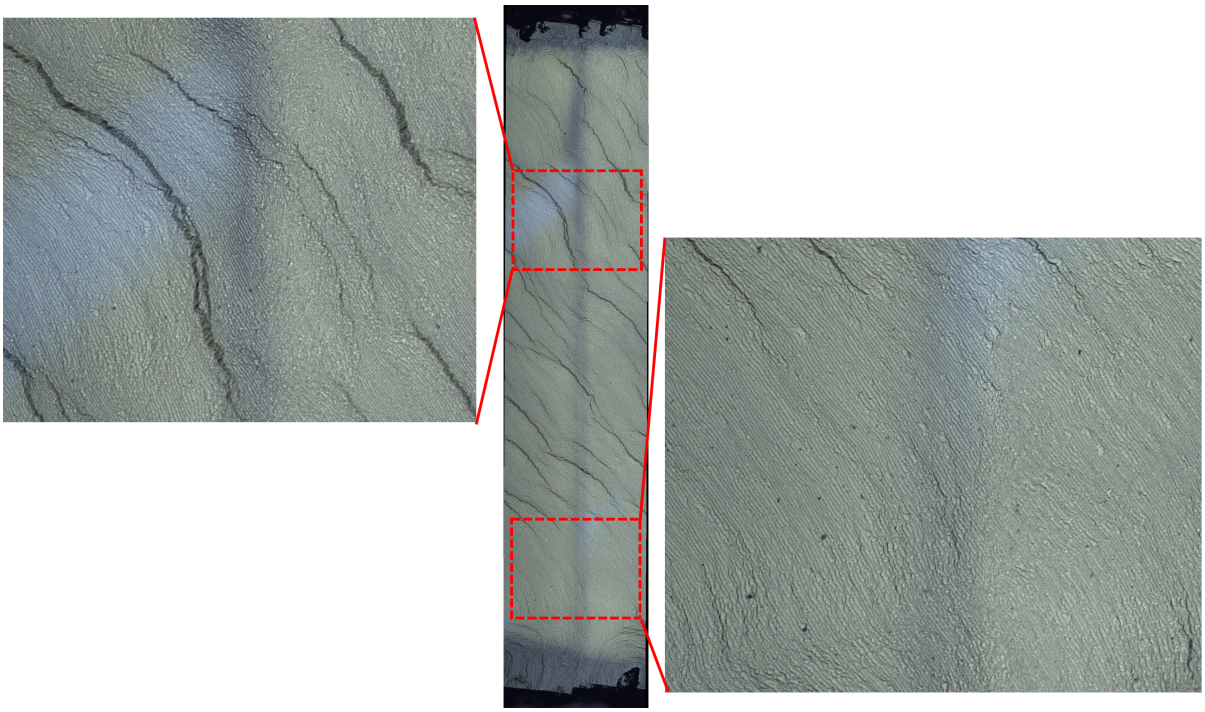

Figure 8.24: As-grown sample. Seamless growth over interface with no cracks, and smooth uninterrupted step flow growth.

This sample still has some cracks, but these do not appear to be related to the initial misorientation between the tiles. Figure 8.25 show the linescan measurements on this grown sample. Besides confirming low misorientation in the grown and back layers, and confirming the effectiveness of the PCD frame and plate in maintaining this misorientation, the data shows how cracks on the sample are caused by lattice curvatures, suspected to be induced by temperature non-uniformities, as discussed in the following section.

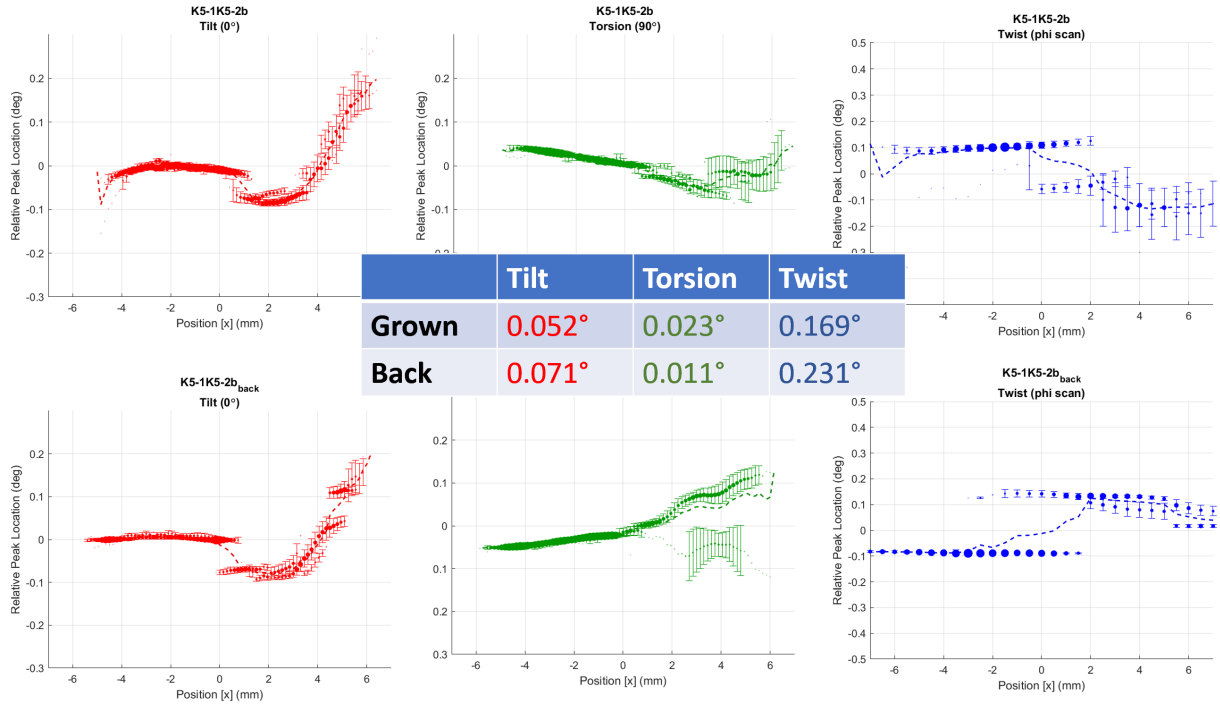

	Tilt	Torsion	Twist
Grown	0.052°	0.023°	0.169°
Back	0.071°	0.011°	0.231°

Figure 8.25: Full as-grown (top row) and back side (bottom row) XRC Linescan measurements with estimated misorientations at the interface.

8.3.1.1 Lattice Curvature

A deformed lattice, illustrated as a conceptual 2-D example in Figure 8.26, will lead to measuring shifting XRC peak positions across a sample. This type of lattice deformation is to be expected when there are significant temperature gradients within the sample [276]. If the temperature over the top surface is high relative to the back surface, the diamond

will expand such that plane defect edge dislocations might be introduced in grown layers, as illustrated in Figure 8.27. If this is the case, the deformation will remain fixed in the lattice as the sample is cooled down to room temperature.

If the net combination of dislocations across a sample is uniform over a certain region, then the rate of change of peak positions across a linescan would be measured as constant, generating an effective radius of curvature across the sample depending on the direction of any thermal gradients, as illustrated in Figure 8.28.

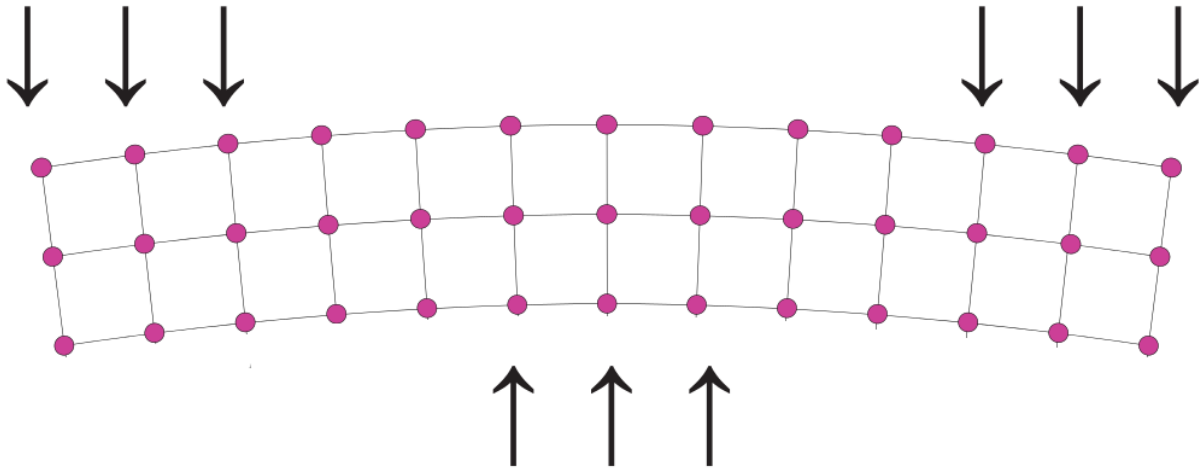

Figure 8.26: Lattice Bending. Image adapted from [275].

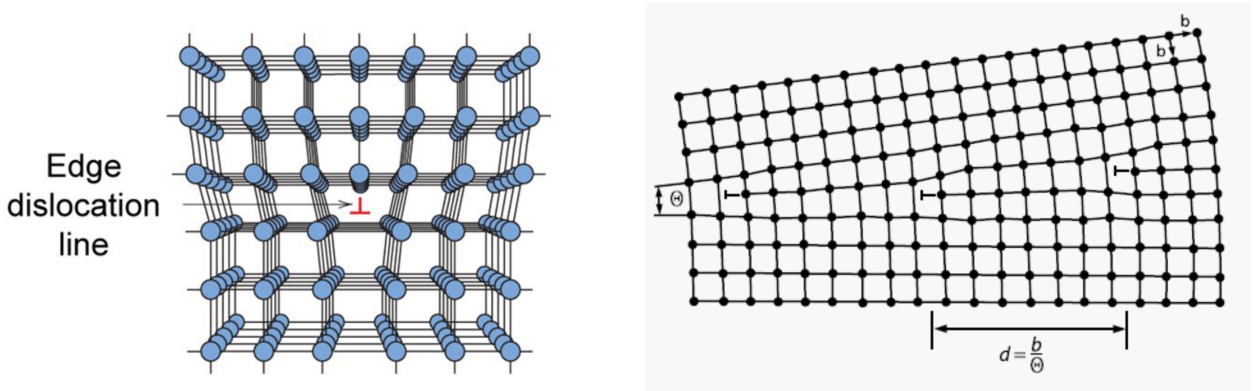

Figure 8.27: Edge dislocation defects introduced in grown layers [277], and resulting low angle (Θ) grain boundaries from an array of edge dislocations spaced by a distance (d), where (b) is the length of the burgers vector [278].

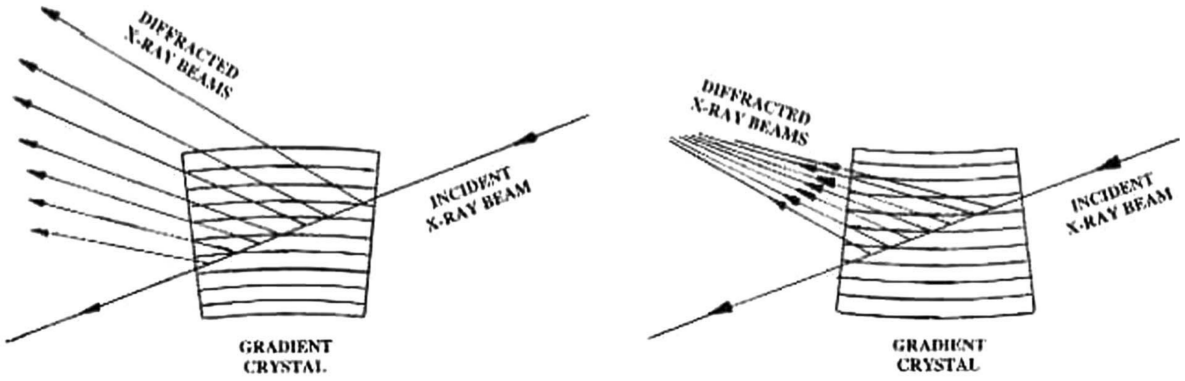

Figure 8.28: Thermal gradients over a sample for a "hot top" case (left), and a "cold top" case (right) and how this deformation affects XRC measurements [276].

Lattice curvatures can be approximated based on the rate of change in peak locations across a linescan, as illustrated in Figure 8.29.

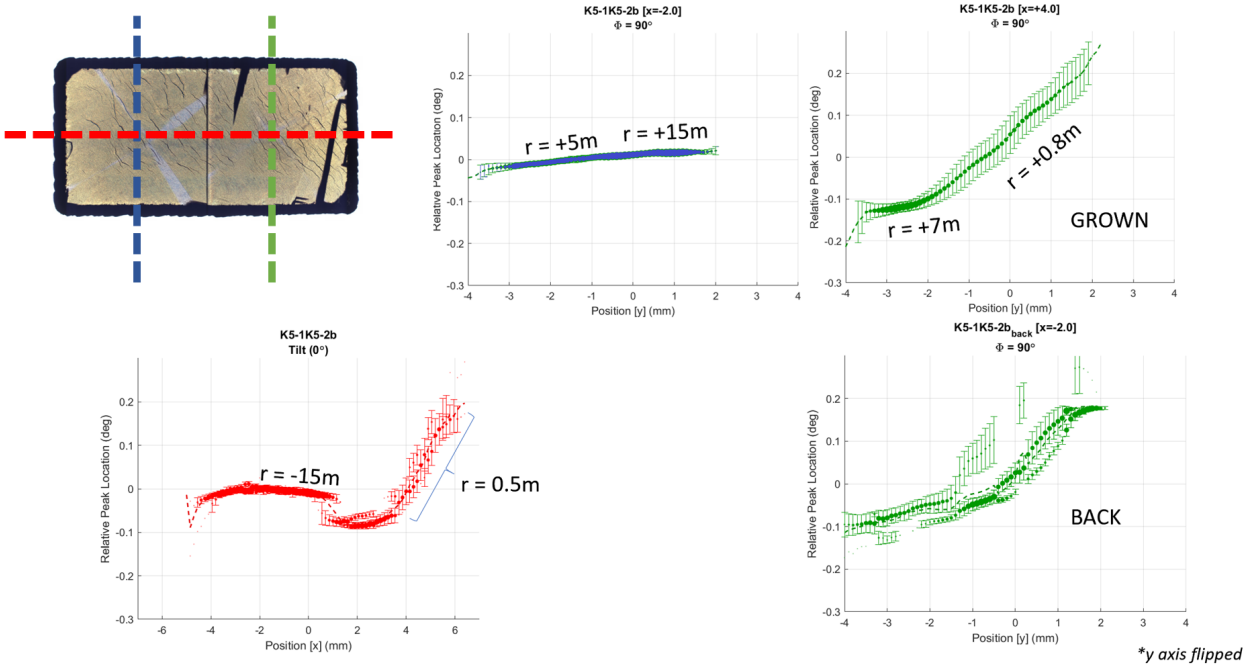

Figure 8.29: Radius of curvatures measured over different regions and directions in the sample.

Measured curvatures tend to be similar for grown layers and their back surfaces, suggesting that the entire sample bends during the deposition process and the structure is retained after

cooldown. Cracks in some samples, measured as multiple peaks per point on a linescan, may be detected in the back surface, but not the grown layer, suggesting stress from grown regions may crack the initial seed relieving stress on the overall lattice deformation. In more recent linescan measurements, bending effects are shown to have a more significant effect on lattice deformations than any resulting misorientations between mosaic tiles. These temperature gradients leading to bending and cracking could be caused by several factors. One significant effect to consider is non-uniform power distribution over substrates based on the shape of the discharge region. Preliminary experiments show how lattice curvature measurements in grown samples is dependent on the radial distance from the center of the sample holder, as illustrated in Figure 8.30.

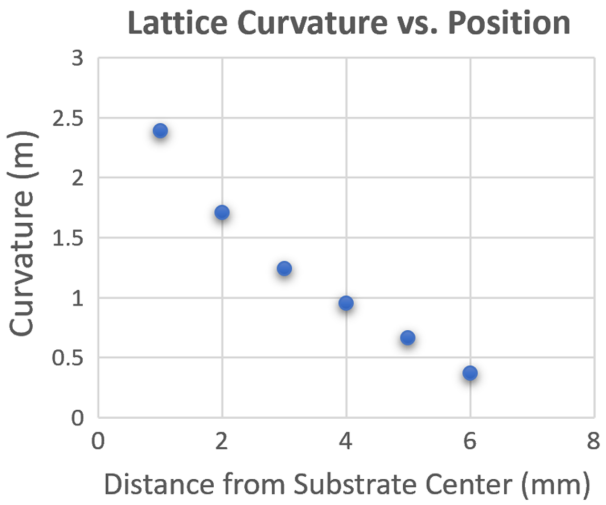

Figure 8.30: Lattice curvature of grown samples as a function of radial distance at a pressure of 240 Torr.

8.3.2 Pressure

One way to improve lattice curvature has been to reduce the operating pressure during the growth. Two experiments performed under similar conditions at different pressures resulted

in a dramatic improvement in lattice curvature over a single 3.5 mm wide HPHT seed as illustrated in Figure 8.31. There is no observable difference in the as-grown samples based on microscope pictures, but the radius of curvature for the sample grown at higher pressure is approximately 0.5 m. This curvature range guarantees cracking in larger substrates.

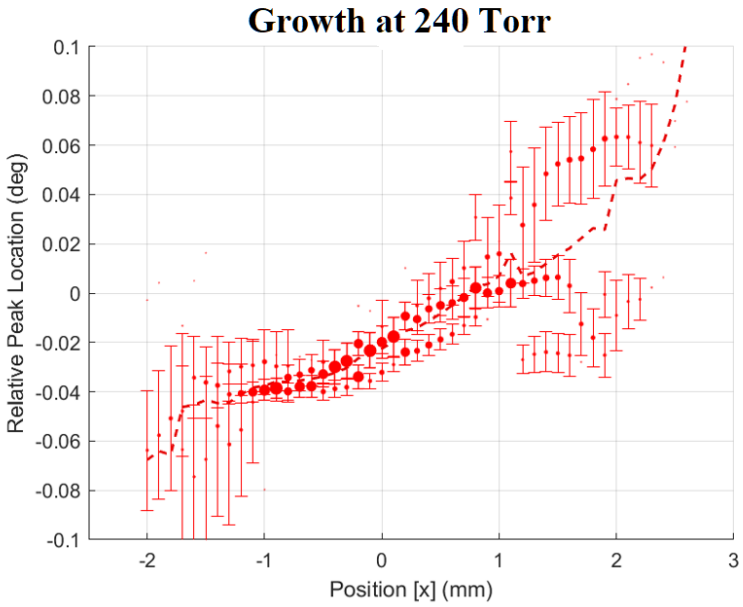

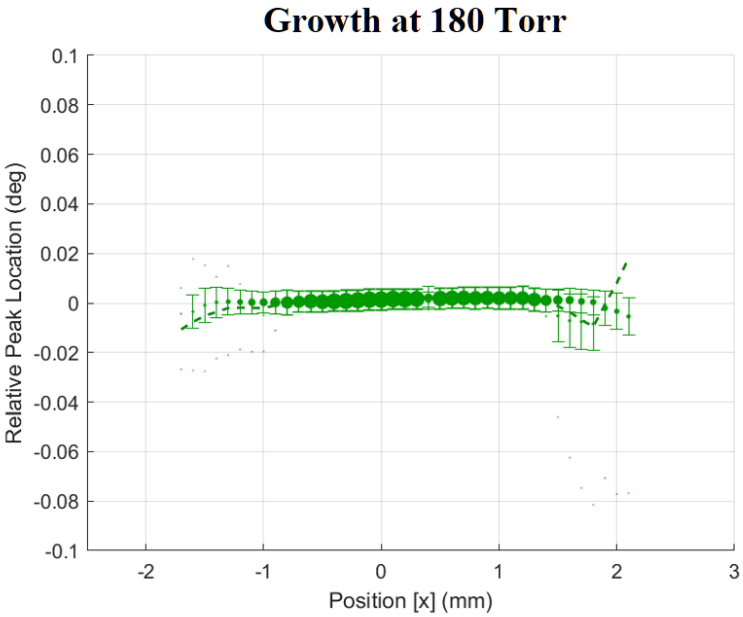

Figure 8.31: Samples grown at two different pressures. Higher pressure shows a lattice curvature or approximately 0.5 m.

8.3.3 Final Growth

A second pair of tiles was grown, framed, and polished to the same height as the first pair shown in Figure 8.22. Additional care was taken in terms of applying a lower pressure and other adjustments for improved temperature uniformity. The growth still resulted in cracks but only at the edge. The interface was again seamless and the two pairs were highly aligned as can be seen in Figure 8.32.

Figure 8.33 shows the mosaic seed assembly planarized and ready for deposition. This growth was performed at an even lower pressure of 150 Torr to cover more area with uniform power distribution, and a thicker holder than usual to promote more uniform temperature gradients.

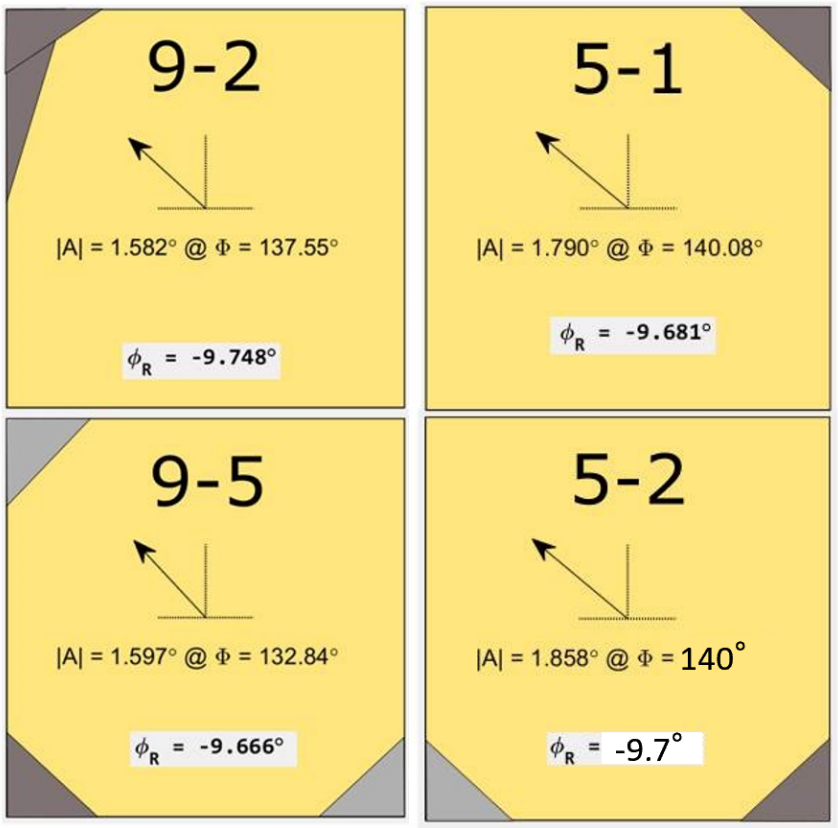

Figure 8.32: Seed alignment for samples K9-2K9-5 and K5-1K5-2.

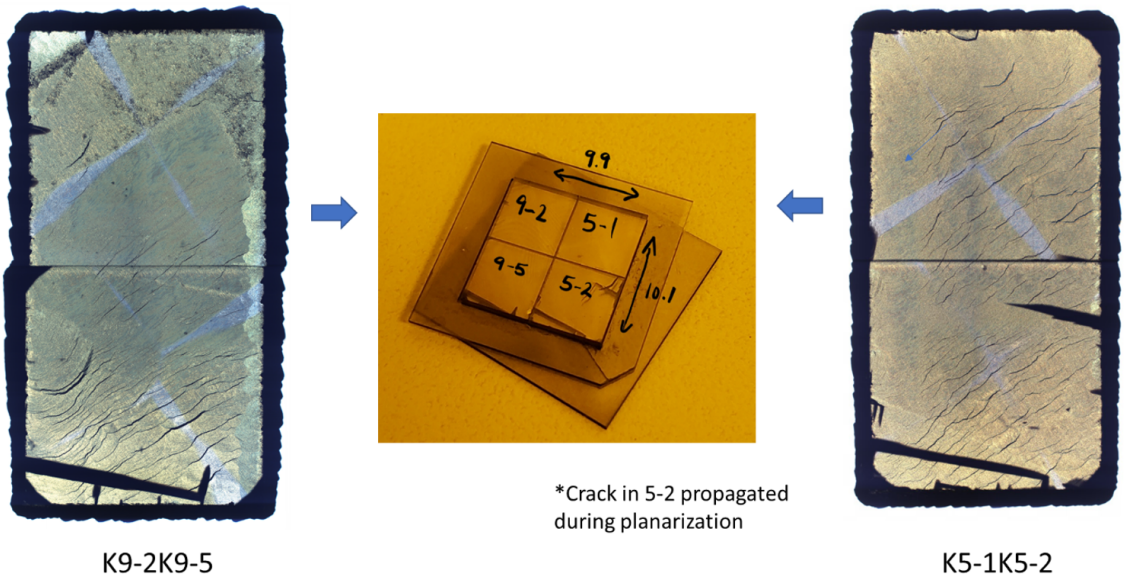

Figure 8.33: Mosaic tiling from the two 5 mm x 10 mm substrates.

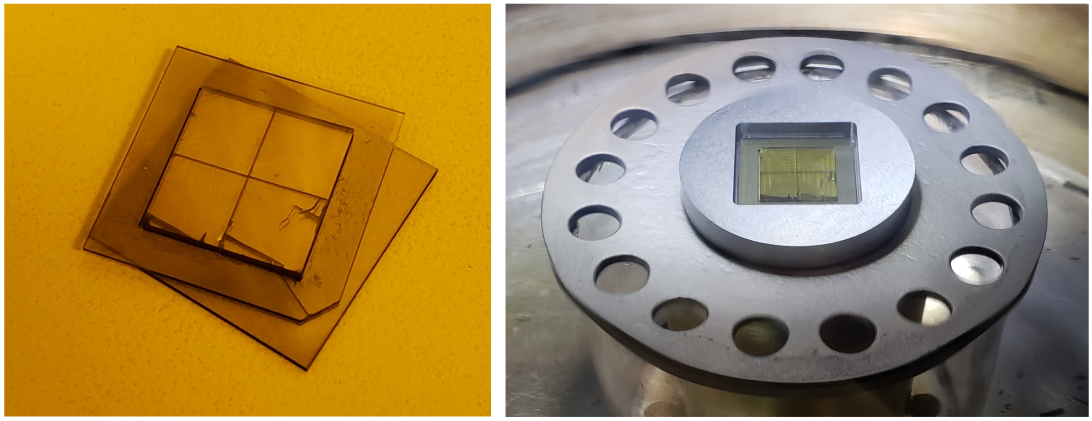

Figure 8.34: Large Area mosaic substrate, 10 mm x 10 mm ready for deposition.

The as-grown sample is shown in Figures 8.35 - 8.37. Growth on this four tile mosaic was successful as appreciated from high magnification pictures of the boundary region in Figure 8.36. The new interface region again shows smooth step flow growth as seen previously within each underlying pair. This consistency suggests that the main problem of creating smooth boundaries is now effectively under control.

Figure 8.35: 10 mm x 10 mm mosaic substrate grown from four diamond tiles.

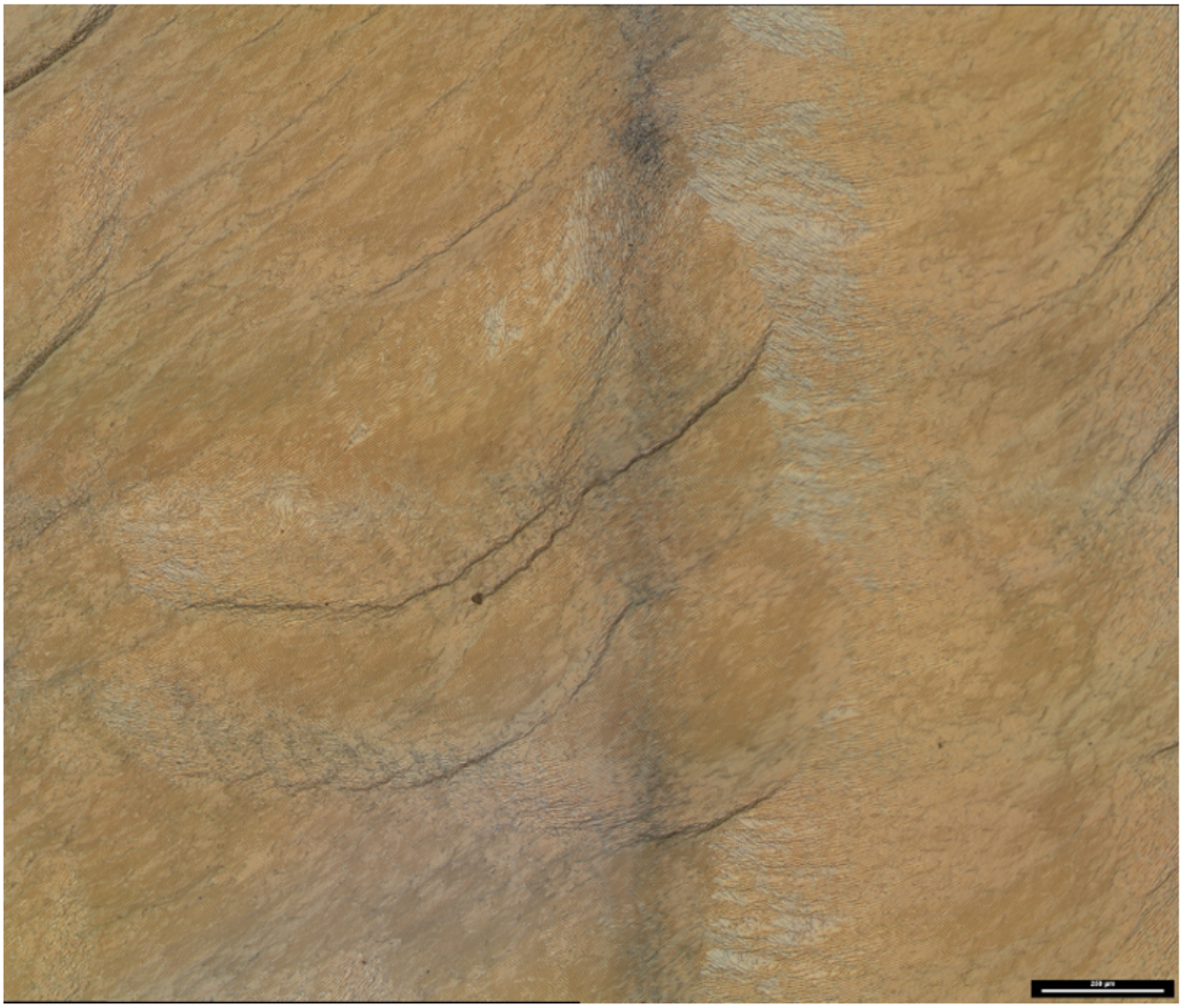

Figure 8.36: Mosaic Boundary at higher magnification showing consistently smooth step flow growth over the interface.

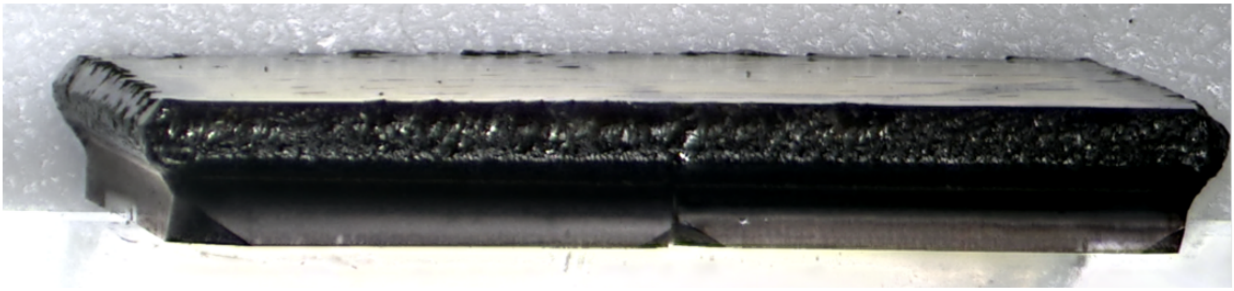

Figure 8.37: Low angle side view of as-grown sample.

Cracks on the sample propagated after performing additional polishing as the sample was being prepared for preliminary electrical measurements. Line scan measurements suggest that this effect originates from the stress caused by underlying lattice curvatures, not from the boundary regions. The remaining issue to solve now is ensuring temperature uniformity to reduce lattice bending as much as possible. Other issues, such as surface roughness on the top left corner of tile 9-2 as labeled in Figure 8.35, was caused by poor surface quality on the initial HPHT seed. These details are easily solved by repeating the process with higher quality tiles. The success of this last experiment is based on the demonstration that the most significant problem in the mosaic technique has been effectively solved. Adjusting orientations and maintaining tile alignments during growth are no longer limiting factors in the plate production process.

Chapter 9

Plate Production by Ion Implantation and Lift-off Technique

9.1 Introduction

Angle corrections by polishing has been proven effective, but it is still arguably a very labor intensive process. Given how sample framing, planarization, measurement techniques and rotation corrections have been well developed by our group as part of this investigation, an ideal technique for producing mosaic plates is the cloning technique, as described in detail in Section 3.3.2. This chapter covers the progress made during this investigation towards implementing this technique.

9.2 Low-Energy Ion Implantation

As covered in Section 3.3.2, the ion implantation and lift-off technique has only been reported to be successful at energies of 3 MeV in order for the lattice to retain the structural integrity needed for quality CVD diamond growth. Several options for particle accelerators operating at this energy level are available, including a facility at Western Michigan University, but

this accelerator is only accessible for experimental research. The goal for this project is to be able to replicate this process at industrial levels, but this is only possible with commercial facilities operating at relatively low energies of 180 keV.

The approach used during this investigation was to revisit the previously reported result on shallow implantations. We can estimate the penetration depth of low energy ions based on the profiles calculated for high energy implantations. At low energies, the nuclear stopping power is approximately linear [25], and we also know that the first order approximation of the electronic stopping power at low energies is also linear as estimated in Figure 3.18. By superposition, the penetration depth of low energy ions can then be estimated as a simple linear interpolation between zero and the first data point in Figure 3.20. Using this approximation, carbon ions bombarded onto a diamond lattice with an energy of 180 keV will result in a penetration depth of 180 nm. Figure 3.21 suggests that the standard deviation of this penetration depth is too wide and the technique will inevitably fail at lower energies as the straggle region would easily extend onto the surface. The issue is that it is unclear whether the shape of this distribution at high energies is caused by the instrument or by ions interacting with the lattice. SRIM simulations, as illustrated in Figure 3.20, suggests that the straggle is independent of the incident energy and that wide standard deviation reported at high energies is only present in the high energy ion source used for the study. If the ion source is capable of bombarding carbon at a sharp energy level of 180 keV, simulation data predicts a relatively thin straggle region of approximately 36 nm, which should leave plenty of room for the top surface of the sample to retain most of its crystallinity.

9.3 Top Surface Etching

This depth is still relatively shallow given how the standard H_2 etching process would need only 130 seconds to remove the crystalline layers at a reported etch rate as high as $5\,\mu m\,h^{-1}$ for the Type C deposition system used in this project etching at 2.5 kW and 1000°C [7]. The solution developed for this investigation was to modify the standard ramp-up time through a series of iterations with the goal of limiting the exposure of this relatively thin layer to high temperatures and high power from the H_2 discharge region. A new ramp-up sequence was designed such that CH_4 gas was added to the mixture within 6 minutes at much lower temperature and power. This ramp re-design was applied to shallow implanted samples, and the results are shown in Figure 9.1. The damaged layer was successfully conserved. Enough crystalline material at the top surface was retained to ensure homoepitaxial growth. No visible dislocation defects other than rough edges, typical for as-grown samples with sub-optimal pocket configurations. The result confirms low energy ion implantation combined with a re-designed ramp up process as a viable alternative for plate production.

9.4 Plate Separation by Electrochemical Etching

The electrochemical etching process developed by our group is based on maintaining two boron-doped PCD electrodes set to generate a current of 10 - 60 mA flowing through a sample with a graphitized layer immersed in a KCl aqueous solution. The electrochemical process does not involve any oxidation reactions, as the etching mechanism is better described as physical ablation of the graphitic region [145]. This underlying process, as well as a description of the equipment has been already been described in detail from a previous project where the system was first developed [145].

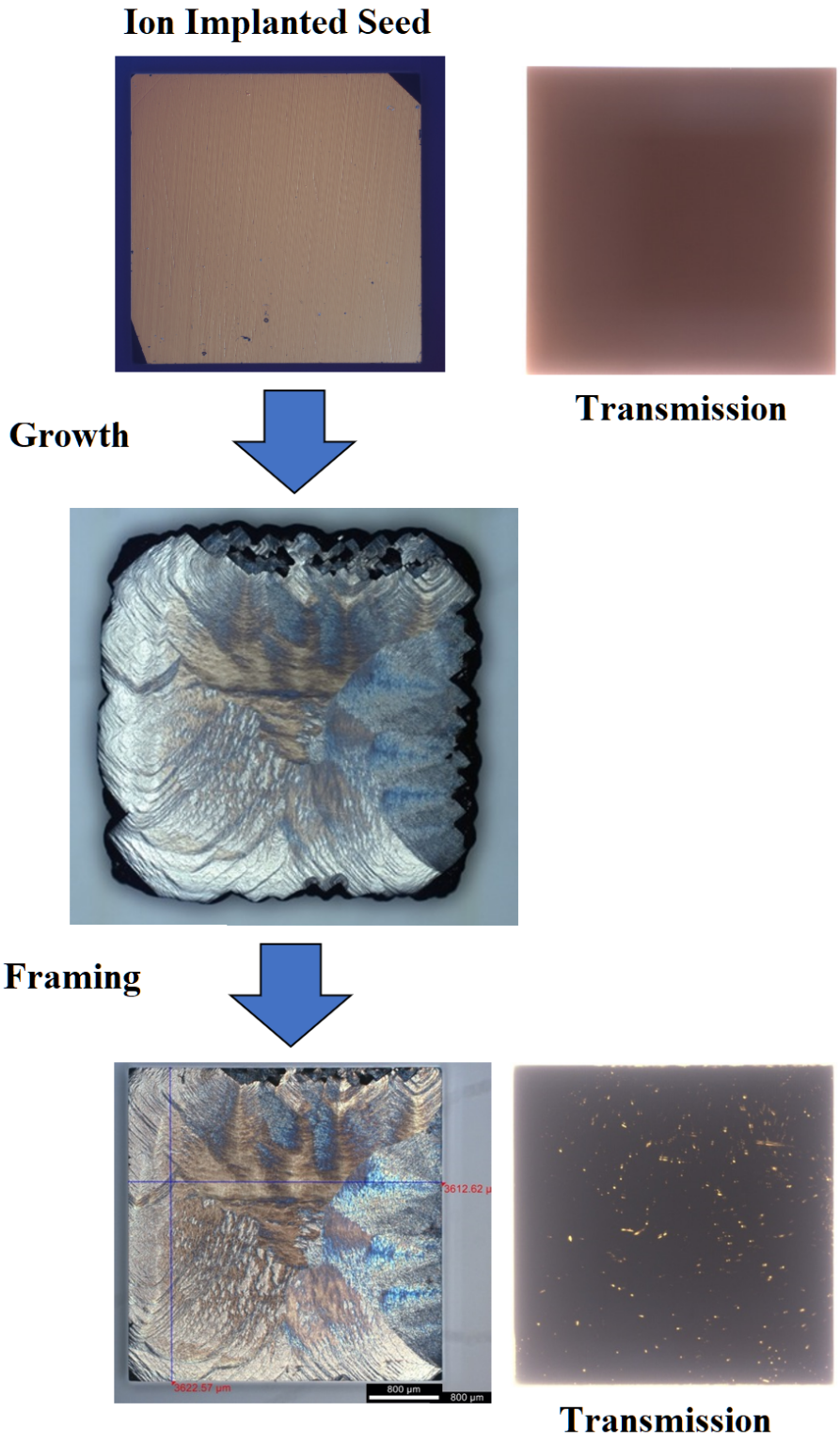

Figure 9.1: Sequence showing a characteristically opaque $3.5 \times 3.5\,\mathrm{mm}^2$ ion implanted seed, up to a mostly opaque grown and framed sample with a few pinholes which penetrated through the damaged layer during ramp-up.

If the voltage between the electrodes is kept between 300 - 600 V, accelerated ions impact the sample with kinetic energy greater than the binding energy of carbon atoms within a graphite lattice, but not enough energy to overcome the binding energy of the diamond lattice, effectively ablating only the damaged layer. If the region is thick enough, grown plates are eventually separated from the underlying seed with minimal kerf loss. The latest iteration of the system developed so far can separate a $3.5 \times 3.5\,\mathrm{mm}^2$ plate in $\sim$60 h, and $7 \times 7\,\mathrm{mm}^2$ plate in $\sim$200 h. Figure 9.2 captures transmission images of a sample during an electrochemical separation process.

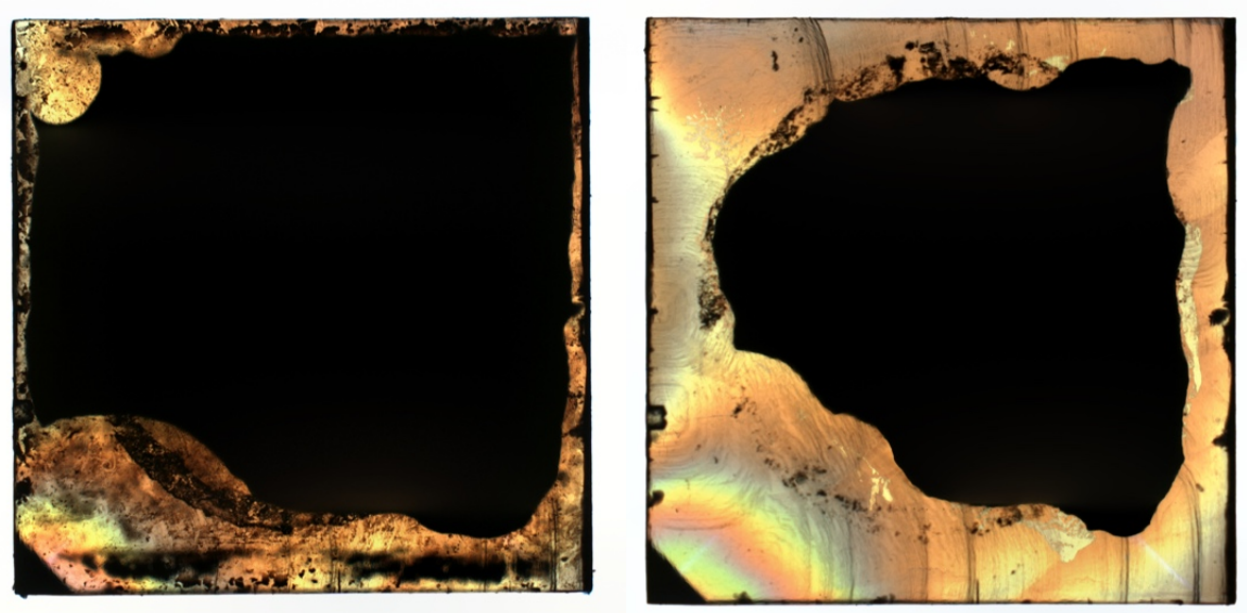

Figure 9.2: Transmission image of a sample as captured after 10 hours (left), and 30 hours (right) of an electrochemical etching process. The black areas reveal portions of the graphitic layer still remaining on the sample.

The sample shown in Figure 9.1 was electrochemically etched and polished, producing the plate shown in Figure 9.3. The sample has some cracks on two sides from the process. Strategies to avoid this type of damage in future runs are currently under evaluation.

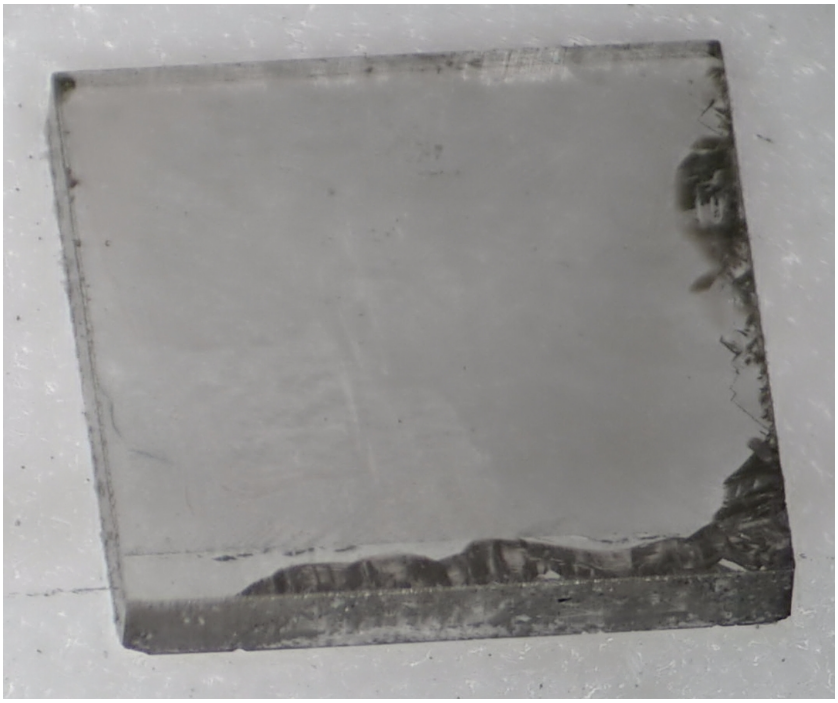

Figure 9.3: Separated CVD grown plate, 400 µm thick.

9.5 Raman Measurements

Raman spectroscopy measurements were performed on this plate at the CCDC Army Research Laboratory to confirm its crystal quality. The FWHM of the 1332 cm^{-1} peak, as illustrated in Figure 9.4 was comparable to a highly crystalline diamond sample from Element Six [279] used as reference.

9.6 XRC measurements

Mosaicity line scans were measured on the initial seed, the as-grown sample, and the recovered seed as illustrated in Figure 9.5. This data shows how the center of the sample has higher quality than the edges. This could be caused by the observed cracks or other factors such as lattice bending. This effect is unlikely to be caused by the ion implantation process and will be improved by fine-tuning growth conditions. The second observation is how the crystallinity

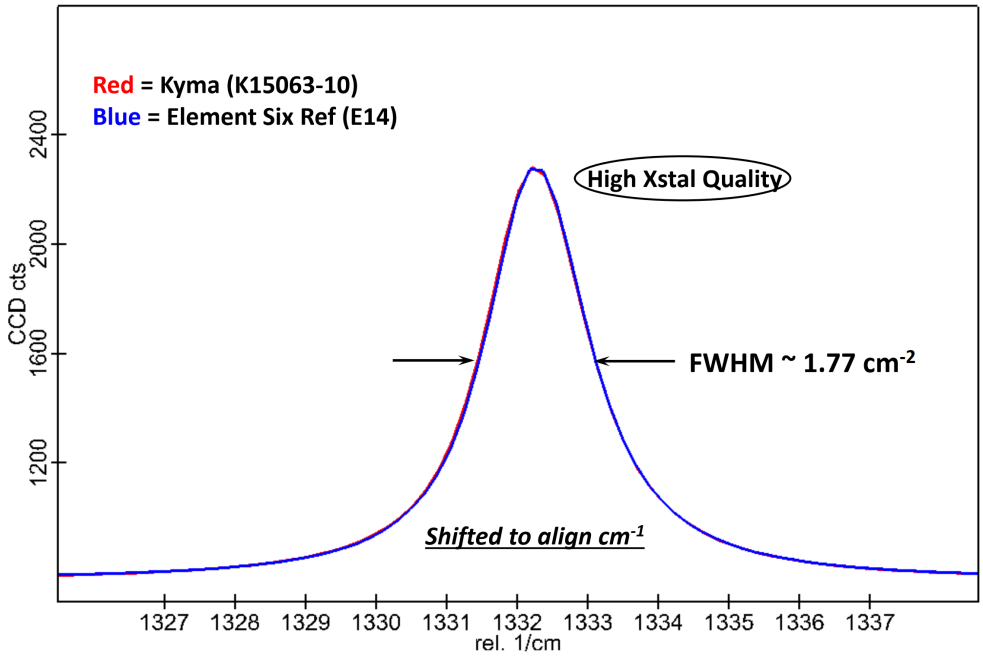

Figure 9.4: Raman Measurements on the electrochemically separated plate as compared to a high quality Element Six reference sample.

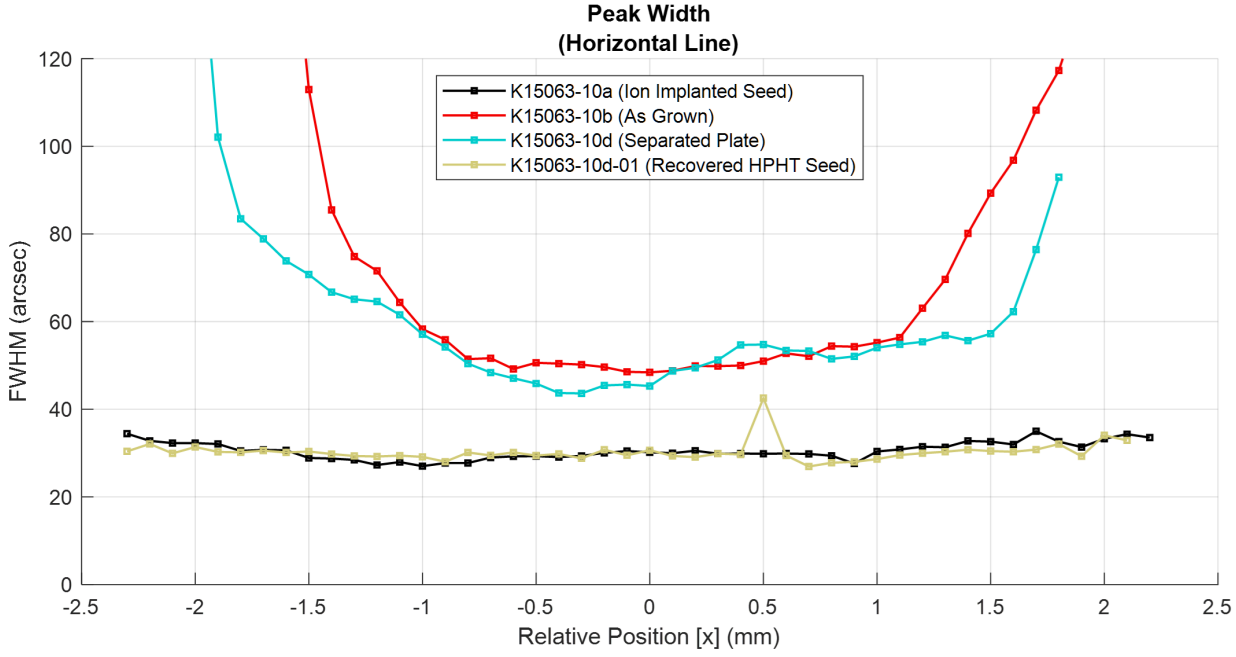

Figure 9.5: XRC peak widths measured along the ion implanted seed, as-grown sample, recovered seed, and separated plate.

of the recovered seed is virtually identical to the ion implanted seed. This result confirms how the damaged region did not measurably extend to the top surface during the low energy implantation procedure. Since the plate separation process did not produce any significant damage to the underlying seed, the process is now repeatable, where many plates can be produced from a master plate. The ion implantation and lift-off technique based on shallow implantations is now demonstrated to be successfully viable and ready to be applied on grown mosaic samples.

Chapter 10

Mosaic Growth Parameters

Summary: Mosaic Requirements

Compiling results for this project is relatively straightforward. Instead of listing all the cases where the mosaic technique fails, a more efficient approach is to list the minimum conditions which translate to a set of required parameters for successful large area mosaic growth. The resulting list can be sorted as a series of pre-requisites that need to be fulfilled in sequence. Failure to meet these conditions leads to either no merging at all, cracking, or at best, a sub-optimal interface between tiles. The list can be summarized in four main sections, where some examples from this investigation are compared to previously reported results. The list is arranged in this specific order with a summary of each analysis outlined as follows:

1. Geometric Alignment.
2. Crystallographic Alignment.
3. Growth Conditions.
4. Scaling.

10.1 Geometric Alignment

These conditions are to be expected by definition. All tiles should be geometrically aligned. This first set of parameters refer to actual placement of tiles relative to each other as the first necessary condition for successful mosaic growth.

Gap Between Tiles

Macroscopic holes might be considered a theoretical issue at an atomic scale, but gaps have been known to be filled by lateral growth from all sides with relatively high quality [186]. An example of this effect from this investigation can be appreciated in Figure 8.16. When applied to a single interface, small gaps between tiles tend to be bridged and are not a problem, but one result from this investigation is that a large gap of 50 µm did not merge at all. This separation was also reported by Yamada et. al. on one of their first reports as the maximum distance between each piece [231]. Every other publication with values at or below this level report no issues [236, 237], but our conclusion is that a limit does exist, therefore, the distance should be reduced as much as possible.

Step Height Difference

This parameter is best described by Findeling-Dufour [233,237], where any macro-step between tiles should be facing towards the step flow growth direction. Boundaries are guaranteed to fail if this requirement is not met. The maximum height difference is not yet determined, but this limit certainly exists. Wang et. al. have concluded that this difference is actually necessary and favorable [239]. They argue that it leads to a relative growth advantage and is precisely the mechanism that drives overgrowth. Based on our analysis, this type of

overgrowth, also reported by other groups [238] is only superficial. Orientation measurements clearly demonstrate that the orientation of the underlying tiles tends to be conserved. The discrepancy between step flow growth direction and actual orientation leads to internal stress that becomes worse with larger relative misorientations. For this reason, growth over more than two tiles makes it difficult, if not impossible, to coordinate cooperative growth fronts. This is presumably the reason why the 40 mm × 60 mm grown sample composed of 24 tiles from the Yamada group illustrated in Figure 3.55 resulted in an unusually stressed and cracked as-grown plate despite their established control of growth parameters over large areas. Based on the set of results in this present investigation, geometric considerations are necessary, but not sufficient for mosaic growth.

10.2 Crystallographic Alignment

Published literature on the Mosaic Technique has been remarkably limited in terms of considering crystallographic alignment. Most of the publications have attempted multiple-tile mosaic growth with no prior adjustments to the individual tiles. The ones that did not crack, are highly stressed [238, 239] and the only indication that tiles have successfully merged is evidence of step flow overgrowth. The one case where the four tiles held together without cracking were assembled with relatively small misorientations [242].

The cloning technique was successful at increasing substrate areas substantially as it virtually eliminated two of the three misorientation types: Tilt and Torsion. Twist adjustments were not considered during their project, but further control over orientation was listed as a possible improvement and left for future work [231].

From our present investigation, the cases where samples are grown with relatively high misorientation will tend to crack in the first growth, second growth, or planarization step. Grown samples with stress originating from relative misorientations are guaranteed to fail eventually. As a result of the set of experiments, misorientation is the next critical set of parameters to consider. Findeling-Dufour suggested a minimum misorientation of 2° [233], but we consider this value is still too high by at least an order of magnitude. Mosaic growth was only successful when the relative misorientation has been set below 0.2°.

10.3 Growth Conditions

Shifting Boundary

Once the mosaic seed is assembled, growth conditions must be set such that the resulting boundary does not remain in place, but shifts away from the original interface. The only way this can be achieved is by incorporating a lattice offcut. This has been known since the early days by Janssen et al. [224], with the concept illustrated in Figure 3.47. Findeling-Dufour et. al. confirmed this direction should be combined with the macro-step direction [233]. Yamada et. al. did not confirm an actual shift, but they did observe an improvement in boundary quality in the offcut direction, as illustrated in Figure 3.53 which was attributed to step flow overgrowth. This present investigation has produced tools to define and measure this boundary region as it shifts and extends over mosaic interfaces, as covered in Chapter 7, with the effect illustrated in Figures 8.15 and 8.20.

Uniformity and Area Conservation

Mosaic plates must be uniformly grown throughout this boundary shifting process. This implies optimizing a controlled deposition system with high thermal uniformity. Only two groups have reported success in fabricating large area plates, the Japanese group led by H. Yamada with two inch plates [234], and the newest publication by a Chinese group led by G. Shu where they have reported one inch wide diamond substrates [247, 250]. The pictures illustrated in Figure 3.70 are impressive, but no type of orientation measurements are provided demonstrating uniformity over the crystal lattice. The group concludes that misorientation is inevitable and perfect alignment is practically impossible.

The technology used in this present investigation is based on previous work where pocket configurations in sample holders have been optimized for quality and uniformity [7], but scaling to larger sizes requires additional development as the parameter space is very wide, as discussed in Chapter 4. The value we have estimated to be close to the cracking threshold is lattice bending where the radius of curvature is greater than 1 meter. This value is precisely the curvature reported by Kim et. al. with the 1-in diameter Kenzan diamond fabricated by heteroepitaxy. The wafer, illustrated in Figure 3.33, cracked during photolitography.

10.4 Scaling

Assembling a new mosaic seed for every plate produced is not an option, as covering all these steps is not a simple process. When scaled to large sizes, laser ablation is no longer a viable option to separate grown layers due to Kerf losses. The only reasonable solution for large area plates developed so far is ion implantation and lift-off. This process is known to produce high quality substrates with no inherent size limitations. In this present investigation, the process

has been demonstrated to be effective and straightforward even under shallow implantations as discussed in Chapter 9. This energy range is commercially available, making the process scalable up to industrial levels.

10.5 Summary of Mosaic Requirements

The sequence of mosaic requirements is organized in Table 10.1, where each parameter is listed next to the technology applied for each step during this investigation. Results for every condition are compared with results published by other groups.

					Geis 94	Janssen 95	Findeling 97-98	Yamada 10-14	Muchnikov 16	Shu 17-21
			Groups:	USA: MSU	USA: MIT-LL	Netherlands	France	Japan	Russia	China
					250μm, natural cubes	cut from larger plate, soldered	multiple seeds	lift-off cloning	multiple seeds	multiple seeds
Type	**Requirements**	**Minimum Condition**	**Developed Technology**	**Obtained**	**Obtained**					
Geometric	Gap	Δg < 50μm	PCD Frame	<5μm	apx	?	<20μm	<50μm	<20μm	?
	Height Difference	Δh → 0	Planarization	<5μm	no	<3μm	<5μm	10μm	<10μm	?
	Step height direction	step flow direction	Polishing	Confirmed	no	toward [010]	varied	polished?	?	?
Crystallographic	Align tilt, torsion	Δα < 0.1°	PCD Frame	0.05°	1.7° stdev	0.2°	varied	clones	up to 10° (?)	3° (?)
	Align twist	Δα < 2°	PCD Plate	0.2°	0.5° stdev	?	?	2°	?	?
Growth	Shifting defects from boundary	θ > 0	Polishing Offcut	~3°	no	6° offcut to [010]	2.5° offcut to [110]	2.9° offcut to [010]	?	?
	Shifting Rate	As fast as possible	Multiple Regrowths	Confirmed	no	impractical (th=1μm/h)	impractical (th=1μm/h)	no	?	no
	Uniformity	r < 1m	Pocket Holder	Confirmed (4mm)	no	?	no	boundary present	no	?
	Area conservation	A2 >= A1	Lateral Growth	Confirmed (10mm x 10mm)	?	?	?	40mm x 60mm	no	1 inch
Scaling	Large Tiles	As large as possible	Lower Pressure (+?)	Pending	no	no	Confirmed	Confirmed	no	no
	Replication	Cloning	Ion Implantation	Confirmed	no	no	no	Confirmed	no	no

Table 10.1 Sequence of requirements for mosaic growth and the different technologies that have been developed to achieve them during this investigation. Results obtained by other groups with their relative success are included for reference.

Chapter 11

Summary, Accomplishments and Pending Work

11.1 Project Summary

The project was divided in three phases, where different aspects of the mosaic technique were explored. Phase 1 was successful in demonstrating fundamental aspects of the mosaic technique, starting with a confirmation of lateral growth conditions for the reactor, development of a new tile alignment process and confirmation that tiles can effectively merge. In this phase, only single-source tiles were used to reduce all the variables related to orientation adjustments. Several analysis techniques were developed to analyze the mosaic boundary over the resulting set of plates produced at different grown layers. Merging effects are described using a set of definitions developed which enable quantitative analysis of the mosaic technique. Results from this phase demonstrate how relative crystal misorientation and mosaicity in general decreases as the sample is grown thicker. Cracking plates started to become an issue, but it was also demonstrated that some cracks will stop propagating as samples are grown. This first phase confirms how there is plenty of potential for dynamic improvement in the mosaic technique.

After a successful first phase, the second phase of the project was to expand the process towards multiple source seeds. This approach required additional development in orientation measurement techniques as well as orientation adjustments for individual tiles. Software tools as well as growth conditions were further improved and the full set of minimum requirements for mosaic growth was compiled.

Phase three in the project was focused on applying the mosaic requirements towards the fabrication of large area substrates. Plates as large as 10 mm × 10 mm were produced where the main problem of cracking due to misorientation has been solved by reducing relative misorientations between tiles well below 0.1°. The plate still has some cracks, but they have been determined to originate from lattice curvatures caused by temperature non-uniformities during the deposition process, not by mismatched lattices.

11.2 Current Status

As covered in Chapter 3, the mosaic technique is not new. It has been over three decades since the first attempt was published [227]. Many groups around the world have made significant progress over the years, but even the best results up to date from all groups show that the technique is still not yet fully developed. It is too early to predict whether the Mosaic Technique or Heteroepitaxy will result as the dominant technology in large area diamond substrate fabrication, and both are still considered promising. Any approach is challenging because diamond growth by itself is challenging in all forms, but progress is accelerating in both cases. Contributions by this project as it compares with reports by other groups has been covered in Chapter 10 and summarized in Table 10.1. A condensed set of specific accomplishments as developed throughout this investigation is listed in the following section.

11.3 Accomplishments

11.3.1 Seed Preparation

- Developed new tile alignment technique based on individually adjusted PCD frames and plates. This alignment technique has been filed for an international patent application.
- Developed new orientation measurement techniques enabling precise offcut measurements for each tile at a resolution of 0.05°.
- Established standard tile adjustment procedures to adjust orientations, height differences and contact areas by laser cutting and polishing. Tile adjustment steps achieve consistent precision well below 0.1°.

11.3.2 Growth Conditions

- Upgraded deposition systems with closed loop Temperature/Power control enabling stable unattended operation during long term growths.
- Confirmed lateral growth conditions ensuring area conservation over multiple re-growths.
- Produced excellent top surface morphology: Smooth surfaces over boundaries and low PCD formation around sample edges.
- Obtained consistently smooth step flow growth over interfaces.
- Established system to generate individual plates from successive re-growths.
- Demonstrated cracks in samples can merge back together with thicker growths.
- Developed growth conditions designed to conserve shallow ion-implanted layers.

11.3.3 Analysis Techniques

- Defined misorientation terms (Tilt, Torsion, Twist) leading to a complete description of relative misorientation between plates.
- Defined quantitative measurement metrics (Aggregate Mosaicity, Mosaic Boundary).
- Developed two experimental methods to measure relative misorientation (XRC, XRT).
- Developed two experimental methods to measure boundary shifting (Regional Etch Pit Density, Birefringence).
- Developed line scan analysis extending the effective XRC measurement resolution below a 100 µm step size, overcoming an inherent collimator-based spot size limitation from the XRD system.
- Developed XRC Analysis mapping software actively used in this investigation and several other ongoing projects related to diamond growth.
- Established procedure to measure and quantify lattice curvatures.

11.3.4 New Conclusions

- Misalignment and mosaicity improves with thick growth on the tilt-type misorientation.
- New measurement techniques confirm mosaic boundary shifting at constant rates over grown layers due to crystallographic off-cuts.
- Lattice mismatch no longer considered the main source of internal stress in grown mosaic samples.
- Identified temperature non-uniformities as primary cause of cracks in large area samples.
- Identified maximum lattice curvature range needed to maintain structural integrity in grown samples.

- Compiled a full set of conditions necessary for successful mosaic growth.
- Shallow ion-implantations from commercially available providers are confirmed as a viable alternative for plate separation, facilitating production at industrial scales based on the lift-off technique.

11.3.5 Plate Production

- Mosaic plates 500 µm thick, composed of 4 tiles grown up to 10mm x 10mm with no cracks originating from the interfaces.
- High quality plate produced from low energy ion-implantation and lift-off technique.

11.4 Pending Work

11.4.1 Temperature non-uniformities

The main issue is evidently temperature non-uniformities resulting from the current system configuration. This is the only problem left to be solved from all the other requirements listed in Chapter 10. There are many options available known to address this issue still left to be explored such as: reducing the pressure even further, redesigning the sample holder configuration, adding sample inserts, or exploring different electromagnetic modes. Previous work from our group has already addressed these issues, generating uniform 200 µm thick PCD wafers as large as 3 inches in diameter with a Type A reactor [194]. The deposition system and necessary technological advances are already available. This uniformity issue is far from critical and at this point is just an optimization problem. A few months of iterations would probably be enough to find enhanced deposition conditions for this project.

11.4.2 Boundary Shift Rate

There is a relationship between the boundary shift rate and the offcut magnitude, but this investigation has not yet produced enough data to establish a direct correlation. Optimizing this relationship would maximize the speed at which the boundary becomes indistinguishable from single peaks.

11.4.3 Quantitative Birefringence

A new system designed to measure quantitative birefringence has very recently developed by our group but there was not enough time to examine mosaic plates from this project. The measurement technique definitely has the potential to reveal detailed information about the shifting boundary. This analysis could prove useful in quantifying internal stress, aiding in the development of improved growth and boundary shifting conditions.

11.4.4 Improved Offcut Adjustments

The offcut adjustment process has been under constant improvement since the beginning of the project, making incremental progress with every assembled mosaic seed. Our team is still developing several new design concepts to improve sample alignments reducing internal stress even further.

REFERENCES

REFERENCES

[1] S. Shen, W. Shen, S. Liu, H. Li, Y. Chen, and H. Qi, "First-principles calculations of co-doping impurities in diamond," *Materials Today Communications*, vol. 23, p. 100847, Jun. 2020.

[2] S. Shikata, "Single crystal diamond wafers for high power electronics," *Diamond and Related Materials*, vol. 65, pp. 168–175, 2016.

[3] H. Umezawa, "Recent advances in diamond power semiconductor devices," *Materials Science in Semiconductor Processing*, vol. 78, pp. 147–156, May 2018.

[4] M. W. Geis, T. C. Wade, C. H. Wuorio, T. H. Fedynyshyn, B. Duncan, M. E. Plaut, J. O. Varghese, S. M. Warnock, S. A. Vitale, and M. A. Hollis, "Progress Toward Diamond Power Field-Effect Transistors," *physica status solidi (a)*, vol. 215, no. 22, p. 1800681, 2018.

[5] M. Schreck, J. Asmussen, S. Shikata, J.-C. Arnault, and N. Fujimori, "Large-area high-quality single crystal diamond," *MRS Bulletin*, vol. 39, no. 06, pp. 504–510, 2014.

[6] M. Schreck, S. Gsell, R. Brescia, and M. Fischer, "Ion bombardment induced buried lateral growth: The key mechanism for the synthesis of single crystal diamond wafers," *Scientific Reports*, vol. 7, p. 44462, Mar. 2017.

[7] A. Charris, "Toward the Rapid Growth of High-Quality, Polycrystalline Rimless, and Large Area Single Crystal Diamond Substrates," Ph.D. dissertation, Michigan State University, 2017.

[8] H. Kagan, "Diamond radiation detectors may be forever!" *Nuclear Instruments and Methods in Physics Research Section A: Accelerators, Spectrometers, Detectors and Associated Equipment*, vol. 546, no. 1, pp. 222–227, Jul. 2005.

[9] S. Kumar, B. A. Reshi, and R. Varma, "Comparison of Silicon, Germanium, Gallium Nitride, and Diamond for using as a detector material in experimental high energy physics," *Results in Physics*, vol. 11, pp. 461–474, Dec. 2018.

[10] A. Shahzad, *Impact of Thermal Conductivity on Energy Technologies*. Books on Demand, Sep. 2018.

[11] C. Kittel, *Introduction to Solid State Physics*. Hoboken, NJ : Wiley, 2005.

[12] J. Lefèvre, J.-M. Costantini, S. Esnouf, and G. Petite, "Silicon threshold displacement energy determined by photoluminescence in electron-irradiated cubic silicon carbide," *Journal of Applied Physics*, vol. 105, no. 2, p. 023520, Jan. 2009.

[13] J. Xi, B. Liu, Y. Zhang, and W. J. Weber, "Ab initio molecular dynamics simulations of AlN responding to low energy particle radiation," *Journal of Applied Physics*, vol. 123, no. 4, p. 045904, Jan. 2018.

[14] H. Y. Xiao, F. Gao, X. T. Zu, and W. J. Weber, "Threshold displacement energy in GaN: Ab initio molecular dynamics study," *Journal of Applied Physics*, vol. 105, no. 12, p. 123527, Jun. 2009.

[15] M. Sayed, J. H. Jefferson, A. B. Walker, and A. G. Cullis, "Computer simulation of atomic displacements in Si, GaAs, and AlAs," *Nuclear Instruments and Methods in Physics Research Section B: Beam Interactions with Materials and Atoms*, vol. 102, no. 1, pp. 232–235, Aug. 1995.

[16] "NSM Archive, Physical Properties of Semiconductors," http://www.ioffe.ru/SVA/NSM/Semicond/.

[17] M. E. Thomas and W. J. Tropf, "Optical properties of diamond," in *Window and Dome Technologies and Materials IV*, vol. 2286. International Society for Optics and Photonics, Sep. 1994, pp. 144–151.

[18] P. T. B. Shaffer, "Effect of Crystal Orientation on Hardness of Beta Silicon Carbide," *Journal of the American Ceramic Society*, vol. 48, no. 11, pp. 601–602, 1965.

[19] J. F. Shackelford, Y.-H. Han, S. Kim, and S.-H. Kwon, *CRC Materials Science and Engineering Handbook*. CRC Press, Apr. 2016.

[20] S. Roberts, P. Warren, and P. Hirsch, "Knoop hardness anisotropy on {001} faces of germanium and gallium arsenide," *Journal of Materials Research*, vol. 1, pp. 162–176, Jan. 1985.

[21] D. C. Harris, *Materials for Infrared Windows and Domes: Properties and Performance*. SPIE Press, 1999.

[22] L. Gan, B. Ben-Nissan, and A. Ben-David, "Modelling and finite element analysis of ultra-microhardness indentation of thin films," *Thin Solid Films*, vol. 290-291, pp. 362–366, Dec. 1996.

[23] J. S. Goela and R. L. Taylor, "Transparent SiC for mid-IR windows and domes," in *Window and Dome Technologies and Materials IV*, vol. 2286. International Society for Optics and Photonics, Sep. 1994, pp. 46–59.

[24] A. R. Acharya, "Group III – Nitride Semiconductors: Preeminent Materials for Modern Electronic and Optoelectronic Applications," *Himalayan Physics*, vol. 5, pp. 22–26, 2014.

[25] S. M. Sze, *Semiconductor Devices, Physics and Technology*, 2nd ed. New York: John Wiley & Sons ,INC., 2002.

[26] M. D. Drory, R. H. Dauskardt, A. Kant, and R. O. Ritchie, "Fracture of synthetic diamond," *Journal of Applied Physics*, vol. 78, no. 5, pp. 3083–3088, Sep. 1995.

[27] M. D. Drory, J. W. Ager, III, T. Suski, I. Grzegory, and S. Porowski, "Hardness and fracture toughness of bulk single crystal gallium nitride," *Applied Physics Letters*, vol. 69, pp. 4044–4046, Dec. 1996.

[28] G. Johnson, P. Jones, M.-T. Wu, and T. Honda, "Determining the Strength of Brittle Thin Films for MEMS," in *Mechanical Properties of Structural Films*, C. Muhlstein and S. Brown, Eds. 100 Barr Harbor Drive, PO Box C700, West Conshohocken, PA 19428-2959: ASTM International, Jan. 2001, pp. 278–278–12.

[29] J. Kriegesmann, A. Lipp, K. Reinmuth, and K. A. Schwetz, "Strength and Fracture Toughness of Silicon Carbide," in *Ceramics for High-Performance Applications III: Reliability*, ser. Army Materials Technology Conference Series, E. M. Lenoe, R. N. Katz, and J. J. Burke, Eds. Boston, MA: Springer US, 1983, pp. 737–751.

[30] "Properties: Aluminium Nitride / Aluminum Nitride (AlN) - Properties and Applications," https://www.azom.com/properties.aspx?ArticleID=610.

[31] C. A. Sweet, K. L. Schulte, J. D. Simon, M. A. Steiner, N. Jain, D. L. Young, A. J. Ptak, and C. E. Packard, "Controlled exfoliation of (100) GaAs-based devices by spalling fracture," *Applied Physics Letters*, vol. 108, no. 1, p. 011906, Jan. 2016.

[32] J. Asmussen and D. Reinhard, Eds., *Diamond Films Handbook*, 1st ed. New York: CRC Press, Jan. 2002.

[33] C. Cercignani and E. Gabetta, *Transport Phenomena and Kinetic Theory: Applications to Gases, Semiconductors, Photons, and Biological Systems*. Springer Science & Business Media, Dec. 2007.

[34] G. Bu, D. Ciplys, M. Shur, L. J. Schowalter, S. Schujman, and R. Gaska, "Surface acoustic wave velocity in single-crystal AlN substrates," *IEEE transactions on ultrasonics, ferroelectrics, and frequency control*, vol. 53, no. 1, pp. 251–254, Jan. 2006.

[35] K. Sarasamak, S. Limpijumnong, and W. R. L. Lambrecht, "Pressure-dependent elastic constants and sound velocities of wurtzite SiC, GaN, InN, ZnO, and CdSe, and their relation to the high-pressure phase transition: A first-principles study," *Physical Review B*, vol. 82, no. 3, p. 035201, Jul. 2010.

[36] M. Kasu, "Diamond epitaxy: Basics and applications," *Progress in Crystal Growth and Characterization of Materials*, 2016.

[37] G. Chiodini, "Diamond particle detectors for high energy physics," in *2011 4th IEEE International Workshop on Advances in Sensors and Interfaces (IWASI)*, Jun. 2011, pp. 37–42.

[38] R. L. Coffie, "High Power High Frequency Transistors: A Material's Perspective," in *High-Frequency GaN Electronic Devices*, P. Fay, D. Jena, and P. Maki, Eds. Cham: Springer International Publishing, 2020, pp. 5–41.

[39] S. R. Bowman, C. G. Brown, and B. Taczak, "Optical dispersion and phase matching in gallium nitride and aluminum nitride," *Optical Materials Express*, vol. 8, no. 4, pp. 1091–1099, Apr. 2018.

[40] E. Berdermann and M. Ciobanu, "CVD-Diamond Detectors for Experiments with Hadrons, Nuclei, and Atoms," in *CVD Diamond for Electronic Devices and Sensors*, R. S. Sussmann, Ed. Chichester, UK: John Wiley & Sons, Ltd, Jan. 2009, pp. 227–255.

[41] M. Feneberg, R. A. R. Leute, B. Neuschl, K. Thonke, and M. Bickermann, "High-excitation and high-resolution photoluminescence spectra of bulk AlN," *Physical Review B*, vol. 82, no. 7, p. 075208, Aug. 2010.

[42] R. W. Francis and W. L. Worrell, "High Temperature Electrical Conductivity of Aluminum Nitride," *Journal of The Electrochemical Society*, vol. 123, no. 3, p. 430, Mar. 1976.

[43] A. Y. Polyakov, N. B. Smirnov, A. V. Govorkov, G. Dang, A. P. Zhang, F. Ren, X. A. Cao, S. J. Pearton, and R. G. Wilson, "Electrical properties and defect states in undoped high-resistivity GaN films used in high-power rectifiers," *Journal of Vacuum Science & Technology B: Microelectronics and Nanometer Structures Processing, Measurement, and Phenomena*, vol. 18, no. 3, pp. 1237–1243, May 2000.

[44] M. D. McCluskey, E. E. Haller, E. E. Haller, E. E. Haller, and E. E. Haller, *Dopants and Defects in Semiconductors*. CRC Press, Feb. 2018.

[45] A. Gicquel, K. Hassouni, F. Silva, and J. Achard, "CVD diamond films: From growth to applications," *Current Applied Physics*, vol. 1, no. 6, pp. 479–496, Dec. 2001.

[46] P. P. Altermatt, A. Schenk, F. Geelhaar, and G. Heiser, "Reassessment of the intrinsic carrier density in crystalline silicon in view of band-gap narrowing," *Journal of Applied Physics*, vol. 93, no. 3, pp. 1598–1604, Feb. 2003.

[47] E. F. Schubert, "AlN GaN intrinsic carrier density," https://www.ecse.rpi.edu/~schubert/Educational-resources/Materials-Semiconductors-III-V-nitrides.pdf.

[48] M. A. Green, "Intrinsic concentration, effective densities of states, and effective mass in silicon," *Journal of Applied Physics*, vol. 67, pp. 2944–2954, Mar. 1990.

[49] S. Poncé, D. Jena, and F. Giustino, "Hole mobility of strained GaN from first principles," *Physical Review B*, vol. 100, no. 8, p. 085204, Aug. 2019.

[50] J. Edwards, K. Kawabe, G. Stevens, and R. H. Tredgold, "Space charge conduction and electrical behaviour of aluminium nitride single crystals," *Solid State Communications*, vol. 3, no. 5, pp. 99–100, May 1965.

[51] A. Bennett, "Diamond — A Laser Engineer's Best Friend," *Optik & Photonik*, vol. 9, no. 4, pp. 49–52, 2014.

[52] N. M. Ravindra, S. R. Marthi, and A. Banobre, *Radiative Properties of Semiconductors*. Morgan & Claypool Publishers, Aug. 2017.

[53] E. Six, "CVD Diamond Handbook."

[54] B. Baliga, "Power semiconductor device figure of merit for high-frequency applications," *IEEE Electron Device Letters*, vol. 10, no. 10, pp. 455–457, Oct. 1989.

[55] E. Johnson, "Physical limitations on frequency and power parameters of transistors," in *1958 IRE International Convention Record*, vol. 13, IEEE. IEEE, 1966, pp. 27–34.

[56] R. S. Balmer, J. R. Brandon, S. L. Clewes, H. K. Dhillon, J. M. Dodson, I. Friel, P. N. Inglis, T. D. Madgwick, M. L. Markham, and T. P. Mollart, "Chemical vapour deposition synthetic diamond: Materials, technology and applications," *Journal of Physics: Condensed Matter*, vol. 21, no. 36, p. 364221, 2009.

[57] R. Keyes, "Figure of merit for semiconductors for high-speed switches," *Proceedings of the IEEE*, vol. 60, no. 2, pp. 225–225, Feb. 1972.

[58] H. Kato, T. Makino, M. Ogura, D. Takeuchi, and S. Yamasaki, "Fabrication of bipolar junction transistor on (001)-oriented diamond by utilizing phosphorus-doped n-type diamond base," *Diamond and Related Materials*, vol. 34, pp. 41–44, 2013.

[59] J. Zhang, J. Liu, Q. He, Z. Ren, K. Su, J. Zhang, and Y. Hao, "Hydrogen terminated diamond diode with high breakdown voltage," in *Sixth Symposium on Novel Optoelectronic Detection Technology and Applications*, vol. 11455. International Society for Optics and Photonics, Apr. 2020, p. 114556Y.

[60] Y. Sasama, T. Kageura, K. Komatsu, S. Moriyama, J.-i. Inoue, M. Imura, K. Watanabe, T. Taniguchi, T. Uchihashi, and Y. Takahide, "Charge-carrier mobility in hydrogen-terminated diamond field-effect transistors," *arXiv:2001.11831 [cond-mat]*, Jan. 2020.

[61] T. Matsumoto, H. Kato, T. Makino, M. Ogura, D. Takeuchi, S. Yamasaki, T. Inokuma, and N. Tokuda, "Inversion channel mobility and interface state density of diamond MOSFET using N-type body with various phosphorus concentrations," *Applied Physics Letters*, vol. 114, no. 24, p. 242101, Jun. 2019.

[62] T. Makino, K. Yoshino, N. Sakai, K. Uchida, S. Koizumi, H. Kato, D. Takeuchi, M. Ogura, K. Oyama, T. Matsumoto, H. Okushi, and S. Yamasaki, "Enhancement in emission efficiency of diamond deep-ultraviolet light emitting diode," *Applied Physics Letters*, vol. 99, no. 6, p. 061110, 2011.

[63] H. Kato, M. Wolfer, C. Schreyvogel, M. Kunzer, W. Müller-Sebert, H. Obloh, S. Yamasaki, and C. Nebel, "Tunable light emission from nitrogen-vacancy centers in single crystal diamond PIN diodes," *Applied Physics Letters*, vol. 102, no. 15, p. 151101, Apr. 2013.

[64] "Diamond Field-effect Transistors as Microwave Power Amplifiers | NTT Technical Review," https://www.ntt-review.jp/archive/ntttechnical.php?contents=ntr201008sf3.html.

[65] J. Schein, K. M. Campbell, R. R. Prasad, R. Binder, and M. Krishnan, "Radiation hard diamond laser beam profiler with subnanosecond temporal resolution," *Review of Scientific Instruments*, vol. 73, no. 1, pp. 18–22, Dec. 2001.

[66] R. P. Mildren, J. E. Butler, and J. R. Rabeau, "CVD-diamond external cavity Raman laser at 573 nm," *Optics Express*, vol. 16, no. 23, pp. 18 950–18 955, 2008.

[67] K. Chrysalidis, K. Chrysalidis, V. N. Fedosseev, B. A. Marsh, R. P. Mildren, D. J. Spence, K. D. A. Wendt, S. G. Wilkins, and E. Granados, "Continuously tunable diamond Raman laser for resonance laser ionization," *Optics Letters*, vol. 44, no. 16, pp. 3924–3927, Aug. 2019.

[68] M. A. Ferrara and L. Sirleto, "Integrated Raman Laser: A Review of the Last Two Decades," *Micromachines*, vol. 11, no. 3, p. 330, Mar. 2020.

[69] R. J. Williams, O. Kitzler, Z. Bai, S. Sarang, H. Jasbeer, A. McKay, S. Antipov, A. Sabella, O. Lux, D. J. Spence, and R. P. Mildren, "High Power Diamond Raman Lasers," *IEEE Journal of Selected Topics in Quantum Electronics*, vol. 24, no. 5, pp. 1–14, Sep. 2018.

[70] S. Stoupin, "Novel diamond X-ray crystal optics for synchrotrons and X-ray free-electron lasers," *Diamond and Related Materials*, vol. 49, pp. 39–47, 2014.

[71] S. Antipov, S. V. Baryshev, J. E. Butler, O. Antipova, Z. Liu, and S. Stoupin, "Single-crystal diamond refractive lens for focusing X-rays in two dimensions," *Journal of Synchrotron Radiation*, vol. 23, no. 1, pp. 163–168, Jan. 2016.

[72] S. Stoupin, S. A. Terentyev, V. D. Blank, Y. V. Shvyd'ko, K. Goetze, L. Assoufid, S. N. Polyakov, M. S. Kuznetsov, N. V. Kornilov, J. Katsoudas, R. Alonso-Mori, M. Chollet, Y. Feng, J. M. Glownia, H. Lemke, A. Robert, M. Sikorski, S. Song, and D. Zhu, "All-diamond optical assemblies for a beam-multiplexing X-ray monochromator at the Linac Coherent Light Source," *Journal of Applied Crystallography*, vol. 47, no. 4, pp. 1329–1336, Aug. 2014.

[73] D. Zhu, Y. Feng, S. Stoupin, S. A. Terentyev, H. T. Lemke, D. M. Fritz, M. Chollet, J. M. Glownia, R. Alonso-Mori, M. Sikorski, S. Song, T. B. van Driel, G. J. Williams, M. Messerschmidt, S. Boutet, V. D. Blank, Y. V. Shvyd'ko, and A. Robert, "Performance of a beam-multiplexing diamond crystal monochromator at the Linac Coherent Light Source," *Review of Scientific Instruments*, vol. 85, no. 6, p. 063106, Jun. 2014.

[74] T. Zhou, W. Ding, M. Gaowei, G. De Geronimo, J. Bohon, J. Smedley, and E. Muller, "Pixelated transmission-mode diamond X-ray detector," *Journal of Synchrotron Radiation*, vol. 22, no. 6, pp. 1396–1402, Nov. 2015.

[75] M. Mathes, M. Cristinziani, H. Kagan, S. Smith, W. Trischuk, J. Velthuis, and N. Wermes, "Characterization of a single crystal diamond pixel detector in a high energy particle beam," *Journal of Instrumentation*, vol. 3, no. 12, p. P12002, 2008.

[76] M. Cristinziani, "Diamond prototypes for the ATLAS SLHC pixel detector," *Nuclear Instruments and Methods in Physics Research Section A: Accelerators, Spectrometers, Detectors and Associated Equipment*, vol. 623, no. 1, pp. 174–176, Nov. 2010.

[77] K. E. Spear, "Diamond—Ceramic Coating of the Future," *Journal of the American Ceramic Society*, vol. 72, no. 2, pp. 171–191, 1989.

[78] A. Gaidarzhy, M. Imboden, P. Mohanty, J. Rankin, and B. W. Sheldon, "High quality factor gigahertz frequencies in nanomechanical diamond resonators," *Applied Physics Letters*, vol. 91, no. 20, p. 203503, Nov. 2007.

[79] Y. Tao, J. M. Boss, B. A. Moores, and C. L. Degen, "Single-crystal diamond nanomechanical resonators with quality factors exceeding one million," *Nature Communications*, vol. 5, no. 1, pp. 1–8, Apr. 2014.

[80] J. A. Davis, P. Lazarakis, J. Vohradsky, M. L. F. Lerch, M. Petasecca, S. Guatelli, and A. B. Rosenfeld, "Tissue equivalence of diamond for heavy charged particles," *Radiation Measurements*, vol. 122, pp. 1–9, Mar. 2019.

[81] A. Qureshi, W. P. Kang, J. L. Davidson, and Y. Gurbuz, "Review on carbon-derived, solid-state, micro and nano sensors for electrochemical sensing applications," *Diamond and Related Materials*, vol. 18, no. 12, pp. 1401–1420, Dec. 2009.

[82] Z. Liao and J. Farrell, "Electrochemical oxidation of perfluorobutane sulfonate using boron-doped diamond film electrodes," *Journal of Applied Electrochemistry*, vol. 39, no. 10, pp. 1993–1999, Oct. 2009.

[83] T. Das, D. Ghosh, T. K. Bhattacharyya, and T. K. Maiti, "Biocompatibility of diamond-like nanocomposite thin films," *Journal of Materials Science: Materials in Medicine*, vol. 18, no. 3, pp. 493–500, Mar. 2007.

[84] Y. Zhou and J. Zhi, "The application of boron-doped diamond electrodes in amperometric biosensors," *Talanta*, vol. 79, no. 5, pp. 1189–1196, Oct. 2009.

[85] T. Wolf, P. Neumann, K. Nakamura, H. Sumiya, T. Ohshima, J. Isoya, and J. Wrachtrup, "Subpicotesla Diamond Magnetometry," *Physical Review X*, vol. 5, no. 4, p. 041001, Oct. 2015.

[86] J. Achard, V. Jacques, and A. Tallaire, "Chemical vapour deposition diamond single crystals with nitrogen-vacancy centres: A review of material synthesis and technology for quantum sensing applications," *Journal of Physics D: Applied Physics*, vol. 53, no. 31, p. 313001, May 2020.

[87] V. Acosta and P. Hemmer, "Nitrogen-vacancy centers: Physics and applications," *MRS Bulletin*, vol. 38, no. 2, pp. 127–130, Feb. 2013.

[88] B. Hensen, H. Bernien, A. E. Dréau, A. Reiserer, N. Kalb, M. S. Blok, J. Ruitenberg, R. F. L. Vermeulen, R. N. Schouten, C. Abellán, W. Amaya, V. Pruneri, M. W. Mitchell, M. Markham, D. J. Twitchen, D. Elkouss, S. Wehner, T. H. Taminiau, and R. Hanson, "Loophole-free Bell inequality violation using electron spins separated by 1.3 kilometres," *Nature*, vol. 526, no. 7575, pp. 682–686, Oct. 2015.

[89] L. F. Dobrzhinetskaya, "Microdiamonds — Frontier of ultrahigh-pressure metamorphism: A review," *Gondwana Research*, vol. 21, no. 1, pp. 207–223, Jan. 2012.

[90] F. P. Bundy, "The P, T phase and reaction diagram for elemental carbon, 1979," *Journal of Geophysical Research: Solid Earth*, vol. 85, no. B12, pp. 6930–6936, 1980.

[91] I. V. Gridneva, Y. V. Milman, and V. I. Trefilov, "Phase transition in diamond-structure crystals during hardness measurements," *physica status solidi (a)*, vol. 14, no. 1, pp. 177–182, 1972.

[92] R. Z. Khaliullin, H. Eshet, T. D. Kühne, J. Behler, and M. Parrinello, "Nucleation mechanism for the direct graphite-to-diamond phase transition," *Nature Materials*, vol. 10, no. 9, pp. 693–697, Sep. 2011.

[93] A. E. Aleksenskii, M. V. Baidakova, A. Y. Vul', V. Y. Davydov, and Y. A. Pevtsova, "Diamond-graphite phase transition in ultradisperse-diamond clusters," *Physics of the Solid State*, vol. 39, no. 6, pp. 1007–1015, Jun. 1997.

[94] H. Xie, F. Yin, T. Yu, J.-T. Wang, and C. Liang, "Mechanism for direct graphite-to-diamond phase transition," *Scientific Reports*, vol. 4, no. 1, p. 5930, Aug. 2014.

[95] J. Robertson, "Preparation and properties of amorphous carbon," *Journal of Non-Crystalline Solids*, vol. 137-138, pp. 825–830, Jan. 1991.

[96] F. P. Bundy, W. A. Bassett, M. S. Weathers, R. J. Hemley, H. U. Mao, and A. F. Goncharov, "The pressure-temperature phase and transformation diagram for carbon; updated through 1994," *Carbon*, vol. 34, no. 2, pp. 141–153, Jan. 1996.

[97] V. R. Howes, "The Graphitization of Diamond," *Proceedings of the Physical Society*, vol. 80, no. 3, pp. 648–662, Sep. 1962.

[98] F. P. Bundy, H. T. Hall, H. M. Strong, and R. H. Wentorfjun, "Man-Made Diamonds," *Nature*, vol. 176, no. 4471, pp. 51–55, Jul. 1955.

[99] R. Abbaschian, H. Zhu, and C. Clarke, "High pressure–high temperature growth of diamond crystals using split sphere apparatus," *Diamond and Related Materials*, vol. 14, no. 11, pp. 1916–1919, Nov. 2005.

[100] H. A. Abato, "Español: Esquema de funcionamiento de una prensa BARS," 2017.

[101] H. Sumiya, N. Toda, Y. Nishibayashi, and S. Satoh, "Crystalline perfection of high purity synthetic diamond crystal," *Journal of Crystal Growth*, vol. 178, no. 4, pp. 485–494, Jul. 1997.

[102] "Diamonds for Modern Synchrotron Radiation Sources," http://www.esrf.eu/UsersAndScience/Publications/Highlights/2005/Imaging/XIO5.

[103] T. R. Anthony, "Stresses generated by impurities in diamond," *Diamond and Related Materials*, vol. 4, no. 12, pp. 1346–1352, Nov. 1995.

[104] K. Iakoubovskii and A. T. Collins, "Alignment of Ni- and Co-related centres during the growth of high-pressure–high-temperature diamond," *Journal of Physics: Condensed Matter*, vol. 16, no. 39, pp. 6897–6906, Sep. 2004.

[105] J. Michl, T. Teraji, S. Zaiser, I. Jakobi, G. Waldherr, F. Dolde, P. Neumann, M. W. Doherty, N. B. Manson, J. Isoya, and J. Wrachtrup, "Perfect alignment and preferential orientation of nitrogen-vacancy centers during chemical vapor deposition diamond growth on (111) surfaces," *Applied Physics Letters*, vol. 104, no. 10, p. 102407, Mar. 2014.

[106] E. Gaubas, T. Ceponis, A. Jasiunas, V. Kalendra, J. Pavlov, N. Kazuchits, E. Naumchik, and M. Rusetsky, "Lateral scan profiles of the recombination parameters correlated with distribution of grown-in impurities in HPHT diamond," *Diamond and Related Materials*, vol. 47, pp. 15–26, Aug. 2014.

[107] H. Sumiya, K. Harano, and K. Tamasaku, "HPHT synthesis and crystalline quality of large high-quality (001) and (111) diamond crystals," *Diamond and Related Materials*, vol. 58, pp. 221–225, 2015.

[108] M. Ohring, *Materials Science of Thin Films*. Academic Press, 2002.

[109] K. E. Spear and J. P. Dismukes, *Synthetic Diamond: Emerging CVD Science and Technology*. John Wiley & Sons, Apr. 1994.

[110] W. G. Eversole, "Synthesis of diamond," US Patent US3 030 187A, Apr., 1962.

[111] B. V. Derjaguin, D. V. Fedoseev, V. M. Lukyanovich, B. V. Spitzin, V. A. Ryabov, and A. V. Lavrentyev, "Filamentary diamond crystals," *Journal of Crystal Growth*, vol. 2, no. 6, pp. 380–384, Dec. 1968.

[112] S. P. Chauhan, J. C. Angus, and N. C. Gardner, "Kinetics of carbon deposition on diamond powder," *Journal of Applied Physics*, vol. 47, no. 11, pp. 4746–4754, Nov. 1976.

[113] S. Matsumoto, Y. Sato, M. Tsutsumi, and N. Setaka, "Growth of diamond particles from methane-hydrogen gas," *Journal of Materials Science*, vol. 17, no. 11, pp. 3106–3112, Nov. 1982.

[114] J. C. Angus, "Diamond synthesis by chemical vapor deposition: The early years," *Diamond and Related Materials*, vol. 49, pp. 77–86, Oct. 2014.

[115] M. Kamo, Y. Sato, S. Matsumoto, and N. Setaka, "Diamond synthesis from gas phase in microwave plasma," *Journal of Crystal Growth*, vol. 62, no. 3, pp. 642–644, 1983.

[116] A. Gicquel, K. Hassouni, S. Farhat, Y. Breton, C. D. Scott, M. Lefebvre, and M. Pealat, "Spectroscopic analysis and chemical kinetics modeling of a diamond deposition plasma reactor," *Diamond and Related Materials*, vol. 3, no. 4, pp. 581–586, Apr. 1994.

[117] H. Yamada, A. Chayahara, Y. Mokuno, and S.-i. Shikata, "Simulation with an improved plasma model utilized to design a new structure of microwave plasma discharge for chemical vapor deposition of diamond crystals," *Diamond and Related Materials*, vol. 17, no. 4, pp. 494–497, Apr. 2008.

[118] F. Silva, K. Hassouni, X. Bonnin, and A. Gicquel, "Microwave engineering of plasma-assisted CVD reactors for diamond deposition." *Journal of Physics: Condensed Matter*, vol. 21, no. 36, p. 364202, 2009.

[119] F. Silva, X. Bonnin, J. Scharpf, and A. Pasquarelli, "Microwave analysis of PACVD diamond deposition reactor based on electromagnetic modelling," *Diamond and Related Materials*, vol. 19, no. 5, pp. 397–403, May 2010.

[120] A. B. Muchnikov, A. L. Vikharev, A. M. Gorbachev, D. B. Radishev, V. D. Blank, and S. A. Terentiev, "Homoepitaxial single crystal diamond growth at different gas pressures and MPACVD reactor configurations," *Diamond and Related Materials*, vol. 19, no. 5-6, pp. 432–436, 2010.

[121] A. P. Bolshakov, V. G. Ralchenko, A. V. Polskiy, V. I. Konov, E. E. Ashkinazi, A. A. Khomich, G. V. Sharonov, R. A. Khmelnitsky, E. V. Zavedeev, A. V. Khomich *et al.*,

"Growth of single-crystal diamonds in microwave plasma," *Plasma physics reports*, vol. 38, no. 13, pp. 1113–1118, 2012.

[122] Q. Liang, C.-S. Yan, Y. Meng, J. Lai, S. Krasnicki, H.-K. Mao, and R. J. Hemley, "Recent advances in high-growth rate single-crystal CVD diamond," *Diamond and Related Materials*, vol. 18, no. 5-8, pp. 698–703, 2009.

[123] X. J. Li, W. Z. Tang, S. W. Yu, S. K. Zhang, G. C. Chen, and F. X. Lu, "Design of novel plasma reactor for diamond film deposition," *Diamond and Related Materials*, vol. 20, no. 4, pp. 480–484, 2011.

[124] J. J. Su, Y. F. Li, M. H. Ding, X. L. Li, Y. Q. Liu, G. Wang, and W. Z. Tang, "A dome-shaped cavity type microwave plasma chemical vapor deposition reactor for diamond films deposition," *Vacuum*, vol. 107, pp. 51–55, Sep. 2014.

[125] Q. Wang, G. Wu, S. Liu, Z. Gan, B. Yang, and J. Pan, "Simulation-Based Development of a New Cylindrical-Cavity Microwave-Plasma Reactor for Diamond-Film Synthesis," *Crystals*, vol. 9, no. 6, p. 320, Jun. 2019.

[126] J. Zhang, B. Huang, D. K. Reinhard, and J. Asmussen, "An investigation of electromagnetic field patterns during microwave plasma diamond thin film deposition," *Journal of Vacuum Science & Technology A: Vacuum, Surfaces, and Films*, vol. 8, no. 3, pp. 2124–2128, 1990.

[127] K.-P. Kuo and J. Asmussen, "An experimental study of high pressure synthesis of diamond films using a microwave cavity plasma reactor," *Diamond and Related Materials*, vol. 6, no. 9, pp. 1097–1105, 1997.

[128] Y. Gu, J. Lu, T. A. Grotjohn, T. Schuelke, and J. Asmussen, "Microwave plasma reactor design for high pressure and high power density diamond synthesis," *Diamond and Related Materials*, vol. 24, pp. 210–214, 2012.

[129] Y. Gu, "The New Generation Microwave Plasma Assisted CVD Reactor for Diamond Synthesis," Ph.D. dissertation, Michigan State University, 2011.

[130] P. K. Bachmann, H. J. Hagemann, H. Lade, D. Leers, D. U. Wiechert, H. Wilson, D. Fournier, and K. Plamann, "Thermal properties of C/H-, C/H/O-, C/H/N- and C/H/X-grown polycrystalline CVD diamond," *Diamond and Related Materials*, vol. 4, no. 5, pp. 820–826, May 1995.

[131] J. C. Angus and C. C. Hayman, "Low-Pressure, Metastable Growth of Diamond and "Diamondlike" Phases," *Science*, vol. 241, no. 4868, pp. 913–921, Aug. 1988.

[132] A. R. Badzian, T. Badzian, R. Roy, R. Messier, and K. E. Spear, "Crystallization of diamond crystals and films by microwave assisted CVD (Part II)," *Materials Research Bulletin*, vol. 23, no. 4, pp. 531–548, Apr. 1988.

[133] M. Frenklach, "The role of hydrogen in vapor deposition of diamond," *Journal of Applied Physics*, vol. 65, no. 12, p. 5142, 1989.

[134] T. R. Anthony, "Metastable Synthesis of Diamond," in *The Physics and Chemistry of Carbides, Nitrides and Borides*, ser. NATO ASI Series, R. Freer, Ed. Dordrecht: Springer Netherlands, 1990, pp. 133–158.

[135] J. C. Angus, A. Argoitia, R. Gat, Z. Li, M. Sunkara, L. Wang, Y. Wang, A. H. Lettington, and J. W. Steeds, "Chemical vapour deposition of diamond," *Philosophical Transactions of the Royal Society of London. Series A: Physical and Engineering Sciences*, vol. 342, no. 1664, pp. 195–208, Feb. 1993.

[136] J. E. Butler, R. L. Woodin, L. M. Brown, P. Fallon, A. H. Lettington, and J. W. Steeds, "Thin film diamond growth mechanisms," *Philosophical Transactions of the Royal Society of London. Series A: Physical and Engineering Sciences*, vol. 342, no. 1664, pp. 209–224, Feb. 1993.

[137] M. Chandran, "Chapter Six - Synthesis, Characterization, and Applications of Diamond Films," in *Carbon-Based Nanofillers and Their Rubber Nanocomposites*, S. Yaragalla, R. Mishra, S. Thomas, N. Kalarikkal, and H. J. Maria, Eds. Elsevier, Jan. 2019, pp. 183–224.

[138] W. L. Hsu, "Chemical erosion of graphite by hydrogen impact: A summary of the database relevant to diamond film growth," *Journal of Vacuum Science & Technology A*, vol. 6, no. 3, pp. 1803–1811, May 1988.

[139] B. B. Pate, "The diamond surface: Atomic and electronic structure," *Surface Science*, vol. 165, no. 1, pp. 83–142, Jan. 1986.

[140] N. Tokuda, "Homoepitaxial Diamond Growth by Plasma-Enhanced Chemical Vapor Deposition," in *Novel Aspects of Diamond: From Growth to Applications*, ser. Topics in Applied Physics, N. Yang, Ed. Cham: Springer International Publishing, 2019, pp. 1–29.

[141] G. Lombardi, K. Hassouni, G.-D. Stancu, L. Mechold, J. Röpcke, and A. Gicquel, "Modeling of microwave discharges of H2 admixed with CH4 for diamond deposition," *Journal of Applied Physics*, vol. 98, no. 5, p. 053303, 2005.

[142] S. J. Harris and D. G. Goodwin, "Growth on the reconstructed diamond (100) surface," *The Journal of Physical Chemistry*, vol. 97, no. 1, pp. 23–28, 1993.

[143] D. G. Goodwin, "Scaling laws for diamond chemical-vapor deposition. I. Diamond surface chemistry," *Journal of Applied Physics*, vol. 74, no. 11, p. 6888, 1993.

[144] ——, "Scaling laws for diamond chemical-vapor deposition. II. Atomic hydrogen transport," *Journal of Applied Physics*, vol. 74, no. 11, p. 6895, 1993.

[145] M. Muehle, "Process Development To Solve Critical Challenges Moving Towards Two Inch Single Crystalline Diamond Wafers," Ph.D. dissertation, Michigan State University, 2017.

[146] F. Silva, J. Achard, O. Brinza, X. Bonnin, K. Hassouni, A. Anthonis, K. De Corte, and J. Barjon, "High quality, large surface area, homoepitaxial MPACVD diamond growth," *Diamond and Related Materials*, vol. 18, no. 5-8, pp. 683–697, 2009.

[147] M. Frenklach and S. Skokov, "Surface Migration in Diamond Growth," *The Journal of Physical Chemistry B*, vol. 101, no. 16, pp. 3025–3036, Apr. 1997.

[148] W. K. Burton, N. Cabrera, F. C. Frank, and N. F. Mott, "The growth of crystals and the equilibrium structure of their surfaces," *Philosophical Transactions of the Royal Society of London. Series A, Mathematical and Physical Sciences*, vol. 243, no. 866, pp. 299–358, Jun. 1951.

[149] M. Uwaha, "Introduction to the BCF theory," *Progress in Crystal Growth and Characterization of Materials*, vol. 62, no. 2, pp. 58–68, Jun. 2016.

[150] J.-H. Zhang, Y. Zhang, Y.-H. Wen, and Z.-Z. Zhu, "Comparative study of Cu13 and Co13 clusters deposition and diffusion on the Cu(001) surface," *Computational Materials Science*, vol. 48, no. 2, pp. 250–257, Apr. 2010.

[151] U. W. Pohl, "Atomistic Aspects of Epitaxial Layer-Growth," in *Epitaxy of Semiconductors: Physics and Fabrication of Heterostructures*, ser. Graduate Texts in Physics, U. W. Pohl, Ed. Cham: Springer International Publishing, 2020, pp. 251–309.

[152] G. Ehrlich, "Atomic Displacements in One- and Two-Dimensional Diffusion," *The Journal of Chemical Physics*, vol. 44, no. 3, pp. 1050–1055, Feb. 1966.

[153] R. L. Schwoebel and E. J. Shipsey, "Step Motion on Crystal Surfaces," *Journal of Applied Physics*, vol. 37, no. 10, pp. 3682–3686, Sep. 1966.

[154] S. Blel and A. Hamouda, "Formation of Ag and Co nanowires at the step of the Cu(100) vicinal surfaces: A kinetic Monte Carlo study," *Vacuum*, vol. 151, Feb. 2018.

[155] K. Yagi, H. Minoda, and M. Degawa, "Step bunching, step wandering and faceting: Self-organization at Si surfaces," *Surface Science Reports*, vol. 43, no. 2, pp. 45–126, Jul. 2001.

[156] F. K. de Theije, J. J. Schermer, and W. J. P. van Enckevort, "Effects of nitrogen impurities on the CVD growth of diamond: Step bunching in theory and experiment," *Diamond and Related Materials*, vol. 9, no. 8, pp. 1439–1449, Aug. 2000.

[157] T. Yamamoto, S. D. Janssens, R. Ohtani, D. Takeuchi, and S. Koizumi, "Toward highly conductive n-type diamond: Incremental phosphorus-donor concentrations assisted by surface migration of admolecules," *Applied Physics Letters*, vol. 109, no. 18, p. 182102, Oct. 2016.

[158] Wang, P. Duan, Z. Cao, C. Liu, Y. Peng, X. Hu, X. Wang, and D. Wang, "Homoepitaxy Growth of Single Crystal Diamond under 300 torr Pressure in the MPCVD System," *Materials*, vol. 12, no. 23, p. 3953, Nov. 2019.

[159] Y. Tanaka, K. Miyake, and A. Saito, "Diamond-like Carbon Film for Bearing Parts and Its Mass Production Technology," *SEI Technical Review*, no. 88, p. 5, Apr. 2019.

[160] J. Robertson, "Diamond-like amorphous carbon," *Materials Science and Engineering: R: Reports*, vol. 37, no. 4, pp. 129–281, 2002.

[161] N. Ludovic, "Characterization of a dislocation (Edge dislocation)," http://www.ltas-cm3.ulg.ac.be/FractureMechanics/overview_P3.html.

[162] A. K. Batra and M. D. Aggarwal, "Linear Defects: Dislocations," *Field Guide to Crystal Growth*, pp. 14–15, Aug. 2018.

[163] C. Newey and G. Weaver, *Materials Principles and Practice*. Butterworth-Heinemann, 1990.

[164] B. E. Williams, H. S. Kong, and J. T. Glass, "Electron microscopy of vapor phase deposited diamond," *Journal of Materials Research*, vol. 5, no. 4, pp. 801–810, Apr. 1990.

[165] S. Masuya, K. Hanada, T. Uematsu, T. Moribayashi, H. Sumiya, and M. Kasu, "Determination of the type of stacking faults in single-crystal high-purity diamond with

a low dislocation density of <50 cm-2 by synchrotron X-ray topography," *Japanese Journal of Applied Physics*, vol. 55, no. 4, p. 040303, Mar. 2016.

[166] D. J. Paul, "Prof. Douglas J. Paul :: University of Glasgow :: School of Engineering," http://userweb.eng.gla.ac.uk/douglas.paul/SiGe/misfit.html.

[167] S. C. Jain and M. Willander, "Chapter 3 - Mechanism of Strain Relaxation," in *Semiconductors and Semimetals*, ser. Silicon-Germanium Strained Layers and Heterostructures. Elsevier, Jan. 2003, vol. 74, pp. 41–60.

[168] T. Sato, K. Ohashi, T. Sudoh, K. Haruna, and H. Maeta, "Thermal expansion of a high purity synthetic diamond single crystal at low temperatures," *Physical Review B*, vol. 65, no. 9, p. 092102, Feb. 2002.

[169] A. R. Lang, M. Moore, A. P. W. Makepeace, W. Wierzchowski, and C. M. Welbourn, "On the Dilatation of Synthetic Type Ib Diamond by Substitutional Nitrogen Impurity," *Philosophical Transactions of the Royal Society A: Mathematical, Physical and Engineering Sciences*, vol. 337, no. 1648, pp. 497–520, 1991.

[170] N. Tsubouchi, H. Umezawa, Y. Mokuno, A. Chayahara, and S.-i. Shikata, "Lattice structure of a freestanding nitrogen doped large single crystal diamond plate fabricated using the lift-off process: X-ray diffraction studies," *Diamond and Related Materials*, vol. 25, pp. 119–123, May 2012.

[171] A. Tallaire, J. Achard, F. Silva, O. Brinza, and A. Gicquel, "Growth of large size diamond single crystals by plasma assisted chemical vapour deposition: Recent achievements and remaining challenges," *Comptes Rendus Physique*, vol. 14, no. 2-3, pp. 169–184, 2013.

[172] A. Tallaire, J. Barjon, O. Brinza, J. Achard, F. Silva, V. Mille, R. Issaoui, A. Tardieu, and A. Gicquel, "Dislocations and impurities introduced from etch-pits at the epitaxial growth resumption of diamond," *Diamond and Related Materials*, vol. 20, no. 7, pp. 875–881, Jul. 2011.

[173] M. Schreck, M. Mayr, O. Klein, M. Fischer, S. Gsell, A. F. Sartori, and B.-C. Gallheber, "Multiple role of dislocations in the heteroepitaxial growth of diamond: A brief review," *physica status solidi (a)*, vol. 213, no. 8, pp. 2028–2035, 2016.

[174] A. Tallaire, M. Kasu, K. Ueda, and T. Makimoto, "Origin of growth defects in CVD diamond epitaxial films," *Diamond and Related Materials*, vol. 17, no. 1, pp. 60–65, Jan. 2008.

[175] N. Tokuda, H. Umezawa, K. Yamabe, H. Okushi, and S. Yamasaki, "Growth of atomically step-free surface on diamond {111} mesas," *Diamond and Related Materials*, vol. 19, no. 4, pp. 288–290, Apr. 2010.

[176] W. J. P. van Enckevort, G. Janssen, J. J. Schermer, and L. J. Giling, "Step-related growth phenomena on exact and misoriented {001} surfaces of CVD-grown single-crystal diamonds," *Diamond and Related Materials*, vol. 4, no. 4, pp. 250–255, Apr. 1995.

[177] N. Lee and A. Badzian, "A study on surface morphologies of (001) homoepitaxial diamond films," *Diamond and Related Materials*, vol. 6, no. 1, pp. 130–145, Jan. 1997.

[178] D. Takeuchi, H. Watanabe, S. Yamanaka, H. Okushi, and K. Kajimura, "Homoepitaxial diamond films grown by step-flow mode in various misorientation angles of diamond substrates," *Diamond and Related Materials*, vol. 9, no. 3, pp. 231–235, Apr. 2000.

[179] M. N. R. Ashfold, J. P. Goss, B. L. Green, P. W. May, M. E. Newton, and C. V. Peaker, "Nitrogen in Diamond," *Chemical Reviews*, vol. 120, no. 12, pp. 5745–5794, Jun. 2020.

[180] S. Eaton-Magaña and J. Shigley, "Observations on CVD-Grown Synthetic Diamonds: A Review," *Gems and Gemology*, vol. 52, p. 222, Nov. 2016.

[181] C. M. Breeding and J. E. Shigley, "The "Type" Classification System of Diamonds and Its Importance in Gemology," *Gems & Gemology*, vol. 45, no. 2, pp. 96–111, Jul. 2009.

[182] F. Silva, J. Achard, X. Bonnin, O. Brinza, A. Michau, A. Secroun, K. De Corte, S. Felton, M. Newton, and A. Gicquel, "Single crystal CVD diamond growth strategy by the use of a 3D geometrical model: Growth on (113) oriented substrates," *Diamond and Related Materials*, vol. 17, no. 7, pp. 1067–1075, Jul. 2008.

[183] F. Silva, X. Bonnin, J. Achard, O. Brinza, A. Michau, and A. Gicquel, "Geometric modeling of homoepitaxial CVD diamond growth: I. The {100}{111}{110}{113} system," *Journal of Crystal Growth*, vol. 310, no. 1, pp. 187–203, Jan. 2008.

[184] A. Tallaire, J. Achard, O. Brinza, V. Mille, M. Naamoun, F. Silva, and A. Gicquel, "Growth strategy for controlling dislocation densities and crystal morphologies of single crystal diamond by using pyramidal-shape substrates," *Diamond and Related Materials*, vol. 33, pp. 71–77, Mar. 2013.

[185] A. Boussadi, A. Tallaire, M. Kasu, J. Barjon, and J. Achard, "Reduction of dislocation densities in single crystal CVD diamond by confinement in the lateral sector," *Diamond and Related Materials*, vol. 83, pp. 162–169, Mar. 2018.

[186] A. Tallaire, O. Brinza, V. Mille, L. William, and J. Achard, "Reduction of Dislocations in Single Crystal Diamond by Lateral Growth over a Macroscopic Hole," *Advanced Materials*, 2017.

[187] A. Tallaire, V. Mille, O. Brinza, T. N. Tran Thi, J. M. Brom, Y. Loguinov, A. Katrusha, A. Koliadin, and J. Achard, "Thick CVD diamond films grown on high-quality type IIa HPHT diamond substrates from New Diamond Technology," *Diamond and Related Materials*, vol. 77, pp. 146–152, Aug. 2017.

[188] Y. Mokuno, A. Chayahara, Y. Soda, Y. Horino, and N. Fujimori, "Synthesizing single-crystal diamond by repetition of high rate homoepitaxial growth by microwave plasma CVD," *Diamond and Related Materials*, vol. 14, no. 11-12, pp. 1743–1746, 2005.

[189] H. Yamada, A. Chayahara, Y. Mokuno, Y. Soda, Y. Horino, S.-I. Shikata, and N. Fujimori, "Qualitative correspondences of experimentally obtained growth rates and morphology of single-crystal diamond with numerical predictions of plasma and gas dynamics in microwave discharges for various substrate holder shapes," *Japanese Journal of Applied Physics, Part 1: Regular Papers and Short Notes and Review Papers*, vol. 45, no. 10 B, pp. 8177–8182, 2006.

[190] H. Yamada, Y. Mokuno, A. Chayahara, Y. Horino, and S.-i. Shikata, "Predominant physical quantity dominating macroscopic surface shape of diamond synthesized by microwave plasma CVD," *Diamond and Related Materials*, vol. 16, no. 3, pp. 576–580, Mar. 2007.

[191] Y. Mokuno, A. Chayahara, Y. Soda, H. Yamada, Y. Horino, and N. Fujimori, "High rate homoepitaxial growth of diamond by microwave plasma CVD with nitrogen addition," *Diamond and Related Materials*, vol. 15, no. 4-8, pp. 455–459, 2006.

[192] S. Nad, A. Charris, and J. Asmussen, "MPACVD growth of single crystalline diamond substrates with PCD rimless and expanding surfaces," *Applied Physics Letters*, vol. 109, no. 16, p. 162103, 2016.

[193] A. Charris, S. Nad, and J. Asmussen, "Exploring constant substrate temperature and constant high pressure SCD growth using variable pocket holder depths," *Diamond and Related Materials*, vol. 76, pp. 58–67, Jun. 2017.

[194] S. S. Zuo, "Microwave plasma-assisted CVD polycrystalline diamond films deposition at higher pressure conditions," Ph.D. dissertation, Michigan State University, 2009.

[195] S. Nad, Y. Gu, and J. Asmussen, "Growth strategies for large and high quality single crystal diamond substrates," *Diamond and Related Materials*, vol. 60, pp. 26–34, 2015.

[196] B. Yang, Q. Shen, Z. Gan, and S. Liu, "Improving the edge quality of single-crystal diamond growth by a substrate holder – An analysis," *Comptes Rendus Physique*, vol. 20, no. 6, pp. 583–592, Sep. 2019.

[197] Z.-Y. Ren, J.-F. Zhang, J.-C. Zhang, S.-R. Xu, C.-F. Zhang, K. Su, Y. Li, and Y. Hao, "Growth and Characterization of the Laterally Enlarged Single Crystal Diamond Grown by Microwave Plasma Chemical Vapor Deposition," *Chinese Physics Letters*, vol. 35, no. 7, p. 078101, 2018.

[198] Z.-Y. Ren, J. Liu, K. Su, J.-F. Zhang, J.-C. Zhang, S.-R. Xu, and Y. Hao, "Multiple enlarged growth of single crystal diamond by MPCVD with PCD-rimless top surface," *Chinese Physics B*, vol. 28, no. 12, p. 128103, Dec. 2019.

[199] M. Muehle, M. F. Becker, T. Schuelke, and J. Asmussen, "Substrate crystal recovery for homoepitaxial diamond synthesis," *Diamond and Related Materials*, vol. 42, pp. 8–14, Feb. 2014.

[200] J. F. Ziegler, *Ion Implantation Science and Technology*. Elsevier, Dec. 2012.

[201] N. R. Parikh, J. D. Hunn, E. McGucken, M. L. Swanson, C. W. White, R. A. Rudder, D. P. Malta, J. B. Posthill, and R. J. Markunas, "Single-crystal diamond plate liftoff achieved by ion implantation and subsequent annealing," *Applied Physics Letters*, vol. 61, no. 26, pp. 3124–3126, Dec. 1992.

[202] J. B. Posthill, D. P. Malta, T. P. Humphreys, G. C. Hudson, R. E. Thomas, R. A. Rudder, and R. J. Markunas, "Method of fabricating a free-standing diamond single crystal using growth from the vapor phase," *Journal of Applied Physics*, vol. 79, no. 5, pp. 2722–2727, 1996.

[203] J. D. Hunn, S. P. Withrow, C. W. White, R. E. Clausing, L. Heatherly, C. Paul Christensen, and N. R. Parikh, "The separation of thin single crystal films from bulk diamond by MeV implantation," *Nuclear Instruments and Methods in Physics Research Section B: Beam Interactions with Materials and Atoms*, vol. 99, no. 1, pp. 602–605, 1995.

[204] J. F. Ziegler, M. D. Ziegler, and J. P. Biersack, "SRIM – The stopping and range of ions in matter (2010)," *Nuclear Instruments and Methods in Physics Research Section B: Beam Interactions with Materials and Atoms*, vol. 268, no. 11, pp. 1818–1823, Jun. 2010.

[205] G. Braunstein, A. Talmi, R. Kalish, T. Bernstein, and R. Beserman, "Radiation damage and annealing in Sb implanted diamond," *Radiation Effects*, vol. 48, no. 1-4, pp. 139–143, Jan. 1980.

[206] J. Suk, H. Kim, W. C. Lim, J. Yune, S. Moon, J. A. Eliades, J. Kim, J. Lee, and J. Song, "Fabrication of thin diamond membranes by using hot implantation and ion-cut methods," *Applied Physics Letters*, vol. 110, no. 10, p. 101903, Mar. 2017.

[207] M. Marchywka, P. E. Pehrsson, D. J. Vestyck, and D. Moses, "Low energy ion implantation and electrochemical separation of diamond films," *Applied Physics Letters*, vol. 63, no. 25, p. 3521, 1993.

[208] S. Koizumi, H. Umezawa, J. Pernot, and M. Suzuki, *Power Electronics Device Applications of Diamond Semiconductors*, ser. Woodhead Publishing Series in Electronic and Optical Materials. Woodhead Publishing, Jun. 2018.

[209] Y. Mokuno, A. Chayahara, and H. Yamada, "Synthesis of large single crystal diamond plates by high rate homoepitaxial growth using microwave plasma CVD and lift-off process," *Diamond and Related Materials*, vol. 17, no. 4-5, pp. 415–418, 2008.

[210] N. Tsubouchi, Y. Mokuno, A. Chayahara, and S. Shikata, "Crystallinity of freestanding large undoped single crystal diamond plates produced using pre-ion-implanted substrates and lift-off processes," *Diamond and Related Materials*, vol. 19, no. 10, pp. 1259–1262, 2010.

[211] H. Yamada, A. Chayahara, Y. Mokuno, N. Tsubouchi, S. Shikata, and N. Fujimori, "Developments of elemental technologies to produce inch-size single-crystal diamond wafers," *Diamond and Related Materials*, vol. 20, no. 4, pp. 616–619, 2011.

[212] M. P. Gaukroger, P. M. Martineau, M. J. Crowder, I. Friel, S. D. Williams, and D. J. Twitchen, "X-ray topography studies of dislocations in single crystal CVD diamond," *Diamond and Related Materials*, vol. 17, no. 3, pp. 262–269, 2008.

[213] H. Yamada, A. Chayahara, and Y. Mokuno, "Method to increase the thickness and quality of diamond layers using plasma chemical vapor deposition under (H, C, N, O) system," *Diamond and Related Materials*, vol. 101, p. 107652, Jan. 2020.

[214] W. Holber and R. J. Basnett, "Toroidal Plasma Processing Apparatus with a Shaped Workpiece Holder," US Patent US20 200 010 976A1, Jan., 2020.

[215] Y. Mokuno, A. Chayahara, H. Yamada, and N. Tsubouchi, "Improving purity and size of single-crystal diamond plates produced by high-rate CVD growth and lift-off process using ion implantation," *Diamond and Related Materials*, vol. 18, no. 10, pp. 1258–1261, 2009.

[216] J. E. Ayers, T. Kujofsa, P. Rago, and J. Raphael, *Heteroepitaxy of Semiconductors: Theory, Growth, and Characterization, Second Edition.* CRC Press, Oct. 2016.

[217] M. Schreck, K.-H. Thürer, and B. Stritzker, "Limitations of the process window for the bias enhanced nucleation of heteroepitaxial diamond films on silicon in the time domain," *Journal of Applied Physics*, vol. 81, no. 7, pp. 3092–3095, 1997.

[218] M. Schreck, H. Roll, and B. Stritzker, "Diamond/Ir/SrTiO3: A material combination for improved heteroepitaxial diamond films," *Applied Physics Letters*, vol. 74, no. 5, pp. 650–652, Jan. 1999.

[219] S. Gsell, T. Bauer, J. Goldfuß, M. Schreck, and B. Stritzker, "A route to diamond wafers by epitaxial deposition on silicon via iridium/yttria-stabilized zirconia buffer layers," *Applied Physics Letters*, vol. 84, no. 22, pp. 4541–4543, 2004.

[220] S. Fujii, Y. Nishibayashi, S. Shikata, A. Uedono, and S. Tanigawa, "Study of various types of diamonds by measurements of double crystal x-ray diffraction and positron annihilation," *Journal of Applied Physics*, vol. 78, no. 3, pp. 1510–1513, Aug. 1995.

[221] S.-W. Kim, Y. Kawamata, R. Takaya, K. Koyama, and M. Kasu, "Growth of high-quality one-inch free-standing heteroepitaxial (001) diamond on (11 2 $^{-}$0) sapphire substrate," *Applied Physics Letters*, vol. 117, no. 20, p. 202102, Nov. 2020.

[222] K. Ichikawa, K. Kurone, H. Kodama, K. Suzuki, and A. Sawabe, "High crystalline quality heteroepitaxial diamond using grid-patterned nucleation and growth on Ir," *Diamond and Related Materials*, vol. 94, pp. 92–100, Apr. 2019.

[223] L. Mehmel, R. Issaoui, O. Brinza, A. Tallaire, V. Mille, J. Delchevalrie, S. Saada, J. C. Arnault, F. Bénédic, and J. Achard, "Dislocation density reduction using overgrowth on hole arrays made in heteroepitaxial diamond substrates," *Applied Physics Letters*, vol. 118, no. 6, p. 061901, Feb. 2021.

[224] G. Janssen and L. J. Giling, ""Mosaic" growth of diamond," *Diamond and Related Materials*, vol. 4, no. 7, pp. 1025–1031, May 1995.

[225] M. W. Geis, N. N. Efremow, R. Susalka, J. C. Twichell, K. A. Snail, C. Spiro, B. Sweeting, and S. Holly, "Mosaic diamond substrates approaching single-crystal quality using cube-shaped diamond seeds," *Diamond and Related Materials*, vol. 4, no. 1, pp. 76–82, Dec. 1994.

[226] M. W. Geis and J. C. Angus, "Diamond Film Semiconductors," *Scientific American*, vol. 267, no. 4, pp. 84–89, 1992.

[227] M. W. Geis, H. I. Smith, A. Argoitia, J. Angus, G.-H. M. Ma, J. T. Glass, J. Butler, C. J. Robinson, and R. Pryor, "Large-area mosaic diamond films approaching single-crystal quality," *Applied Physics Letters*, vol. 58, no. 22, pp. 2485–2487, Jun. 1991.

[228] M. W. Geis, "Device quality diamond substrates," *Diamond and Related Materials*, vol. 1, no. 5, pp. 684–687, Apr. 1992.

[229] R. W. Pryor, M. W. Geis, and H. R. Clark, "Growth Technique For Large Area Mosaic Diamond Films†," *MRS Online Proceedings Library (OPL)*, vol. 242, 1992/ed.

[230] J. E. Field and J. E. Field, *Properties of Natural and Synthetic Diamond*. Elsevier Science, Nov. 1992.

[231] H. Yamada, A. Chayahara, Y. Mokuno, H. Umezawa, S. Shikata, and N. Fujimori, "Fabrication of 1 Inch Mosaic Crystal Diamond Wafers," *Applied Physics Express*, vol. 3, no. 5, p. 051301, 2010.

[232] H. Yamada, A. Chayahara, H. Umezawa, N. Tsubouchi, Y. Mokuno, and S. Shikata, "Fabrication and fundamental characterizations of tiled clones of single-crystal diamond with 1-inch size," *Diamond and Related Materials*, vol. 24, pp. 29–33, 2012.

[233] C. Findeling-Dufour, A. Gicquel, and R. Chiron, "Growth of large single-crystal diamond layers: Analysis of the junctions between adjacent diamonds," *Diamond and Related Materials*, vol. 7, no. 7, pp. 986–998, Jul. 1998.

[234] H. Yamada, A. Chayahara, Y. Mokuno, N. Tsubouchi, and S. Shikata, "Uniform growth and repeatable fabrication of inch-sized wafers of a single-crystal diamond," *Diamond and Related Materials*, vol. 33, pp. 27–31, 2013.

[235] H. Yamada, A. Chayahara, Y. Mokuno, Y. Kato, and S. Shikata, "A 2-in. mosaic wafer made of a single-crystal diamond," *Applied Physics Letters*, vol. 104, no. 10, p. 102110, 2014.

[236] J. B. Posthill, D. P. Malta, G. C. Hudson, R. E. Thomas, T. P. Humphreys, R. C. Hendry, R. A. Rudder, and R. J. Markunas, "Demonstration of a method to fabricate a large-area diamond single crystal," *Thin Solid Films*, vol. 271, no. 1, pp. 39–49, Dec. 1995.

[237] C. Findeling-Dufour and A. Gicquel, "Study for fabricating large area diamond single-crystal layers," *Thin Solid Films*, vol. 308-309, pp. 178–185, Oct. 1997.

[238] A. B. Muchnikov, D. B. Radishev, A. L. Vikharev, A. M. Gorbachev, A. V. Mitenkin, M. N. Drozdov, Y. N. Drozdov, and P. A. Yunin, "Characterization of interfaces in mosaic CVD diamond crystal," *Journal of Crystal Growth*, vol. 442, pp. 62–67, May 2016.

[239] X. Wang, P. Duan, Z. Cao, C. Liu, D. Wang, Y. Peng, X. Xu, and X. Hu, "Surface Morphology of the Interface Junction of CVD Mosaic Single-Crystal Diamond," *Materials*, vol. 13, no. 1, p. 91, Jan. 2020.

[240] C. Wang, M. Irie, and T. Ito, "Growth and characterization of hillock-free high quality homoepitaxial diamond films," *Diamond and Related Materials*, vol. 9, no. 9, pp. 1650–1654, Sep. 2000.

[241] J. Cumalat, K. Stenson, and S. Wagner, "Mosaic Diamond Detector Research for High Energy Physics Experiments," University of Colroado, Tech. Rep. CUHEP-ADR-2013-01r1, 1156591, Sep. 2014.

[242] A. Matsushita, N. Fujimori, Y. Tsuchida, N. Ohtani, D. Dojima, K. Koide, T. Kaneko, and S. Shikata, "Evaluation of diamond mosaic wafer crystallinity by electron backscatter diffraction," *Diamond and Related Materials*, vol. 101, p. 107558, Jan. 2020.

[243] G. Shu, B. Dai, V. G. Ralchenko, A. A. Khomich, E. E. Ashkinazi, A. P. Bolshakov, S. N. Bokova-Sirosh, K. Liu, J. Zhao, J. Han, and J. Zhu, "Epitaxial growth of mosaic diamond: Mapping of stress and defects in crystal junction with a confocal Raman spectroscopy," *Journal of Crystal Growth*, vol. 463, pp. 19–26, Apr. 2017.

[244] H. Yamada, A. Chayahara, Y. Mokuno, Y. Kato, and S. Shikata, "Effects of crystallographic orientation on the homoepitaxial overgrowth on tiled single crystal diamond clones," *Diamond and Related Materials*, vol. 57, pp. 17–21, Aug. 2015.

[245] G. Shu, B. Dai, V. G. Ralchenko, A. P. Bolshakov, A. A. Khomich, E. E. Ashkinazi, J. Han, and J. Zhu, "Growth of three-dimensional diamond mosaics by microwave plasma-assisted chemical vapor deposition," *CrystEngComm*, vol. 20, no. 2, pp. 198–203, 2018.

[246] G. Shu, B. Dai, V. G. Ralchenko, A. P. Bolshakov, A. A. Khomich, E. E. Ashkinazi, V. Y. Yurov, K. Yao, K. Liu, J. Zhao, J. Han, and J. Zhu, "Vertical-substrate epitaxial growth of single-crystal diamond by microwave plasma-assisted chemical vapor deposition," *Journal of Crystal Growth*, vol. 486, pp. 104–110, Mar. 2018.

[247] G. Shu, B. Dai, A. Bolshakov, W. Wang, Y. Wang, K. Liu, J. Zhao, J. Han, and J. Zhu, "Coessential-connection by Microwave Plasma Chemical Vapor Deposition: A Common

Process Towards Wafer Scale Single Crystal Diamond," *Functional Diamond*, vol. 0, no. ja, pp. 1–22, Jan. 2021.

[248] C. Weiß, E. Griesmayer, C. Guerrero, S. Altstadt, J. Andrzejewski, L. Audouin, G. Badurek, M. Barbagallo, V. Bécares, F. Bečvář, F. Belloni, E. Berthoumieux, J. Billowes, V. Boccone, D. Bosnar, M. Brugger, M. Calviani, F. Calviño, D. Cano-Ott, C. Carrapiço, F. Cerutti, E. Chiaveri, M. Chin, N. Colonna, G. Cortés, M. A. Cortés-Giraldo, M. Diakaki, C. Domingo-Pardo, I. Duran, R. Dressler, N. Dzysiuk, C. Eleftheriadis, A. Ferrari, K. Fraval, S. Ganesan, A. R. García, G. Giubrone, M. B. Gómez-Hornillos, I. F. Gonçalves, E. González-Romero, F. Gunsing, P. Gurusamy, A. Hernández-Prieto, D. G. Jenkins, E. Jericha, Y. Kadi, F. Käppeler, D. Karadimos, N. Kivel, P. Koehler, M. Kokkoris, M. Krtička, J. Kroll, C. Lampoudis, C. Langer, E. Leal-Cidoncha, C. Lederer, H. Leeb, L. S. Leong, R. Losito, A. Mallick, A. Manousos, J. Marganiec, T. Martínez, C. Massimi, P. F. Mastinu, M. Mastromarco, M. Meaze, E. Mendoza, A. Mengoni, P. M. Milazzo, F. Mingrone, M. Mirea, W. Mondalaers, C. Paradela, A. Pavlik, J. Perkowski, A. Plompen, J. Praena, J. M. Quesada, T. Rauscher, R. Reifarth, A. Riego, M. S. Robles, F. Roman, C. Rubbia, M. Sabaté-Gilarte, R. Sarmento, A. Saxena, P. Schillebeeckx, S. Schmidt, D. Schumann, G. Tagliente, J. L. Tain, D. Tarrío, L. Tassan-Got, A. Tsinganis, S. Valenta, G. Vannini, V. Variale, P. Vaz, A. Ventura, R. Versaci, M. J. Vermeulen, V. Vlachoudis, R. Vlastou, A. Wallner, T. Ware, M. Weigand, T. Wright, and P. Žugec, "A new CVD diamond mosaic-detector for (n, α) cross-section measurements at the n_TOF experiment at CERN," *Nuclear Instruments and Methods in Physics Research Section A: Accelerators, Spectrometers, Detectors and Associated Equipment*, vol. 732, pp. 190–194, Dec. 2013.

[249] V. G. Ralchenko, E. Pleuler, F. X. Lu, D. N. Sovyk, A. P. Bolshakov, S. B. Guo, W.Z.Tang, I.V.Gontar, A. A. Khomich, E. V. Zavedeev, and V. I. Konov, "Fracture strength of optical quality and black polycrystalline CVD diamonds," *Diamond and Related Materials*, vol. 23, pp. 172–177, Mar. 2012.

[250] G. Shu, V. Ralchenko, A. Bolshakov, K. Liu, M. Sun, K. Yao, J. Zhao, G. Gao, B. Liu, W. Wang, Y. Li, X. Liu, B. Dai, and J. Zhu, "Coessential-joint growth technology of large size single crystal diamond," *Chinese Journal of Nature*, vol. 41, no. 02, pp. 100–110, 2019.

[251] S. Ohmagari, H. Yamada, N. Tsubouchi, H. Umezawa, A. Chayahara, S. Tanaka, and Y. Mokuno, "Large reduction of threading dislocations in diamond by hot-filament chemical vapor deposition accompanying W incorporations," *Applied Physics Letters*, vol. 113, no. 3, p. 032108, Jul. 2018.

[252] S. Ohmagari, H. Yamada, N. Tsubouchi, H. Umezawa, A. Chayahara, Y. Mokuno, and D. Takeuchi, "Toward High-Performance Diamond Electronics: Control and Annihila-

tion of Dislocation Propagation by Metal-Assisted Termination," *physica status solidi (a)*, vol. 216, no. 21, p. 1900498, 2019.

[253] S. Ohmagari, H. Yamada, N. Tsubouchi, H. Umezawa, A. Chayahara, A. Seki, F. Kawaii, H. Saitoh, and Y. Mokuno, "Schottky barrier diodes fabricated on diamond mosaic wafers: Dislocation reduction to mitigate the effect of coalescence boundaries," *Applied Physics Letters*, vol. 114, no. 8, p. 082104, Feb. 2019.

[254] P. Sittimart, S. Ohmagari, and T. Yoshitake, "Enhanced in-plane uniformity and breakdown strength of diamond Schottky barrier diodes fabricated on heteroepitaxial substrates," *Japanese Journal of Applied Physics*, vol. 60, no. SB, p. SBBD05, Jan. 2021.

[255] K. W. Hemawan, "Investigation of microwave cavity applicators for plasma assisted CVD diamond synthesis and plasma assisted combustion," Ph.D. dissertation, Michigan State University, 2010.

[256] J. Asmussen and D. K. Reinhard, "Method for treating a surface with a microwave or UHF plasma and improved apparatus," US Patent US4 585 668A, Apr., 1986.

[257] J. Lu, Y. Gu, T. A. Grotjohn, T. Schuelke, and J. Asmussen, "Experimentally defining the safe and efficient, high pressure microwave plasma assisted CVD operating regime for single crystal diamond synthesis," *Diamond and Related Materials*, vol. 37, pp. 17–28, 2013.

[258] J. Lu, "Single crystal microwave plasma assisted chemical vapor diamond synthesis at high pressures and high power densities," Ph.D. dissertation, Michigan State University, 2013.

[259] S. Nad, "Growth and characterization of large, high quality single crystal diamond substrates via microwave plasma assisted chemical vapor deposition," Ph.D. dissertation, Michigan State University, 2016.

[260] S. Nicley, "The boron doping of single crystal diamond for high power diode applications," Ph.D. dissertation, Michigan State University, 2015.

[261] T. Schuelke and T. A. Grotjohn, "Diamond polishing," *Diamond and Related Materials*, vol. 32, pp. 17–26, Feb. 2013.

[262] O. A. Ivanov, A. B. Muchnikov, V. V. Chernov, S. A. Bogdanov, A. L. Vikharev, and J. E. Butler, "Experimental study of hydrogen plasma etching of (100) single crystal diamond in a MPACVD reactor," *Materials Letters*, vol. 151, pp. 115–118, Jul. 2015.

[263] V. Yurov, E. Bushuev, A. Bolshakov, E. Ashkinazi, I. Antonova, E. Zavedeev, A. Khomich, V. Voronov, and V. Ralchenko, "Etching Kinetics of (100) Single Crystal Diamond Surfaces in a Hydrogen Microwave Plasma, Studied with In Situ Low-Coherence Interferometry," *physica status solidi (a)*, vol. 214, no. 11, p. 1700177, Nov. 2017.

[264] "University of Pennsylvania X-Ray Crystallography Facility - Online Course: Introduction," http://macxray.chem.upenn.edu/course/intro1.html.

[265] A. Macrander, M. Erdmann, N. Kujala, S. Stoupin, S. Marathe, X. Shi, M. Wojcik, D. Nocher, R. Conley, J. Sullivan, K. Goetze, J. Maser, and L. Assoufid, "X-ray optics testing beamline 1-BM at the advanced photon source," *AIP Conference Proceedings*, vol. 1741, no. 1, p. 030030, Jul. 2016.

[266] X. R. Huang and A. T. Macrander, "Influence of Stacking Faults on Diffraction Properties of Diamond by Synchrotron Topographic Imaging," *AIP Conference Proceedings*, vol. 1234, no. 1, pp. 191–194, Jun. 2010.

[267] W. H. Zachariasen, "A general theory of X-ray diffraction in crystals," *Acta Crystallographica*, vol. 23, no. 4, pp. 558–564, Oct. 1967.

[268] A. M. Khounsary, R. K. Smither, S. Davey, and A. Purohit, "Diamond monochromator for high heat flux synchrotron x-ray beams," Argonne National Lab., Tech. Rep. ANL/XFD/CP–78515, 1992.

[269] "Rigaku Introduces Newest SmartLab Intelligent X-ray Diffraction (XRD) System," https://www.prweb.com/releases/2018/03/prweb15375945.htm.

[270] F. Cembali, R. Fabbri, M. Servidori, A. Zani, G. Basile, G. Cavagnero, A. Bergamin, and G. Zosi, "Precise X-ray relative measurement of lattice parameters of silicon wafers by multiple-crystal Bragg-case diffractometry. Computer simulation of the experiment," *Journal of Applied Crystallography*, vol. 25, no. 3, pp. 424–431, Jun. 1992.

[271] C.-P. Kau, T.-S. Gau, and S.-L. Chang, "X-ray diffraction studies of miscut crystal surfaces and overlayers: A dynamical diffraction approach," *Materials Chemistry and Physics*, vol. 41, no. 2, pp. 128–133, Jul. 1995.

[272] L. D. Doucette, M. P. da Cunha, and R. J. Lad, "Precise orientation of single crystals by a simple x-ray diffraction rocking curve method," *Review of Scientific Instruments*, vol. 76, no. 3, p. 036106, Mar. 2005.

[273] "Technology -Methods to Manufacture Large Area Single Crystal Diamond Substrates," http://msut.technologypublisher.com/technology/28830.

[274] "Gaussian Models - MATLAB & Simulink," https://www.mathworks.com/help/curvefit/gaussian.html.

[275] ManosHacker, "English: 2d square lattice, bent," https://w.wiki/fCA, 10 July 2014, 02:59:18.

[276] R. Smither, K. A. Saleem, M. Beno, C. Kurtz, A. Khounsary, and N. Abrosimov, "Diffraction efficiency and diffraction bandwidth of thermal-gradient and composition-gradient crystals," *Review of Scientific Instruments*, vol. 76, no. 12, p. 123107, Dec. 2005.

[277] W. D. Callister and D. G. Rethwisch, *Fundamentals of Materials Science and Engineering: An Integrated Approach*, 3rd ed. John Wiley & Sons, 2007.

[278] K. W. Böer, "Crystal Defects," in *Handbook of the Physics of Thin-Film Solar Cells*, K. W. Böer, Ed. Berlin, Heidelberg: Springer, 2013, pp. 51–71.

[279] "Element Six | Synthetic Diamond and Tungsten Carbide Experts," https://www.e6.com/en/home.